Analyzing Field Performance of Steel-Reinforced HDPE (SRHDPE) Pipes during Installation and under Traffic Loading

By

Fei Wang

Submitted to the Department of Civil, Environmental, and Architectural Engineering and the Graduate Faculty of the University of Kansas in partial fulfillment of the requirements for the degree of Doctor of Philosophy

Prof. Jie Han, Chairperson

Prof. Ronald M. Barrett-Gonzalez

Prof. Anil Misra

Prof. Robert L. Parsons

Prof. Steven D. Schrock

Date Defended: 11/30/2015

The dissertation committee for Fei Wang certifies that this is the approved version of the following dissertation:

Analyzing Field Performance of Steel-Reinforced HDPE (SRHDPE) Pipes during Installation and under Traffic Loading

Prof. Jie Han, Chairperson

Date Approved: 01/28/2016

ABSTRACT

Steel-Reinforced High Density Polyethylene (SRHDPE) pipes have been developed and introduced to the market to overcome the disadvantages of HDPE pipes (i.e., low strength and stiffness and high creep deformation and potential buckling) and steel pipes (i.e., corrosion). SRHDPE pipe uses steel ribs to carry load and plastic covers of steel ribs to prevent any possible corrosion. However, no widely accepted method is available to design the SRHDPE pipe. The objective of this study is to evaluate the field performance of the SRHDPE pipes during installation and under traffic loading and to recommend the parameters for the design method.

A field test was conducted in Kansas City, Kansas to investigate the performance of the SRHDPE pipe during installation and under static loading. Four 2.13 m-long SRHDPE pipes with a diameter of 0.6 m were connected and buried in a trench with a dimension of 1.52 m wide, 9.15 m long, and 1.40 m deep. Two types of material were backfilled in the trench, namely, AB3 aggregate and crushed stone. Two pipes were buried in the AB3 aggregate section while the other two pipes were installed in the crushed stone section. Deflections in the vertical, horizontal, and 45^{o} directions from the pipe crown were monitored during the backfilling process. Earth pressures and strains of the SRHDPE pipes were measured during the construction.

Hardening soil model was used to simulate the backfill material under compaction, while an Equivalent Modulus Method (EMM) was proposed to model the SRHDPE pipe. The test results from the field were used to verify the effectiveness of the proposed numerical model. A parametric study was conducted to evaluate the effects of the trench width, the soil cover thickness, the magnitude of the compaction load and the friction angle of the backfill material on the performance of the SRHDPE pipe during installation. Earth pressure, pipe deflection, strains and moments in the pipes were measured to analyze the pipe performance.

Considering the relative higher stiffness of the SRHDPE pipe, the pipe deflections during installation and under traffic loading should be small. The existing soil arching theories widely used to analyze the load transfer mechanism assume the soil is at a yielding state. This assumption may not be realistic in the soil cover above the SRHDPE pipe since the shear stress in the soil is highly related to the displacement. Partially-mobilized soil arching equations were derived in this study to investigate the load transfer mechanism in the soil cover above the SRHDPE pipe during installation and under traffic loading considering the displacement of backfill material in the soil cover is less than the critical displacement (i.e., a displacement of the soil can induce a shear stress equal to the shear strength). Two calculation examples are provided to illustrate the calculation procedures.

Long-term monitoring (i.e. two years) of the performance of the SRHDPE pipe was conducted at a field test site in Lawrence, Kansas. The trench was 2 m wide, 1.72 m deep and 24 m long. Three SRHDPE pipes with a dimeter of 0.9 m and a length of 7.2 m were installed in the trench. Half length of the trench was backfilled with AB3 aggregate and the other half was backfilled with crushed stone. Earth pressures, pipe deflections in the horizontal and the vertical directions, strains on steel ribs, plastic covers and plastic valleys were monitored. Two empirical correlations were developed to predict the Vertical Arching Factor (VAF) on the pipe top and the pipe stiffness factor (EI) at a specific time.

ACKNOWLEDGEMENTS

First of all, I want to express my great appreciation to my advisor Prof. Jie Han who raised me up when I was down, encouraged me when I was struggling and confused, and supported me when any help for me was needed. His advice leads me all the way forward through my Ph.D. study at the University of Kansas. His knowledge, wisdom, and diligence impressed and influenced me deeply since I met him eight years ago. I will remember my wonderful academic life under the supervision of Prof. Han forever.

I would also like to thank my Ph.D. committee members, Profs. Robert L. Parsons, Anil Misra, Steven D. Schrock, and Ronald M. Barrett-Gonzalez for their valuable advices and also for serving as members of my graduate advisory committee.

This study was financially supported by the Kansas Department of Transportation (KDOT). Mr. James J. Brennan, the Chief Geotechnical Engineer of KDOT, was the monitor for this project. Contech Construction Products, Inc. provided SRHDPE pipes and connectors. The KDOT Maintenance Branch for the great assistance in the field test. I also want to thank Mr. Matthew Maksimowiczat (laboratory manager at KU) for providing great technical support during my tests.

I want to thank all Kansas University Geotechnical Society (KUGS) members for their great cooperation and help throughout my study. I want to give special thanks to Mr. Jun Guo, Dr. Xiaohun Sun, and Dr. Ryan Corey for the guidance in my lab tests and numerical modeling.

Finally, my gratitude is given to my family for the understanding throughout my study. My wife Jiewen Zhao and my little daughter Kate Wang brought a lot of happiness to me which inspired me to finish my study.

TABLE OF CONENTS

LIST OF FIGURES

LIST OF TABLES

CHAPTER 1 INTRODUCTION

1.1 Background

High density polyethylene (HDPE) pipes have been widely used all over the world for several decades due to their light weight, low cost, and chemical resistance (Masada and Sargand, 2007). More than 54% of natural gas pipeline projects all over the world have used HDPE pipes. In the United States, this percentage is even higher than 90%. However, HDPE pipes also have some disadvantages, including low strength, limited pressure rating, and high potential buckling, which limit the usage of HDPE pipes in some specific working conditions.

Metal pipe is another popularly used pipe type in the practice, which has a high load carrying capacity for dead and live loads. However, corrosion is a major problem for metal pipes considering the long service life of buried pipes (typically, 50-100 years). The corroding process of metal pipes is affected by the following factors: (1) the material properties of pipes; (2) the chemical properties of the soil surrounding the pipes; (3) the groundwater properties and conditions; and (4) the fluid transmitting in the pipes. Corrosion is a result of electrochemical electron exchanges between metals and solutions (Centers for Diseases Control and Prevention, 2015).

Steel-reinforced high-density polyethylene (SRHDPE) pipes combine the advantages of metal and HDPE pipes to overcome their disadvantages (Khatri et al., 2013; Corey et al. 2014 and Wang et al., 2015). **Figure 1.1** shows the schematic representation of an SRHDPE pipe section. The steel rib is used to enhance the load-carrying capacity of the pipe and the plastic cover for the

steel ribs prevents any possible corrosion. Based on the document published by American Concrete Pipe Association (ACPA) (2009), SRHDPE pipe is being marketed nationwide for storm drainage systems. Due to the advantages of the SRHDPE pipes, they would become a popular type of pipe to be used for replacement of corroded pipes in the pipeline system. The ASTM published a specification for SRHDPE pipes to be used for non-pressure drainage and sewerage purposes. This specification covers the requirements and test methods for materials, dimensions, workmanship, impact resistance, pipe stiffness, flattening, buckling tensile strength, shipment, and storage for SRHDPE pipes (ASTM F2562, 2008).

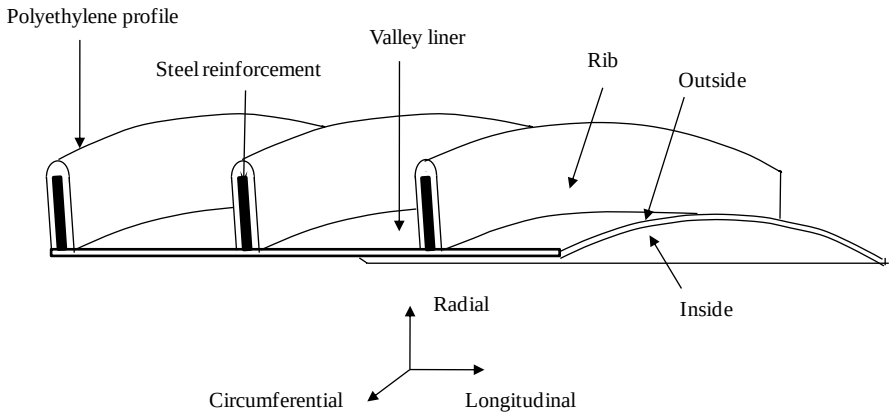

Figure 1.1 Schematic representation of a cross section of the corrugated SRHDPE pipe (after ASTM F2562, 2008)

1.2 Problem Statement

Several standards and specifications have been developed for design, installation, and materials for precast concrete pipe, corrugated metal pipes, and HDPE pipes. **Table 1.1** lists the coverage of these standards and specifications. However, no nationally accepted installation

standard or design method is available for SRHDPE pipes, which limit their usage. Even though ASTM F2652 (2008) provides the requirements for the SRHDPE pipe product, it does not provide engineers any guidance or instructions how to design SRHDPE pipes during installation and under traffic loading.

Table 1.1 Specifications for different types of pipes (ACPA, 2009)

Specifications	Material	Construction & Installation	Trench width
Concrete Pipe	ASTM C78, AASHTO-M170, ASTM C14	ASTM C1479, AASHTO LRFD Bridge Construction Specifications (Sec. 27)	ASTM C1479, AASHTO section 27
HDPE Pipe	ASTM F2306, AASHTO M294	ASTM D2321, AASHTO LRFD Bridge Construction Specifications (Sec. 30)	AASHTO section 30
SRHDPE Pipe	ASTM F2562	Not Available	Not Available

Moser and Folkman (2008) summarized that flexible pipe design is mainly based on the following three parameters: (a) load; (b) soil stiffness in the pipe zone; and (c) pipe stiffness. Load on pipes can be divided as static load and live load (i.e., traffic loading). Load transfer mechanism of buried pipes is attributed to trench width, soil cover depth, and backfill and its compaction degree. Soil stiffness in the pipe zone also depends on the backfill properties and the compaction and construction procedures. In addition, long-term reduction in HDPE pipe stiffness is always considered in HDPE pipe design due to the material relaxation and temperature effect. However, no existing method can be used to evaluate the performance of the SRHDPE pipe during installation, under traffic loading and in long-term service conditions. The lack of knowledge about the SRHDPE performance would limit the expansion of this innovative pipe.

1.3 Objectives

The objective of this research was to investigate the performance of the SRHDPE pipes during installation, under traffic loading and in long-term service conditions. This objective has been achieved by the following tasks:

- To investigate the installation of SRHDPE pipes considering the compaction effect;
- To develop the calculation methods for the load at the top of the SRHDPE pipe during installation and under traffic loading; and
- To evaluate the field performance of the SRHDPE pipe with time and establish evaluation criteria for long-term performance of SRHDPE pipes in field.

1.4 Research Methodology

The research methodology adopted for this study includes: (1) a literature review on pipe installation, load transfer mechanism above buried pipes, and long-term behavior of HDPE pipes, (2) laboratory tests to determine the properties of the backfill materials (i.e., Aggregate Base Class 3 (AB3) and crushed stone) used in the field tests, (3) a field test to investigate the performance of the SRHDPE pipes during installation and under static loading, (4) numerical modeling on the compaction effect on the performance of the SRHDPE pipes; (5) theoretical derivations of the calculation methods of the load at the pipe top during installation and under traffic loading; and

(6) long-time monitoring of pipes in the field to investigate the long-term performance of the SRHDPE pipe.

1.5 Organization of Dissertation

This dissertation includes seven chapters. Chapter one is the introduction and the background of this research. Chapter two focuses on the literature review. Chapter three presents a field installation test in Kansas City, KS. Chapter four presents the numerical modeling on the compaction effect of the performance of the SRHDPE pipe. Chapter five develops the calculation method for the load at the pipe top during installation and under traffic loading. Chapter six discusses the evaluation of the long-term performance of the SRHDPE pipe based on the monitoring data of the tested pipes in the field. Chapter seven presents the conclusions and recommendations from this research.

CHAPTER 2 LITERATURE REVIEW

2.1 Introduction

Based on the objectives of this research, the literature review includes the following sections: (a) installation of pipes; (b) load transfer mechanism above buried pipes; (c) long-term behavior of flexible pipe considering material relaxation and stiffness reduction; (d) existing research on the SRHDPE pipe; and (e) performance limits of buried pipes used in the pipe installation design.

2.2 Installation of Pipes

Researchers have investigated the following aspects of the pipe installation: (a) determination of the trench width and/or soil cover thickness (e.g., Katona, 1988; and Moser and Folkman, 2008); (b) backfill material selection and compaction (e.g., Molin, 1981); and (c) stress and strain evaluation of the pipes after construction (Meyerhof and Baike, 1963; and Moser and Folkman, 2008). These investigations may be attributed to the following reasons: (1) trench width and soil cover thickness are related to the load transfer mechanism during pipe service period and they are essential for buried pipe design and evaluation; (2) backfill material provides support for flexible pipes and is therefore important for their performance (compaction is mainly responsible for peaking deflection of a pipe and enhances its capacity to carry more loads); and (3) stresses and strains of a pipe after construction serve as the initial condition of the pipe before subjected to

service loading (the initial condition is essential to evaluate the pipe behavior during service loading, especially possible failure).

2.2.1 Trench Width and Soil Cover Thickness

Marston and Anderson (1913) proposed the following equation to calculate the load at the top of a rigid pipe in a ditch condition:

$$W_d = C_d \gamma B_c B_d \tag{2-1}$$

where W_d = the load at the crown of the pipe; C_d = the load coefficient for ditch pipes; γ = the unit weight of backfill; B_c = the horizontal breadth of the pipe (i.e., the diameter of the pipe); B_d = the horizontal width of the ditch at top of the pipe.

Equation (2-1) shows that the vertical load on the top of the pipe is proportional to the width of the trench. It reflects the soil arching effect in the soil cover through the load coefficient, i.e., the narrower trench can induce more reduction in the vertical load on the pipe top. Under this condition, the load on the rigid pipe would increase from the prism load due to the negative soil arching effect. Moser and Folkman (2008) found that when the trench width was equal to or greater than a specific value, the ditch condition could be treated as the embankment condition. The trench width when the ditch condition turns into the embankment condition is referred to as the *transition width*.

ASTM C1479 (2013) and AASHTO (2012) required the trench width for a rigid pipe should be equal to four thirds of the pipe outside diameter. Space for compaction at both sides of

the pipes should be adequate. ASTM D 2321 (2014) suggests that the minimum width of the trench for a thermoplastic pipe should be not less than the greater of the pipe outside diameter plus 400 mm or pipe outside diameter times 1.25 plus 300 mm. AASHTO (2012) recommended that the trench width for an HDPE pipe should be 1.50 times the pipe outside diameter plus 300 mm

Adequate soil cover thickness not only ensures the safety of the pipe subjected to compaction loads above the pipe but also affects the load distribution mechanism around the buried pipe. Based on Boussinesq's solution, Moser and Folkman (2008) concluded that the live load effect induced by an AASHTO H-20 truck above a buried pipe can be neglected when the soil cover thickness is greater than 2.4 m. AASHTO (2012) suggested that the negligible depth of the live load caused by an H-25 truck is 3 m. Katona (1988) proposed an empirical formula to determine of the minimum soil cover thickness for a pipe subjected to various standard AASHTO truck loadings without considering the effect of the pavement. **Table 2.1** summarizes the minimum soil cover thickness from the KDOT specification (2007). ASTM D 2321 (2014) provides the minimum soil cover thickness requirements for different types of backfill material. For a good soil (referred to as Class I), a soil cover thickness of greater of 0.6 m and one diameter of the pipe is required before construction vehicles are allowed to pass; while for a Class III soil, the soil cover thickness should be at least the greater of 1.0 m and one diameter of the pipe. A 1.3 m thick soil cover should be placed above the pipe before hydro-hammer compaction.

Table 2.1 Minimum cover over the top of the pipe (KDOT, 2007)

PE and PVC diameter (m)	Axle Load (kN) 80 to 222	222 to 333	333 to 489	489 to 667
	Soil Cover (m)			
0.3 to 1	0.6	0.75	1.0	1.0
1.1 to 1.2	1.0	1.0	1.0	1.3
1.35 to 1.5	1.0	1.0	1.05	1.3

2.2.2 Backfill Material

Properties of backfill material are essential to the performance of flexible pipes. For flexible pipes, cohesionless backfill materials are widely adopted. However, silty sand and clayey sand may be also acceptable for economic purposes for pipes under low to moderate loads (Molin, 1981). For cohesive soil, compaction should be operated at the optimum moisture content (Rogers, 1985; ASTM A798, 2013; and ASTM D2321, 2014).

Different types of soils are commonly classified based on the Unified Soil Classification System (USCS) (ASTM D2487, 2011). The soil types defined in the USCS are divided into five classes according to the thermoplastic pipe design (ASTM D2321, 2014). **Table 2.2** lists the backfill material classifications for thermoplastic pipes.

Table 2.2 Backfill material classifications for thermoplastic pipes (ASTM D2321, 2014)

Backfill class	I	II	III	IV	V
Soil type symbols	Manufactured	GW	GM	ML	OL
	angular	GP	GC	CL	OH
	granular	SW	SM	MH	PT
	material	SP	SC	CH	

Note: All symbols listed in this table follow the definitions in ASTM D2487 (2011).

ASTM C1479 (2013) defined the backfill categories for rigid pipe design. It combined the USCS system with the AASTHO soil classification system (AASHTO M145, 2003) and proposed four categories of backfill material for rigid pipes as shown in **Table 2.3**.

Table 2.3 Backfill material categories for rigid pipes (ASTM C1479, 2013)

Soil category	USCS	AASHTO
I	SW, SP, GW, GP	A-1, A-3
II	GM, GC, SM, SC, CL, ML, CL-ML with 30% or more retained on #200 sieve	A-2-4, A-2-5, A-2-6, or A-4, or A-6 with 30% or more retained on #200 sieve
III	CL, ML, CL-ML with less than 30% retained on #200 sieve	A-2-7, or A-4, or A-6 with less than 30% retained on #200 sieve
IV	MH, CH, OL, OH, PT	A-5, A-7

Note: all symbols listed in the above table follow the definitions in ASTM D2487 and AASHTO M145.

The stiffness of a flexible pipe influences the compaction effect of backfill soil because more deflection of the pipe causes more stress relaxation in the pipe. AASHTO (2012) requires a minimum pipe stiffness to minimize this distortion of flexible pipes during installation. Over-

compacted soil could limit the lateral deformation of the pipe after construction so that it increased the possibility of pipe buckling at the pipe crown (Cameron, 2006). Initial peaking deflection of flexible pipes if not excessive is favorable (Webb et al, 1996). The non-symmetric backfilling at two sides of the pipe could cause distortion of the pipe (Rogers, et al., 1995 and Cameron, 2006). The clear spacing of the profile ribs for profile pipes should be smaller than 0.6 or larger than 2.6 times the maximum size of backfill soil to prevent potential voids around the pipe (Sargand et al., 1996). The particle size of the bedding soil should be smaller than 32 mm (AASHTO 2012).

Controlled Low Strength Material (CLSM), known as flowable fill, is also adopted as the backfill material in pipeline projects. Typical mix of CLSM uses sand, fly ash, and water; however, cement content is on the order of 30-60 kg/m^3, which is extremely low relative to structural concrete mixes (Howard, 1996).

The trench width and backfill material are essential for buried pipe design. However, for SRHDPE pipes, no specification is available for design. It is necessary to investigate the width and backfill effects on the mechanical behavior of the SRHDPE pipes.

2.2.3 Compaction Techniques and Simulation Methods

Compaction is important for installation of buried pipes, especially for flexible pipes. Compaction has been recognized as the source for increasing the load carrying capacity of a flexible pipe due to its low stiffness (Katona, 1978). Vibratory plate compactor and rammer are two commonly used compactors in pipe installation. A rammer has a smaller size of foot and higher compaction pressure and is normally used for the hunch zone compaction. Duncan et al.

(1991) proposed a method to estimate the earth pressure induced by compaction using different types of compactors from different manufactures.

Duncan et al. (1991) explained the mechanism of compaction as follows: (1) during compaction, both the vertical and horizontal stresses in soil increase due to the weight of the compactor and the dynamic force generated by the compactor; (2) when the compactor moves away, the increment of the vertical stress becomes zero; however, the horizontal earth pressure decrease to a certain value, which is referred to as the residual horizontal stress. Several investigators (e.g., Duncan and Seed, 1986; Seed and Duncan, 1986; Filz and Duncan, 1996; Chen and Fang, 2008; and Yang et al., 2012) developed different methods to simulate the compaction-induced stresses in different types of applications, for example, retaining walls and buried culverts. These methods can be grouped into two types and are briefly discussed below:

(1) Hysteretic K_0 method. The hysteretic K_0 method was originally proposed by Duncan and Seed (1986). They assumed the multiple cycles of loading and unloading happened under a K_0-condition; in other words, the lateral stress increment is proportional to the vertical stress increment by a factor of K_0. They treated the compaction-induced residual horizontal stress as an over-consolidation case, and the lateral earth pressure coefficient can be modified from K_0 considering the over-consolidation effect. **Figure 2.1** presents the basic concept of the K_0 hysteretic method, which can explained by the following stress path: (a) the initial stress condition in the soil can be represented as Point A in **Figure 2.1** due to the overburden pressure caused by the placement of the backfill lift; (b) during the compaction, both the vertical and horizontal stresses increase to Point B following the K_0 line; (c) when the compaction load moves away, the stress condition moves to Point C following the K_p line; (4) the vertical stress continues to decrease following the K_p line to Point D at the same vertical pressure of Point A. During the compaction, the maximum

increase of the horizontal stress is Δ; and the residual horizontal stress can be expressed as $\beta\Delta$, where β is fraction of Δ in fully reloading. They also proposed simplified steps which allow hand calculations by this method. These steps are briefly described as follows:

- Determine the maximum increase of the horizontal stress using Boussinesq's solution by the compaction load. A factor between zero and one should be multiplied by the maximum horizontal stress increase to obtain the residual horizontal stress increase;
- Calculate the residual horizontal stress as the summation of the residual horizontal stress increase and the horizontal stress at rest; and
- The near surface horizontal stress should be limited to the Rankine passive lateral earth pressure.

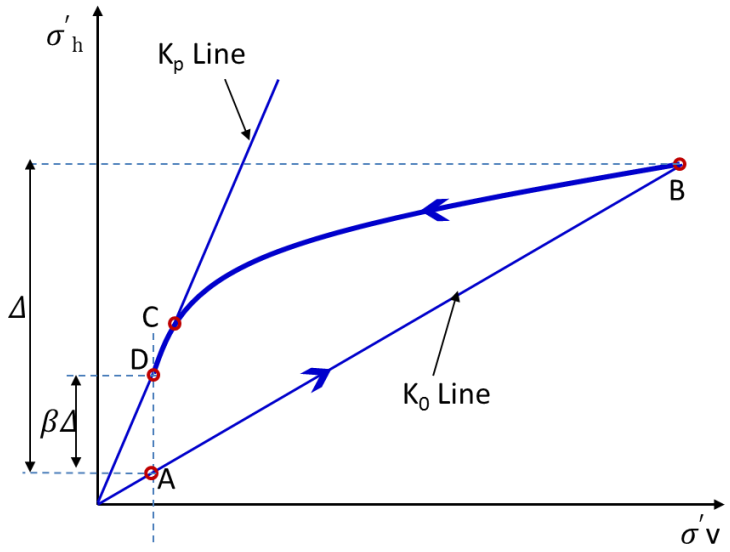

Figure 2.1 Basis concept of the hysteretic K0 method (Duncan and Seed, 1986)

Seed and Duncan (1986) incorporated the hysteretic K_0 method into the FE analysis to analyze the compaction effect in retaining walls and buried culverts. In their model, the

compaction-induced horizontal stress was applied to the mesh to simulate the compaction. They ignored the relaxation of the residual horizontal stress due to the deformation of the mesh. This method was also evaluated by Filz and Duncan (1996) through laboratory and field tests. Chen and Fang (2008) developed a laboratory-scale model test to investigate the compaction effect on sand without any consideration of movement of the wall behind the sand. They compared the measured data, the Jaky at-rest earth pressure line, the Rankine active earth pressure line, and the Rankine passive earth pressure line. They concluded that in the compaction zone, the lateral stress could be calculated using the Rankine passive earth pressure theory, while below the compaction zone, the lateral stress was close to the Jaky at-rest earth pressure. Yang et al. (2012) modified the hysteretic K_0 method and allowed the stress path to cross the Rankine passive earth pressure line to consider the geocell reinforcement effect on the soil during the compaction.

The hysteretic K_0 method uses the concept of the over-consolidation ratio to consider the compaction-induced horizontal stress. In this method, the compaction effect is expressed by an equivalent over-consolidation ratio. This method has proven difficult to analyze the elastic-plastic behavior of the soil during compaction (Elshimi and Moore, 2013).

(2) Additional surcharge method. Additional surcharge method is a more straight forward method. One should apply additional surcharge load to the soil to simulate the compaction; however, the load has to be maintained all the way even after the completion of the compaction. Katona (1978) proposed to apply a temporary surcharge on the surface of the newly placed layer to simulate the compaction around the pipe. This surcharge remains after the compaction, which is not real in the engineering practice. In order to solve this problem, Katona (1978) suggested applying a pressure in the opposite direction on the placed layer before the placement of the next layer. This method was named as the “squeeze layer method”. However, the above two methods could not create a

comparable lateral movement of soil during compaction because of the use of the elastic model. Furthermore, the additional load could not be removed; otherwise the residual deformation would become zero. The lateral earth pressure coefficient during the compaction is assumed as K_0, which is not accurate because the soil moves towards the pipe. Taleb and Moore (1999) proposed to apply horizontal pressure directly on the soil to simulate the compaction. The magnitude of the earth pressure can be calculated as the vertical earth pressure times the passive lateral earth pressure coefficient. Elshimi and Moore (2013) considered the possible relaxation of the horizontal pressure caused by the deformation of the flexible pipe and suggested to use two as the lateral earth pressure coefficient. The applied horizontal load should be maintained after the completion of compaction. McGrath et al. (1999) summarized the above-mentioned techniques as shown in **Figure 2.2** and assessed the advantages and disadvantages of each method. Katona (2015 a and b) modified the Duncan-Selig soil model to simulate the plastic-like behavior of soil during compaction and incorporated the modified model into the Culvert Analysis and DEsign (CANDE) software for different types of pipes to demonstrate the effectiveness of this model.

Even though the above methods can simulate the compaction-induced stresses, they cannot address the following three characteristics of compaction behavior:

- applied load should be removed after the completion of the compaction for each layer;
- residual horizontal stress and strain should remain after the compaction load is removed;
- pipe interacts with soil during the compaction should be reflected. In other words, the deformation of the pipe is induced by the lateral deformation of the surrounding soil.

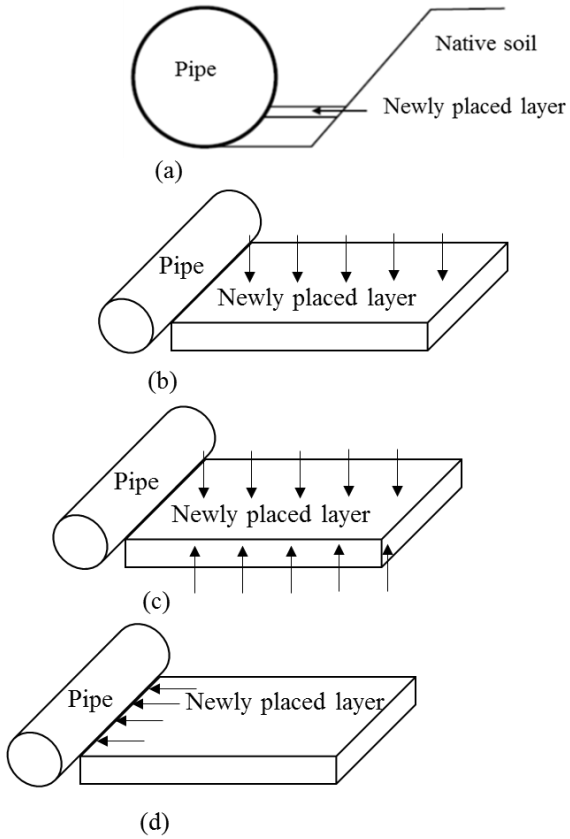

Figure 2.2 Compaction models for buried pipes by applying additional pressure: (a) placement of a new layer; (b) applying vertical pressure method; (c) squeeze layer method; and (d) applying horizontal pressure method (modified from McGrath et al., 1999)

2.3 Load Transfer Mechanism above Buried Pipes

2.3.1 Loads and Deflections of Pipes during Installation

Several methods have been proposed to estimate the earth pressure at the top of pipes (Marston and Anderson, 1913; Spangler, 1941; McGrath, et al., 1999; Sargand et al., 2001 and 2008; and Corey et al., 2014). Marston and Anderson (1913) developed a theoretical solution for

the vertical load transferred to the top of a pipe considering the friction between the soil above the pipe and the trench walls. Marston (1930) investigated the earth pressures on pipes buried in an embankment. He suggested that the embankment height could be increased by introducing a compressible layer over the pipe to enhance the soil arching effect. Spangler (1941) assumed a horizontal passive earth pressure distributed like a parabolic at the side of the flexible pipe, and the magnitude of this horizontal pressure was a function of the soil stiffness and the pipe horizontal deflection. Spangler (1962) considered the complete and incomplete projection conditions to calculate the earth pressures on the top of pipes buried in an embankment. However, the Marston-Spangler theory likely overestimates the earth pressure at the top of the pipe by the following reasons: (1) the backfill above the pipe was assumed at an active state, thus underestimating the friction between the trench wall and the backfill material; and (2) the cohesion of the backfill soil was neglected (Schofield, 1980; Moser and Folkman, 2008; and McAffee and Valsangkar, 2008). In addition, the existing methods (Marston, 1930; Spangler, 1941; and Spangler, 1962) using the Marston-Spangler theory require ten empirical parameters. Determination of each parameter includes uncertainty. Therefore, the uncertainty of earth pressure estimation could be enlarged (Moser and Folkman, 2008). Höeg (1968) investigated the pipe-soil interaction and found that the influence zone of the pipe-soil interaction was one to two times the rigid pipe diameter. Meyerhof and Adams (1968) developed a formula for the earth pressure on a buried rigid pipe similar to the Marston-Spangler theory. They assumed that the lateral earth pressure coefficient of the soil above the rigid pipe was 0.95. The American Water Works Association (Lischer, 1969) adopted a simplified approach based on the Marston-Spangler theory. In this method, the product of the settlement ratio (r_{sd}) and the projection ratio (p) was estimated as 0.75. The frustum calculation method (Matyas and Davis, 1983 and Li, 2009) assumed the soil load on a buried rigid pipe was

equal to the weight of the soil column above the pipe. The China Association for Engineering Construction Standardization (CECS, 2004) simplified the earth pressure acting on the top of a buried flexible pipe as that equal to the geostatic stress of the overburden soil. AASHTO (2012) has widely been used in the design of buried pipes in the United States. This standard includes two methods to calculate the earth pressure on the top of the pipe: (1) the soil prism pressure which is equal to the overburden stress at the top of the pipe level; (2) the soil arch pressure which is equal to the overburden stress multiplied by the vertical arching factor (VAF). The VAF can be calculated by an empirical method, which was originally proposed by McGrath (1998). The vertical load on the top of the pipe can be calculated as follows:

$$W = VAF \times W_{sp} \tag{2-2}$$

For a fully-bonded interface between pipe and soil (McGrath et.al., 1999),

$$VAF = 1.06 - 0.96\left(\frac{S_H - 0.7}{S_H + 1.75}\right) \tag{2-3}$$

For a free-slip interface between pipe and soil (McGrath et al., 1999 and AASHTO, 2012)

$$VAF = 0.76 - 0.71\left(\frac{S_H - 0.7}{S_H + 1.75}\right) \tag{2-4}$$

$$S_H = \frac{M_s}{EA/R} \tag{2-5}$$

where W_{sp} = the soil prism load above a pipe; S_H = the hoop stiffness parameter; M_s= the constrained modulus of elasticity of soil; E = the Young's modulus of elasticity of the pipe material; A = the wall cross-sectional area of the pipe; and R = the radius of the pipe.

The load on a pipe during installation can cause the deflection of the pipe. Spangler (1941) considered the following reasons for the ability of a flexible pipe to carry the load: (1) the redistribution of the load around the pipe; and (2) the passive pressure at sides of the pipe induced by the outward movement of the pipe against the trench walls. The pipe deflection results in the above two benefits. Spangler (1941) proposed the Iowa formula to calculate the deflection of a flexible pipe as expressed in **Equation (2-6)**.

$$\Delta Y = \frac{D_L K W_c r^3}{EI + 0.061 E' r^3} \tag{2-6}$$

where D_L = the deflection lag factor; K = a bedding constant; W_c = Marston's load; r = the mean radius of a pipe; E = the modulus of elasticity of pipe material; I = the moment of inertia of pipe wall; E' = the modulus of passive resistance of side fill; ΔY = the vertical deflection or change in pipe diameter.

The modulus of passive resistance of the side fill e in **Equation (2-6)** was difficult to determine since it was not a soil property. Watkins and Spangler (1958) modified the Iowa formula by introducing a new parameter referred to as the modulus of reaction instead of e. They also developed a test method to determine the modulus of reaction. However, great efforts have been made by researchers attempting to measure the modulus of reaction without much success. A more reliable method of estimating the modulus of soil reaction was proposed by Howard (1996) using the back-calculation method. The deflections, strains, buckling deformations, bending and hoop stresses can be calculated and used as the design criteria for buried flexible pipes using the above methods (Spangler, 1941; and Watkins and Spangler, 1958). However, these methods assumed the deformation of the pipe was only caused by the overburden pressure of the soil cover and the

weight of a superstructure above the buried pipe. Design methods, including Spangler (1941), Watkins and Spangler (1958), CECS (2004), and AASHTO (2012), do not consider the initial deformation of the pipe caused by the compaction during backfilling. The Spangler (1941) method assumed the pipe deformed like a horizontal ellipse; however, a vertical ellipse was observed due to the installation effect (Arockiasamy et al., 2006 and Mai et al., 2014). McGrath (1998), and Masada and Sargand (2007) pointed out that the flexible pipe deformed into a shape like a vertical ellipse when the backfilling and compaction were below the pipe crown level. The shape of the pipe gradually returned to be round when the backfilling was above the pipe crown level. This phenomenon was referred to as "peaking behavior", which is beneficial for improving the load carrying capacity of the flexible pipe verified by field test results. Masada and Sargand (2007) proposed a theoretical formula to calculate the peaking deflection as shown in **Equation (2-7)**:

$$\frac{\Delta y}{D} = \frac{4.7P_c + K_0 r\gamma}{3.874(PS)} \tag{2-7}$$

where Δy = the vertical deflection of the pipe; D = the diameter of the pipe; K_0 = the lateral earth pressure coefficient at rest; r = the radius of the pipe; γ = the unit weight of the backfill material; PS = the pipe stiffness.

2.3.2 Load Transfer Mechanism of Buried Pipes in Service

Buried pipes have been commonly for drainage in highway and railway projects, which are often subjected to traffic loading. Boussinesq's solution is a basic formula commonly used to calculate the additional stress in the soil cover of the pipe at different depth. Hall and Newmark

(1977) developed a load coefficient based on Boussinesq's solution for calculating the concentrated load on a pipe:

$$W_{sc} = \frac{C_s P F'}{L} \tag{2-8}$$

where W_{sc} = the load per length on the pipe; P = the concentrated load; L = the effective length of the pipe; C_s = a load coefficient, which is a function of the trench width and the soil cover thickness, and F' = an impact factor (typically 1.0-1.5 for pipes under highways).

Antaki (1997) suggested that the pressure on the top of the pipe induced by the surface load can be calculated using the following equation:

$$p_p = \frac{3P_S}{2\pi H^2 \left[1+\left(\frac{d_s}{H}\right)^2\right]^{\frac{5}{2}}} \tag{2-9}$$

where p_p = the pressure transmitted to the pipe; P_s = the concentrated load on the road surface; H = the soil cover thickness; d_s = the offset distance from the pipe to the line of the load application on the surface.

Moser and Folkman (2008) suggested that the total load on the pipe was the surface load plus the weight of the soil cover. Typically, the weight of the soil cover is ignored. The surface load transferred to the top of the pipe with a distribution angle of $\theta = 45^o - \phi/2$ (ϕ is the soil friction angle). In practice, the pressure on the pipe top can be simply calculated as follows with an angle of 27°:

$$p = \frac{W}{(B+H)(L+H)} \tag{2-10}$$

where p = the pressure on the pipe top; W = the surface load; B = the width of the stress distribution area; H = the soil cover thickness; and L = length of the stress distribution area.

AASHTO (2012) suggested the live load transferred to the pipe with the distribution width based on the AASHTO H-25 truck load as shown in **Table 2.4**. The live load distribution coefficient was also suggested in AASHTO (2012) as the lesser of the ratio of the distribution width to the outside diameter of the pipe and one.

Table 2.4 Live load distribution under the AASHTO H-25 truck (AASHTO, 2012)

Soil cover thickness (ft.)	Live load transfer to pipe (psi)	Live load distribution width (ft.)
1	15.6	2.3
2	7.0	4.0
3	5.2	5.5
4	3.5	7.2
5	2.2	8.8
6	1.7	10.3
7	1.6	12
8	0.9	13.6
10	negligible	N/A
12	negligible	N/A

Giroud and Han (2004) suggested an approximate solution for the vertical pressure distribution angle from a base course to a subgrade based on Burmister's layered elastic solution as follows:

$$\tan\alpha_1 = \tan\alpha_o \left[1 + 0.204\left(\frac{E_1}{E_2} - 1\right)\right] \quad (2\text{-}11)$$

where α_1 = the pressure distribution angle in the base coarse, α_o = the reference pressure distribution angle for a uniform medium defined by $E_1 = E_2$, E_1 = the modulus of elasticity of the base coarse, and E_2 = the modulus of elasticity of the subgrade. The reference distribution angle for a uniform medium can be taken as 27^o (i.e., 2:1 distribution).

The compatibility of pipe and soil (i.e., the soil deformation and the pipe deflection) was not considered. In other words, if the deflection of the pipe is larger than the deformation of the surrounding soil, more load will transfer to the surrounding soil; if the deflection of the pipe is smaller than the deformation of the surrounding soil, the pipe will carry more load. These phenomena are referred to as the soil arching effect.

2.4 Long-term Behavior of HDPE Pipes

AASHTO (2012) proposed a method to calculate the vertical load on the top of the pipe as shown in **Equations (2.2-2.4)**. In **Eq. (2.4)**, the hoop stiffness depends on the elastic modulus of the pipe material. For HDPE pipes, the pipe material is polyethylene. The recommended short-term modulus of polyethylene is 759 MPa while its long-term modulus is only 152 MPa. Consequently, load would gradually transfer from the pipe to the surrounding soil considering the soil arching effect. However, it has to be pointed out that the soil arching effect may lose with elapsed time caused by the traffic loading. Therefore, the soil prism load is widely used as the design load for flexible pipes in practice. The long-term behavior of HDPE pipe is more critical

for the HDPE pipe design. A series of research was conducted by Hsuan and her co-researchers for the Florida Department of Transportation (FDOT) on the long-term behavior of the HDPE pipe material (Hsuan and Zhang, 2005; and Hsuan and McGrath, 2005). They used accelerated creep tests to simulate the HDPE pipe under different environments and temperatures. The recommended short-term and long-term tensile strengths of the HDPE material are 20.7 and 6.2 MPa, respectively; while their short-term and long-term moduli are the same as those suggested by AASHTO (2012).

Khatri (2012) conducted a creep test on an SRHDPE pipe section in the air for one month under a constant temperature of 27°C. He found that the pipe stiffness decreased by 25% with time. No stiffness reduction factor is available for the current SRHDPE pipe design.

2.5 Previous Research on SRHDPE Pipes

Moser and Folkman (2008) buried SRHDPE pipes in the field with different pipe diameters, while the soil compacted was 87% of standard proctor density. The test results indicated that the SRHDPE pipes had a similar behavior with the low stiffness metal corrugated pipes. Moore (2009) performed stub compression and hoop compression tests on SRHDPE pipe samples or sections with diameters of 0.6 and 1.5 m. He found that the helically-wounded steel ribs provided sufficient safety for the SRHDPE pipes at required buried depths. To evaluate the performance of a deeply buried pipe system, large-scale buried pipe tests were also conducted on 0.6 and 1.5 m diameter pipes. The pipe deflected like a conventional buried metal culvert and the deflection was less than

the limit of 5%. He concluded that the AASHTO method for the flexible steel pipe can be used to design the SRHDPE pipe to meet the deflection requirement.

One steel-reinforced and one conventional HDPE pipes were installed with crushed stone as a backfill on the Manhead Road by the Utah Department of Transportation (UDOT) (Folkman, 2011). The diameter of both pipes was 0.6 m. These two pipes were installed in parallel at a clear spacing of 127 mm using the same installation method. The thickness of the soil cover over both pipes was approximately 1 m. The vertical and horizontal deflections of the pipes were measured immediately after the installation and during the service life. The conventional HDPE pipe had larger deflections than the steel reinforced HDPE pipe. The maximum average vertical and horizontal deflections were -1.99% and 2.24%, respectively for the SRHDPE pipe, while the conventional HDPE pipe had -4.24% vertical and 4.06% horizontal deflections after one month of installation. In addition, the maximum average vertical and horizontal deflections were -1.63% and 1.78%, respectively for the SRHDPE pipe, while the HDPE pipe had -4.19% vertical and 3.97% horizontal deflections after one year of installation. Three SRHDPE pipes with a diameter of 2.4 m and a length of 30 m were installed in Fort Benning, Georgia (Hardert, 2011). The thickness of the soil cover was 5.4 m. The vertical and horizontal diameter changes in one year were 39.1 and 30 mm, respectively.

Research on SRHDPE pipes has also been conducted at the University of Kansas. Khatri (2012, 2014) did a series of laboratory tests to determine the mechanical properties of the SRHDPE pipe. Khatri et al. (2013) conducted parallel plate load tests on the SRHDPE to determine the pipe stiffness. Corey et al. (2014) conducted large-scale box tests to evaluate the protection effect of the geogrid on the shallow buried SRHDPE pipes. Khatri et al. (2015) investigated the installation effect of the SRHDPE pipe in a large test box.

2.6 Performance Limits

Buried pipes should first survive during installation. There are the performance limits for a pipe during installation, which are related to stress, strain, deflection, and buckling of the pipe. The following performance limits are usually considered in the buried pipe design (Moser and Folkman, 2008):

- *Wall Crushing* (Primary performance limit for rigid pipes and stiffer flexible pipes)

This performance limit describes the stress condition in the pipe reaches the yield stress or the ultimate stress of the pipe material. Wall crushing check can be easily conducted by comparing the compressive stress in the pipe with the yield strength of the pipe. The compressive stress in the pipe can be calculated as follows:

$$\sigma_{rc} = \frac{P_v D}{2A} \tag{2-12}$$

where σ_{rc} = the compressive stress of the pipe; P_v = the vertical soil pressure as shown in **Figure 2.3**; D = the pipe diameter; and A = the cross section area of the pipe wall per unit length.

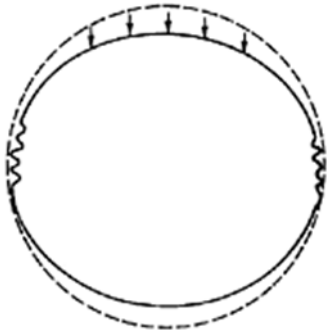

Figure 2.3 Schematic of the wall crushing (Moser and Folkman, 2008)

Wall crushing can also be influenced by the bending stress in the pipe wall. The bending stress is:

$$\sigma_b = \frac{Mt}{2I} \tag{2-13}$$

where σ_b = the bending stress in the pipe; M = the bending moment per unit length; t = the thickness of the pipe wall; and I = the moment of inertia of pipe wall per unit length.

- *Wall Buckling*

Wall buckling can occur when the pipe stiffness is not sufficient. Wall buckling may control the design when the bucking strain is greater than the strain limit of the pipe wall.

For a circular ring (without buried in a soil) in a plane stress condition subjected to uniform external pressure, its critical buckling pressure is:

$$P_{cr} = \frac{3EI}{R^3} \tag{2-14}$$

where P_{cr} = the critical buckling pressure; E = the elastic modulus of the ring; I = the moment of inertia; and R = the radius of the ring.

For a long tube, its elastic modulus should be changed to:

$$E_L = \frac{E}{1-\nu^2} \quad (2\text{-}15)$$

where E_L = the elastic modulus of the long tube; E = the elastic modulus of the tube material; and ν = the Poisson's ratio of the long tube. The moment of inertia of the pipe is:

$$I = \frac{t^3}{12} \quad (2\text{-}16)$$

where I = the moment of inertia of the pipe wall; and t = the thickness of the pipe wall.

When **Equations (2-15)** and **(2-16)** are substituted into **Equation (2-14)**, it becomes:

$$P_{cr} = \frac{Et^3}{4R^3(1-\nu^2)} \quad (2\text{-}17)$$

The limiting value of P_{cr} should be less than $\frac{Et^3}{4R^3}$ or $\frac{\sigma_y t}{R}$, where σ_y is the yield stress of the pipe material.

The above equation of the buckling pressure is only valid for the pipe submerged in water. For pipes buried in the soil, Meyerhof and Baike (1963) developed the following equation:

$$P_{cr} = 2\sqrt{\frac{E'}{1-\nu^2}\left(\frac{EI}{R^3}\right)} \quad (2\text{-}18)$$

where E' = the soil reaction modulus, which is equal to the soil constrained modulus.

Equation (2-18) can also be rewritten as:

$$P_{cr} = 1.15\sqrt{E'P_b}, \quad P_b = \frac{2E}{1-\nu^2}\left(\frac{t}{D}\right)^3 \tag{2-19}$$

where D = the diameter of the pipe.

Test results showed that the above equation worked well for steel pipes; however, it was conservative for plastic pipes (Moser and Folkman, 2008). The more exact approach for pipe buckling is:

$$q_a = \frac{1}{FS}\left(32R_W B' E' \frac{EI}{D^3}\right)^{1/2} \tag{2-20}$$

where q_a = the allowable buckling pressure; FS = the design factor of safety, 2.5 (h/D > 2) and 3.0 (h/D > 2), in which h is the soil cover thickness and D is the pipe diameter; R_W = the water buoyancy factor, $R_W = 1 - 0.33\left(\frac{h_w}{h}\right)$, in which h_w is the height of the groundwater surface above the top of the pipe; $B' = \frac{4\left(h^2 + Dh\right)}{(1+\nu)[(2h+D)^2 + D^2(1-2\nu)]}$, if the Poisson's ratio of the pipe is assumed to be 0.5, it can be simplified as $B' = \frac{4\left(h^2 + Dh\right)}{1.5(2h+D)^2}$.

- *Buckling Check for the Pipe Installation*

If a live load is considered, the following equation should be required for pipe installation:

$$\gamma_w h_w + R_w \frac{W_c}{D} + \frac{W_L}{D} \le q_a \tag{2-21}$$

where W_c = the vertical soil load on the top of the pipe per length; W_L = the live load above the top of the pipe.

Equation (2-21) is not valid for the condition when a large diameter pipe is buried shallowly below the groundwater surface.

- *Over-deflection*

Over-deflection was defined as the deflection larger than 7.5% at a factor of safety of 4. The design deflection limit is recommended as 5% in most standards considering a factor of safety of 4.

- *Strain Limit*

Strain is related to the deflection of a pipe. Strain limit can be satisfied by controlling the deflection limit during installation. Brittle, composite pipe, or deeply buried pipeis often controlled by a strain limit.

The strain described in the strain limit is referred to as the total circumferential strain, which includes bending strain, ring compression strain, hoop strain due to internal pressure, and strain due to Poisson's ratio effect in the longitudinal direction. For gravity sewer pipes, the bending strain is typically the largest and other types of strain may be negligible.

Bending Strain. If a pipe is assumed to deform elliptically, the bending strain of the pipe can be calculated as:

$$\varepsilon = \pm\left(\frac{t}{D}\right)\left(\frac{3\,\Delta y/D}{1-2\,\Delta y/D}\right) \qquad (2\text{-}22)$$

where ε = the maximum strain in the pipe due to ring bending; t = the pipe wall thickness; Δy = the pipe diameter change in the vertical direction; D = the pipe diameter.

For profile wall pipes, **Equation (2-22)** can be simplified into:

$$\varepsilon = \pm\left(6\frac{t}{D}\right)\left(\frac{\Delta y}{D}\right) \tag{2-23}$$

In **Equation (2-23)**, the ratio of the pipe deflection to the pipe diameter ($\frac{\Delta y}{D}$) is assumed as 0.25.

Compression Strain. From **Equation (2-12)**, the compression strain of the pipe is:

$$\varepsilon_{rc} = \frac{P_v D}{2AE} = \frac{P_v D}{2tE} \tag{2-24}$$

where ε_{rc} = the compression strain; P_v= the vertical soil pressure as shown in **Figure 2.3**; D = the pipe diameter; t = the thickness of the pipe wall; and A = the cross section area of the pipe wall per unit length.

Circumferential Strain due to Poisson's Ratio Effect. The circumferential strain can be calculated as follows:

$$\varepsilon_c = v\varepsilon_L \tag{2-25}$$

where ε_c = the circumferential strain; ε_L = the longitudinal strain; and v = the Poisson's ratio of the pipe wall.

- *Delamination*

Reinforced pipes may experience delamination when subjected to a ring deflection due to the radial tension and inter-laminar shear. The radial tensile stress is given by:

$$\sigma_r = \frac{T}{t(R+y)} \tag{2-26}$$

$$T = \int_{-c}^{y} \sigma da \tag{2-27}$$

where σ_r = the radial tensile stress, t = the pipe wall thickness, R = the pipe radius, y = the distance from the neutral axis to the point in question, $c = t/2$, σ = the stress in the tangential direction as function of the position in the pipe wall (My/I); $da = (dy) \times$ (unit length).

CHAPTER 3 FIELD PERFORMANCE OF THE SRHDPE PIPES

3.1 Introduction

A field test was conducted in Kansas City, Kansas to evaluate the possible damage and the field performance of the SRHDPE pipe during installation. The diameter of SRHDPE pipes used in this field test was 0.6 m. **Figure 3.1** shows the location of the field test site, which is located at the right side of the Interstate highway I-635 towards the Missouri River, close to the state line of Kansas and Missouri. This test site was a KDOT storage yard which was relatively flat and no groundwater was observed during the trench excavation. Therefore, the groundwater effect was not considered in the field test.

Figure 3.1 Location of the second field test site (from Google Earth)

3.2 Properties of Backfill Material

Two types of backfill material were used in the field test: AB3 aggregate and crushed stone. **Figure 3.2** presents the particle size distribution curves of these two backfill materials. The coefficients of uniformity for the AB3 aggregate and the crushed stone were 15.0 and 1.9, respectively; while the coefficients of curvature for the AB3 aggregate and the crushed stone were 1.03 and 1.32, respectively. The liquid limit and the plasticity index of the particles passing the No. 40 sieve size in the AB3 aggregate were 20 and 13, respectively; therefore, it can be classified as **CL-ML** based on the Unified Soil Classification System (USCS) plasticity chart. Based on ASTM D2487 (2011), the AB3 aggregate can be classified as well-graded gravel (**GW-GC**) while the crushed stone can be classified as poorly-graded gravel (**GP**). **Figure 3.2** clearly shows that the AB3 aggregate had a much wider range of particle sizes than the crushed stone. The maximum dry density of the AB3 aggregate was determined as 2.18 Mg/m^3 and its optimum moisture content was 7.2% determined by the modified Proctor tests per the ASTM D1557 (2012). **Figure 3.3** shows the compaction curve of the AB3 aggregate. The maximum density of the crushed stone was 1.56 Mg/m^3 determined by ASTM D4253 (2014). Plate loading tests were conducted on the fill material in a wooden box with a dimension of 820 mm long, 820 mm wide, and 457.2 mm deep to determine their moduli of the subgrade reaction. The loading plate was a circular plate with a diameter of 150 mm. **Figure 3.4** shows the load-settlement curves of these two materials obtained in the plate loading tests. From **Figure 3.4**, the moduli of the AB3 aggregate and the crushed stone can be calculated as 23.6 and 19.6 MPa, respectively. In other words, the moduli of the AB3 aggregate was higher than that of the crushed stone because the AB3 aggregate had a wider range of particle sizes, which could form a denser state. Traxial compression tests were used to determine the shear strength parameters at three confining pressures of 34.5, 69 and 138 kPa. The height of the samples was 203 mm, while the diameter of the samples was 101.6 mm.

The samples for the AB3 aggregate were prepared at the optimum moisture content (i.e., 7.2%), while the crushed stone samples were tested in a dry condition. **Figures 3.5 and 3.6** shows the stress-strain curves of the AB3 aggregate and the crushed stone, respectively. **Figure 3.7** shows the Mohr circles of the AB3 aggregate and the crushed stone, respectively. The friction angle of both materials was 45^{o}.

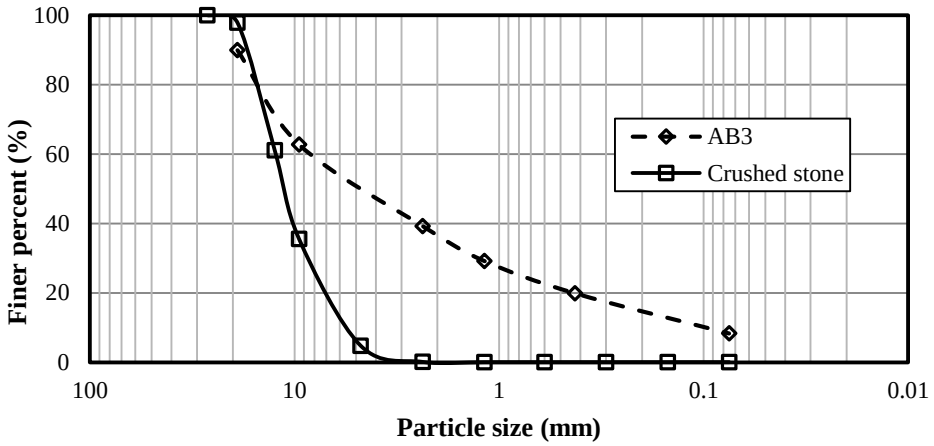

Figure 3.2 Particle size distribution curves of the AB3 aggregate and the crushed stone

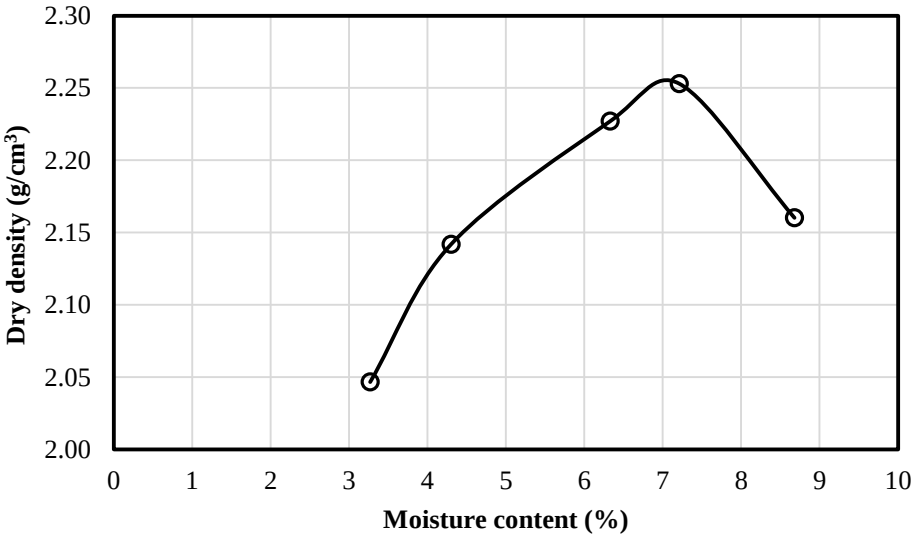

Figure 3.3 The compaction curve of the AB3 aggregate

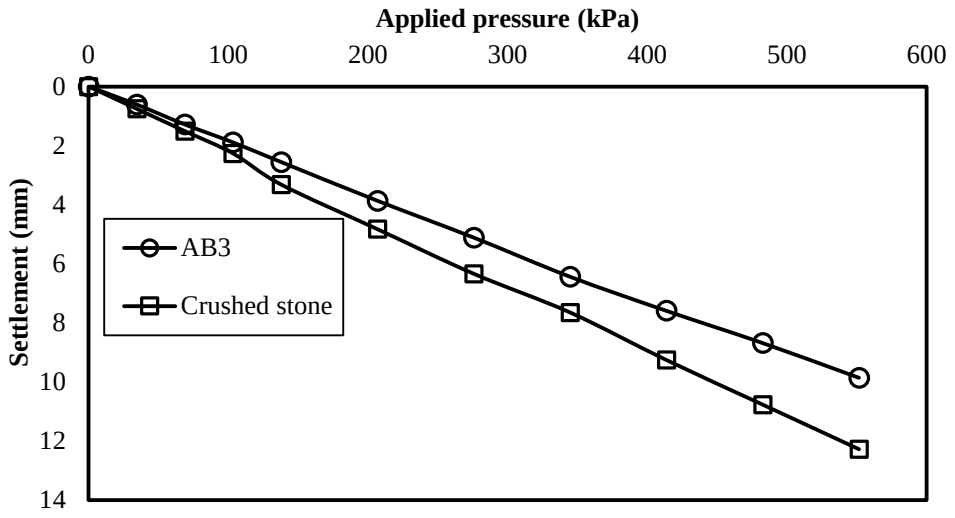

Figure 3.4 Plate loading test results of the AB3 aggregate and the crushed stone

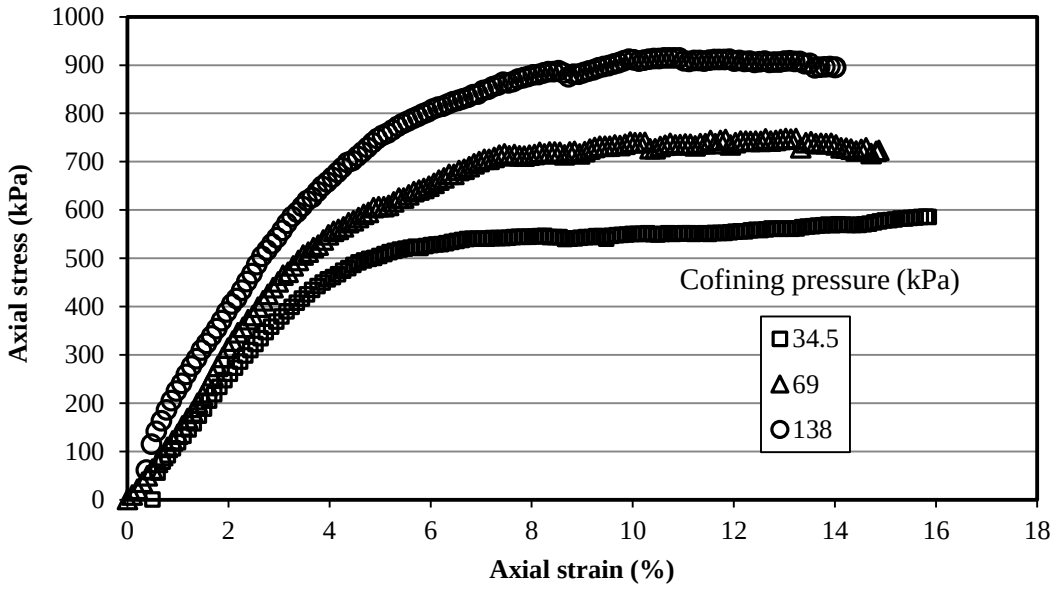

Figure 3.5 Stress-strain curves of the AB3 aggregate from the triaxial compression tests at different confining pressures

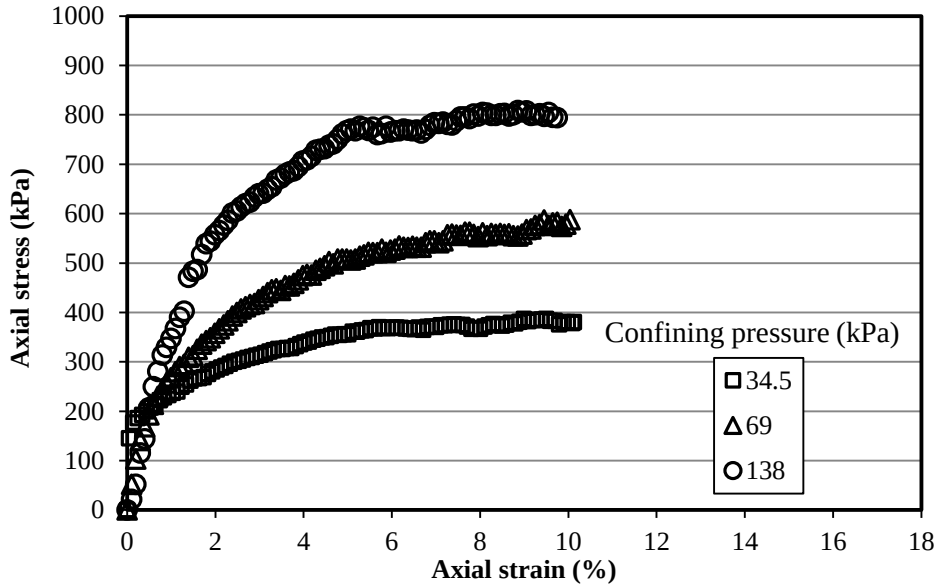

Figure 3.6 Stress-strain curves of the crushed stone from the triaxial compression tests at different confining pressures

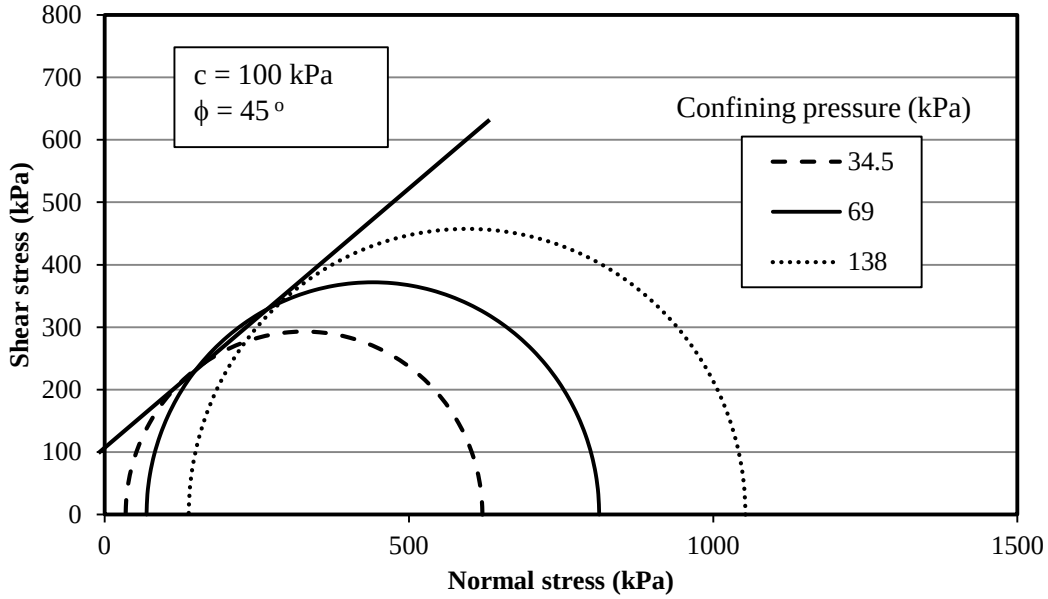

(a) AB3 aggregate

Figure 3.7 Mohr's circles of the AB3 aggregate and the crushed stone

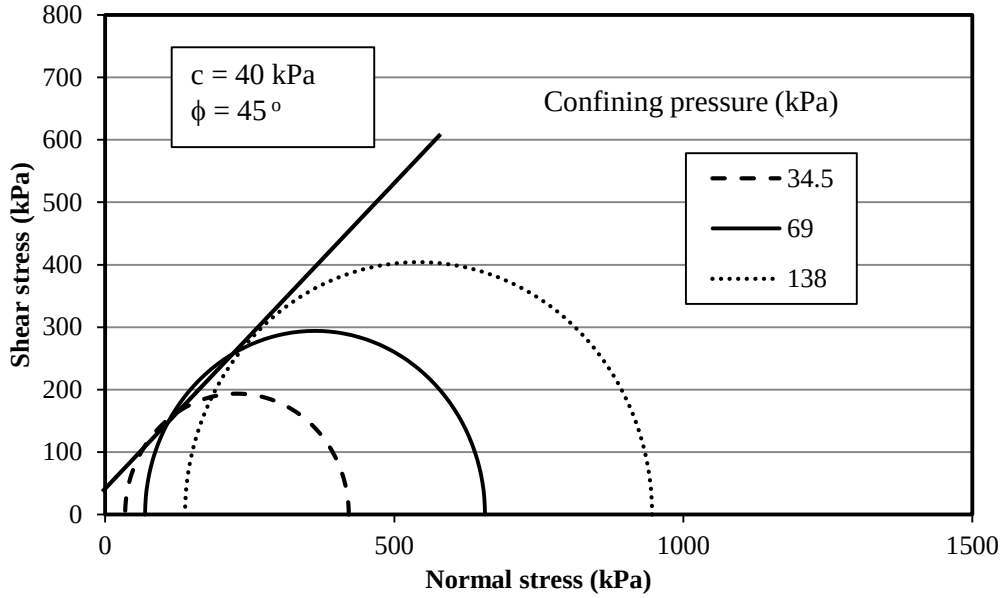

(b) Crushed stone

Figure 3.7 Mohr's circles of the AB3 aggregate and the crushed stone (continued)

3.3 Test Site, Test Pipes, and Instrumentation

3.3.1 Test Site

A 1.38 m wide, 8.25 m long, and 1.26 m deep trench was excavated on the site. The bottom of the trench was leveled before backfilling. The side walls of the trench were vertical and stable during and after the excavation. **Figure 3.8** presents the installation plan of the SRHDPE pipes in Sections A and B. Two pipes were buried in the AB3 aggregate in Section A, while the other two pipes were installed in the crushed stone in Section B. The following procedure was followed for the installation: (1) before the installation of the pipe in the trench, Zone I was filled and compacted to form a 15 mm thick bedding layer both in Sections A and B; (2) the connected SRHDPE pipes

were placed into the trench and Zone II was filled and compacted to reach the springline level of the pipe (the thickness of Zone II was 300 mm); (3) Zone III was filled and compacted with a thickness of 300 mm to reach the top of the pipe level; (4) Zone IV was filled and compacted with a lift thickness of 340 mm; and (5) finally, Zone V was filled and compacted with a lift thickness of 300 mm. Section A was filled with the AB3 aggregate while Section B was filled with the crushed stone in Zones I to IV. Zone V in both sections was filled with the AB3 aggregate as a base course layer. Two instrumented rings are shown in **Figure 3.8b**.

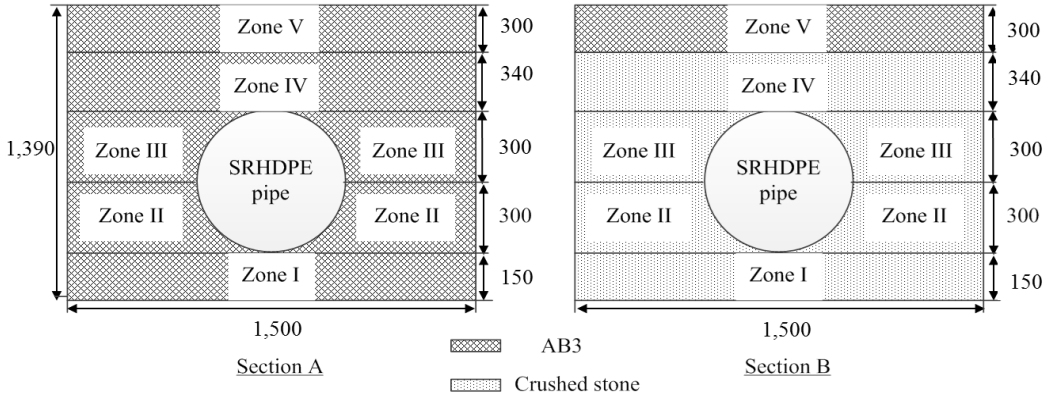

(a) Cross section in the transversal direction

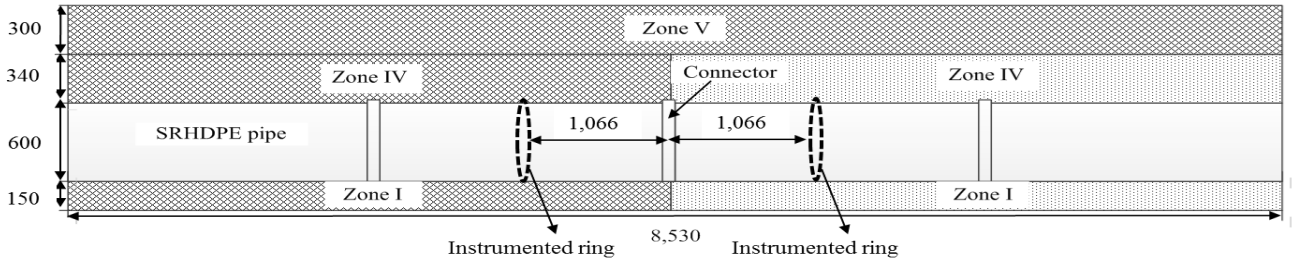

(b) Cross section in the longitudinal direction

Figure 3.8 Schematic of the installation plan (not to scale, unit: mm)

3.3.2 Test Pipes

Figure 3.9 shows the schematic cross section of the corrugated SRHDPE pipe. This pipe consisted of steel spiral ribs for load carrying and stiffness and high-density polyethylene cover and liner for corrosion resistance. The width of the rib including the steel reinforcement and the plastic cover was 2.25 mm and the height was 17 mm. Steel reinforcement with a thickness of 1.5 mm was covered by the plastic material to form the rib and the center to center spacing of the ribs was 25.4 mm. The diameter of the pipe used in the test was 0.6 m and the thickness of the valley liner was 2.0 mm. Khatri et al. (2013) reported the stiffness of the same SRHDPE pipe from the parallel plate load tests, which was 294 kPa based on the ASTM D2412 (2011). SRHDPE pipes used in the field test are same as pipes used in the parallel plate load tests reported by Khatri et al. (2013).

Soil-tight pipe metal connectors with a dimension of 330 mm wide, 2095.5 mm long, and 1.0 mm thick, were used to connect the pipes. Before the installation of the connector, a rubber band was used to cover the pipe to ensure a tight connection of the pipe with the connector. Expandable foam was filled in the corrugations of the pipe to seal the possible gap between the rubber band and the pipe. Each connector was wrapped around the pipe and two bolts (205 mm long and 10 mm in diameter) attached on the connector were tightened to finish the connection. **Figure 3.10** shows two connected pipes using the soil-tight type connector.

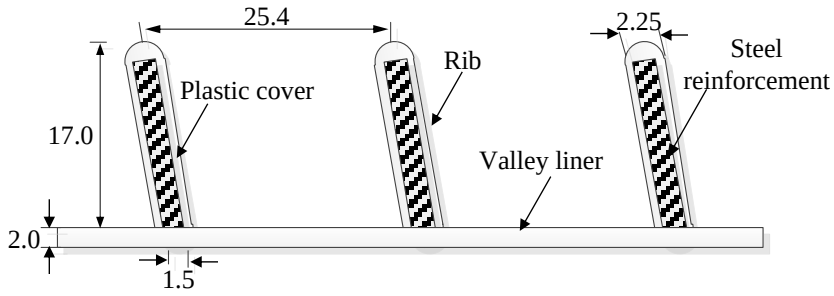

Figure 3.9 Schematic of cross-section of the corrugated SRHDPE pipe (unit: mm, not to scale)

Figure 3.10 Two connected pipes with a soil-tight type connector

3.3.3 Instrumentation

Figure 3.11 shows the locations of earth pressure cells. KDE-500KPA pressure cells with the maximum capacity of 500 kPa were used in the field test in this study. These pressure cells had an outside diameter of 50 mm, a sensitive surface diameter of 45.7 mm and a thickness of 10 mm. Four pressure cells were installed in the instrumented rings in each section as shown in **Fig. 3.8b** and they are labeled as E1, E2, E3, and E4. E1 and E4 were used to measure the vertical pressures at the springline and the crown of the pipe while E2 and E3 were installed to monitor the lateral earth pressures at the springline and 150 mm above the springline of the pipe. The locations of the pressure cells were determined with the following reasons: (1) E1 and E4 could be used to analyze the soil arching effect during backfilling and under static loading; (2) E2 and E3 could be used to examine the assumption made by Masada and Sargand (2007) that the pressure induced by compaction of backfill material is constant with the buried depth of the pipe (recognized as the reason for the peaking behavior); and (3) E1 and E2 could be used to calculate the coefficient of lateral earth pressure. **Figure 3.12** shows the installation of pressure cells. The base of the pressure cell was leveled using the Kansas River sand to ensure the leveling of the pressure cell during the pipe installation. Then the pressure cell was placed and the wires of the pressure cells were covered by a plastic tube with a diameter of 50 mm to protect the wires during compaction. Self-made sand bags, which were geotextile bags filled with sand, were placed on the top of the pressure cells to protect the pressure cells during the compaction.

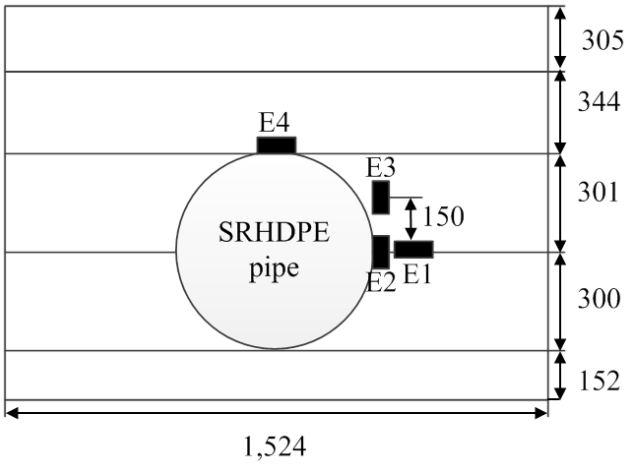

Figure 3.11 Schematic of the locations of pressure cells (unit: mm, not to scale)

Figure 3.12 Placement of a pressure cell

Figure 3.13 shows the positions of displacement transducers. Four displacement transducers, labeled as L1, L2, L3, and L3', were installed in the instrumented rings in each section as shown in **Fig. 3.8b**. L1 was used to measure the diameter change in the horizontal direction and L2 was installed to monitor the deformation of the pipe at 45^{o} from the pipe crown. L3 and

L3’ were used to evaluate the vertical deflections of the pipe. Between these two transducers, L3 was positioned at the valley liner profile while L3’ was positioned at the steel reinforcement profile to investigate a possible deflection difference between the pipe wall and the steel reinforcement ribs. **Figure 3.14** shows the installed displacement transducers inside of the pipe. Four small holes with a diameter of 12.7 mm were drilled in the instrumented pipe at the displacement transducer locations as shown in **Figure 3.13**. Four steel bars with a diameter of 12.7 mm and length of 508 mm were fixed in the pipe through those four holes with nuts and washers. Displacement transducers were banded with the steel bars using clamps.

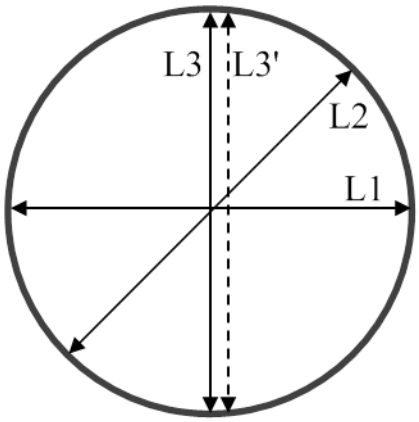

Figure 3.13 Schematic of the locations of the displacement transducers

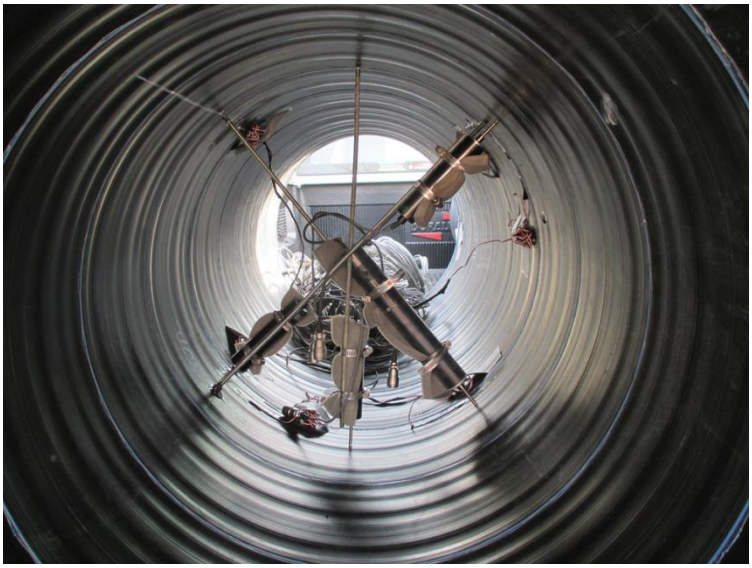

Figure 3.14 Installed displacement transducers inside of the SRHDPE pipe

Uniaxial foil-type electrical resistance (C2A-13-250 LW-120) strain gages, manufactured by the Vishay Precision Group, were used to measure the circumferential and radial strains of the pipe at various locations as shown in **Figure 3.15**. The strain gages were installed at three elements, namely, the steel ribs, the plastic cover of ribs and the plastic valley. For each element, 12 strain gages were installed at both sides including four at the pipe crown, four at the invert, and four at the springline. Strain gages on the steel rib were labeled as G, while those at the plastic cover and plastic valley were named as G' and G'', respectively. "C" following G, G' and G'' denotes the crown. "R" means the strain gage in the radial direction, the second "C" means in the circumferential direction and "L" represents the longitudinal direction (i.e., along the pipe). "1" and "2" illustrate the strain gages attached at two sides of the element. For example, G_{CR1} is the strain gage attached in the radial direction on one side of the steel rib at the pipe crown. In total, 24 strain gages were installed at each instrumented ring.

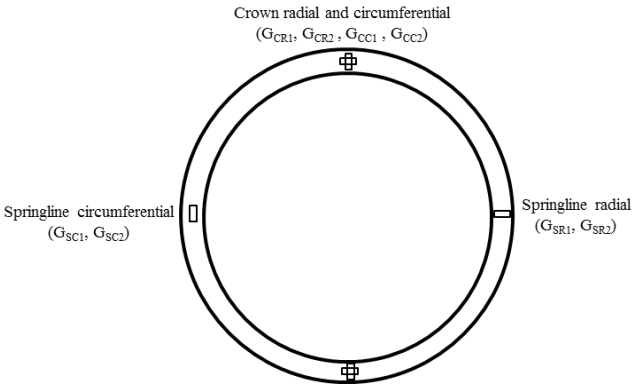

(a) On steel ribs

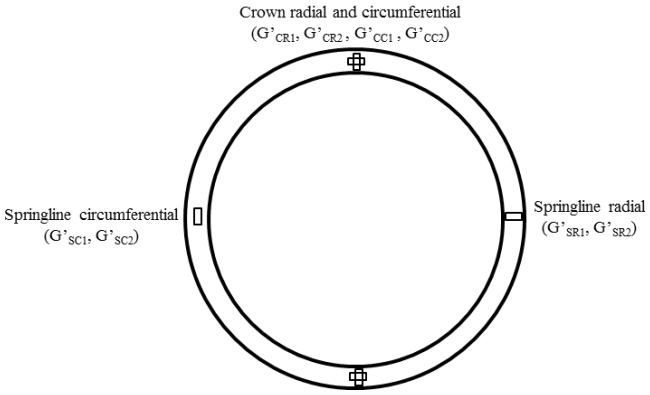

(b) On plastic cover of ribs

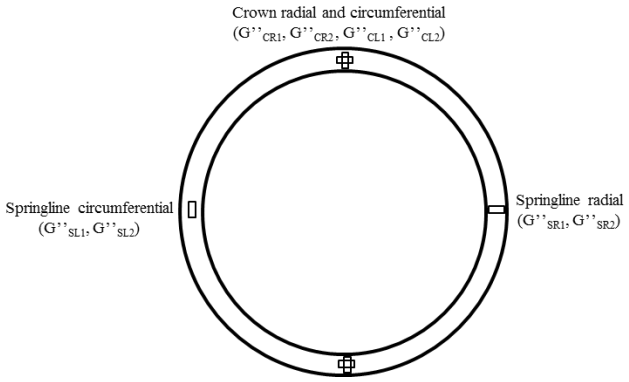

(c) At plastic valley

Figure 3.15 Symbols, locations, and orientations of the strain gages on the pipe

3.4 Pipe Installation and Static Loading

3.4.1 Trench Excavation

A John Deere 310G Loader Backhoe was used to excavate the trench as shown in **Figure 3.16**. The model of the machine was 4045D, and the net and gross power were 73 and 78 hp, respectively. The width of the trench was chosen according to the Pipe and Culvert Specifications (KDOT, 2007) so as to provide sufficient working space for compaction equipment in order to properly and safely place and compact bedding, hunching, and backfill materials. A minimum trench width was maintained so as not to be less that greater of either 1.5 times the pipe outside diameter plus 300 mm or the pipe outside diameter plus 400 mm as suggested by ASTM D2321 (2014). Considering the size of the excavator, the trench width was determined as 1.5 m. The average moisture content of the native soil was 21.2%.

Figure 3.16 Excavation of a trench

3.4.2 Bedding

The AB3 aggregate and the crushed stone were dumped into the trench by the Loader Backhoe in two sections. The length for each section was 4265 mm (i.e., half length of the trench), and then both sections compacted by a vibratory compactor SFA 3500 with a 15.6 kN eccentric force as shown in **Figure 3.17**. The compaction pressure was 49 kPa. The compacted thickness of the bedding was 63.5 mm based on ASTM D2321 (2014). **Figure 3.18** shows the LWD test conducted on the bedding after the compaction to ensure the construction quality. Three tests were conducted in each section. The average modulus of the AB3 aggregate section was 12.7 MPa, while that of the crushed stone section was 12.2 MPa. **Figure 3.19** presents the sand cone test used to determine the field density. Sand cone tests were conducted at three locations in each section. Considering the gap between particles may influence the result in the crushed stone section, sand cone tests in this section were done for three times in each location and the average value was used. The average compaction degrees of the AB3 aggregate and the crushed stone sections were 88.3 and 85.5%, respectively.

Figure 3.17 Compaction of the bedding

Figure 3.18 LWD test on the bedding

Figure 3.19 Sand cone tests on the bedding in the crushed stone section

3.4.3 Placement of the Pipe

After the quality control tests of the bedding were finished, four pipes were lifted up by an ALTEC crane and placed into the trench as shown in **Figure 3.20**. The pipes were lifted up at the locations of two connectors, which could make the lift force evenly and avoid the bending of the pipes. During the placement of the pipes, the wires of the sensors were collected together to prevent the damage of the sensors by the pipe lifting. **Figure 3.21** shows the pipes after the placement into the trench. Then, all sensors were connected with the data acquistition system and set the initial to zero.

Figure 3.20 Placement of the pipes

Figure 3.21 Pipes placed on the bedding

3.4.4 Backfilling of Sidefill and Soil Cover

As shown in **Figure 3.8**, the sidefill and the soil cover were placed and compacted in four lifts. The first lift (i.e., zone II in **Figure 3.8**) was up to the pipe springline. The AB3 aggregate section was filled first and then the crushed stone section. Subsequently, two sections were compacted together. A vibratory compactor SFA 3500 was used for the compaction of the main zone and a STANLEY TA45 rammer with a working pressure of 10 MPa was used to compact the difficult zones near the pipe and the trench as shown in **Figure 3.22**. No pipe lift was observed during the compaction process. The average elastic moduli determined using the LWD tests for the AB3 aggregate section and the crushed stone section were 8.13 and 9.13 MPa, respectively. The compaction degrees for the AB3 aggregate section and the crushed stone section from sand cone tests were 90.8% and 85.5%, respectively.

Figure 3.22 The compaction of difficult zones using the STANLEY TA45 rammer

The second lift of the backfill was up to the level of the pipe top (i.e., zone III in **Figure 3.8**). The construction procedures and the quality control were the same with the first lift. The top of the pipe was not compacted. The average elastic moduli determined using LWD tests for the AB3 aggregate section and the crushed stone section were 9.10 and 9.93 MPa, respectively. The compaction degrees for the AB3 aggregate section and the crushed stone section from sand cone tests were 88.4 and 84.3 %, respectively. The third lift was up to the bottom of the base course layer (i.e., zone IV in **Figure 3.8**). The construction procedures and the quality control were the same with the first two lifts. The average elastic moduli determined using the LWD tests for the AB3 aggregate section and the crushed stone section were 18.3 and 20.1 MPa, respectively. The compaction degrees for the AB3 aggregate section and the crushed stone section from sand cone tests were 91.2 and 90.3%, respectively. The base course layer (i.e., zone V in **Figure 3.8**) in both sections was backfilled with the AB3 aggregate. Three lines were marked on the ground after the compaction to locate the positions of the pipes for the static loadings. The average elastic moduli determined using the LWD tests for the AB3 aggregate in Sections A and B were 16.0 and 17.4 MPa, respectively. The compaction degrees for the AB3 aggregate section and the crushed stone section from sand cone tests were 89.8 and 90.5%, respectively.

3.4.5 Static Loading

To investigate the performance of pipes under the static loading, two static loads were applied on the ground surface above the pipe after the completion of the pipe installation. First, the back axle of the Loader Backhoe stopped above the pipe for two minutes as shown in **Figure 3.23**. The weight of the back axle was 56.9 kN. The diameter of the rear tire was 1338.6 mm, while the width of the rear tire was 254 mm. The contact area of the rear tire with the ground

surface was 0.26 m^2. The contact pressure was 221 kPa. Then, a CAT 953D crawler loader stopped at the ground surface above the pipes as shown in **Figure 3.24**. The operating weight of the CAT 953D was 152.2 kN. The track shoe width was 480 mm, and the ground contact area was 2.3 m^2. The contact pressure was 65.5 kPa.

Figure 3.23 The John Deere 310G Loader Backhoe above the pipes

Figure 3.24 The CAT 953D crawler loader above the pipes

3.4.6 Quality Control

To ensure the quality of construction, the following tests were conducted during the compaction of each lift: (1) LWD test; (2) sand cone test; (3) Leveling measurement; and (4) DCP test. LWD and sand cone tests were described in the construction section. A WILD N3 leveling device was used for the leveling measurement to ensure the leveling and thickness of each lift as shown in **Figure 3.25**. Two DCP tests were conducted after the construction in the AB3 aggregate section to eveluate the CBR value of the AB3 aggregate after the construction. **Figure 3.26** shows the DCP test results of the AB3 aggregate after the construction. The CBR values at two loactions were almost consistent in a range of 10 to 20 with the exception of #2 at the depth of 0.76 m, which was extremly high. At that depth, the DCP cone might pentrate on a big aggregate particle. The rib gaps were marked before the installation on both instrumented pipes as shown in **Figure 3.27** to investigate the gap change during the pipe installation.

Figure 3.25 Leveling measurements during the pipe installation

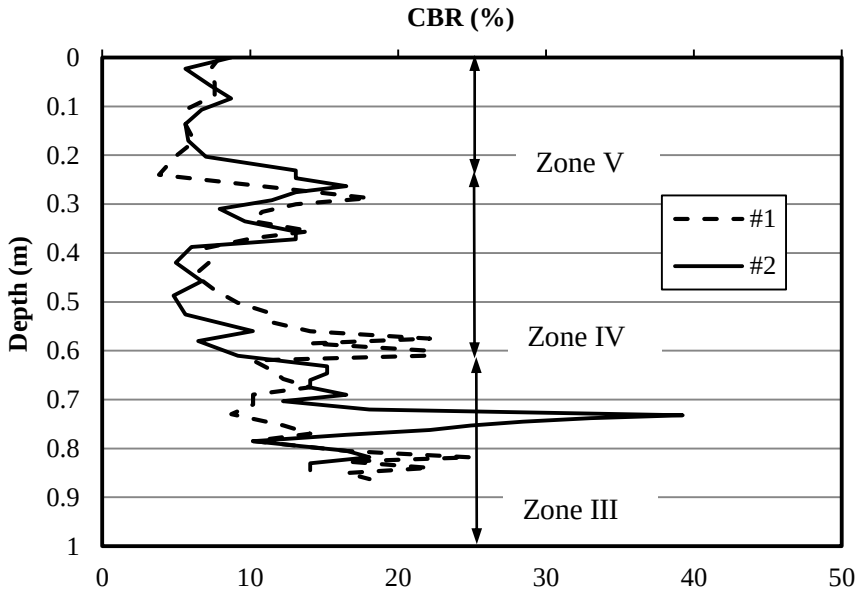

Figure 3.26 DCP test results of the AB3 aggregate section after the construction

Figure 3.27 Markers of the rib gaps before the installation

3.4.7 Pipe Exhumation

The pipes were exhumed on the second day of the installation to observe any possible damage of the pipes during installation. **Figure 3.28** shows an exhumed pipe.

Figure 3.28 An exhumed pipe

3.5 Analysis of Test Results during Pipe Installation

3.5.1 Earth Pressure

Figure 3.29(a) shows the vertical earth pressures at the springline and on the top of the pipes in both sections. The measured vertical pressure in Section A was higher than that in Section B. The vertical pressure at the top of the pipe increased with an increase of the soil cover thickness after the backfill reached the pipe level. The soil arching factors, VAF, defined as the ratio of the measured vertical pressure (σ_v) at the top of the pipe to the overburden stress (γh), were calculated as 1.10 and 1.27 for Sections A and B at the end of backfilling, respectively (σ_v = 15.7 kPa, γh = 21.9 x 0.65 = 14.2 kPa for Section A and σ_v = 17.6 kPa, γh = 15.6 x 0.35 + 21.9 x 0.3 = 12.0 kPa for Section B). The soil arching factors in both sections demonstrated that some overburden stress of the soil cover was transferred from the surrounding soil to the pipe due to the negative soil arching effect (i.e, VAF is greater than one). **Figure 3.29(b)** shows the lateral earth pressure at the springline and 150 mm above the springline of the pipe. From **Figures 3.29,** the lateral earth pressure coefficient at the springline of the pipe was calculated and is shown in **Figure 3.30.** It illustrates that the lateral earth pressure coefficient decreased with an increase of the soil thickness. This finding is the same as that from the laboratory study by Khatri et al. (2015). The lateral earth pressure coefficient for the AB3 aggregate was higher than that for the crushed stone; however, their difference decreased with the increase of the soil thickness and they were approximately equal at the end of backfilling. The lateral earth pressure coefficients in both sections were lower than the passive earth pressure coefficients but higher than the earth pressure coefficients at rest. The measured lateral earth pressures at E2 and E3 in Section A with the backfilling at the top of the pipe were 7.8 and 6.7 kPa, respectively; and their difference was 1.1 kPa. The difference

induced by the soil overburden stress (i.e., 0.15 m (distance between two pressure cells) x 21.9 kN/m^3 (unit weight of AB3) x 0.29 (lateral earth pressure coefficient at rest) = 0.95 kPa). Therefore, the lateral earth pressures caused by the compaction were approximately equal at the positions of E2 and E3. Similarly, for Section B, the difference between E2 and E3 was 0.14 psi, which is also close to the difference induced by the soil overburden stress (i.e., 0.15 m x 15.6 kN/m^3 x 0.29 = 0.67 kPa). This analysis demonstrates that the lateral earth pressure induced by the compaction was constant within the range of 40^o to 140^o from the pipe crown as suggested by Masada and Sargand (2007).

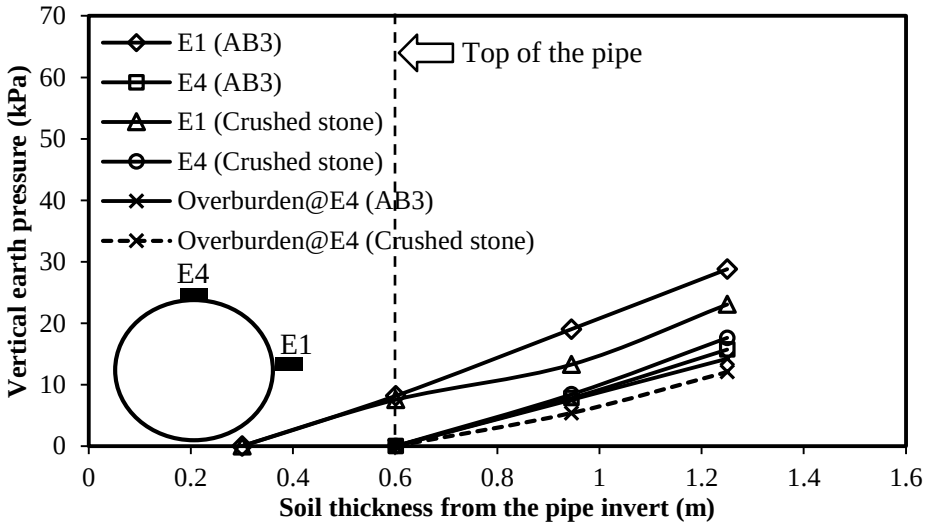

(a) Vertical earth pressure

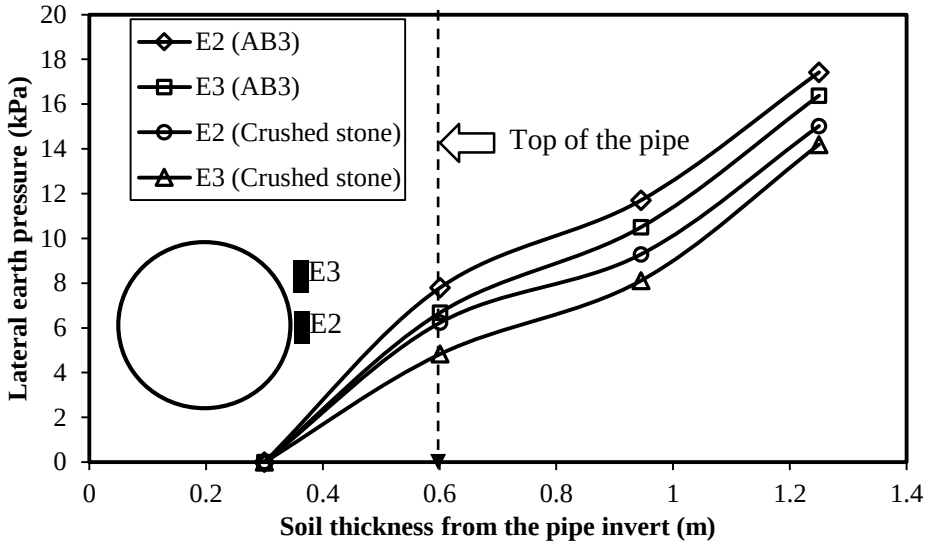

(b) Lateral earth pressure

Figure 3.29 Development of earth pressures around pipes with soil thickness

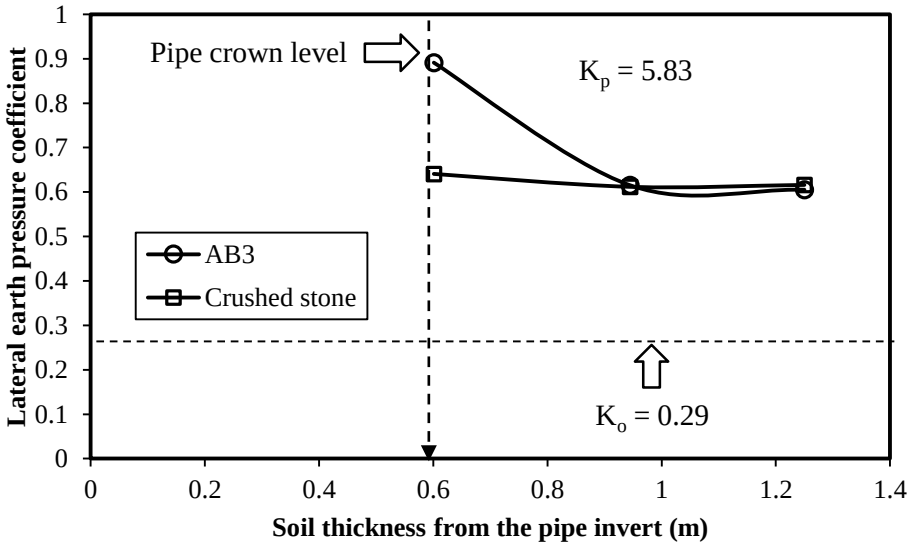

Figure 3.30 Lateral earth pressure coefficients at the springline of the pipe with soil thickness

3.5.2 Deflections

In this field study, the increase of the pipe diameter as compared with that of the undeformed pipe in all three directions (i.e, vertical, 45°, and horizontal) was defined as positive, vice versa. **Figure 3.31(a)** presents the vertical deflections at the valley liner and the steel reinforcement in both sections. It is obvious that the vertical diameter was increased before the backfill reached the top of the pipe, i.e., the peaking behavior, followed by the decrease of the vertical diameter. The peaking deflection of the pipe in Section A (i.e., the AB3 aggregate section) was approximately 1.5 mm while that in Section B (i.e., the crushed stone section) was 1.0 mm. Masada and Sargand (2007) proposed the following equation to calculate the peaking deflection:

$$\frac{\Delta y}{D} = \frac{4.7 p_c + K_0 r \gamma}{3.874(PS)} \qquad (3\text{-}1)$$

where Δy = the vertical deflection; D = the diameter of an undeformed pipe; p_c = the lateral pressure induced by compaction; K_0 = the lateral earth pressure coefficient at rest; r = the radius of the undeformed pipe; γ = the unit weight of backfill material; and PS = the pipe stiffness.

Equation (3-1) shows that the vertical deflection increases with the density of the backfill material considering the same friction angles of the AB3 aggregate (i.e., 45°) and the crushed stone (i.e., 45°). Since the densities for the AB3 aggregate and the crushed stone were 21.9 and 15.6 kN/m^3, respectively, the vertical deflection in Section A should be larger than that in Section B. The calculated peaking deflections using **Eq. (3-1)** are 1.27 and 1.0 mm, respectively for Sections A and B using the following parameters: p_c =0.207 psi as suggested by McGrath et al. (1999) for a vibratory plate compactor; K_0 = 0.29 (i.e., K_0 = 1 - sin 45° = 0.29) for the AB3 aggregate and 0.29

(i.e., K_0 = 1 - sin 45^o = 0.29) for the crushed stone; PS = 294 kPa; γ = 21.9 kN/m^3 for the AB3 aggregate and 15.6 kN/m^3 for the crushed stone; r = 300 mm. The measured peaking deflections are close to the calculated ones in both sections.

The vertical deflection at the valley liner was slightly larger than that at the steel reinforcement rib. The vertical diameter was reduced by 1.0 mm from the peaked vertical diameter in Section A at the end of backfilling while that in Section B was reduced by 3.56 mm from the peaked vertical diameter. The larger reduction of the vertical deflection in Section B might be attributed to the fact that the crushed stone had a lower modulus of subgrade reaction and stress on the surrounding soil due to soil arching. **Figure 3.31(b)** presents the diameter change of the pipe at 45^o from the pipe crown. It was observed that the diameter at 45^o from the pipe crown first increased with backfilling (i.e., Zones II and III) in both sections and then decreased with the increase of the soil cover thickness (i.e., Zones IV and V). The test results also show that the diameter change in the crushed stone was larger than that in the AB3 aggregate. **Figure 3.31(c)** shows the horizontal deflection at the valley liner was opposite to the vertical one. In other words, when the vertical deflection increased, the horizontal deflection decreased, and vice versa. In three directions (i.e., vertical, 45^o from the pipe crown, and horizontal), the maximum deflections in both sections were 2.5 mm (i.e., 0.4% of the pipe diameter), which was much smaller than the typical deflection limit of 5% suggested by AASHTO (2012).

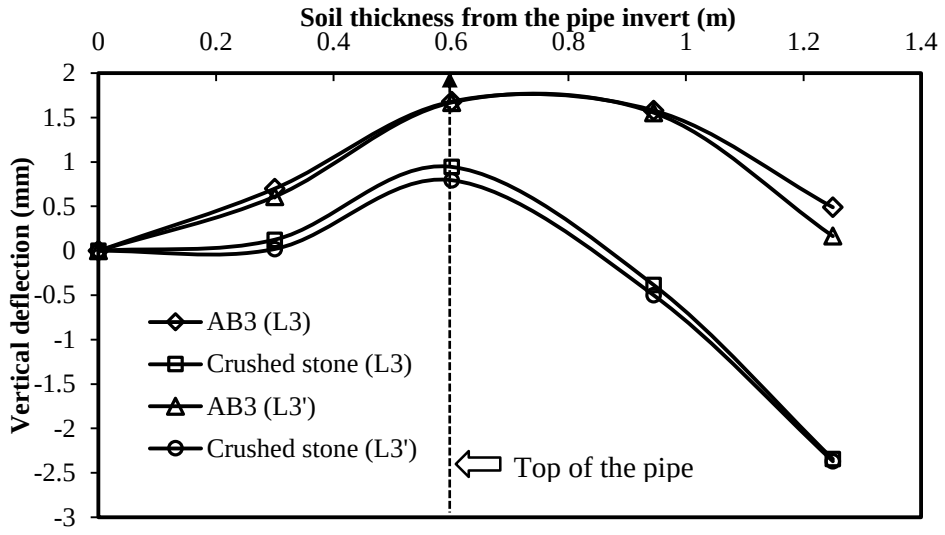

(a) Vertical deflection (L3=deflection at the valley liner; L3'=deflection at the steel reinforcement)

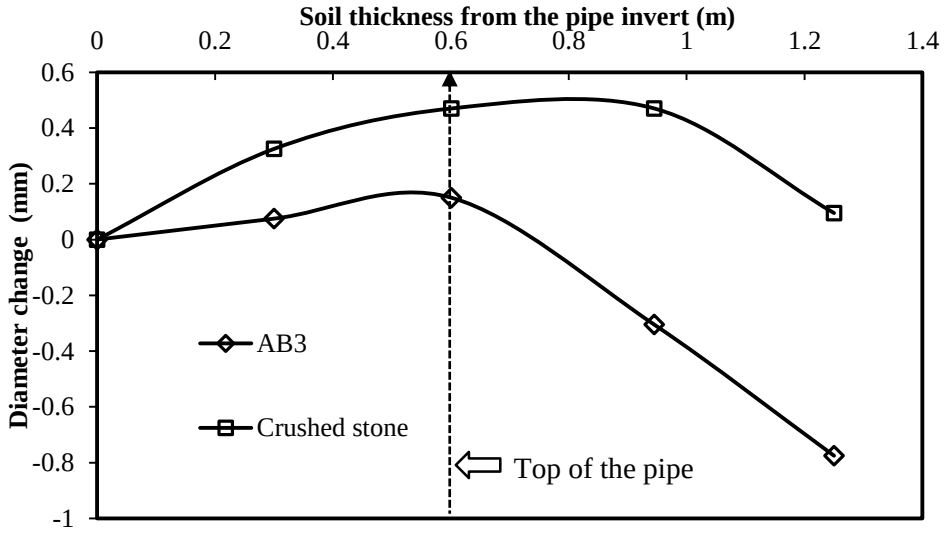

(b) Diameter change at 45° from the pipe crown

Figure 3.31 Development of deflections with soil thickness in three directions during backfilling

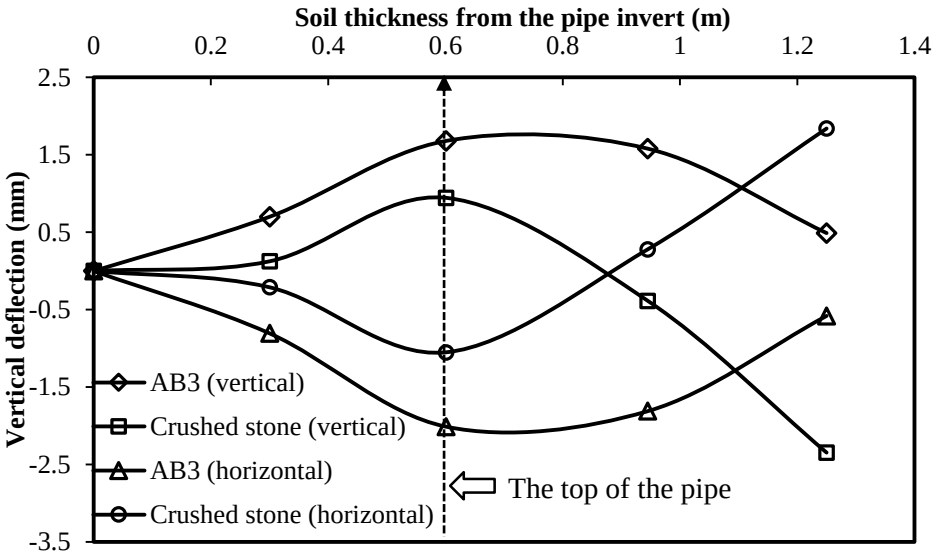

(c) Comparison of vertical and horizontal deflections at the valley liner

Figure 3.31 Development of deflections with soil thickness in three directions during backfilling (continued)

3.5.3 Strains

Test Section A

Figure 3.32 shows the strains on the steel ribs during the backfilling. "Crown_R" and "Crown_C" represent the strains at the crown in the radial and the circumferential directions, respectively. "Springline_R" and "Springline_C" denote the strains at the springline in the radial and the circumferential directions, respectively. **Figure 3.32** illustrates that all the strains at the steel ribs increased with an increase of the soil thickness. The magnitude of the strain increase at the crown was greater than that at the springline in both of the radial and circumferential directions. The compaction was directly above the pipe when the backfill above the pipe top level which would cause the strain increase at the pipe crown. However, the strain increase at the springline was induced by the lateral earth pressure increase, which should be lower than the vertical earth

pressure increase at the pipe crown. It is worth noting that the maximum strain on the steel ribs (i.e., 0.0053%) was much smaller than the typical steel strain at the yield strain of 0.5% (Mamlouk and Zaniewski, 2011). It can be concluded that the compaction in Section A did not fail the steel ribs.

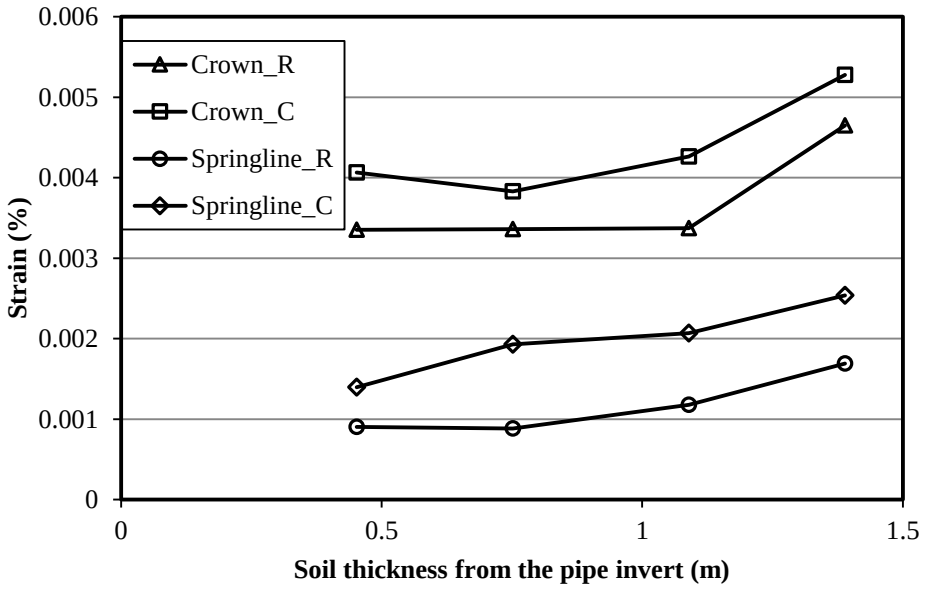

Figure 3.32 Strains of the steel ribs in Section A during the pipe installation

The strains at the plastic covers and valleys were adjusted by multiplying a factor of 1.29 according to Brachman et al. (2008). **Figure 3.33** shows the strains on the plastic cover of the steel ribs. The strains in the radial direction both at the crown and the springline increased slightly; however, the strains in the circumferential direction at both locations increased significantly. In other words, the perimeter of the pipe increased with the backfilling and no local buckling occurred. The maximum strain of the plastic cover was 0.044% at the pipe springline, which was much lower than the long-term strain limit of the thermoplastic pipes of 5% suggested by AASHTO (2012).

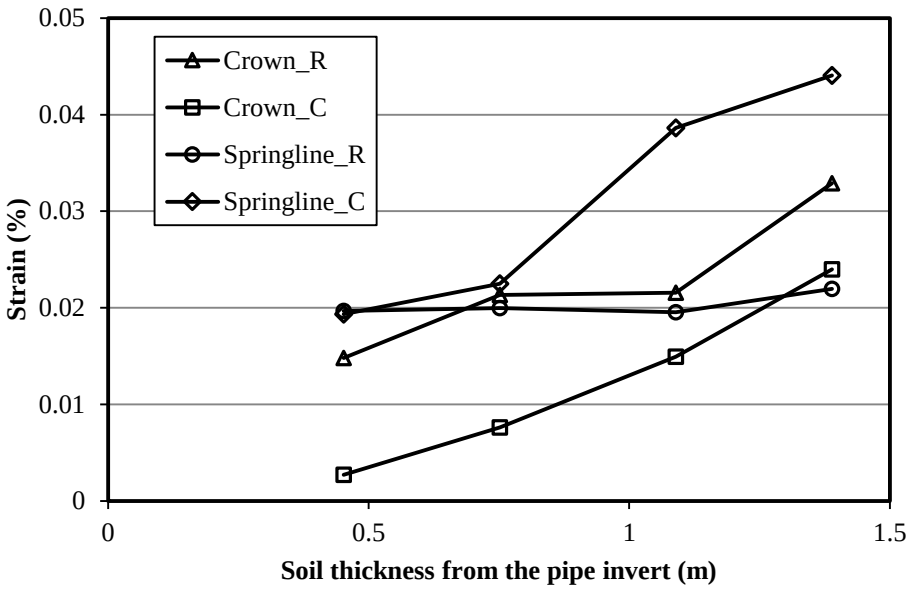

Figure 3.33 Strains of the plastic cover in Section A during the pipe installation

Figure 3.34 presents the strains of the plastic valley. "Crown_L" and "Springline_L" represent the strain in the longitudinal direction at the crown and the springline, respectively. The strain gages were fixed on the plastic valley in two directions, namely, the hoop direction and the longitudinal direction. This figure shows the strains of the plastic valley increased with an increase of the soil thickness. The strains in the longitudinal direction at both the pipe crown and the pipe springline were higher than the strains in the circumferential direction. The possible explanation is that the pipe is reinforced in the circumferentia direction and the steel ribs can limit the development of the strain; however, the pipe in the longitudinal direction is only an HDPE liner, which has a low elastic modulus. The measured maximum strain of the plastic valley was 0.14%, which was much higher than the strains of the plastic cover and the steel ribs. The strains of the plastic valley were also lower than the 5% long-term strain limit suggested by AASHTO (2012).

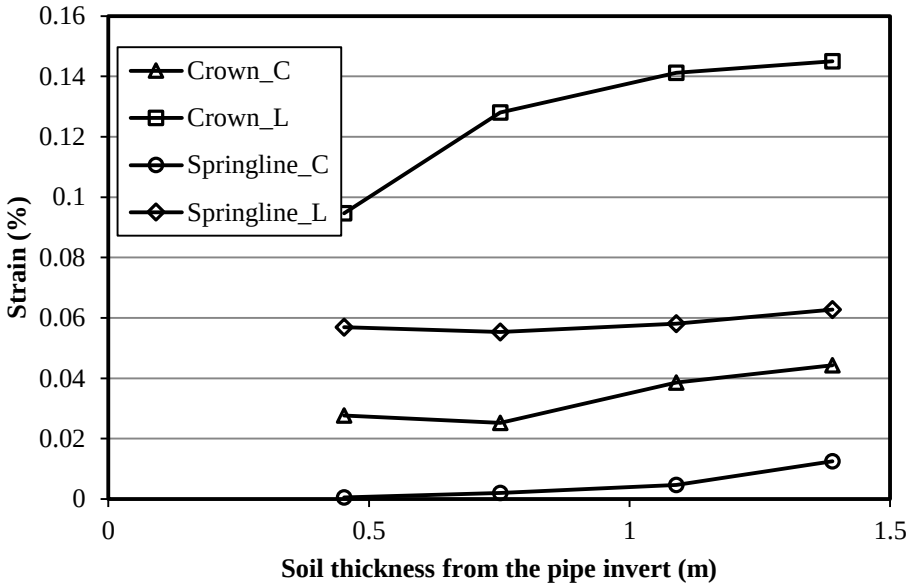

Figure 3.34 Strains of the plastic valley in Section A during the pipe installation

The strains of the pipe in the Section A (i.e., the AB3 aggregate section) all increased with an increase of the soil cover thickness. The maximum strains on the steel ribs and the plastic valley occurred at the pipe crown, while the maximum strain on the plastic cover was located at the pipe springline. The strains of the plastic valley were higher than those of the steel ribs and the plastic covers; however, they were much lower than the strain limit. The strains of the steel ribs were also much lower than the yield strain of the steel (0.5%). In summary, the tested SRHDPE pipes in the AB3 section did not have any strain problem during the pipe installation.

Test Section B

Figure 3.35 shows the strains of the steel ribs in the crushed stone section during the pipe installation. The strains at the springline changed slightly; however, the strains at the pipe crown changed significantly with the pipe installation. These strains are consistent with the strains of the steel ribs in Section A. The compaction of the soil cover should be responsible for the increase of the strains at the pipe crown. The strains of the steel ribs in the crushed stone were 2 to 4 times

those in the AB3 section. The possible reason is that the vertical deflection of the pipes in the crushed stone (2.3 mm) was larger than that in the AB3 section (1.8 mm) when the backfilling was above the level of the pipe top.

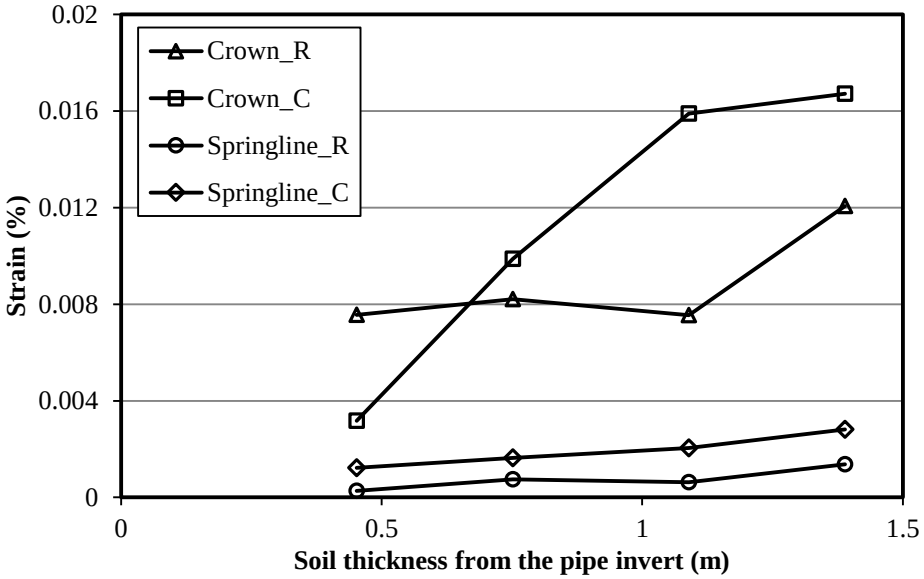

Figure 3.35 Strains of the steel ribs in Section B during the pipe installation

Figure 3.36 presents the strains of the plastic cover in the crushed stone section during the pipe installation. The strains of the plastic cover in both directions at the pipe springline increased slightly, while those at the pipe crown increased significantly. This finding was opposite to that in the AB3 aggregate section. The modulus of the crushed stone was relative lower than that of the AB3 aggregate section based on the plate loading tests and the LWD tests. In the crushed stone section, the side fill could provide less support than that in the AB3 aggregate section to the pipe, which resulted in the lower modulus of the pipe buried in the backfill material. Therefore, the earth pressure at the pipe top in the crushed stone section was lower than that in the AB3 section. The maximum value of the strain was 0.062%, which was approximately 1.5 times that in the AB3

aggregatee section but much lower than the long-term strain limit of 5% suggested by AASHTO (2012).

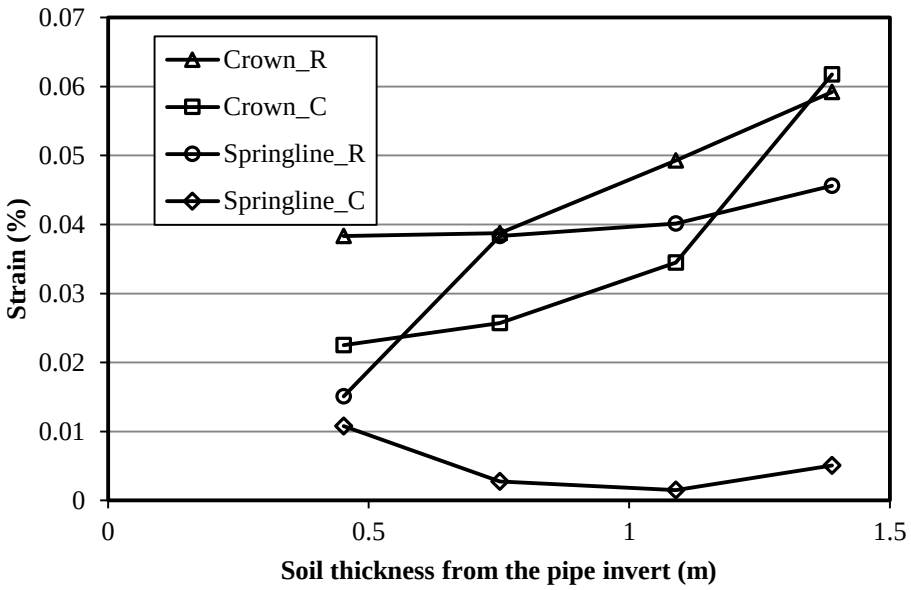

Figure 3.36 Strains of the plastic cover in the crushed stone section during the pipe installation

Figure 3.37 shows the strains of the plastic valley in the crushed stone section during the pipe installation. The strains of the plastic valley were measured in two directions, namely, the circumferential direction and the longitudinal direction (i.e., along the pipe). The test results demonstrate that the strain in the circumferential direction increased slightly; however, the strain in the longitudinal direction increased significantly. This finding is the same as that in the AB3 section. The maximum strain of the plastic valley in the crushed stone section was 0.19%, which was approximately 1.5 times that in the AB3 section. However, the strain of the plastic valley was much smaller than the strain limit of 5%.

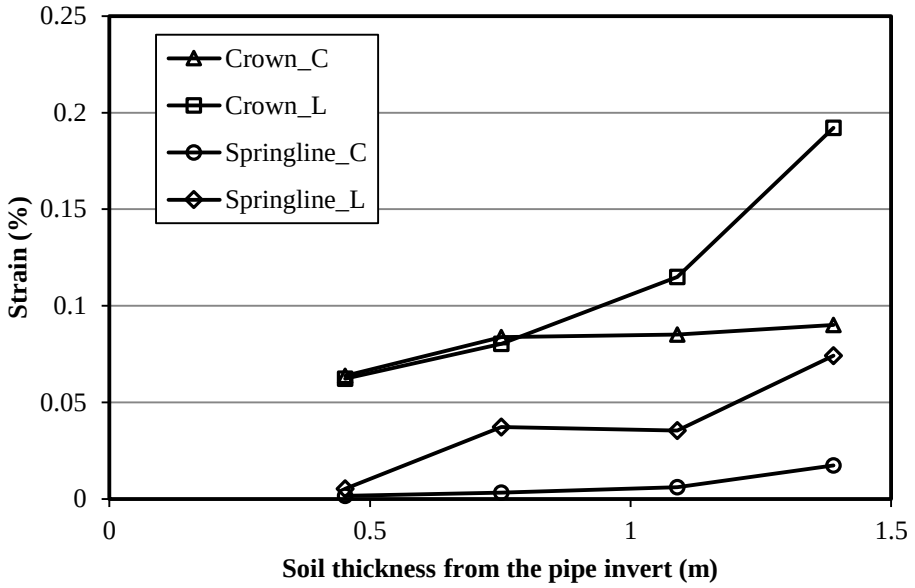

Figure 3.37 Strains of the plastic valley in the crushed stone section during the pipe installation

The strains of the pipe in the Section B (i.e., the crushed stone section) at different locations increased during the construction. The maximum strains on the steel ribs, the plastic covers and the plastic valley all occurred at the pipe crown. The strains of the plastic valley were higher than those of the steel ribs and the plastic covers; however, they were much smaller than the strain limit of 5%. The maximum strain of the steel ribs (i.e., 0.02%) was also much smaller than the yield strain of steel (0.5%). Even though the strains in the crushed stone section were all higher than those in the AB3 section at the same position, no failure happened to any elements in the crushed stone section during the pipe installation.

Figure 3.38 shows the comparison of the measured maximum strains on the plastic in the longitudinal and the circumferential directions and the calculated strains in the circumferential direction in both sections. **Equations (2-23) and (2-24)** were used to calculate the strain based on the deflection and the load above the pipe. In both sections, the measured strains were larger than

the calculated ones. The calculated strains are the maximum strain of the plastic in the circumferential direction, which is typically recognized as the design criteria. The longitudinal strain is often neglected in most pipe design. However, for the SRHDPE pipe, the stiffness in the longitudinal direction is much lower than that in the circumferential direction. This is why the measured strains in the longitudinal direction were higher than those in other directions in this field test. In other words, the longitudinal strain is more critical for the SRHDPE pipe.

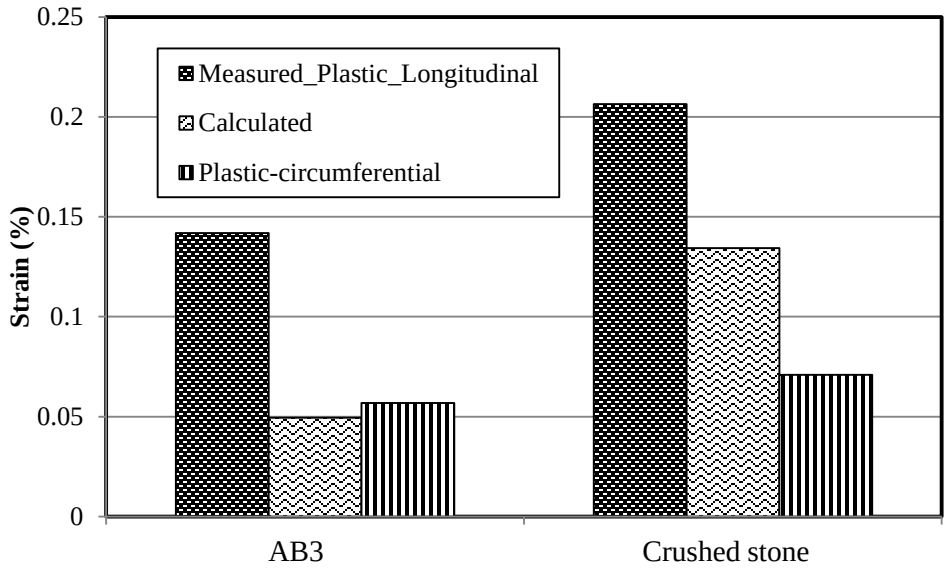

Figure 3.38 Comparison of the measured strains and calculated strains on the plastic in both sections

3.6 Analysis of Test Results under Static Loading

3.6.1 Earth Pressure

Figure 3.39 shows the earth pressure around the pipe at the end of the construction and under the static loading in Section A. Two types of static loading were applied above the pipe,

namely, the use of the loader backhoe and the use of the crawler loader. The earth pressures at the pipe springline and the shoulder increased 13.8 to 27.6 kPa under static loading from those at the end of construction, while the earth pressures at the pipe crown increased by 75.9 and 62.1 kPa under the loading of the loader backhoe and the crawler loader, respectively. **Figure 3.39** indicates that static loading increased the earth pressure at the pipe crown up to 4 times that at the end of the construction.

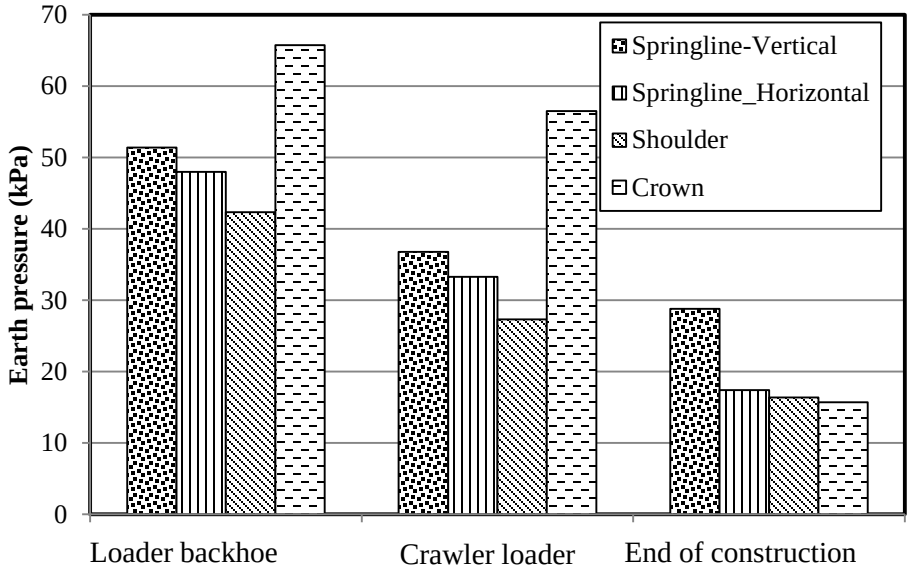

Figure 3.39 The measured earth pressures in Section A at the end of the construction and under static loading

Figure 3.40 presents the earth pressures around the pipe at the end of construction and under static loading in Section B. Static loading increased the earth pressures at the springline and the shoulder by 13.8 to 27.6 kPa from those at the end of construction. This result is the same as that for Section A. The earth pressures at the pipe crown were 63.0 and 51.9 kPa under the loading of the loader backhoe and the crawler loader, respectively, which are 3.6 and 3 times those at the end of the construction. The magnitude of the earth pressure increased by static loading in the

crushed stone section was lower than that in the AB3 aggregate section. The sidefill in Section A could provide support to the pipe due to the high stiffness which could make the pipe stiffer than that in Section B, which resulted in the higher earth pressure on the pipe top in Section A.

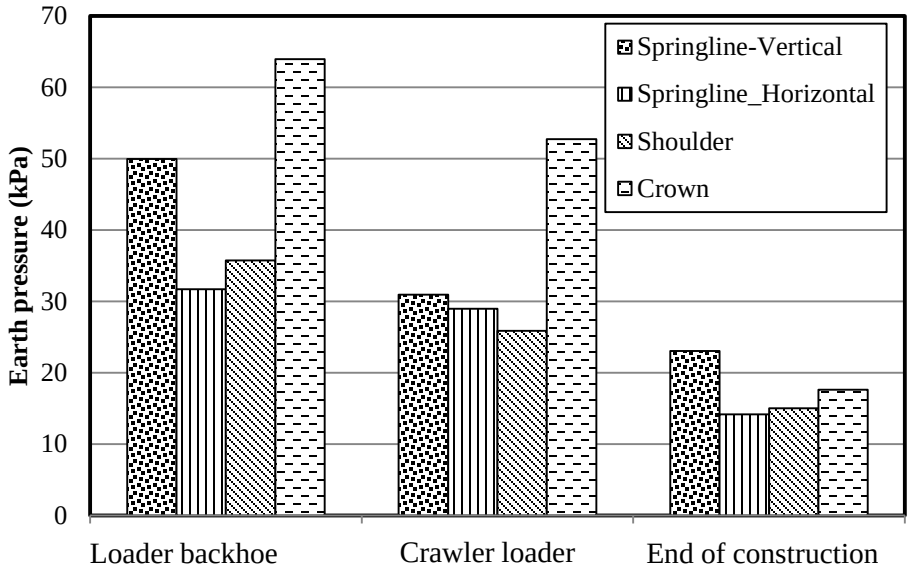

Figure 3.40 The measured earth pressures in Section B at the end of the construction and under static loading

Figure 3.41 shows the comparison of the measured earth pressures at the pipe crown with the calculated earth pressures in both sections. This figure indicates the calculated pressures in both sections by the AASHTO (2012) method are higher than those by the Giroud and Han (2004) method. However, the calculated pressures by both methods were close to the measured ones. It can be concluded that both methods can be used to predict the earth pressures induced by static loading above the SRHDPE pipe.

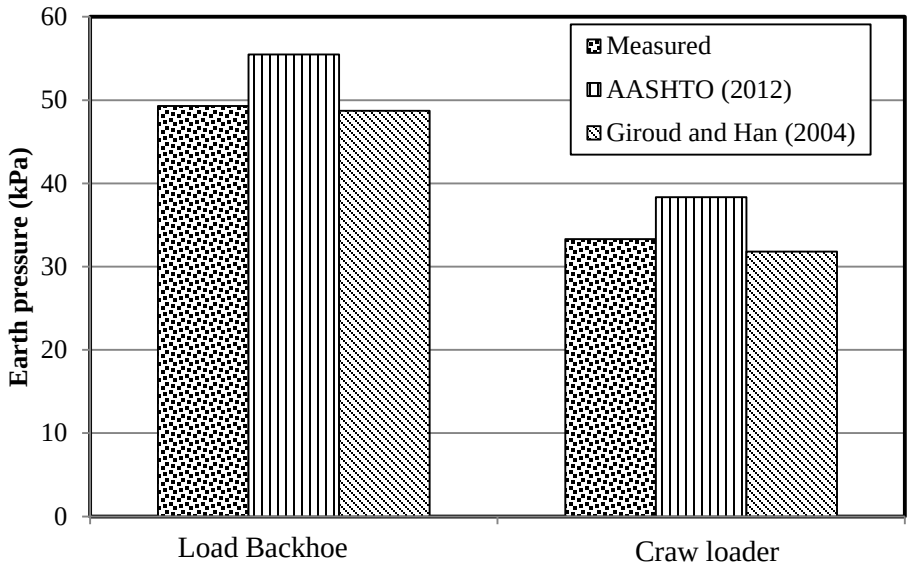

(a) Section A

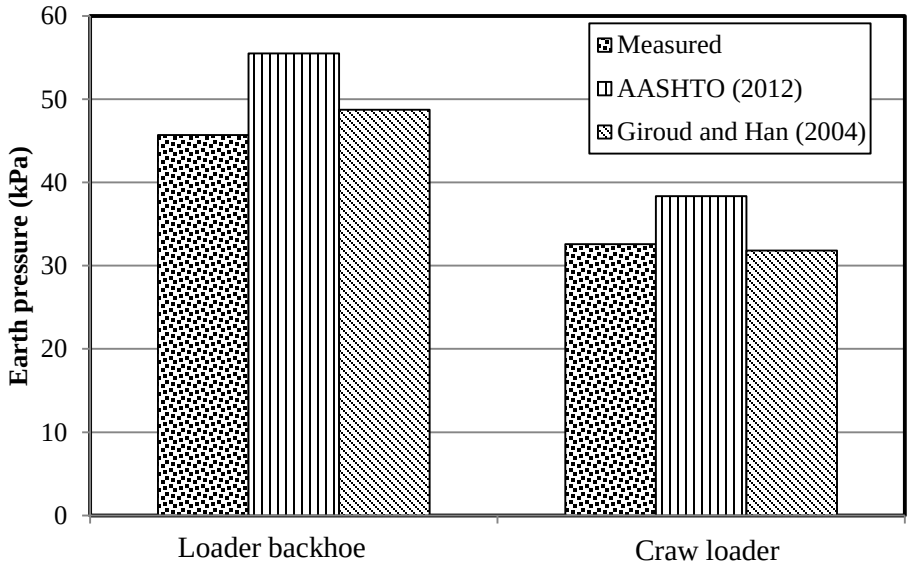

(b) Section B

Figure 3.41 Comparison of the measured earth pressures at the pipe crown with the calculated ones under static loading

3.6.2 Deflections

Figure 3.42 presents the diameter change of the pipes under static loading in both sections. The maximum diameter changes occurred at the plastic valley. The vertical deflections were 0.28 and 0.23 mm the Sections A and B, respectively. The deflections at the steel ribs were smaller but close to the deflections at the plastic valley. The horizontal deflections were close to the vertical deflections at the plastic valley with an exception of the horizontal deflection in Section B, which was 0.51 mm and two times the vertical deflection. In both sections, the deflection at the same position under the loading by the loader backhoe was larger than that induced by the crawler loader due to their different load magnitudes. The deflections of the pipes under static loading in Section A were larger than those in Section B. The possible reason is that more load was carried by the pipe in Section A than that in Section B.

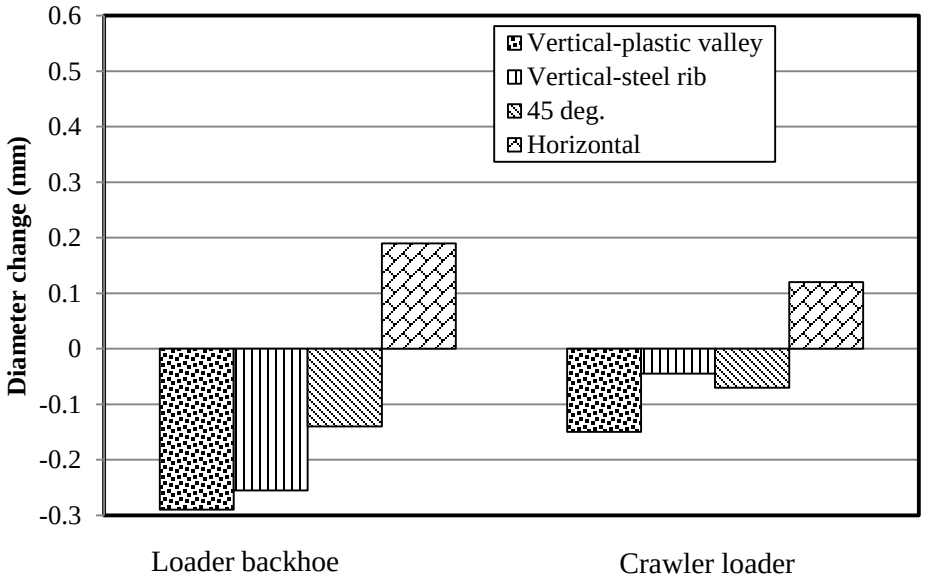

(a) Section A

Figure 3.42 Diameter changes of the pipes under static loading

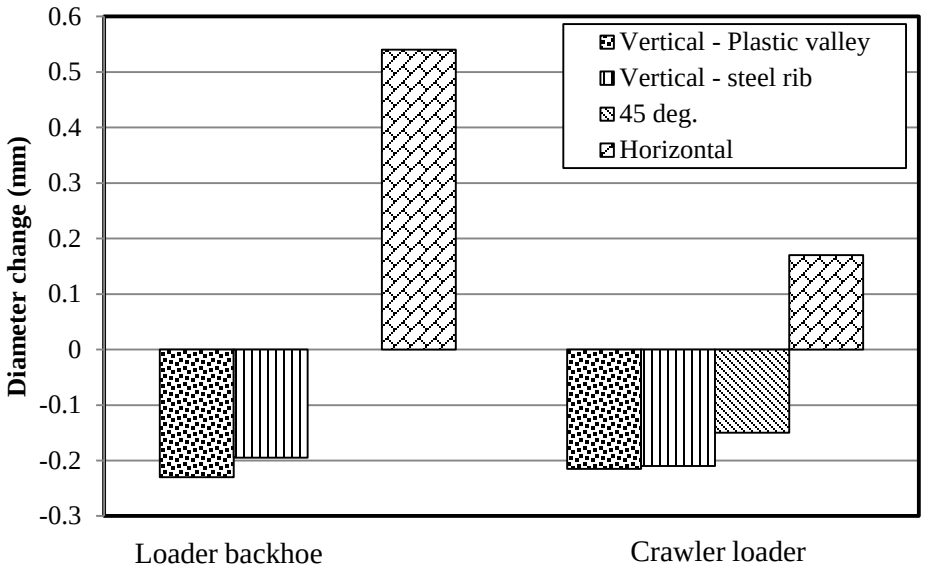

(b) Section B

Figure 3.42 Diameter changes of the pipes under static loading (continued)

Equation (2-6) (i.e., the Iowa Formula) was used to calculate the deflection caused by static loading. The loads on the pipe top used in the calculation were the measured earth pressures reported in the earlier section. The deflection lag factor was determined as one since the short duration of the test. The bedding factor was 0.11 based on the suggestion by Moser and Folkman (2008). The pipe stiffness was 294 kPa based on the parallel plate load tests in Khatri (2014). The constrained moduli were 23.5 and 19.6 MPa for the AB3 aggregate and the crushed stone determined from the plate load tests, respectively. **Table 3.1** compares the calculated deflections using the Iowa Formula and the measured ones. This table illustrates that the calculated results are close to the measured ones. This comparison confirms that the Iowa Formula can be used to estimate the deflection of the SRHDPE pipe induced by static loading.

Table 3.1 Comparison of the calculated and measured deflections under static loading

Section	Loading type	Measured (mm)	Calculated (mm)
A	Loader backhoe	0.28	0.18
	Crawler loader	0.15	0.18
B	Loader backhoe	0.23	0.20
	Crawler loader	0.20	0.15

3.6.3 Strains

The strains at the plastic cover and the plastic valley in this section were also adjusted using a factor of 1.29 according to Brachman et al. (2008). **Figure 3.43** shows the measured strains of the pipe in Section A caused by static loading. The strain changes of the steel ribs at the pipe crown were almost three times those at the pipe springline. The maximum strain on the steel ribs at the pipe crown was 0.004%, which is much smaller than the steel yield strain limit of 0.5%. The strains of the plastic cover induced by static loading ranged from 0.015 to 0.045%, which are much smaller than the plastic strain limit of 5%. The strains at the pipe crown in both the circumferential and the radial directions were larger than the strain in the circumferential direction at the springline but close to the strain in the radial direction at the springline. The strains of the plastic valley in the longitudinal direction at the pipe crown were larger than the strains in the same direction at other locations under both static loadings. The maximum strain of the plastic valley in the longitudinal direction was approximately 0.13%, which is much smaller than the plastic strain limit of 5%.

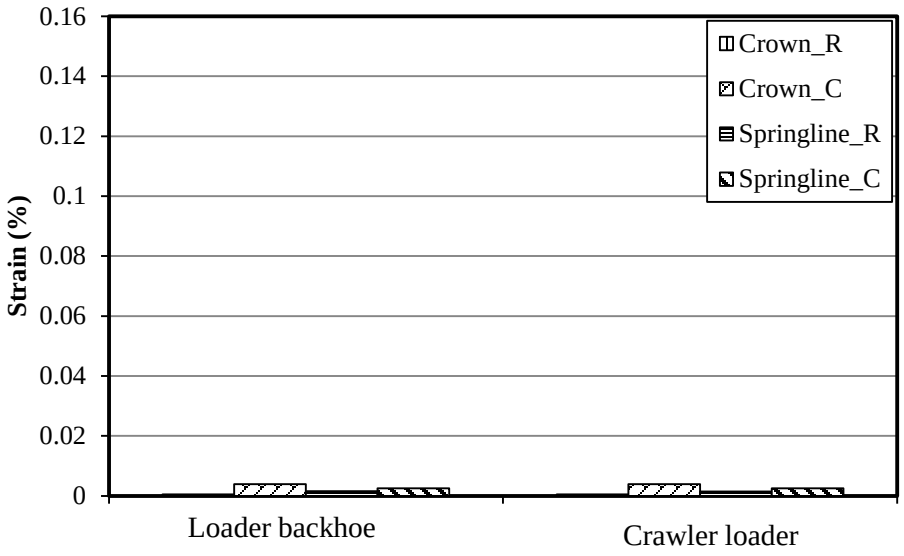

(a) On steel ribs

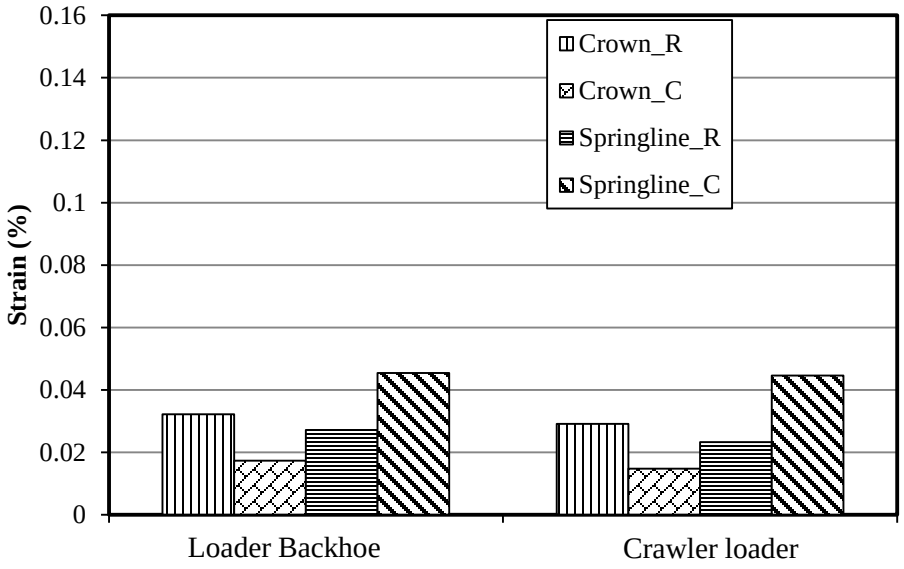

(b) On plastic cover

Figure 3.43 The measured strains of the pipe in Section A

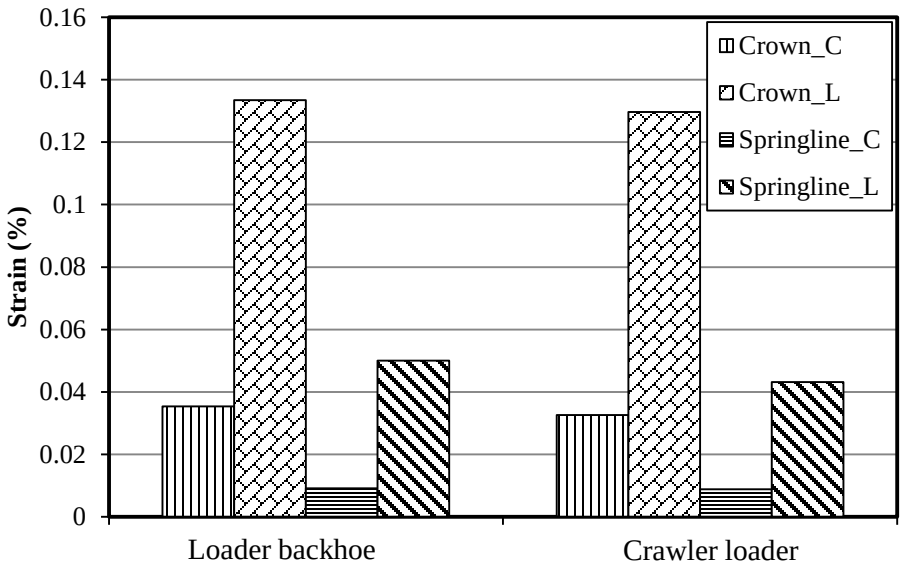

(c) On plastic valley

Figure 3.43 The measured strains of the pipe in Section A (continued)

Figure 3.44 shows the measured strains of the pipe in Section B caused by static loading. Similar to Section A, the strains of the steel ribs at the pipe crown were larger than those at the pipe springline. The maximum strain on the steel ribs at the pipe crown was 0.007%. The strains of the plastic cover caused by static loading ranged from 0.015 to 0.035%, which are much smaller than the plastic strain limit of 5%. The strains at the pipe crown in both the circumferential and the radial directions were higher than the strain in the hoop direction at the pipe springline but close to the strain in the radial direction at the springline. The strains of the plastic valley in the longitudinal direction were larger than the strains of steel ribs and plastic covers, which was caused by the lower stiffness of the pipe in the longitudinal direction. The maximum strain of the plastic valley was approximately 0.15%, which is much smaller than the plastic strain limit of 5%.

In summary, the strains induced by the loader backhoe at all positions in both sections were slightly larger than those caused by the track loader due to their pressure difference. All the strains

of the pipes induced by static loadings were smaller than their strain limits; therefore, it can be concluded that the pipes were safe under these two types of static loadings in this field test.

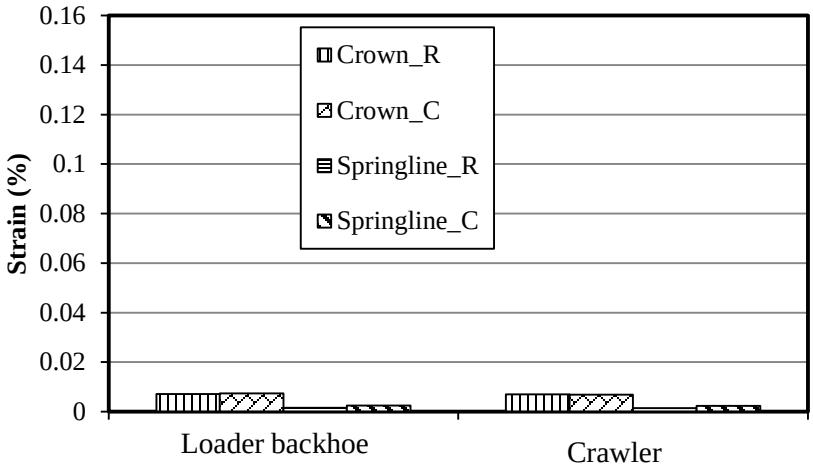

(a) On steel ribs

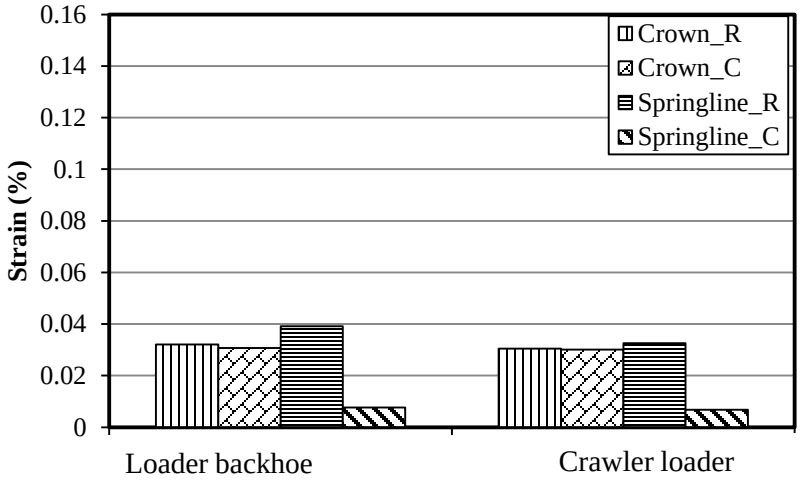

(b) On plastic cover

Figure 3.44 The measured strains of the pipe in Section B

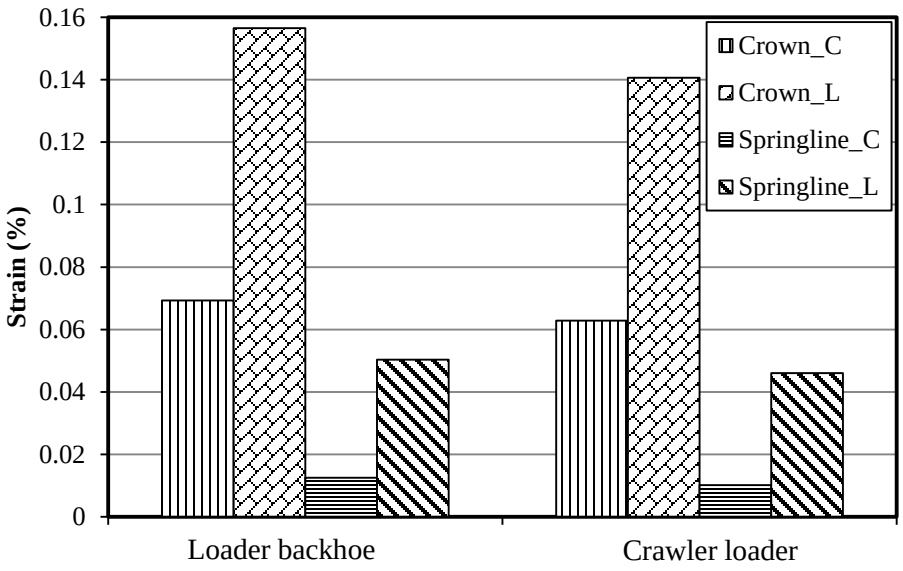

(c) On plastic valley

Figure 3.44 The measured strains of the pipe in Section B (continued)

3.7 Observation of Exhumed pipes

The buried pipes were exhumed for visual observations after the installation. No obvious damage to the ribs and liners of the pipes was observed. To investigate the deformations of ribs during installation, the displacements of ribs at the springline in both sections were monitored. Before the installation, 14 ribs at the springline of each of the middle two pipes were marked and the gap distances (i.e., 13 gaps) between two adjacent ribs were measured and recorded. After field testing, the gap distances were measured again to evaluate possible distortions of the ribs during the installation. **Figure 3.45** shows the gap distances before and after the installation in both sections. Generally, the gap distance changes in Section B were larger than those in Section

A. The possible reason is that more large stone particles were pushed into the gaps in Section B by compaction than those in Section A.

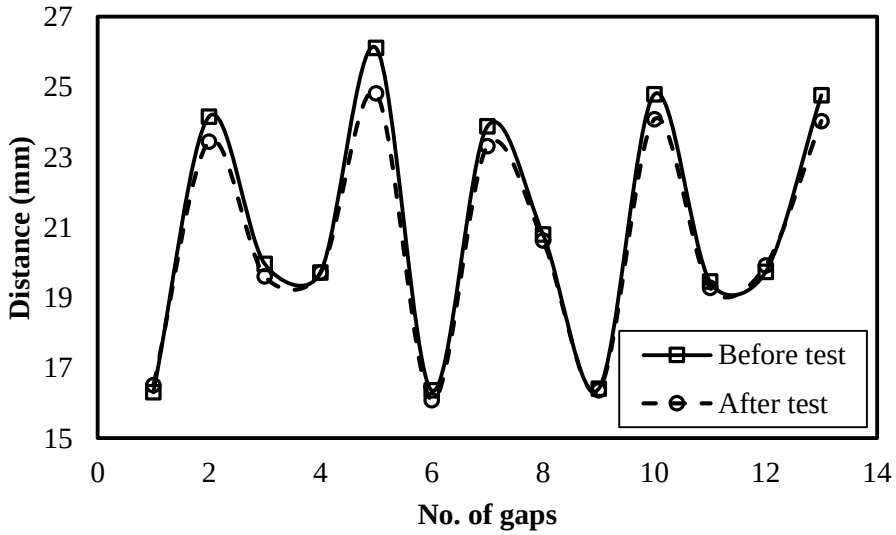

(a) Section A

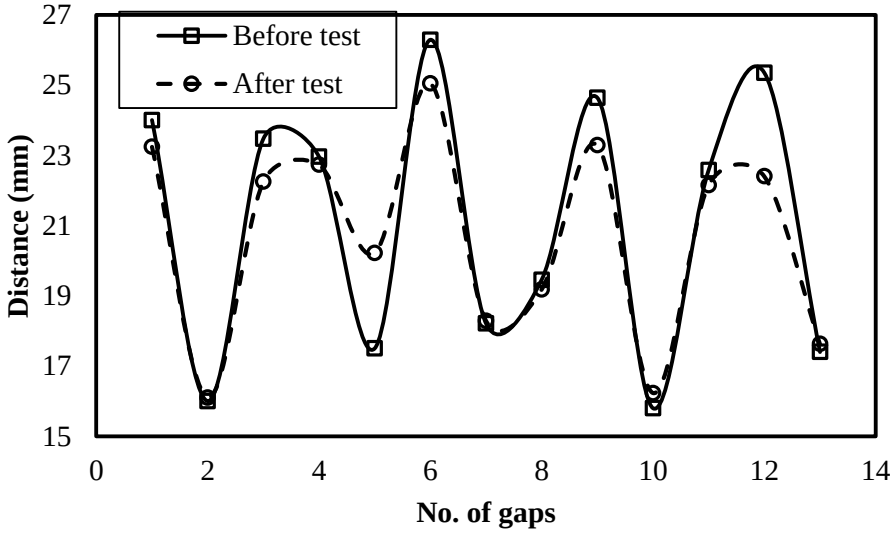

(b) Section B

Figure 3.45 Displacements of ribs at the springline of pipes in two sections

3.8 Summary

A full-scale field test was conducted to investigate the installation effect on the SRHDPE pipes in the AB3 aggregate and the crushed stone with the soil cover thickness of 0.65 m in both sections. The diameter of the pipe is 0.6 m. The deflections and strains of the pipes and the earth pressures in the backfills were monitored during backfilling. The following conclusions can be made from the analysis of the test results:

(1) The peaking deflection of the pipe in the AB3 aggregate was 1.5 times that in the crushed stone. However, the vertical diameter of the pipe in the crushed stone decreased by 3.5 times that in the AB3 aggregate at the final level of the backfill. The vertical deflection of the pipe at the valley liner was slightly greater than that at the steel reinforcement rib. The diameter change of the pipe at 45^{o} from the pipe crown in the crushed stone was larger than that in the AB3 aggregate. The horizontal deflection of the pipe during backfilling was opposite to the vertical deflection. The maximum deflections in the AB3 aggregate and the crushed stone were both much less than the 5% deflection limit for the steel and HDPE pipes suggested by the AASHTO standards. The deflection of the SRHDPE pipe during the installation and the loading can both be calculated based on the Iowa formula.

(2) The vertical soil arching factors at the top of the pipe for Sections A and B were 1.10 and 1.47 at the end of backfilling, respectively; which demonstrated that some load was transferred from the surrounding soil to the pipe due to negative soil arching effect. The vertical pressure on the SRHDPE pipe induced by static loading on unpaved roads (i.e., during construction) can be calculated by the Giroud and Han (2004) method and the AASHTO (2012) method. When the base course had higher stiffness than the backfill above the pipe, the Giroud and Han (2004)

method more accurately estimated the vertical pressure than the AASHTO (2012) method. The lateral earth pressure coefficient in the AB3 aggregate was higher than that in the crushed stone. The lateral earth pressure measurements verified that the lateral earth pressure caused by the compaction of the backfill with depth was constant.

(3) The maximum strain of the pipe occurred on the plastic valley in the longitudinal direction at the pipe crown, but it was much smaller than the strain limit of 5% suggested by AASHTO (2012);

(4) The SRHDPE pipe performed well in the AB3 aggregate and the crushed stone during the installation. The displacements of ribs at the springline of the pipe in the crushed stone section were greater than those in the AB3 aggregate section.

CHAPTER 4 NUMERICAL MODELING ON THE INSTALLATION OF THE SRHDPE PIPE

4.1 Introduction

The allowable deflection of an SRHDPE pipe is 5%, thus the SRHDPE pipe can be classified as flexible pipe. As discussed in the literature review, the load carrying capacity of the flexible pipes mainly depends on the compaction of the sidefill. In other words, compaction and the performance of the SRHDPE pipe under compaction are essential for the installation design of the SRHDPE pipe. Numerical modeling is a powerful tool to investigate the performance of the SRHDPE pipe under different conditions to recommend design parameters and the criteria for evaluating the installation quality. Two problems have to be solved in the numerical modeling on the installation of the SRHDPE pipe: (1) simulation of the compaction behavior; and (2) model of the corrugated pipe.

Two characteristics of the compaction behavior were not included in the hysteretic K_0 method and the additional surcharge method: (1) the compaction load should be removable; and (2) pipe-soil interaction could be reflected in the simulation of the compaction. The deformation of the pipe should be directly caused by the lateral compaction-induced movement of the side fill rather than applied loads.

Corrugated pipes in numerical models are widely converted to plain pipes (Flener, 2010; and Tamer and Moore, 2013). The equivalence of the corrugated pipes to plain pipes typically includes two steps: (1) calculate the moment of inertia of the corrugated pipe using **Equation (4-1)** based on the pipe stiffness determined from the parallel plate load test; and (2) calculate the equivalent thickness for the plain pipe through **Equation (4-2)**.

$$E_p I = 0.149 R^3 PS \tag{4-1}$$

where E_p = the elastic modulus of the corrugated pipe; I = the moment of inertia of the pipe; R = the radius of the pipe; PS = the pipe stiffness which can be determined through the parallel plate load test.

$$t = \sqrt[3]{12I} \tag{4-2}$$

where t = the equivalent thickness of the pipe in the numerical model.

The equivalent method is not applicable for the SRHDPE pipe since the pipe wall is a composite material including steel and high-density polyethylene. The elastic modulus of the pipe E_p in **Equation (4-1)** is difficult to be determined. If the elastic modulus of steel is used, the calculated pipe wall thickness would be too thin to reflect the bending and thrust behavior of the SRHDPE pipe. If the elastic modulus of the high-density polyethylene is adopted, the pipe wall thickness might become an irrational number even greater than the real pipe radius.

Mlynarski et al. (2007) pointed out that the simulation of the plastic pipes were limited to smooth walls in the previous versions of pipe design software CANDE (Culvert ANalysis and DEsign) 2007. In CANDE 2007, the pipe type was extended to the profile wall and corrugated pipes which can be simulated using an approximation model as shown in **Figure 4.1**. One corrugation period includes eight elements, including two link elements, two web elements, two valley elements, one crest element, and one liner element. This model is not suitable for the SRHDPE pipe since steel ribs could not be included. McGrath and Schafer (2003) modeled a quarter of a corrugated HDPE pipe cross section with the real size of the corrugations. However, it is difficult to treat the steel-plastic interface behavior of the SRHDPE pipe in the full-size model, even more difficult to model the pipe-soil interaction.

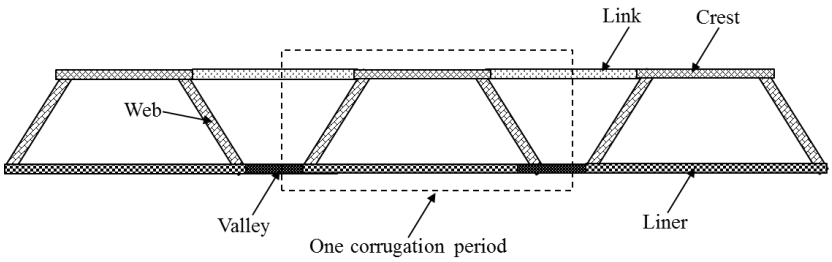

Figure 4.1 Schematic of the approximation model for the corrugations in CANDE

Hardening soil model was used in this study to model the backfill material, which can reflect the plastic-elastic behavior of the backfill material during and after the compaction and the residual horizontal stress after the removal of the compaction loads. Triaxial compression test results of Cook's Bayou sand (Katona, 2015b), AB3 aggregate and crushed stone were used to verify the effectiveness of the hardening soil model. A numerical model with a 1.5 m wide and 2.0 m deep trench backfilled with AB3 aggregate was conducted to demonstrate the applicability of the hardening soil model to simulate the compaction behavior. An equivalent modulus method was proposed to model the SRHDPE pipe in the numerical model and was verified using test data from the literature. The numerical modeling method was verified using the field test in Chapter 3. Subsequently, a numerical study using PLAXIS 2D was conducted to investigate the effects of the soil cover thickness, the trench width, the magnitude of compaction load, and the friction angle of the backfill material on the performance of SRHDPE pipes during installation. The Bending moment, the hoop strain, the earth pressure, and the pipe deflection were used to evaluate the pipe performance.

4.2 Hardening Soil Model

4.2.1 Introduction of the Hardening Soil Model

In contrast to an elastic perfectly-plastic model, the yield surface of the hardening model is not fixed in a stress space, which can expand due to the plastic strain development (Schanz and Vermmer, 1998). The hardening soil model includes two types of soil hardening, namely the shear hardening and the compression hardening. Shear hardening is used to model irreversible strains due to the deviator loading. Compression hardening can model the irreversible strains due to the compression loading. Those two characteristics of the hardening soil model are capable of simulating the residual strains due to the compaction. The hardening soil model has eight parameters to simulate the plastic strain induced both by the shearing and the compression loading:

- Stress-dependent stiffness according to a power, *m*;
- Plastic strain due to the deviator loading E_{50}^{ref};
- Plastic strain due to the compression loading E_{oed}^{ref};
- Elastic unloading and reloading E_{ur}^{ref} and ν_{ur};
- Failure according to the Mohr-Coulomb model *c*, φ, ψ.

The parameter E_{50} is a confining stress-dependent modulus with respect to the shear loading can be calculated as follows:

$$E_{50} = E_{50ref}\left(\frac{c\cos\phi + \sigma_3 \sin\phi}{c\cos\phi + 100\sin\phi}\right)^m \tag{4-3}$$

where *c* = the cohesion; ϕ = the friction angle of soil; σ_3 = the confining pressure; *m* = the stress dependent power.

$$E_{oed} = E_{oedref}\left(\frac{c\cos\phi + \sigma_3 \sin\phi}{c\cos\phi + 100\sin\phi}\right)^m \quad (4\text{-}4)$$

where E_{oed} = the modulus with respect to the compression loading.

The Poisson's ratio for unloading v_{ur} is usually taken as 0.2. Schanz and Vermmer (1998) suggested $E_{oed}^{ref} = E_{50}^{ref}$ and $E_{ur}^{ref} = 3 \sim 5E_{50}^{ref}\sqrt{a^2 + b^2}$. The hyperbolic stress strain relationship was adopted in the hardening soil model which was originally proposed by Kondner (1963).

4.2.2 Verification of Backfill Material Behavior Modeled by the Hardening Soil Model

Granular material is widely used as the backfill material for buried pipes. In this section, triaxial compression test results of three types of typical backfill materials, namely, Cook's Bayou sand, AB3 aggregate and crushed stone, were compared with the numerical results to demonstrate the effectiveness of the hardening soil model.

Katona (2015b) presented a series of triaxial test results of the Cook's Bayou sand conducted by the U.S. Army Corp Engineers, which was used for soil model calibration. All soil samples were taken from a natural sand quarry with a small amount of fines. Soil samples were tested at a density of 1.79 Mg/m^3 in a dry condition. Three confining pressures of 172.5, 345 and 690 kPa were adopted for the triaxial tests. Based on the test data, E_{50} for the triaxial tests at those three confining pressures were determined as 19.8, 23.2, and 25.3 MPa, respectively. The friction angle and the cohesion were 35.6^o and 8.6 kPa, respectively. Substituting any two E_{50} values at two confining pressures into **Equation (4-3)**, the *m* value and E_{50}^{ref} can be calculated as 0.336 and

17.5 MPa, respectively. According to Schanz and Vermmer (1998)'s suggestion, E_{oed}^{ref} was also assumed as 17.5 MPa and the unloading modulus E_{ur}^{ref} was 70 MPa. The hardening soil model parameters of the Cook's Bayou sand are summarized in **Table 4.1**. Inputting all parameters listed in **Table 4.1** of the hardening soil model in the numerical model, the stress strain curves from triaxial tests can be obtained. **Figure 4.2** shows the comparison of the calculated and measured triaxial test results of the Cook's Bayou sand at different confining pressures. The comparison demonstrates the hardening soil model can simulate the stress and strain behavior of the Cook's Bayou sand very well.

Table 4.1 Hardening soil model parameters of the Cook's Bayou sand

Parameters	Cook's Bayou sand
Unit weight γ (kN/m^3)	19.0
Cohesion C (kPa)	86.3
Friction angle ϕ (^{o})	35.6
m	0.336
E_{50}^{ref} (MPa)	17.5
E_{oed}^{ref} (MPa)	17.5
E_{ur}^{ref} (MPa)	70
ν_{ur}	0.2
ψ (^{o})	5.6

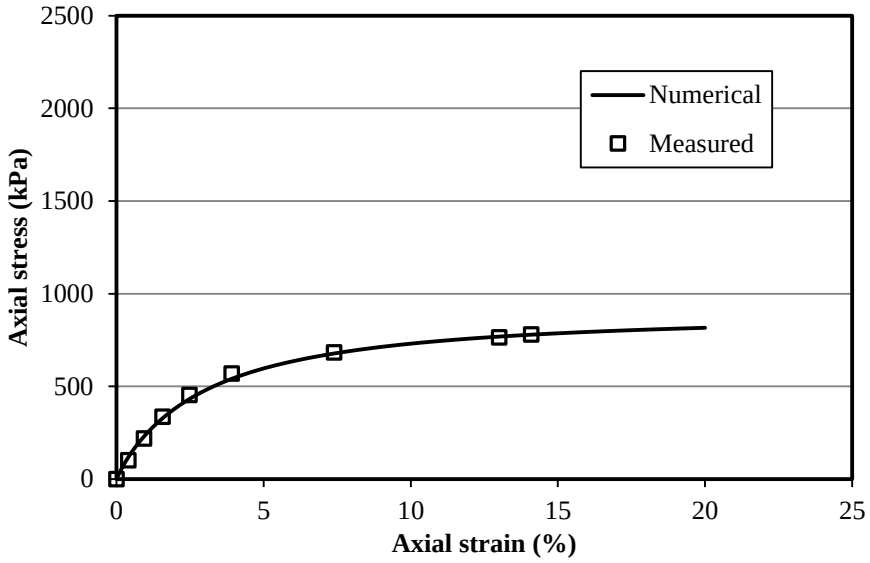

(a) 172.5 kPa

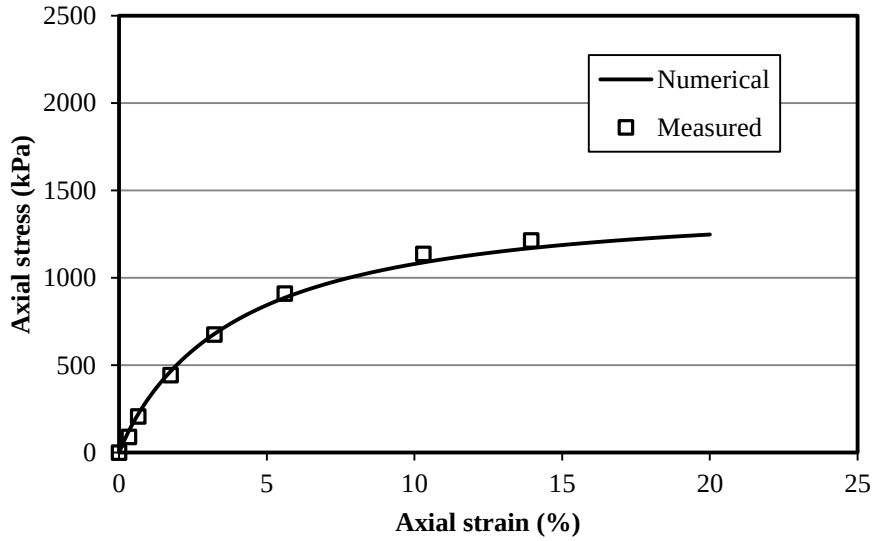

(b) 345 kPa

Figure 4.2 Comparison of the calculated and measured triaxial test results

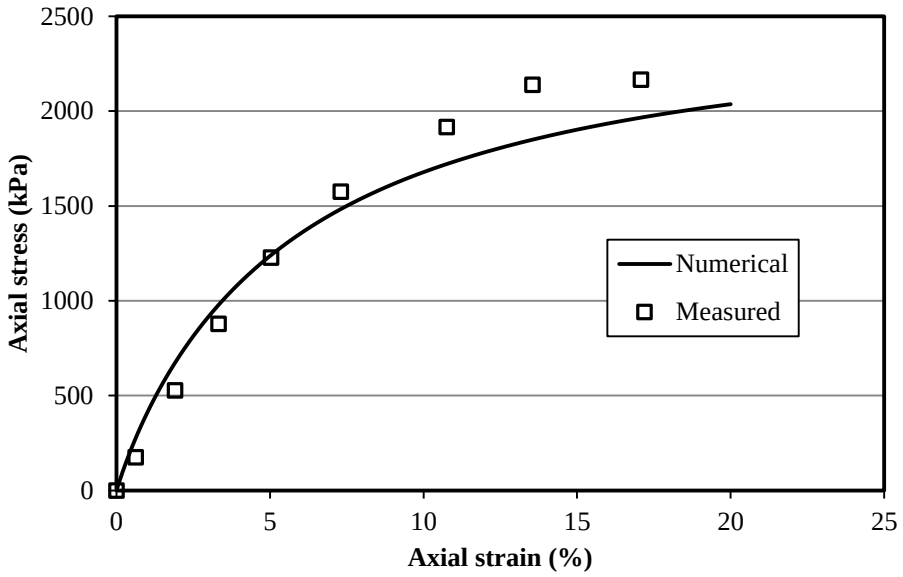

(c) 690 kPa

Figure 4.2 Comparison of the calculated and measured triaxial test results (continued)

The AB3 aggregate and the crushed stone were used as backfill material for buried SRHDPE pipes in a field study (Wang et al., 2015). Based on the ASTM D2487 (2011), the AB3 aggregate can be classified as well-graded gravel (**GW-GC**) while the crushed stone can be classified as poorly-graded gravel (**GP**). The optimum moisture content of the AB3 aggregate was 11.2%, and the maximum dry density was 2.1 Mg/m^3. The minimum and maximum densities of the crushed stone were 1.44 and 1.68 Mg/m^3, respectively. Triaxial compression test was used to evaluate the effectiveness of the hardening soil model. The confining pressures were 34.5, 69 and 138 kPa. The AB3 aggregate triaxial samples were prepared at the optimum moisture content of 7.2%, while the crushed stone samples were prepared in a dry condition with the maximum dry density. The diameter and length of the samples were 100 and 200 mm, respectively. The hardening soil parameters of the AB3 aggregate and the crushed stone were determined and are

summarized in **Table 4.2** using the same method adopted for the Cook's Bayou sand. **Figures 4.3** and **4.4** show the comparison of the calculated and measured triaxial test results of the AB3 aggregate and the crushed stone, respectively. The comparison demonstrates the hardening soil model is also applicable to simulate the AB3 aggregate and the crushed stone.

Table 4.2 Hardening soil model parameters of the AB3 aggregate and the crushed stone

Parameters	AB3 aggregate	Crushed stone
Unit weight γ (kN/m^3)	21.9	15.6
Cohesion C (kPa)	100	40
Friction angle ϕ (^{o})	45	45
m	0.620	0.491
E_{50}^{ref} (MPa)	26.6	22.2
E_{oed}^{ref} (MPa)	26.6	22.2
E_{ur}^{ref} (MPa)	66.4	112.8
ν_{ur}	0.2	0.2
ψ (^{o})	15	15

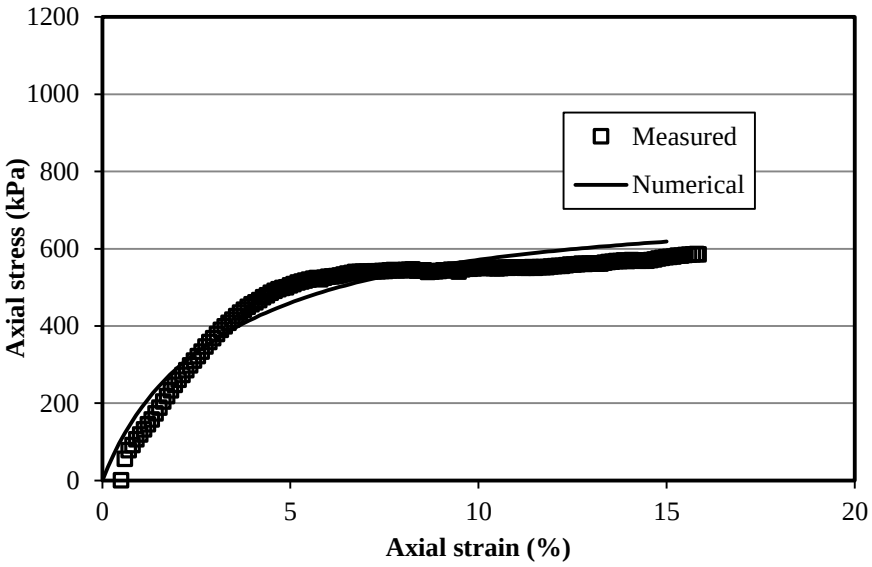

(a) 34.5 kPa

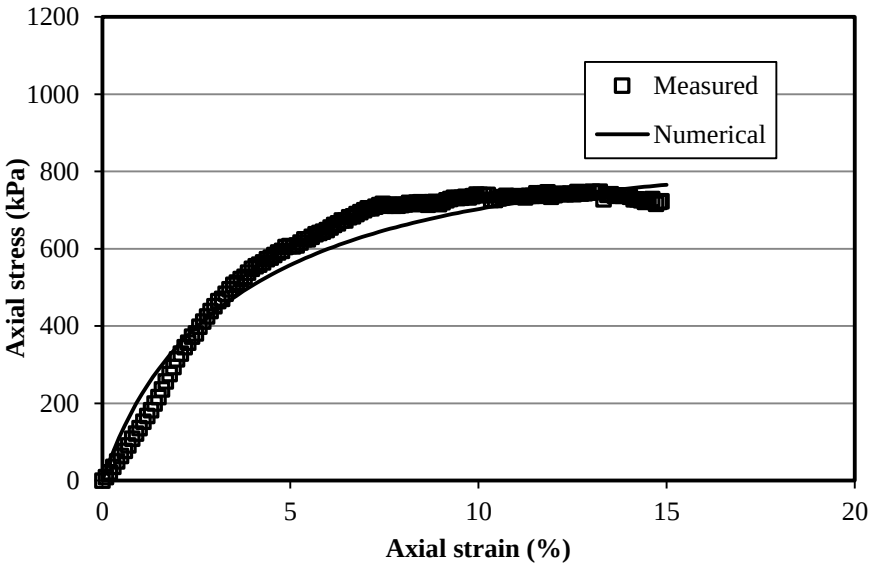

(b) 69 kPa

Figure 4.3 Comparison of the calculated and measured test results of the AB3 aggregate at different confining pressure

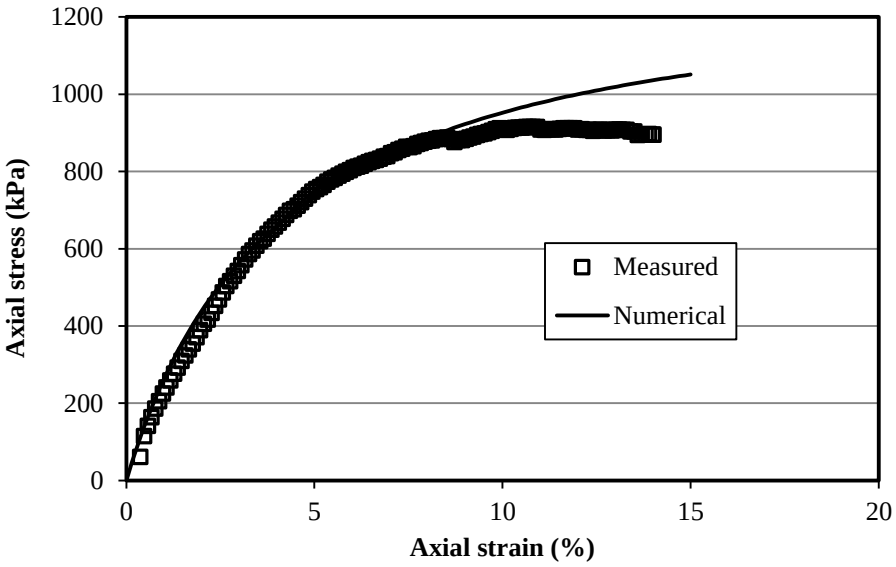

(c) 138 kPa

Figure 4.3 Comparison of the calculated and measured test results of the AB3 aggregate at different confining pressure (continued)

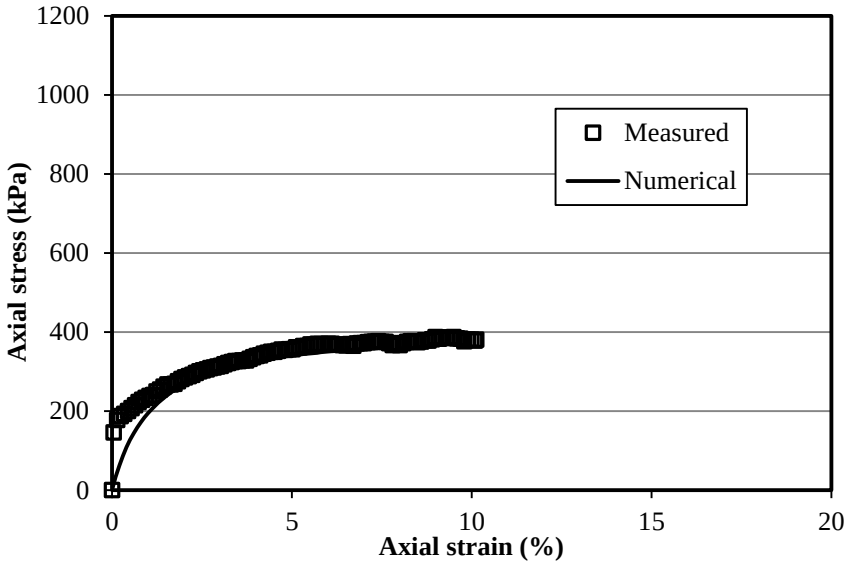

(a) 34.5 kPa

Figure 4.4 Comparison of the calculated and measured test results of the crushed stone at different confining pressure

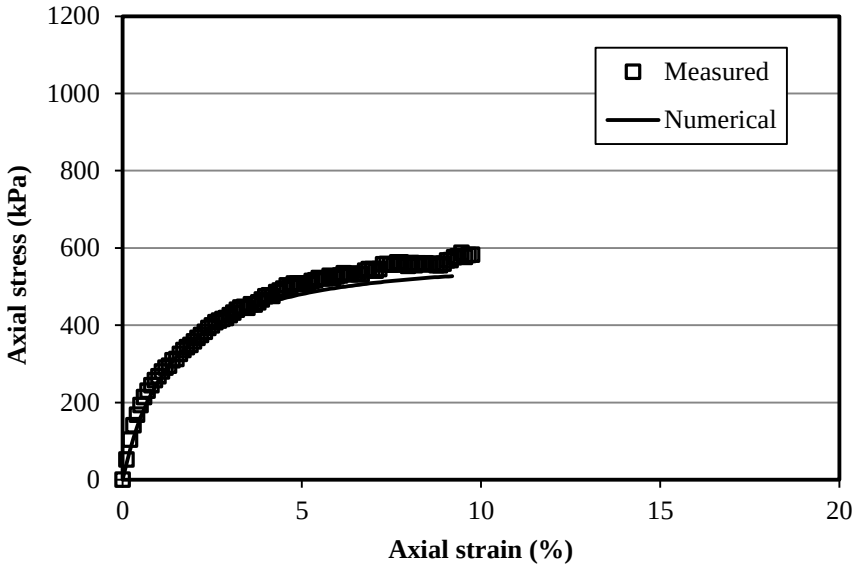

(b) 69 kPa

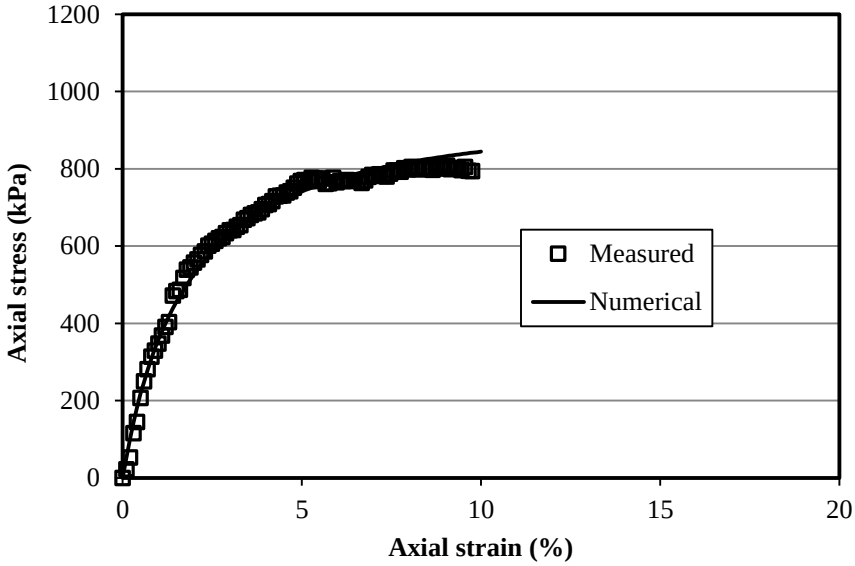

(c) 138 kPa

Figure 4.4 Comparison of the calculated and measured test results of the crushed stone at different confining pressure (continued)

4.2.3 Verification of the Effectiveness of the Hardening Soil Model for the Compaction Behavior

A trench model backfilled with AB3 aggregate was used to verify the effectiveness of the hardening soil model for the compaction behavior. **Figure 4.5** shows the dimension of this model. The width and the height of this model were 13.5 and 4.0 m, respectively. A 1.5 m wide and 2.0 m deep trench was excavated at the center of the model which was filled with AB3 aggregate as five equal lifts with a thickness of 0.3 m. The variation of the stress and strain at points #1-#5 (i.e., middle point of each layer) as shown in **Figure 4.5** was monitored during the modeling. The hardening soil model was adopted for the AB3 aggregate, while the surrounding soil was modeled using the Mohr-Columba model. The properties of the AB3 aggregate as listed in **Table 4.2** and those of the surrounding soil are summarized in **Table 4.3**. The bottom of the model was fixed in both of the vertical and horizontal directions, while the side boundaries were only fixed in the horizontal direction. Groundwater was neglected in this model. A uniformly-distributed pressure of 80 kpa was applied at the surface of each lift to simulate the compaction. **Figure 4.6** shows the residual horizontal stresses and strains at points #1-#5 during the modeling. The residual horizontal stress at all these points are approximately 10 kPa and the residual horizontal strain increased with the decrease of the depth. **Figure 4.6** demonstrates that the hardening soil model is adaptable to simulate the compaction behavior.

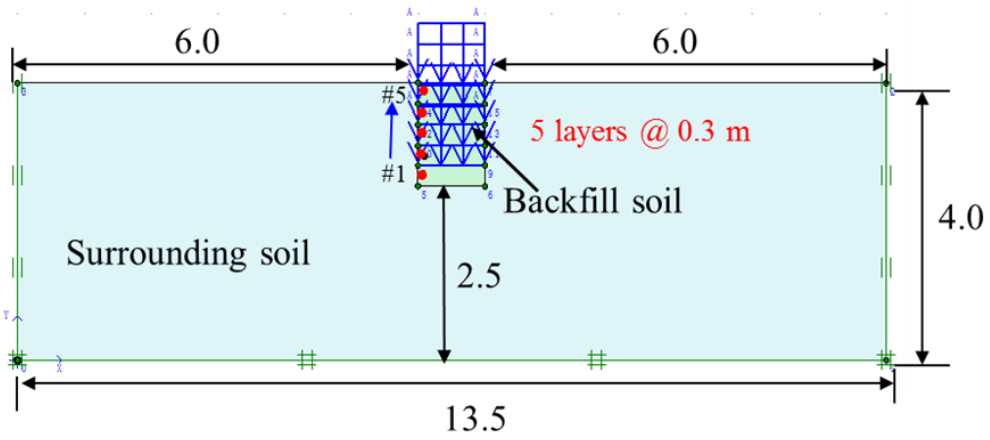

Figure 4.5 Numerical model for the verification of the residual horizontal stress and strain after removal of the compaction loads (Unit: m)

Table 4.3 Properties of the surrounding soil

Parameters	Surrounding soil
Unit weight γ (kN/m^3)	18
Cohesion C (kPa)	90
Friction angle ϕ (^{o})	22
E (MPa)	15.8
v	0.3
ψ (^{o})	0

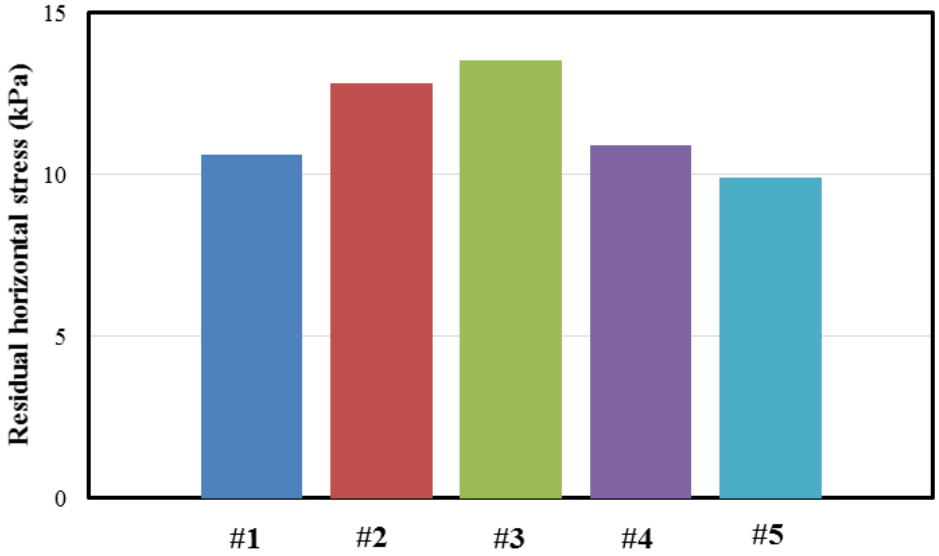

(a) Residual horizontal stress

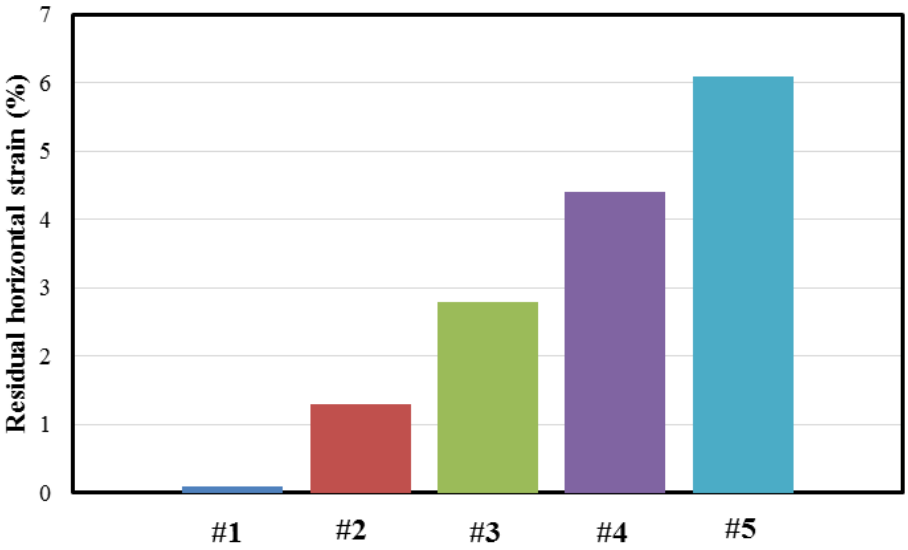

(b) Residual horizontal strain

Figure 4.6 Variation of the residual horizontal stress and strain at points #1-#5 A during the modeling

4.3 Simulation of the SRHDPE Pipe

4.3.1 Element in PLAXIS for Modeling Pipes

The software provides a tool, so-called as "tunnel designer", to model tunnels and pipes. In fact, the tunnel designer generates plate element segments to form a circular structure. After calculation, the internal forces of the plate elements could be plotted out. The plate element includes five parameters: (1) normal Stiffness, *EA*; (2) flexural Rigidity, *EI*; (3) equivalent thickness, *d*, which can be calculated from *EA* and *EI* automatically; (4) unit weight, γ; (5) Poisson's ratio, ν, which is equal to zero if the area of the solid structure (i.e., pipe wall) is much smaller than the whole cross-sectional area.

4.3.2 Equivalent Modulus Method (EMM)

Since the huge difference of the steel and HDPE in modulus, the equivalent method for the corrugated pipe mentioned previously is not valid for the SRHDPE pipe. The steel ribs and the plastic (i.e., HDPE) covers should deform together; in other words, an equal strain condition can be observed during the deformation of the SRHDPE pipe. Therefore, the EMM is applicable to the SRHDPE pipe. **Figure 4.7** shows the schematic of the EMM for the SRHDPE pipe modeling. For conservation purpose, the modulus of soil between gaps was neglected. The equivalence includes the following procedures:

- *Equivalent modulus of the pipe wall*. Calculate the elastic modulus times the area for each portion (i.e., the plastic cover, the steel rib, and the pipe wall). The elastic modulus of the

HDPE material is denoted as E_{PE}, and the elastic modulus of the steel rib is represented as E_{ST}. The area of the plastic corrugation is A_c, the area of steel rib is A_{ST}, the area of the pipe wall is A_w, and the total area of a unit cell is A_{ut}. The equivalent modulus can be calculated using the following expression:

$$E_{eq} = \frac{A_c E_{PE} + A_{ST} E_{ST} + A_w E_{PE}}{A_{ut}} \tag{4-5}$$

- *Equivalent thickness of the pipe wall*. The flexural rigidity of the pipe *EI* can be expressed as follows:

$$EI = 0.149 R^3 PS = E_{eq} \frac{t_{eq}^{\ 3}}{12} \tag{4-6}$$

where R = the radius of the pipe, PS = pipe stiffness which can be determined from the parallel plate load test $PS = \frac{F}{\Delta y}$, F = the applied load, Δy = the vertical deflection of the pipe; E_{eq} = the equivalent modulus determined in **Equation (4-5)**, and t_{eq} = the equivalent thickness.

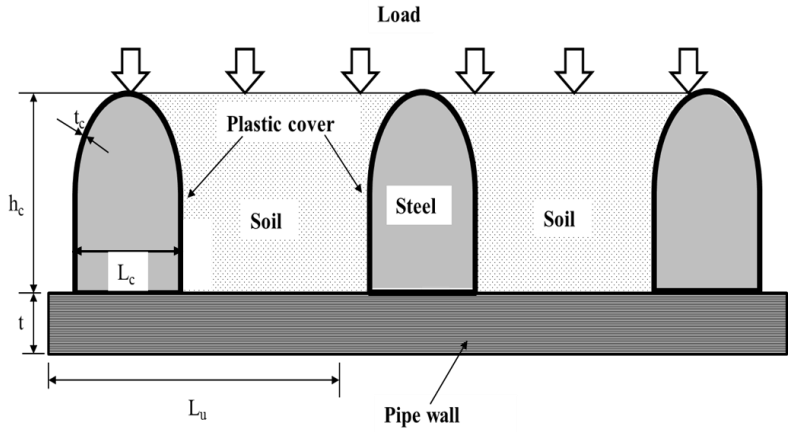

Figure 4.7 Schematic of the equivalent modulus method of the SRHDPE pipe (Not to scale)

Based on the profile of the SRHDPE presented in **Figure 3.9**, the equivalent modulus and thickness of the SRHDPE used in this study can be calculated as follows:

$A_c = 12.75mm^2$, $A_{ST} = 25.5mm^2$, $A_W = 50.8mm^2$, $A_{ut} = 431.8mm^2$, $E_{PE} = 441MPa$,

$E_{ST} = 200000MPa$, $PS = 294kPa$, $R = 0.3m$.

$$E_{eq} = \frac{12.75 \times 441 + 25.5 \times 200000 + 50.8 \times 441}{431.8} = 11875MPa \quad (4\text{-}7)$$

$$t_{eq} = \sqrt[3]{\frac{0.149 \times 294 \times 0.3^3 \times 12}{11875000}} = 10.6mm \quad (4\text{-}8)$$

4.3.3 Verification of EMM

Measured parallel plate load test data was compared with the numerical and theoretical results to verify the EMM. Blake (1959) proposed a method to calculate the vertical deflection of a ring subjected to a concentrated loading at its top as shown in the following equation:

$$\Delta y = \frac{F\lambda}{E}\left[1.788\lambda^2 + 3.091 - \frac{0.637}{1+12\lambda^2}\right] \quad (4\text{-}9)$$

where Δy = the vertical deflection of the pipe at the top; F = the concentrated load the top of the pipe; E = elastic modulus of the pipe; and λ = the ratio of the radius to the thickness of the pipe wall.

Tunnel designer tool was used to model the SRHDPE pipe. The bottom of the pipe was fixed in both the vertical and horizontal directions as shown in **Figure 4.8**. A concentrated load was applied at the top of the pipe. The parameters used for the pipe are summarized in **Table 4.4**.

Figure 4.9 shows the comparison of the numerical, theoretical and measured data. The measured data was reported by Khatri et al. (2013). It indicates that the EMM is effective to model the SRHDPE pipe.

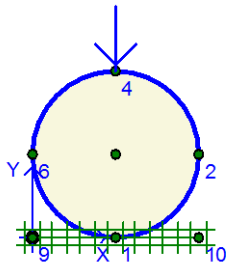

Figure 4.8 Numerical model of the pipe parallel plate load test

Table 4.4 Parameters used in the numerical model of the parallel plate load test of the SRHDPE pipe

Parameters	Value
Normal Stiffness, *EA* (kN/m)	1.2×10^5
Flexural Rigidity, *EI* (kNm^2/m)	1.2
Equivalent thickness, *d* (m)	0.011
Unit weight, *w* (kN/m/m)	0.864
Poisson's ratio, *v*	0
Radius, *R* (m)	0.3

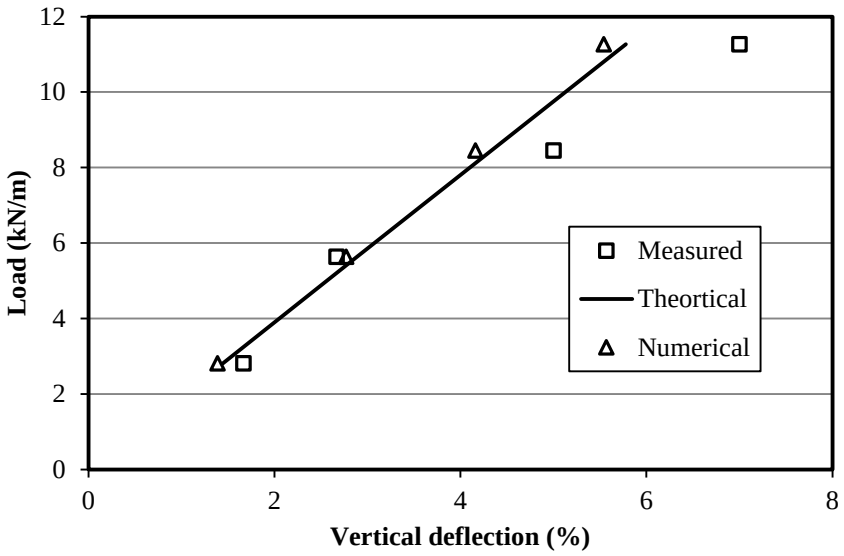

Figure 4.9 Comparison of numerical, theoretical and measured results of the parallel plate load test of the SRHDPE pipe

EMM can also be used to simulate other types of pipes with profile wall and corrugations. Chaallal et al. (2014) reported a series of parallel plate test on three different types of HDPE pipes with profile wall and corrugations. **Figure 4.10** shows the schematic of pipe walls of these HDPE pipes. Based on the EMM, the equivalent modulus and thickness were calculated and are listed in **Table 4.5**. A similar model shown in **Figure 4.8** was adopted to calculate the parallel plate load test of these three types HDPE pipes. **Figure 4.11** presents the comparison of the parallel plate load test results for those three types of HDPE pipes. The numerical and the theoretical calculations were based on the elastic theory, so that the load-deflection curves were linear. **Figure 4.11** indicates that the numerical and theoretical results were both close to the measured data when the vertical deflection less than 5%, since the pipe stiffness at 5% vertical deflection used to

determine the equivalent modulus and thickness. The comparisons illustrate that EMM could also be used for the HDPE pipes with corrugations.

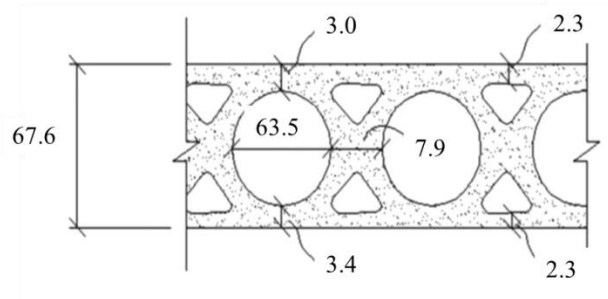

(a) PE-48

Figure 4.11 Wall profiles of three types of HDPE pipes (unit: mm, modified from Chaallal et al. (2014))

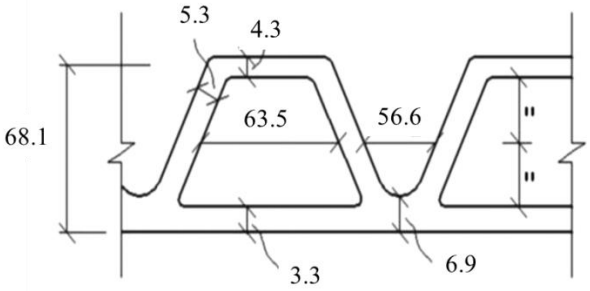

(b) PE1-36

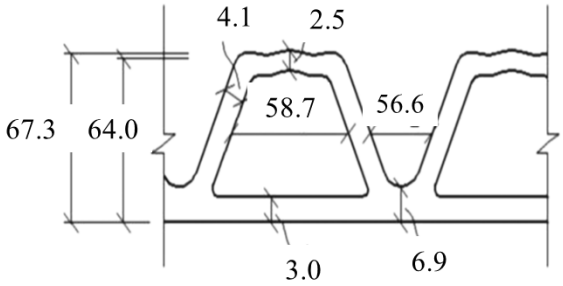

(c) PE2-36

Figure 4.10 Wall profiles of three types of HDPE pipes (unit: mm, modified from Chaallal et al. (2014)) (continued)

Table 4.5 Equivalent modulus and thickness of three types of HDPE pipes

Pipe	Pipe diameter (mm)	Pipe stiffness (kPa)	Equivalent modulus (MPa)	Equivalent thickness (mm)
PE-48	1262	185.68	166	8.3
PE1-36	388	255.9	54.3	10.7
PE2-36	387	176.2	43.2	10.2

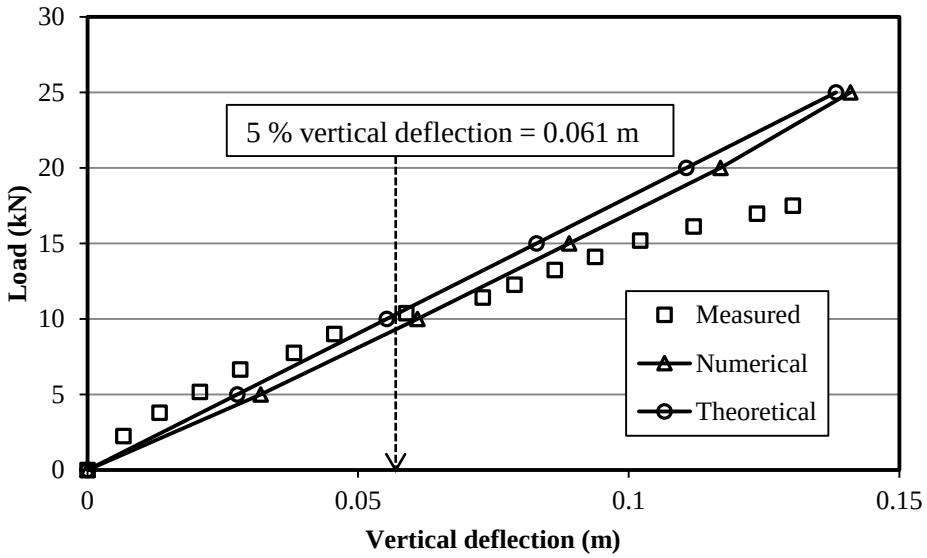

(a) PE-48

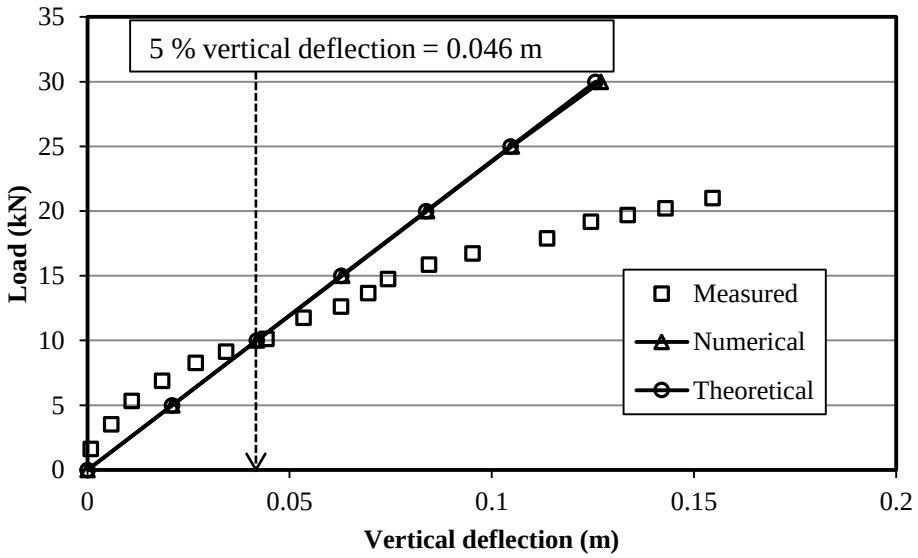

(b) PE1-36

Figure 4.11 Comparisons of the parallel plate load test for three types of HDPE pipes

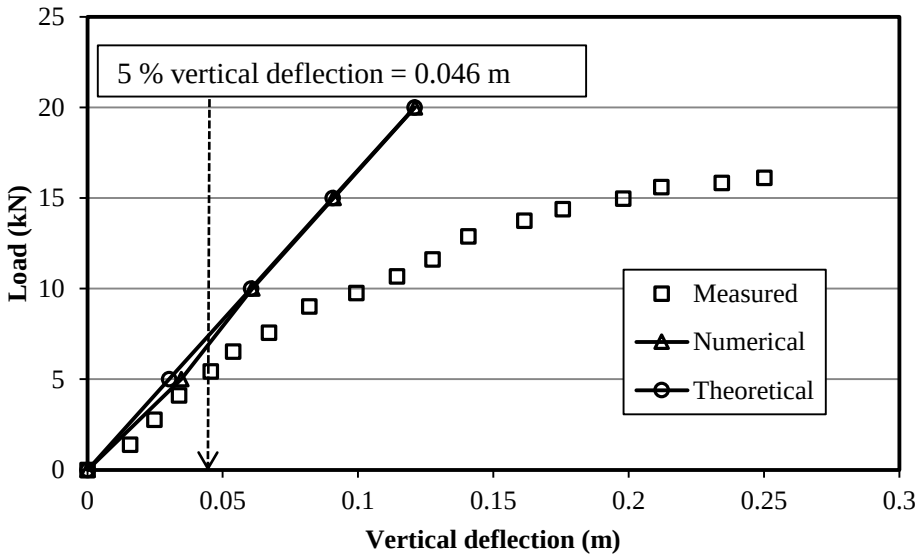

(c) PE2-36

Figure 4.11 Comparisons of the parallel plate load test for three types of HDPE pipes (continued)

4.4 Verification of the Numerical Model

4.4.1 Numerical Model

A field test conducted in Kansas City, Kansas, which was reported in Chapter 3, was used in this section to verify the numerical modeling method. A two dimensional finite element model was created. The dimension of the numerical model is shown in **Figure 4.12**. The width and the height of the numerical model were 2.5 and 7.5 m, respectively. A 1.5 m wide and 1.4 m deep trench was excavated at the center of the numerical model. A 0.15 m thick bedding was placed at the bottom of the trench and the other four equal thick (i.e., 0.31 m) layers of backfill were placed within the pipe zone. The side boundaries were fixed in the horizontal direction, while the bottom

of the model was fixed in both the vertical and the horizontal directions. The pipe was created using the "tunnel designer" with a diameter of 0.6 m. 15-node mesh was used in the numerical model. Groundwater was not considered in this model according to the field test situation. The properties of the backfill material, the surrounding soil and the pipe material used in the model are listed in **Tables 4.2, 4.3 and and 4.4**, respectively.

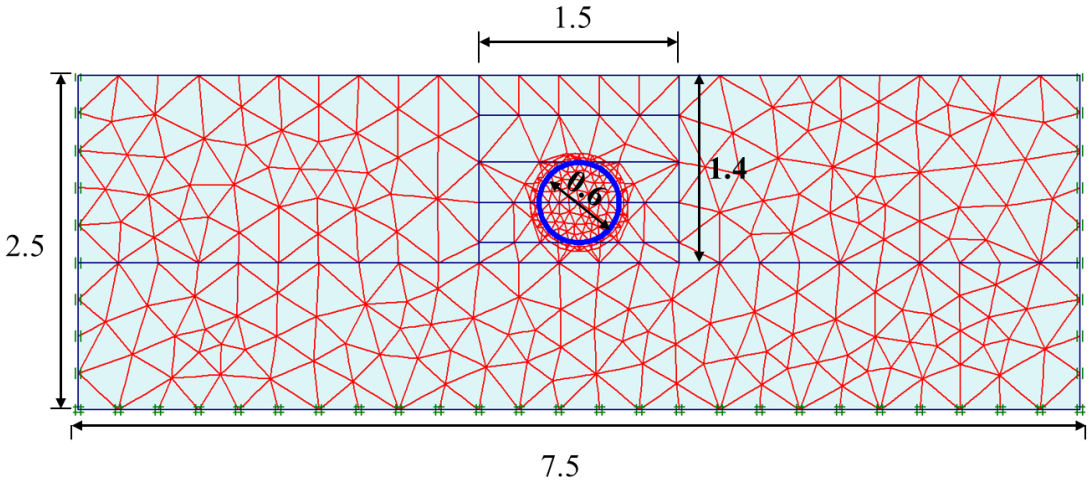

Figure 4.12 Numerical model of the verification case (unit: m)

The compaction load applied on the backfill material depends on the weight of the compactor, the eccentric force, and the number of compaction cycles. Therefore, it is difficult to determine the compaction load from the specifications of the compactor. The compaction load used in the numerical model should result in the equivalent modulus of the backfill material (i.e., equivalent compaction energy) at the required compaction degree. ASTM D 2321 (2014) specified that the satisfied backfill material compaction should achieve an average soil reaction modulus *E'* of 6.9 MPa. Krizek et al. (1971) found that the constrained soil modulus M_s could be 0.7 to 1.5 times of *E'*. Hartley and Duncan (1987) and McGrath (1998) pointed out *E'* can be treated equal to M_s. In this study, $E' = M_s$ was adopted. M_s is also related to the soil Young's modulus E_s and Poisson's ratio v, and the relationship can be expressed as follows:

$$M_s = \frac{E_s(1-\nu)}{(1+\nu)(1-2\nu)} \tag{4-10}$$

Therefore, **Equation (4-10)** can be rearranged as:

$$E_s = \frac{E'(1+\nu)(1-2\nu)}{(1-\nu)} \tag{4-11}$$

Assume Poisson's ratio ν = 0.3 and E' = 6.9 MPa, **Equation (4-11)** becomes:

$$E_s = \frac{6.9\times(1+0.3)\times(1-2\times0.3)}{(1-2\times0.3)} = 5.13MPa \tag{4-12}$$

Recalling the hardening soil model $E_{50} = E_{50ref}\left(\frac{c\cos\phi+\sigma_3\sin\phi}{c\cos\phi+100\sin\phi}\right)^m$ and assuming $E_s = E_{50}$, the additional horizontal stress σ_3 induced by the compaction can be determined for the AB3 aggregate and the crushed stone as 69 and 37.5 kPa, respectively. The field test results in Chapter 3 shows that the lateral earth pressure coefficients at the pipe springline were 0.86 and 0.65 in the AB3 aggregate and crushed stone sections, respectively. Therefore, the compaction pressure for the AB3 aggregate section is equal to 69 / 0.86 = 80 kPa; while that for the crushed stone section can be calculated as 37.5 / 0.65 = 57.8 kPa.

The following procedures were followed to model the SRHDPE pipe performance during the construction phase:

(1) create the model and input the properties of the soil and the pipe;

(2) set up the boundary and initial conditions for the model;

(3) reset the displacement of the model to zero and excavate the trench;

(4) place the bedding layer and apply the compaction pressure (80 kPa for the AB3 aggregate section and 57.8 kPa for the crushed stone section) (i.e., uniformly distributed pressure) on the surface of the bedding;

(5) remove the compaction pressure in step (4) and place a new layer of backfill in the pipe zone;

(6) apply 80 kPa pressure on the surface of the backfill in the AB3 aggregate section and 57.8 kPa in the crushed stone section;

(7) remove the compaction pressure; and

(8) repeat step (5) through step (7) to backfill the trench until reach the top of the model. The compaction pressure for both sections in the top layer (i.e., Zone V) was 80 kPa.

4.4.2 Comparison of Numerical Modeling and Field Test Results

Figure 4.13 shows the comparison of the vertical and horizontal deflections in both the AB3 aggregate and the crushed stone sections. **Figure 4.14** presents the comparisons of the vertical earth pressure at the springline and the pipe top and the horizontal earth pressure at the springline. **Figure 4.15** is the comparison of the lateral earth pressure coefficient at the pipe springline developing during the construction. These three figures clearly demonstrate that the numerical results agree well with the measured data in the field test. It can be concluded that the numerical modeling procedures and parameters adopted in this study were effective to simulate the SRHDPE pipe performance during the installation.

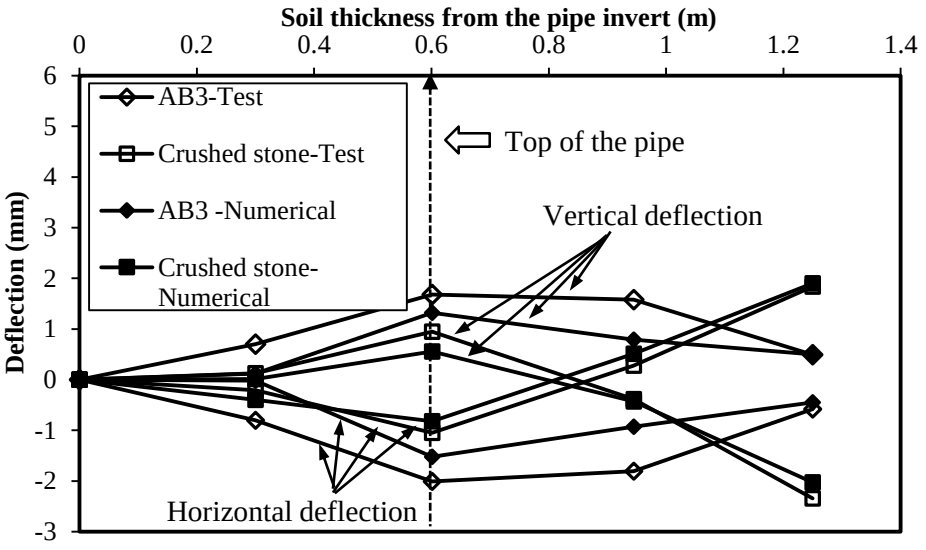

Figure 4.13 Comparisons of the vertical and horizontal deflections both in the AB3 aggregate and crushed stone sections

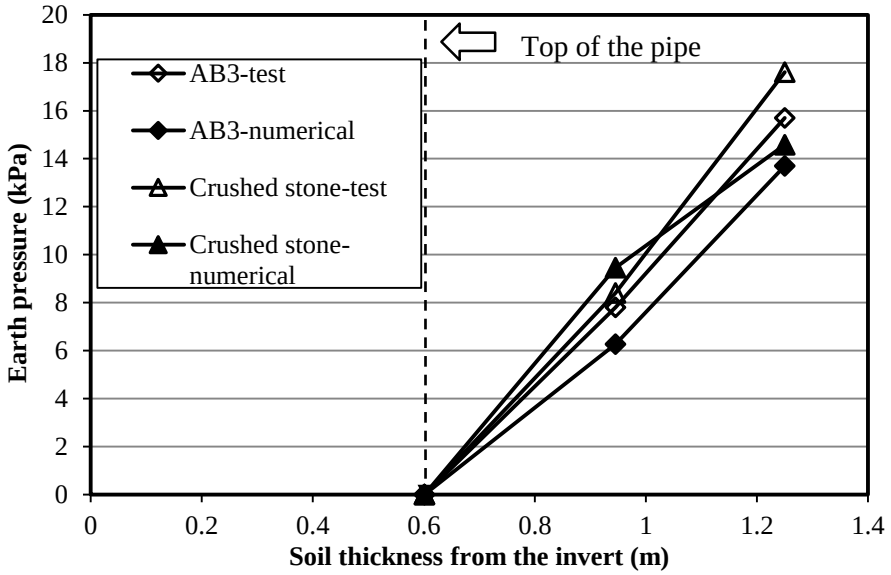

(a) Vertical earth pressure at the top of pipes

Figure 4.14 Comparisons of the earth pressure

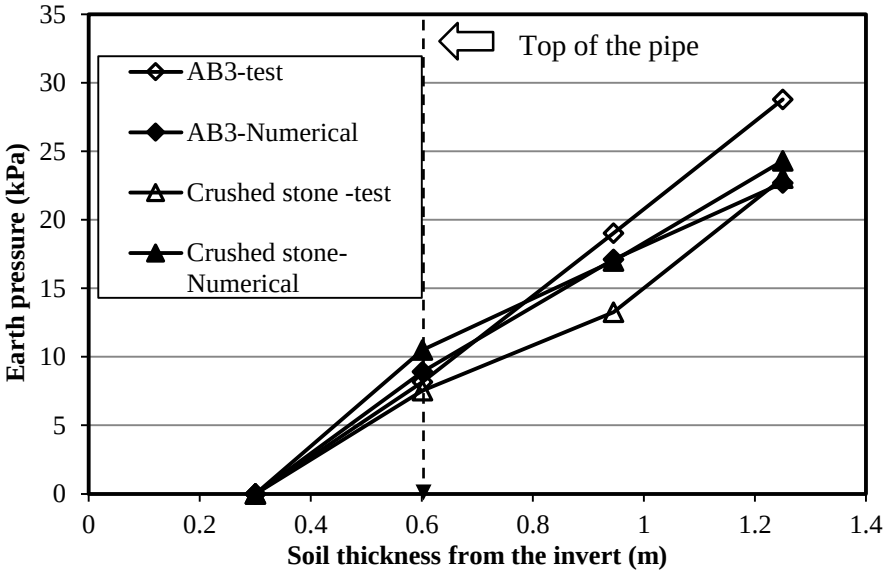

(b) Vertical earth pressure at the springline of pipes

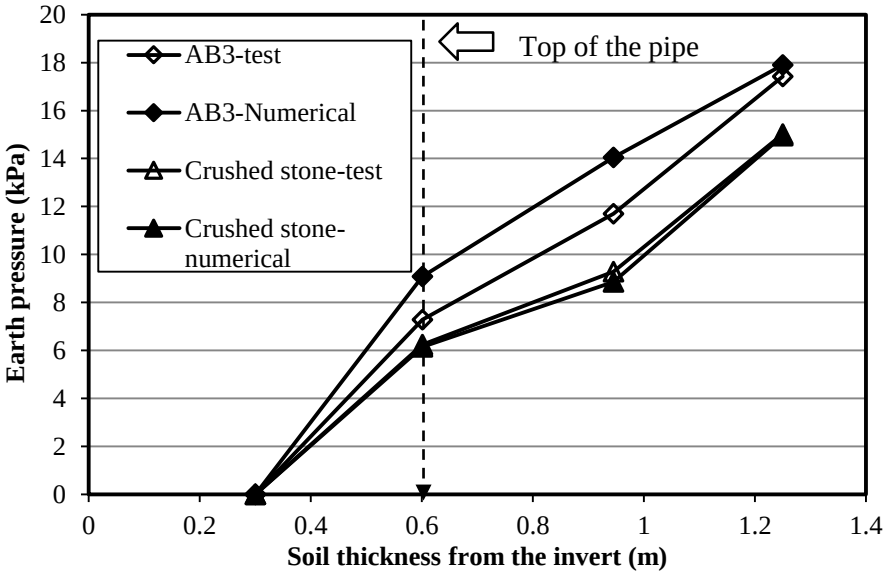

(c) Horizontal earth pressure at the springline of pipes

Figure 4.14 Comparisons of the earth pressure (continued)

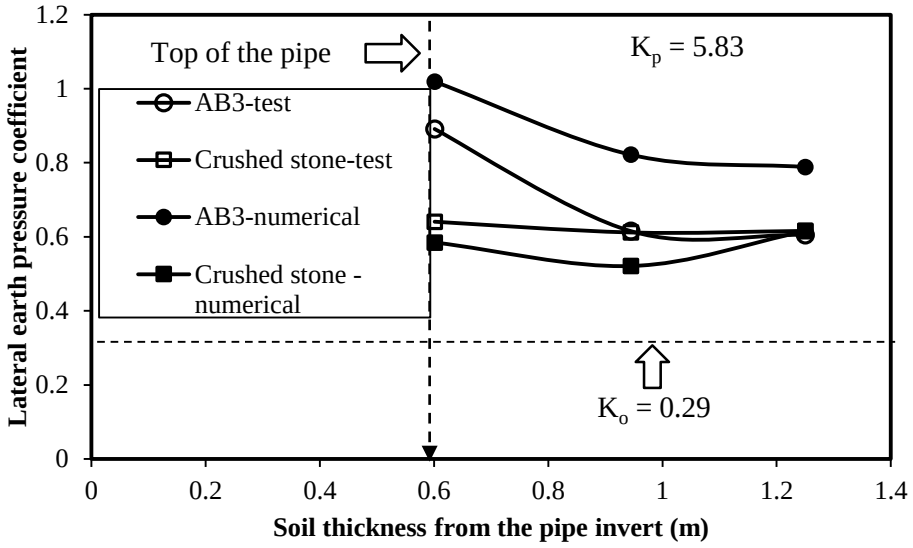

Figure 4.15 Comparison of the lateral earth pressure coefficient at the springline of pipes developing with construction

4.5 Numerical Modeling on the Installation of the SRHDPE Pipe

Field test results was used to verify the effectiveness of the numerical model. Similar numerical modeling and procedures were adopted in this section for the numerical modeling and the parametric study. As discussed earlier, four key parameters in the design of flexible pipes, including the soil cover thickness, the trench width, the magnitude of the compaction load, and the friction angle of the backfill material were focused in this study. The SRHDPE pipe used in the numerical analysis has the same properties with those in the verification model. A baseline case model was created first, and then a parametric study was conducted to evaluate the effects of these four factors on the performance of the SRHDPE pipe during the pipe installation. **Table 4.6** summaries the cases in the numerical modeling. The soil cover thickness of the baseline case was 0.6 m (i.e., the pipe diameter), which was the minimum soil cover thickness required by AASHTO

(2012); while the trench width of the baseline case was 1.2 m suggested by AASHTO (2012) for thermoplastic pipes. AB3 aggregate used in the verification model was also adopted in the baseline case and the compaction load was determined as 80 kPa to achieve the average soil reaction modulus of 6.9 MPa. The soil cover thicknesses in the parametric study were 0.9 (i.e., 1.5 D), 1.2 (i.e., 2.0 D), and 1.8 m (i.e., 3.0 D), where D is the pipe diameter. Three trench widths were adopted in the numerical modeling, namely, 0.8, 1.0, and 1.8 m. The parametric study also included the cases with compaction loads of 40 and 60 kPa to investigate the performance of the SRHDPE pipe under insufficient compaction loads. Two friction angles (i.e., 35^o and 55^o) of the backfill material were adopted to evaluate the effect of the friction angle on the performance of the SRHDPE pipe during the construction.

Table 4.6 Cases of numerical modeling on the SRHDPE pipe installation

Case No.	Soil cover thickness (m)	Trench width (m)	Friction angle of Backfill (^{o})	Compaction pressure (kPa)
1*	0.6 (1.0 D)	1.2	45	80
2	0.9 (1.5 D)	1.2	45	80
3	1.2 (2.0 D)	1.2	45	80
4	1.8 (3.0 D)	1.2	45	80
5	0.6	0.8	45	80
6	0.6	1.0	45	80
7	0.6	1.8	45	80
8	0.6	1.2	45	40
9	0.6	1.2	45	60
10	0.6	1.2	35	80
11	0.6	1.2	55	80

Note: * the baseline case; *D* is the diameter of the pipe.

4.5.1 Baseline Case

Figure 4.16 shows the numerical model of the baseline case. The plan-strain model was used with a length of 7.5 m and a height of 2.45 m. A trench with a width of 1.2m and depth of 1.35 m was excavated at the center of the model and backfilled with AB3 aggregate. The pipe diameter used in the baseline case was 0.6 m. 15-node element was used as the mesh of the model and the global mesh coarseness was set as "fine" with a refinement in the pipe zone. The bottom of the model was fixed both in the vertical and horizontal directions; while the two side boundaries were only fixed in the horizontal direction. Five lifts were backfilled from the bottom to the surface in the trench with the thicknesses of 0.15 (bedding), 0.30, 0.30, 0.30 and 0.30 m, respectively. The properties of the backfill material, the surrounding soil and the SRHDPE pipe were same as those in the verification model as shown in **Tables 4.2, 4.3 and 4.4**. The similar procedures in the verification model were adopted in the baseline case, and the compaction pressure was 80 kPa. Earth pressure was monitored at the top and springline of the pipe during the construction, while the bending moment, hoop strain and vertical and horizontal deflections of the pipe were also recorded.

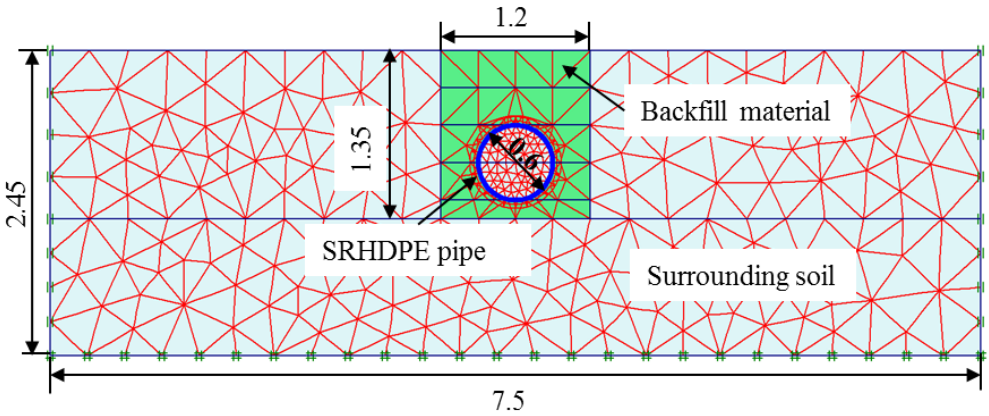

Figure 4.16 Numerical model of the baseline case (unit: m)

Figure 4.17 presents the vertical and horizontal deflections during the pipe installation. When the backfill surface was lower than the top of the pipe, the pipe diameter increased in the vertical direction, while it decreased in the horizontal direction. The shape of the pipe changed from circular to vertically elliptical, which was referred to as "peaking behavior". The maximum vertical peaking deflection was 0.8 mm, while the horizontal peaking deflection was 0.67 mm. The pipe diameter decreased by 0.65 mm in the vertical deflection and increased by 0.88 mm in the horizontal direction at the end of the pipe installation compared with the undeformed pipe. The maximum pipe diameter change was 0.13% of the pipe diameter which was much lower than the 5% deflection limit for flexible pipes.

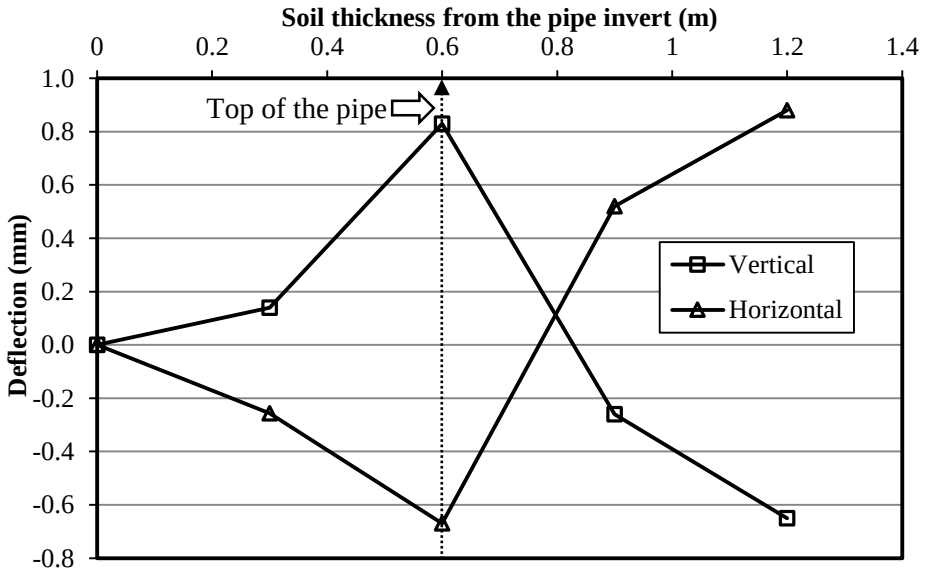

Figure 4.17 Vertical and horizontal deflections during the pipe installation

Figure 4.18 shows the earth pressure at the top and the springline of the pipe in the baseline case during the installation. The vertical earth pressure at the pipe top was higher than the overburden stress. The Vertical Arching Factor (VAF), defined as the measured earth pressure divided by the overburden stress, was 1.22 which demonstrated the negative soil arching effect

(i.e., VAF > 1) occurred at the top of the pipe. The vertical and horizontal earth pressures at the springline of the pipe were both increased with an increase of the soil cover thickness. The lateral earth pressure coefficients, defined as the horizontal earth pressure divided by the vertical earth pressure, were 0.64, 0.65 and 0.67 when the backfill thicknesses from the pipe invert were 0.3, 0.6 and 0.9 m, respectively. It may be able to conclude that the lateral earth pressure coefficient was approximately constant during the pipe installation.

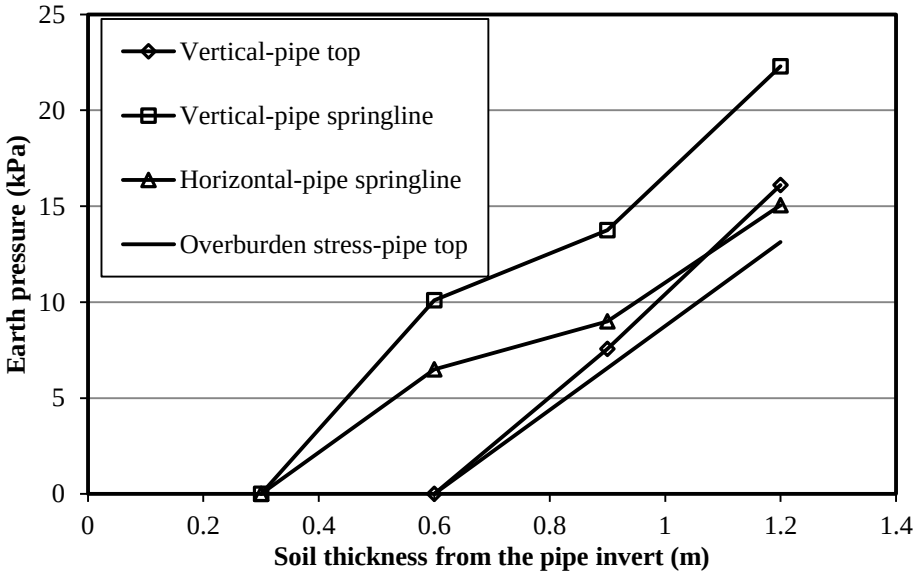

Figure 4.18 Earth pressure at the top and springline of the pipe during the installation

Figure 4.19 illustrates the variation of the bending moment of the pipe during the installation. A positive angle represents clockwise from the pipe crown, while the negative denotes counterclockwise in **Figure 4.19**. The peak bending moment occurred at 90^{o} from the pipe crown (i.e., the pipe springline) as 15.4 N·m/m when the soil thickness from the pipe invert was 0.3 m (i.e., the pipe springline). When the backfill reached the level of the pipe top, the peak bending moment increased to 42.1 Nm/m located at the pipe crown. The location of the peak bending moments moved to the angle of 109^{o} from the pipe crown when the backfill above the top of the

pipe and the magnitude was approximately 40.3 N·m/m. Three conclusions can be made from the investigation of the bending moment variation from the baseline case modeling: (1) the magnitude of the peak bending moment increased and the locations changed when the backfill was lower than the top of the pipe; (2) the bending moment magnitude reached the maximum value when the backfill surface was at the pipe top level; and (3) the location and the magnitude of the peak bending moment were both constant when the backfill was above the top of the pipe.

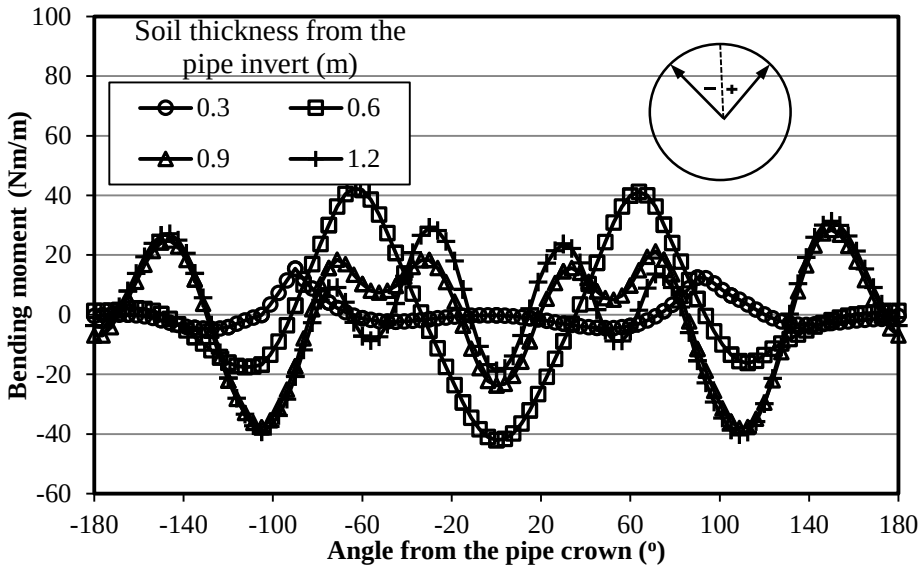

Figure 4.19 Variation of the bending moments of the pipe during the pipe installation

Figure 4.20 is the variation of the hoop strain in the pipe during the installation. Due to the symmetry of the pipe, the hoop strains were recorded only for a half of the pipe at angles of 0, 45, 90, 135 and 180^{o} from the pipe crown. The positive strain represents compression, while the negative value denotes tension. The maximum hoop strain was -1.2% occurred at 90^{o} from the pipe crown (i.e., the pipe springline) when the backfill was at the pipe springline level. Subsequently, the hoop strain decreased slightly with an increase of the soil thickness; however, the locations of the peak strains did not change.

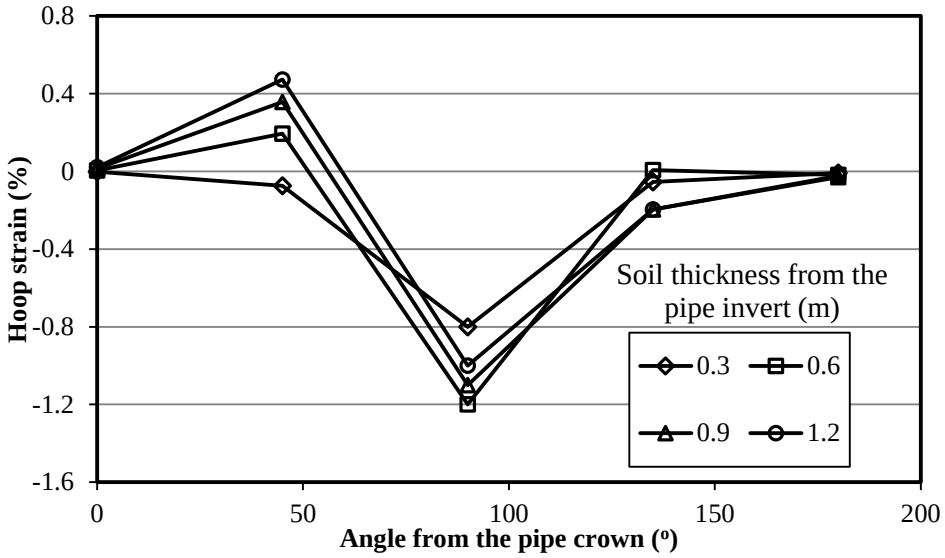

Figure 4.20 Variation of the hoop strain in the pipe during the installation

4.5.2 Effect of the Soil Cover Thickness

The backfill lifts in the pipe zone of Case 1 through Case 4 were all 0.3 m, and the bedding thickness was 0.15 m. **Figure 4.21** shows the vertical and horizontal deflections in cases with different soil cover thickness at the end of the pipe installation. Both of the vertical and the horizontal deflections approximately linearly increased with an increase of the soil cover thickness. They were much lower than the deflection limit of 5% (i.e., 30 mm) for flexible pipes specified in (AASHTO, 2012). The horizontal deflection changed more significantly than the vertical deflection with the change of the soil cover thickness.

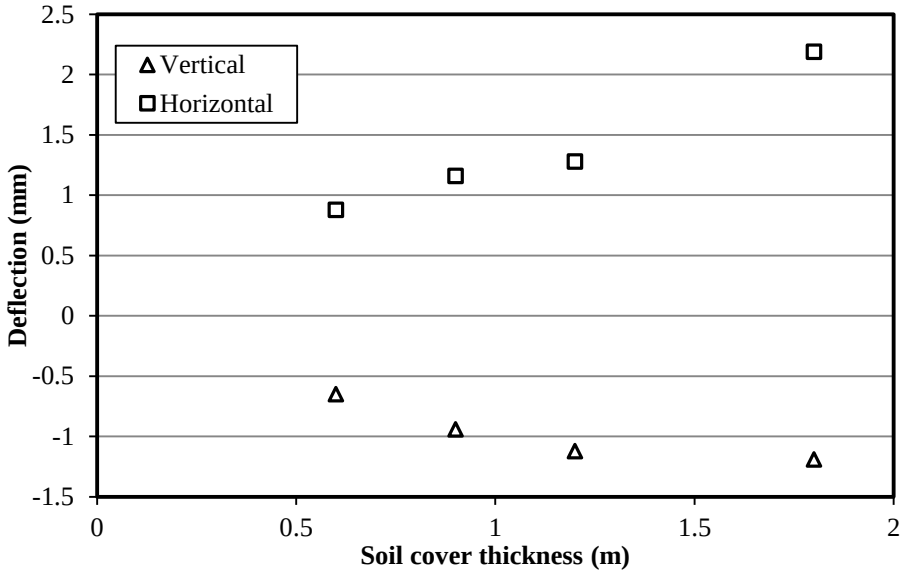

Figure 4.21 Vertical and horizontal pipe deflections at the end of the construction at different soil cover thickness

Figure 4.22 is the lateral earth pressure at the pipe springline in cases with different soil cover thickness. The lateral earth pressure coefficients at the pipe springline varied in a narrow range from 0.59 to 0.67 in Case 1 through Case 4 during the pipe installation. The lateral earth pressure can be approximately assumed as 0.65 in the SRHDPE pipe design. **Figure 4.23** shows the VAFs at the top of the pipe. They varied in a range of 1.05 to 1.28 which demonstrated the negative soil arching effect occurred in Case 1 through Case 4. The average value of VAF was 1.1 at the pipe top which could be recommended as the design parameter for the SRHDPE pipe. Recalling the equivalent modulus and the thickness of the SRHDPE pipe wall, they were 11,875 MPa and 10.6 mm, respectively. Substituting them into **Equations (2-3) and (2-5)** and assuming M_s = 6.9 MPa, S_H and VAF can be calculated as 0.001914 and 1.04, respectively. The calculated VAF is close to the numerical result (i.e., 1.1).

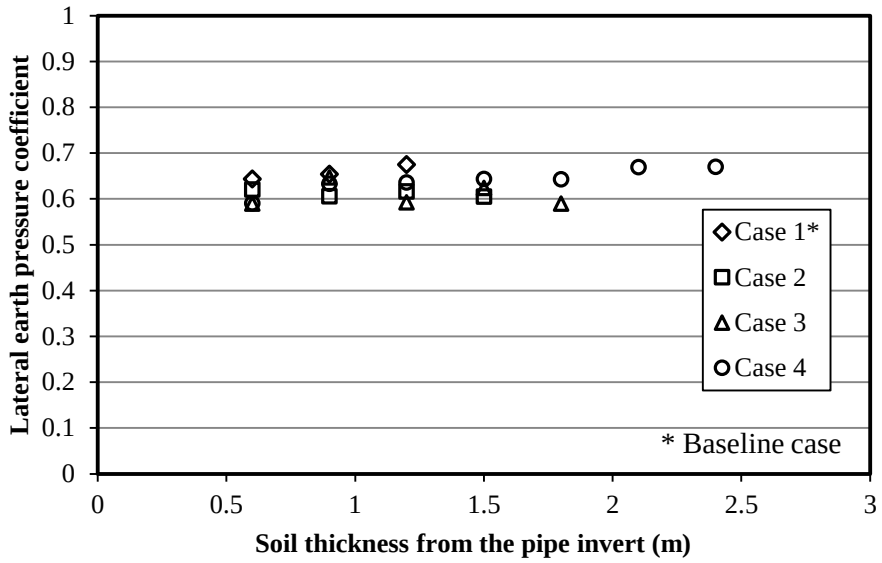

Figure 4.22 Variation of the lateral earth pressure coefficients at the springline of the pipe with backfilling in cases with different soil cover thickness

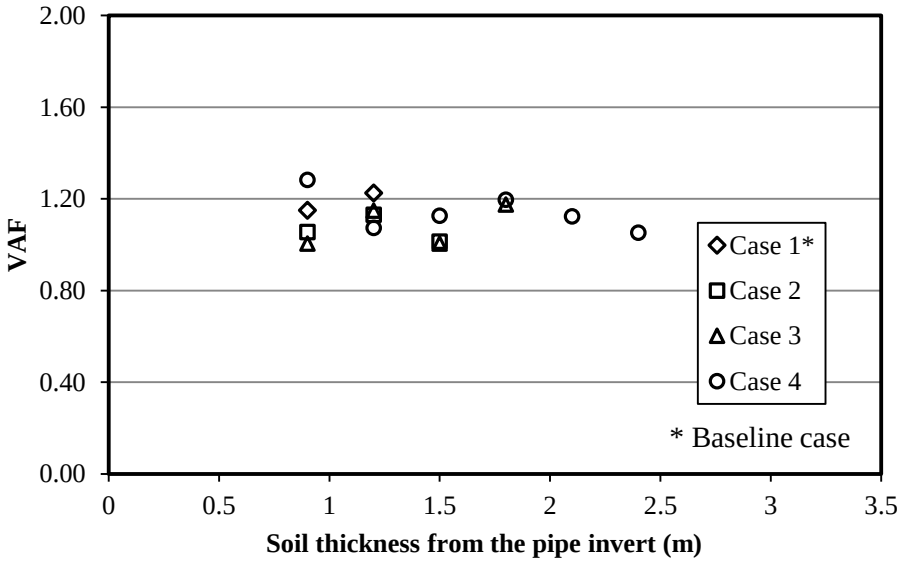

Figure 4.23 Variation of the soil arching factors at the top of the pipe with backfilling in cases with different soil cover thickness

Table 4.7 summarizes the locations and the peak value of the bending moment of the pipe. When the backfill was at the level of the pipe springline, the peak bending moment happened at the pipe springline. The location of the peak bending moment moved to the pipe crown when the backfill reached the level of the pipe top. The location of the peak bending moment moved back to the pipe springline and the magnitude changed slightly from the peak value, when the backfill was above the pipe top. With an increase of the soil cover thickness, the maximum bending moment also increased.

Table 4.7 Locations and peak values of the bending moment of the pipe in cases with different soil cover thickness

	Case 1*		Case 2		Case 3		Case 4	
h (m)	Angle (°)	Peak (Nm/m)	Angle (°)	Peak (Nm/m)	Angle (°)	Peak (Nm/m)	Angle (°)	Peak (Nm/m)
0.3	90	15.4	90	11.7	90	9.2	90	16.1
0.6	0	42.1	0	41.7	0	42.9	0	41.2
0.9	109	38.0	105	41.1	113	37.7	104	40.1
1.2	109	40.3	105	42.3	108	39.7	104	42.5
1.5	-	-	105	43.7	109	41.4	99	44.5
1.8	-	-	-	-	109	43.1	99	46.2
2.1	-	-	-	-	-	-	99	47.7
2.4	-	-	-	-	-	-	99	49.0

Note: *h* is the soil thickness from the pipe invert; *Angle* represents the angle from the pipe crown; *Peak* is the peak value of bending moment of the pipe at a specific soil thickness.

The peak hoop strains happened at the springline during the backfilling in Case 1 through Case 4. **Figure 4.24** presents the peak hoop strain of the pipe during the construction. The

maximum hoop strain happened when the backfill was at the level of the pipe top. Subsequently, it decreased with an increase of the soil thickness. The maximum strain of the pipe was close to 2% in tension which was lower than the long-term service strain limit of 5% for thermoplastic pipes suggested by AASHTO (2012).

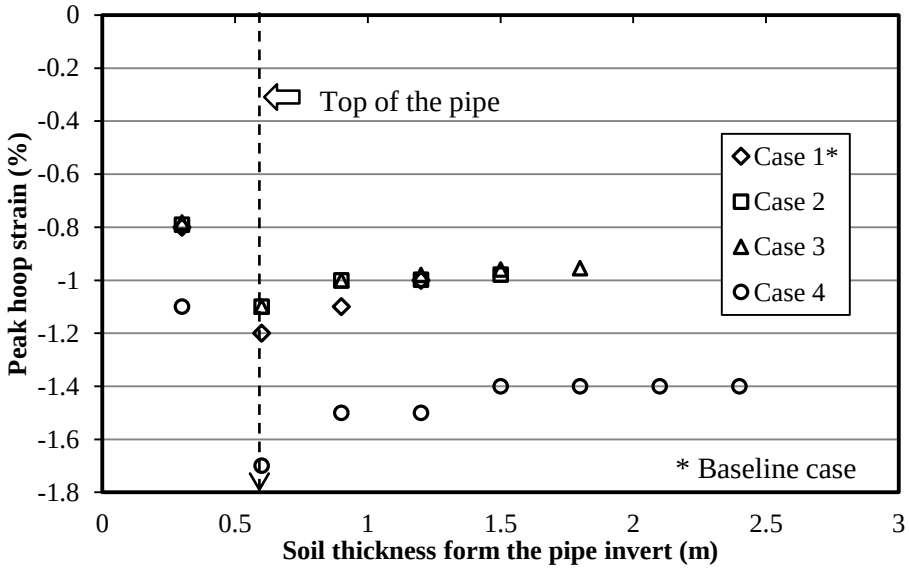

Figure 4.24 Peak hoop strains of the pipe with backfilling in cases with different soil cover thickness

4.5.3 Effect of the Trench Width

Figure 4.25 is the vertical and the horizontal deflections of the pipe in cases with different trench width. The peaking deflections of the pipe increased with an increase of the trench width; however, the pipe diameter change from the peaking point to the end of the construction were approximately same for all of the four cases (Case 1: 1.45 mm; Case 5: 1.48 mm; Case 6:1.48 mm; and Case 6: 1.33 mm.). Since the soil cover thicknesses in these four cases were same, the pipe diameter change from the peaking to the end of the construction should be same.

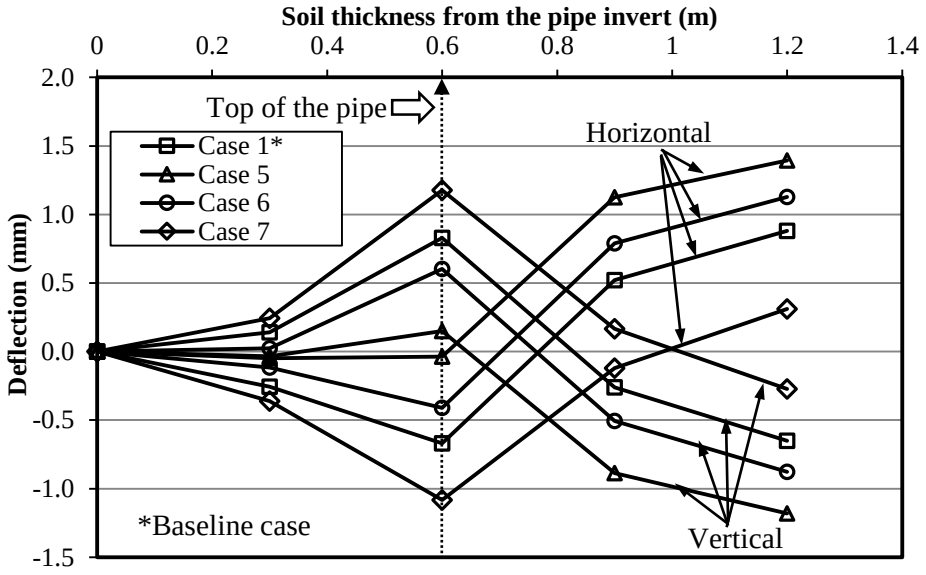

Figure 4.25 Vertical and horizontal deflections of the pipe at different trench width

Figure 4.26 shows the lateral earth pressure coefficients at the pipe springline for cases with different trench width. They varied from 0.59 to 0.69, and the average value is 0.65. **Figure 4.27** is the VAF at the top of the pipe. They were all greater than 1.0 (i.e., negative soil arching), the average value 1.1 can be recommended for the SRHDPE pipe design.

Table 4.8 is the locations and the peak value of the bending moment of the pipe in cases with different trench width. The maximum bending moment happened when the backfill was at the level of the pipe top. The locations of the peak bending moments were at the springline when the backfill at the level of the pipe springline. The locations of the peak bending moments moved to the pipe crown when the backfill at the level of the pipe top. When the backfill was above the pipe top, the peak bending moments decreased slightly and the locations were close to the pipe springline. The magnitudes of the peaking bending moments at a specific backfill level increased with an increase of the trench width.

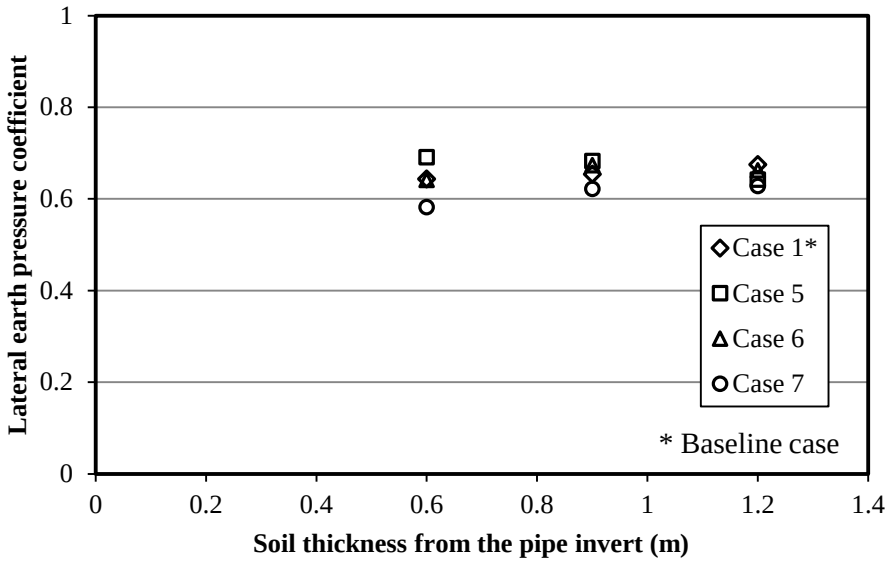

Figure 4.26 Variation of the lateral earth pressure coefficients at the springline of the pipe with backfilling at different trench width

Table 4.8 Locations and peak values of the bending moment of the pipe in cases with different trench width

h (m)	Case 1*		Case 5		Case 6		Case 7	
	Angle (^{o})	Peak (Nm/m)	Angle (^{o})	Peak (Nm/m)	Angle (^{o})	Peak (Nm/m)	Angle (^{o})	Peak (Nm/m)
0.3	90	15.4	90	8.6	90	7.7	90	18.6
0.6	0	42.1	0	36.3	0	35.7	0	51.3
0.9	109	38.0	26	36.1	105	33.5	116	49.3
1.2	109	40.3	104	35.6	105	35.6	98	49.3

Note: *h* is the soil thickness from the pipe invert; *Angle* represents the angle from the pipe crown; *Peak* is the peak value of bending moment of the pipe at a specific soil thickness.

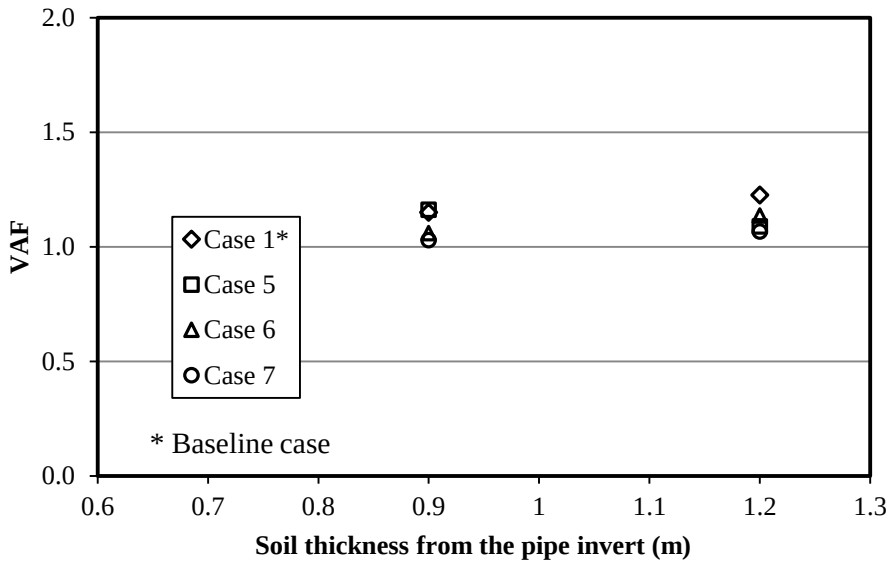

Figure 4.27 Variation of the soil arching factors at the top of the pipe with backfilling at different trench width

Figure 4.28 presents the peak hoop strain of the pipe in cases with different trench width. The maximum hoop strain happened when the backfill was at the level of the pipe top. The maximum hoop strain increased with an increase of the trench width. However, all of the hoop strains were lower than the strain limit of 5% suggested by AASHTO (2012).

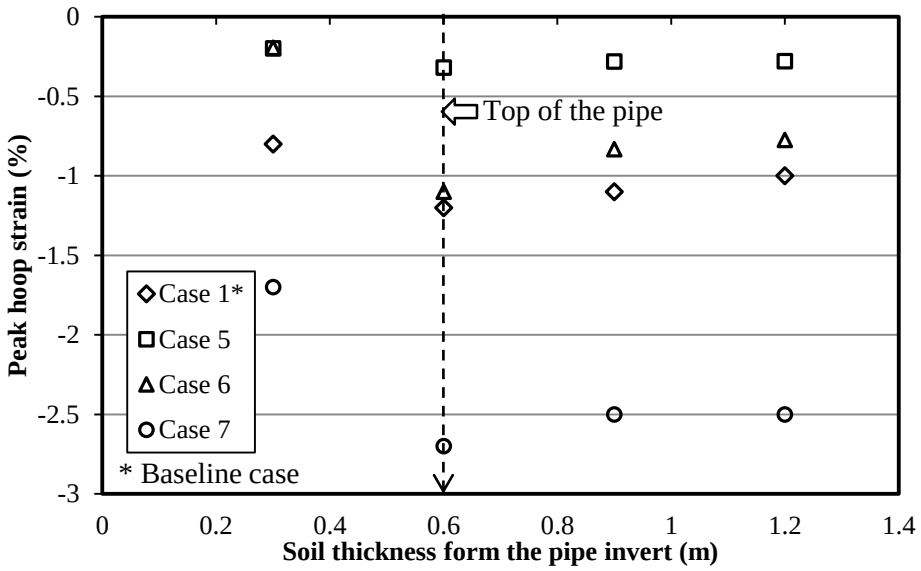

Figure 4.28 Peak hoop strains of the pipe with backfilling in cases with different trench width

4.5.4 Effect of the Insufficient Compaction Pressure

Insufficient compaction is usually encountered in engineering practice due to the existence of the difficult zones (i.e., haunch zones) and/or the low construction quality. Therefore, it is necessary to investigate the performance of the pipe with insufficient compaction. **Figure 4.29** shows the vertical and the horizontal deflections of the pipe subjected to different magnitude of compaction pressure. The peaking deflections increased with an increase of the compaction pressure. However, both of the vertical and horizontal deflections at the end of the construction for all of these three cases were approximately same.

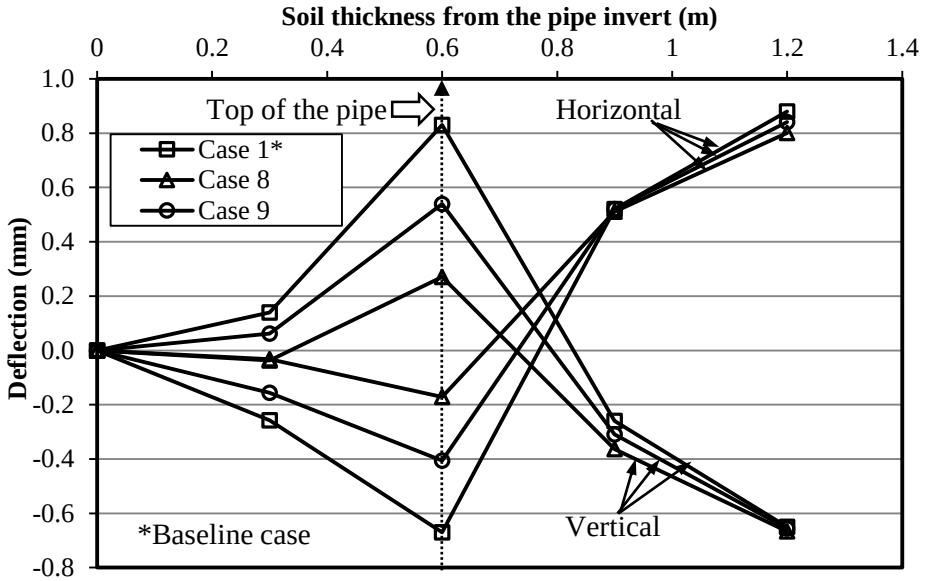

Figure 4.29 Vertical and horizontal deflections of the pipe with different magnitude of compaction load

Figure 4.30 presents the lateral earth pressure coefficient at the springline of the pipe subjected to different magnitude of the compaction pressure. The lateral earth pressure coefficients changed from 0.61 to 0.69, the average value was 0.65 which was consistent with those in the cases with different soil cover thickness and trench width. **Figure 4.31** is the VAFs at the top of the pipe. The VAFs in Cases 8 and 9 (with insufficient load) were in a range of 1.3 to 1.4 greater than that (i.e., 1.1) in the cases with the sufficient compaction pressure (i.e., 80 kPa). The reason could be explained as follows: (1) the backfill with insufficient compaction caused lower soil reaction modulus; and (2) more loads were carried by the pipe due to the relative lower soil modulus which resulted in higher VAF. If a traffic load applies above the pipe with insufficient compaction, more loads would be carried by the pipe which potentially causes problems to the pipe. The effect of insufficient compaction on the pipes under traffic loading will be investigated in the future study.

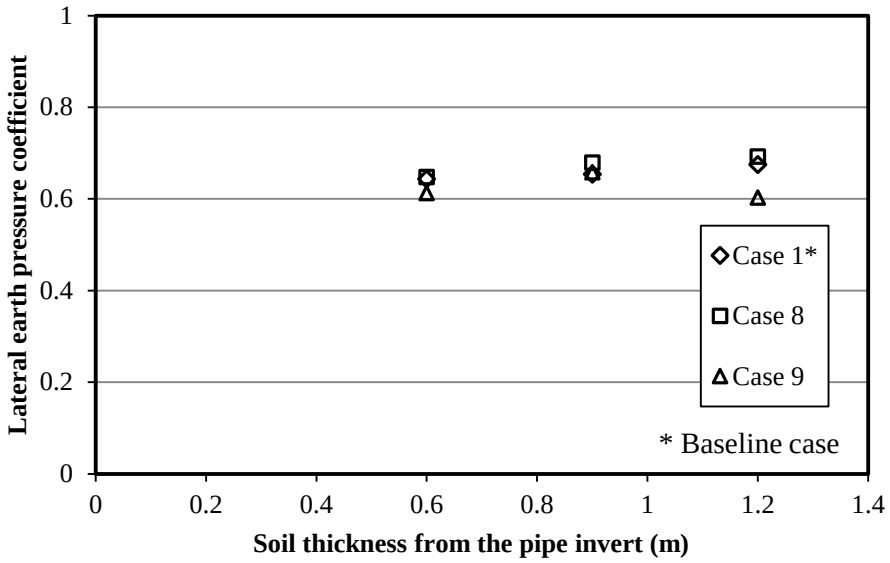

Figure 4.30 Variation of the lateral earth pressure coefficients at the springline of the pipe with backfilling with different magnitude of compaction load

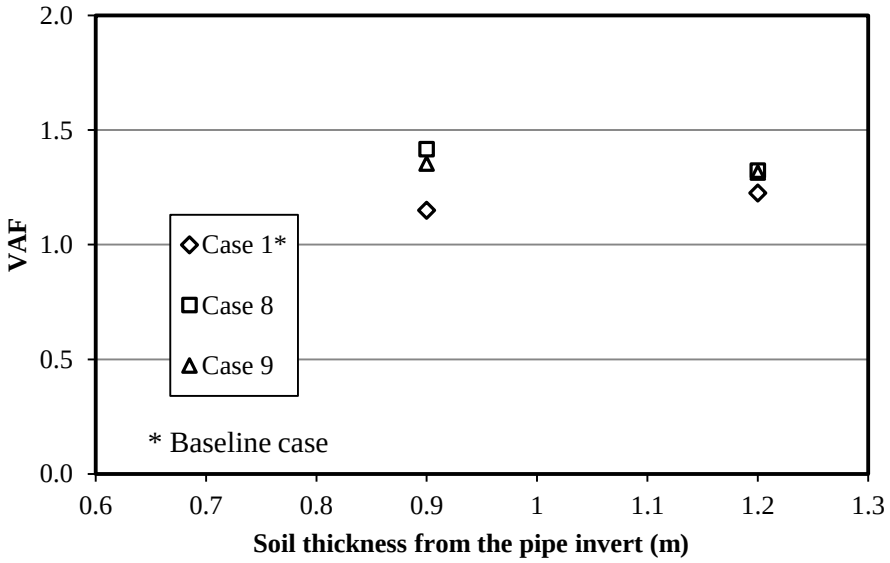

Figure 4.31 Variation of the soil arching factors at the top of the pipe with backfilling with different magnitude of compaction load

Table 4.9 presents the locations and peak values of the bending moments of the pipe with different compaction pressure. The peak bending moment was at the pipe springline when the backfill at the level of the pipe springline, while it moved to the pipe crown when the backfill reached the pipe top level. When the backfill was above the pipe top level, the locations of the peak bending moments were 105^o from the pipe crown. The magnitude of the peak bending moments increased with an increase of the compaction pressure at a specific backfill level.

Table 4.9 Locations and peak values of the bending moment of the pipe in cases with different magnitude of compaction pressure

h (m)	Case 1*		Case 8		Case 9	
	Angle (^{o})	Peak (Nm/m)	Angle (^{o})	Peak (Nm/m)	Angle (^{o})	Peak (Nm/m)
0.3	90	15.4	90	7.0	90	12.3
0.6	0	42.1	0	18.4	0	30.0
0.9	109	38.0	105	26.6	105	35.3
1.2	109	40.3	105	29.8	105	37.6

Note: *h* is the soil thickness from the pipe invert; *Angle* represents the angle from the pipe crown; *Peak* is the peak value of bending moment of the pipe at a specific soil thickness.

Figure 4.32 shows the peak hoop strains of the pipe with different compaction pressure. The maximum hoop strains in all of these three cases (Cases 1, 8 and 9) occurred when the backfill at the level of the pipe top. The magnitude of the peak hoop strains increased with an increase of the compaction pressure at a specific backfill level.

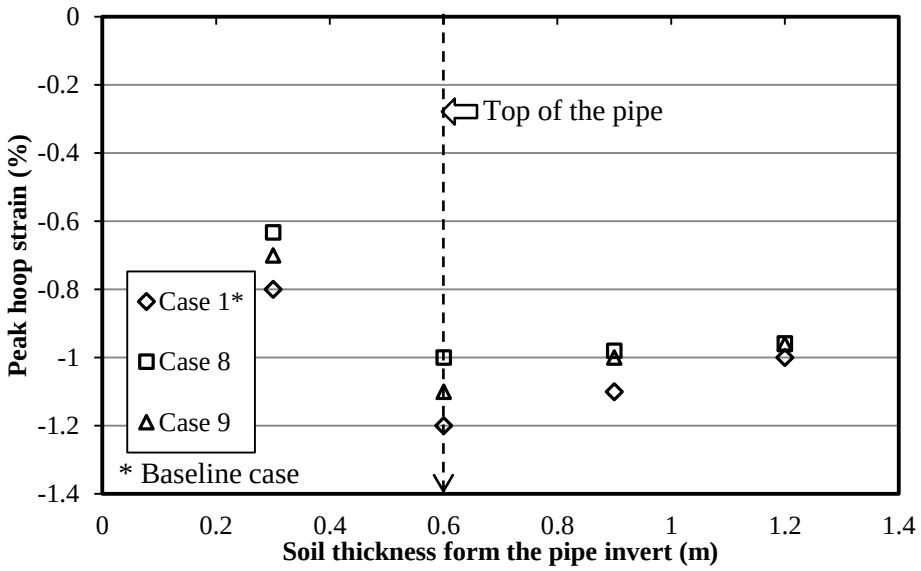

Figure 4.32 Peak hoop strains of the pipe with backfilling in cases with different magnitude of compaction pressure

4.5.5 Effect of the Friction Angle of the Backfill Material

The friction angle is an essential parameter for granular materials which is widely used as backfill material for buried pipes. The friction angle can influence the load transfer mechanism. Therefore, it is necessary to investigate the effect of the friction angle of the backfill material on the performance of the SRHDPE pipe. Two friction angles were adopted in this study, namely, 35 (Case 10: typical value for sand) and 55^{o} (Case 11: typical value for gravel). **Figure 4.33** is the vertical and horizontal deflections of the pipe buried in material with different friction angles. The peaking deflection slightly increased with an increase of the friction angle. The diameter changes after the backfill above the pipe top level were approximately equal for those three cases. The effect of the friction angle on the pipe deflection is insignificant.

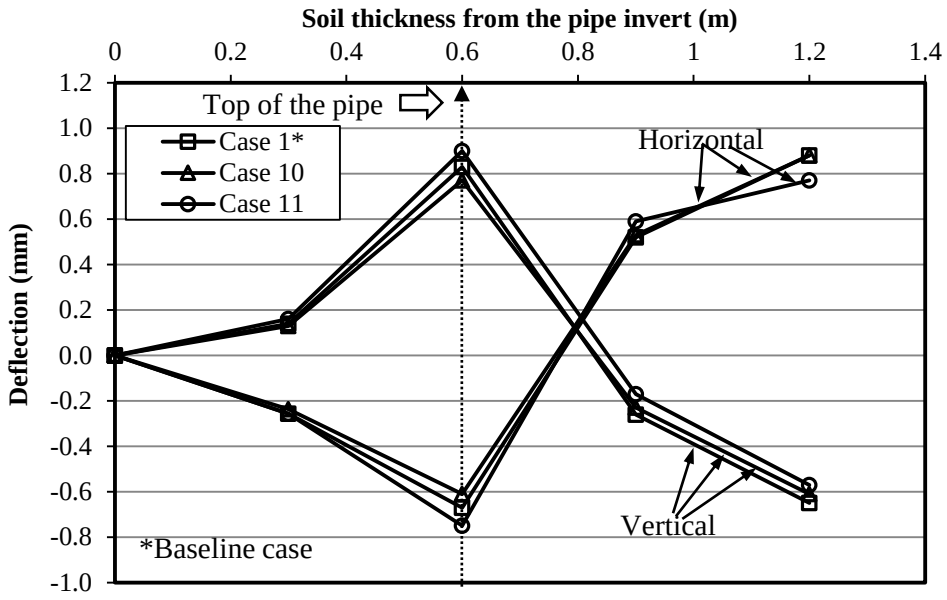

Figure 4.33 Vertical and horizontal deflections of the pipe with different friction angle of the backfill material

Figure 4.34 is the lateral earth pressure coefficient at the springline of the pipe with different friction angle of the backfill material. It demonstrates that the lateral earth pressure increases with an increase of the friction angle. **Figure 4.35** shows the relationship between the lateral earth pressure coefficients at rest with the calculated lateral earth pressure coefficients.

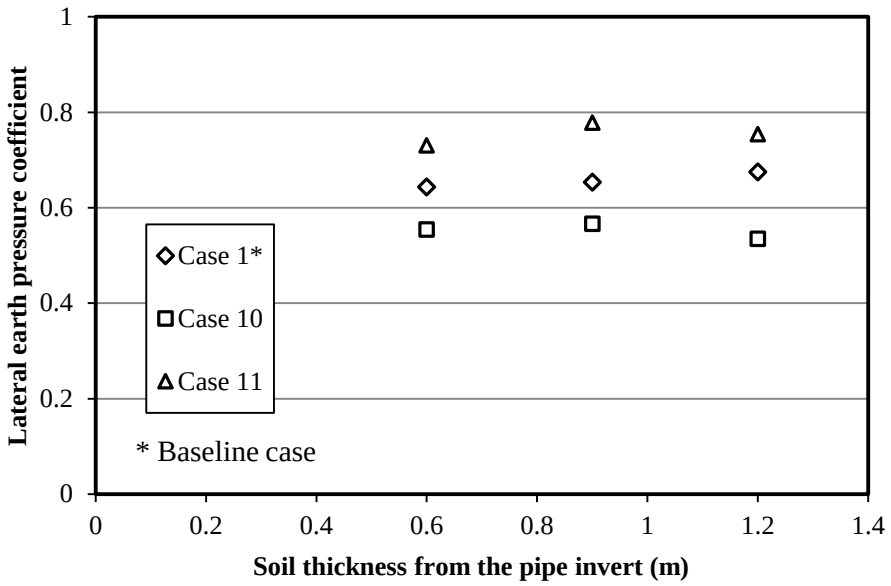

Figure 4.34 Variation of the lateral earth pressure coefficients at the springline of the pipe with different friction angle of the backfill material

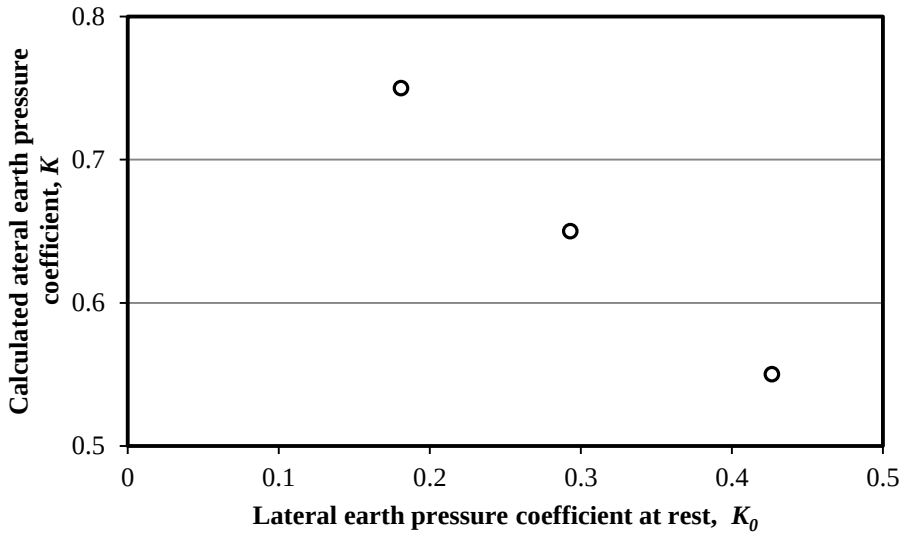

Figure 4.35 Relationship between the lateral earth pressure coefficients at rest with the calculated lateral earth pressure coefficients

Figure 4.36 is the soil arching factors at the top of the pipe at different friction angle of the backfill material. It shows that VAFs varies in a narrow range of 1.1 to 1.2, which indicates the insignificant effect of the friction angle on the VAF. In other words, the above recommended VAF of 1.1 can also be used for the backfill material with different friction angle.

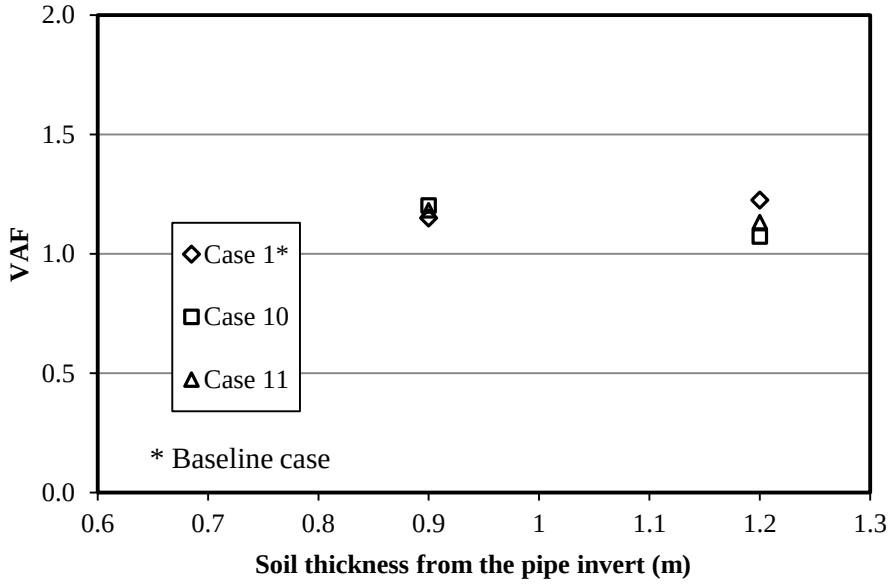

Figure 4.36 Variation of the soil arching factors at the top of the pipe with backfilling at different friction angle of the backfill material

Table 4.10 presents the locations and peak values of the bending moments of the pipe at different friction angle of the backfill material. The locations of the peak bending moments were consistent with above cases. The peak bending moment was at the pipe springline when the backfill at the level of the pipe springline, while it moved to the pipe crown when the backfill reached the pipe top level. When the backfill was over the pipe top level, the locations of the peak bending moments were 105^{o} from the pipe crown. The magnitude of the peak bending moments increased with an increase of the friction angle of the backfill material.

Table 4.10 Locations and peak values of the bending moment of the pipe in cases with different friction angle of the backfill material

h (in.)	Case 1*		Case 10		Case 11	
	Angle (°)	Peak (N·m/m)	Angle (°)	Peak (N·m/m)	Angle (°)	Peak (N·m/m)
12	90	15.42	90	15.69	90	16.49
24	0	42.04	0	39.02	0	44.71
36	105	38.00	105	39.64	105	35.02
48	105	40.27	105	40.04	105	37.56

Note: *h* is the soil thickness from the pipe invert; *Angle* represents the angle from the pipe crown; *Peak* is the peak value of bending moment of the pipe at a specific soil thickness.

Figure 4.37 shows the peak hoop strains of the pipe with different angle of the backfill material. The maximum hoop strains in all of these three cases (i.e., Cases 1, 10 and 11) occurred when the backfill at the level of the top of the pipe. The magnitude of the peak hoop strains increased with an increase of the friction angle of the backfill material. However, they were all lower than the long-term strain limit of 5% for thermoplastic pipes suggested by AASHTO (2012).

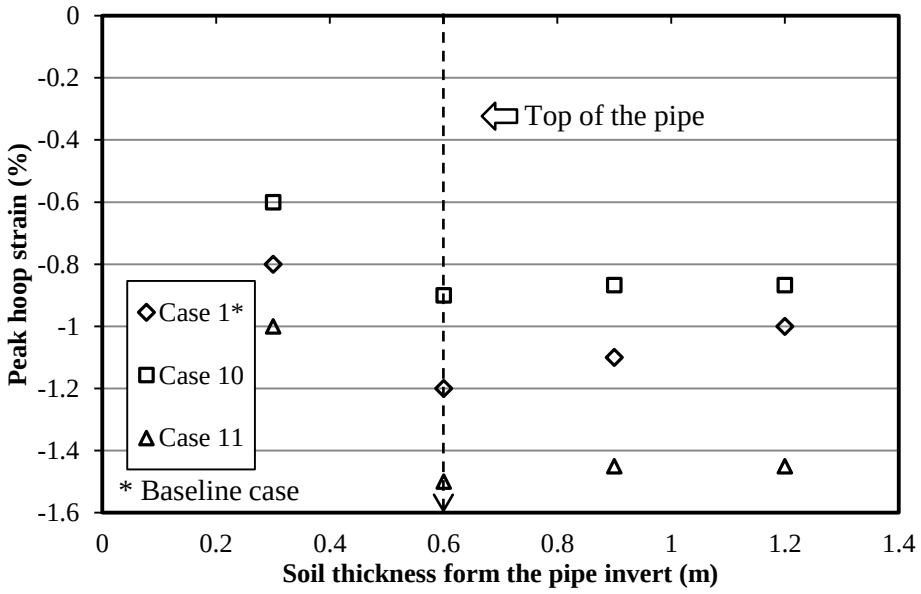

Figure 4.37 Peak hoop strains of the pipe with backfilling in cases at different friction angle of the backfill material

4.6 Summary

The steel-reinforced HDPE pipe combines the advantages of the HDPE and metal pipes which implies a bright future for the SRHDPE pipe. Hardening soil model was adopted to simulate the backfill material, while the EMM was proposed to model the SRHDPE pipe in the numerical model. After the validation of the numerical model, the numerical model was first verified using the field test data to demonstrate the effectiveness of the modeling procedures. Subsequently, a numerical analysis considering the effects of the soil cover thickness, trench width, compaction pressure and the friction angle of the backfill material was conducted to investigate the performance of the SRHDPE pipe during the installation. The vertical and horizontal deflections,

earth pressure at the top and springline of the pipe, bending moment and hoop strain of the pipe were recorded. The following conclusions can be made from the numerical results:

(1) Hardening soil model and EMM were effective to model the performance of the SRHDPE pipes under compaction. Comparisons of the numerical and field test results in the verification demonstrate the effectiveness of the modeling procedures in this study;

(2) The horizontal deflections were greater than the vertical deflections of the pipe in all cases. Both of the vertical and horizontal deflections at end of the construction linearly increased with an increase of the soil cover thickness. The peaking deflections increased with an increase of the trench width and the magnitude of the compaction pressure. The effect of the friction angle on the pipe deflection is insignificant;

(3) The average lateral earth pressure coefficient at the springline of the pipe was 0.65 for all cases. The soil arching factor at the top of the pipe can be assumed as 1.1 with exception of cases with insufficient compaction loads. The insufficient compaction loads resulted in higher soil arching factors in a range of 1.3 to 1.4 due to the lower soil reaction modulus; and

(4) Peak bending moments increased before the backfill reached the pipe top level and then the change of peak bending moments was insignificant. The peak hoop strains was located at the springline of the pipe in all cases which were all lower than the service limit of 5% for thermoplastic pipes specified by AASHTO (2012). The maximum hoop strain happened when the backfill was at the level of the pipe top.

CHAPTER 5 LOAD TRANSFER MECHANISM IN THE SOIL COVER ABOVE THE SRHDPE PIPE

5.1 Introduction

Soil arching effect, firstly proposed by Terzaghi (1943), is defined as the reduction of the soil weight in the mobilized zone due to the friction developed at the interface of the mobilized and stable zones. Soil arching effect has been widely used in different applications in geotechnical engineering, for example, retaining walls, pile-supported earth structures, and buried structures. Relative displacement between the mobilized soil and stable soil is the source of the soil arching effect. In other words, soil arching effect only occurs in soils when relative displacement happens. Since soil arching is important in geotechnical engineering, people has done much research on this topic to understand its mechanism using theoretical derivations (Marston, 1913; Terzaghi, 1943; and Hewlett and Randolph, 1988), numerical methods (Getzler, 1970; Sakguchi and Ozaki, 1992; and Bhandari, 2010) and experimental investigations (Terzaghi, 1936; Harris, 1974; Evans, 1984; and Chen et al., 2008).

Here only two major theoretical solutions of the soil arching effect are briefly presented as follows:

(1) Terzaghi's method (Terzaghi, 1943). Based on the observation in the famous trap door test (Terzaghi, 1936), the mobilized portion of the backfill was curved with the depth. However, he assumed a vertical portion as shown in **Figure 5.1** to simplify the calculation, The vertical pressure at the bottom of the mobilized portion σ_v can be calculated as **Equation (5-1)**:

$$\sigma_v = \frac{B(\gamma - \frac{c}{B})}{K\tan\phi}(1 - e^{-K\tan\phi\frac{z}{B}}) + q \cdot e^{-K\tan\phi\frac{z}{B}} \quad (5\text{-}1)$$

where σ_v = the vertical pressure at the bottom of the mobilized portion; B = the width of the mobilized portion; c = cohesion of soil; ϕ = friction angle of soil; z = the height of the mobilized portion; K = the lateral earth pressure coefficient which can be calculated as $\frac{1-\sin^2\phi}{1+\sin^2\phi}$; q = the surcharge at the surface; and γ = the unit weight of soil.

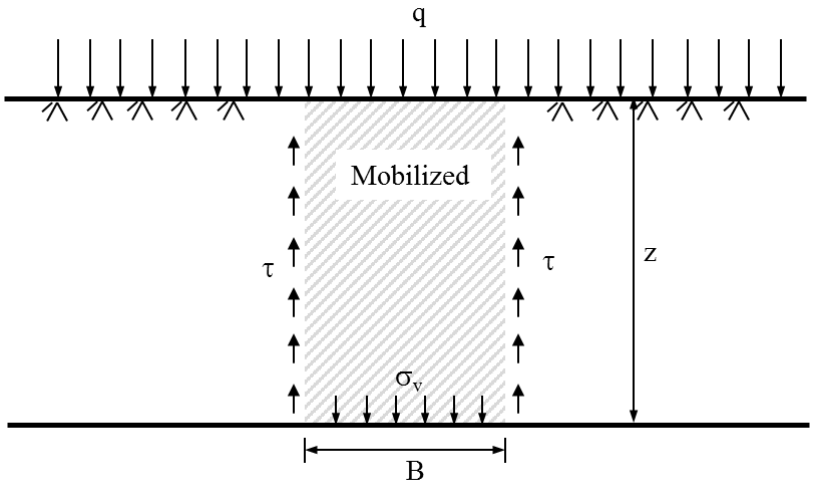

Figure 5.1 Schematic of soil arching effect calculation adopted in Terzaghi (1943)

(2) Hewlett and Randolph's method (Hewlett and Randolph, 1988). They assumed the arch in the pile-supported embankment at a passive equilibrium state and derived the portion of the embankment weight carried by the piles in 2D and 3D conditions as follows:

$$E = 1 - \frac{b\sigma_i}{sH} = 1 - \left(\frac{b}{s}\right)\left(1 - \frac{s}{2H}\right)\left(1 - \frac{b}{s}\right)^{(K_P - 1)} \quad \text{2D Condition} \quad (5\text{-}2)$$

$$E = 1 - \left[1 - \left(\frac{b}{s}\right)^2\right]\left[A - AB + C\right] \quad \text{3D Condition} \quad (5\text{-}3)$$

$$A=\left[1-\left(\frac{b}{s}\right)^2\right]^{2(K_P-1)} \quad B=\frac{s}{\sqrt{2}H}\left[\frac{2K_P-2}{2K_P-3}\right] \quad C=\frac{s-b}{\sqrt{2}H}\left[\frac{2K_P-2}{2K_P-3}\right]$$

where E = the portion of embankment weight supported by piles; b = the pile diameter; s = the center to center spacing of piles; H = the height of embankment; and K_p = the passive lateral earth pressure coefficient.

However, it has to be noted that in both Terzaghi and Hewlett and Randolph method, the soil in the mobilized zone are assumed at a yielding (i.e., failure) state, and the shear stress in the soil is equal to the shear strength of the soil. A yielding soil could result in a fully-mobilized soil arching which is widely used in engineering practice. However, it is widely accepted that the shear stress in the soil is related to the relative displacement in the soil. If the displacement of soil is limited, the shear stress in the soil may not reach the shear strength which in turn induces a partially-mobilized soil arching effect. Han (2015) pointed out that the soil arching effect could not be fully mobilized when the elastic modulus ratio of the pile to soil was lower than 100 which was attributed to the insufficient relative displacement between the pile and the surrounding soil. The curve of displacement ratio and soil arching ratio in trap door test as shown in **Figure 5.2** also demonstrates the soil arching effect is highly displacement related (Terzaghi, 1936). When the relative displacement cannot trigger fully-mobilized soil arching, the relationship of the displacement with the shear stress of the soil should be considered in the partially-mobilized soil arching.

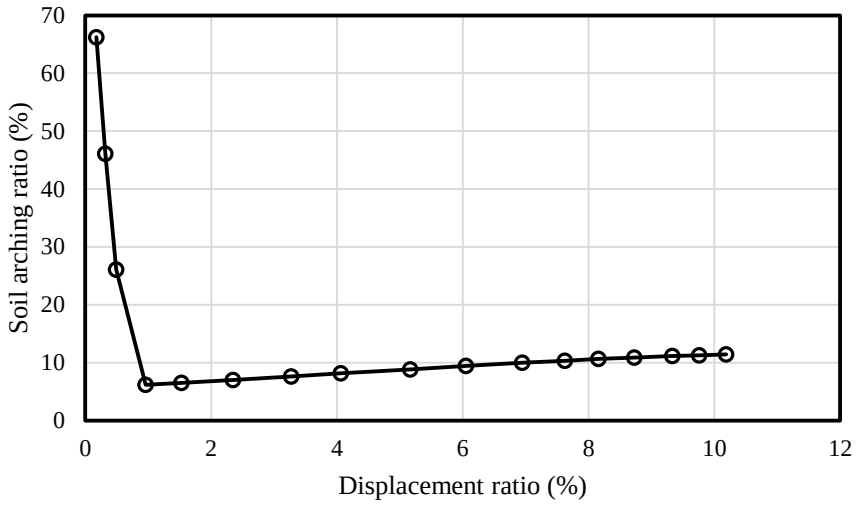

Figure 5.2 Displacement ratio (trap door movement/trap width) versus soil arching ratio (load on trap door/overburden load) (after Terzaghi (1936))

SRHDPE pipe is relative rigid compared with the HDPE pipes. Based on the field test results in Chapter 3, the maximum pipe deflection during installation was only approximately 3 mm which may not induce full-mobilized soil arching in the soil cover. Therefore, partially-mobilized soil arching should be involved in the calculation of the load at the pipe top.

5.2 Partially-Mobilized Soil Arching under Uniformly-Distributed Static Loading

5.2.1 Derivation Considerations

An extreme case of the soil arching is the embankment over a cavity which could be used in this study to illustrate the partially-mobilized soil arching. In this study, the vertical mobilized pattern proposed in Terzaghi (1943) was adopted considering the accuracy and simplicity of the calculation. **Figure 5.3** presents the soil arching developing process with the displacement propagating towards the embankment surface as follows:

(1) when the displacement occurs above the cavity, settlement starts to propagate into the embankment. Initially, the displacement at the interface of the mobilized and stable portions may be greater than the critical displacement (i.e., the relative displacement which can induce shear stress in the soil equals to the shear strength). The shear stress at the interface of the mobilized and stable portions is equal to the shear strength, which can fully mobilize the soil. This zone is referred to as "fully-mobilized zone";

(2) with the settlement propagating, the displacement at the interface of the mobilized and stable portions would decrease with a decrease of the depth. Such that the displacement at the interface is smaller than the critical displacement, which results in a shear stress at the interface is lower than the shear strength. In other words, the soil in the mobilized portion is partially mobilized. This zone is so-called as "partially-mobilized zone"; and

(3) the displacement would decrease to zero if the embankment is enough high. The elevation, where the displacement at the interface becomes zero, is the equal settlement plane. The soil above the equal settlement plane is recognized as "stable zone".

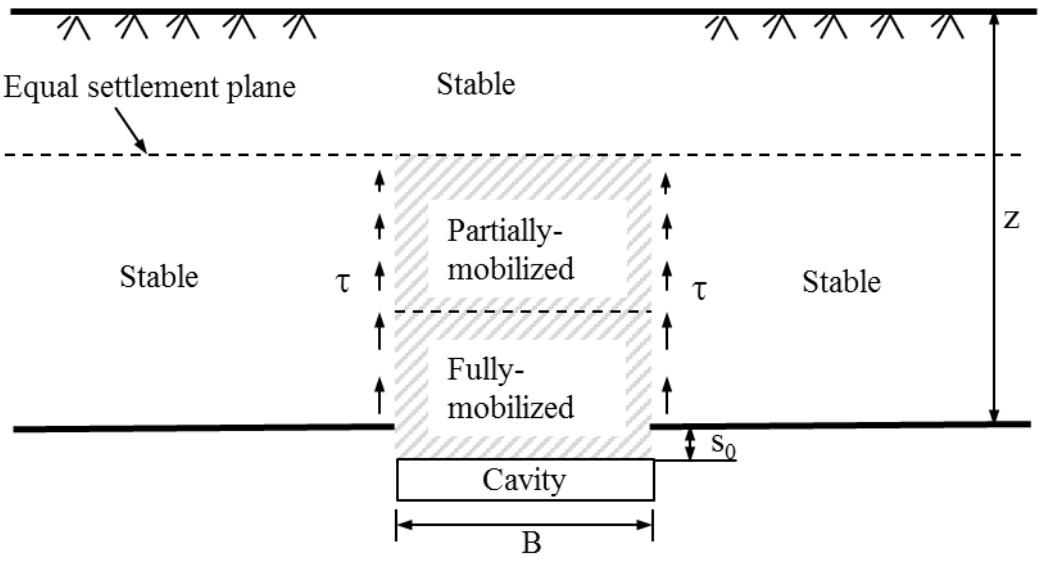

Figure 5.3 Schematic of soil arching developing in an embankment over a cavity

To derive the partially-mobilized soil arching effect equation shown in **Figure 5.3**, two relationships have to be established: (1) the relationship of the displacement at the interface of the mobilized and surrounding stable portions with the depth; and (2) the relationship of the shear stress with the displacement.

5.2.2 Derivation of the Partially-Mobilized Soil Arching Equations under Uniformly-Distributed Static Loading

Relationship of the Vertical Stress with the Depth

The calculation of the vertical stress and free body diagram of the element *i* is shown in **Figure 5.4.** Based on the free body diagram, the vertical stress increment of the element *i* can be calculated as:

$$\Delta\sigma_i = \sigma_i - \sigma_{i+1} = \left(\gamma - \frac{2\tau_i}{B}\right)\Delta z \tag{5-4}$$

where σ_i = the vertical stress at the bottom of the element *i*; σ_{i+1} = the vertical stress at the top of the element *i*; and γ = the unit weight of soil. The shear stress τ_i at the interface of the mobilized and stable portions in element *i* is related to the relative displacement at the interface which will be presented later on.

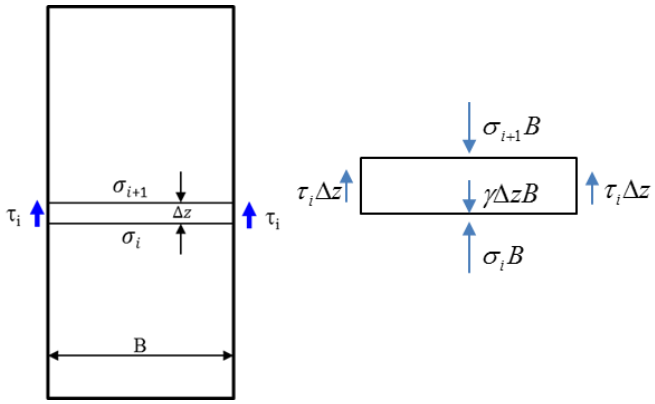

Figure 5.4 Schematic of the vertical stress calculation and free body diagram of the element *i*

Relationship of the Displacement with the Depth

The element *i* is an element in the mobilized portion as shown in **Figure 5.5**. The strain of the element *i* can be expressed as:

$$\varepsilon_i = \frac{\Delta s_i}{\Delta z} = \frac{s_{i+1} - s_i}{\Delta z} = \frac{\Delta \sigma_i}{E} = \left(\gamma - \frac{2\tau_i}{B}\right)\frac{\Delta z}{E} \tag{5-5}$$

where ε_i = the strain of the element *i*; Δs_i = the displacement decrease in the element *i*; Δz = the thickness of the element *i*; τ_i = the shear stress at the interface of the mobilized and stable portions at element *i*; *B* = the width of the mobilized portion; and *E* = the elastic modulus of the embankment backfill material.

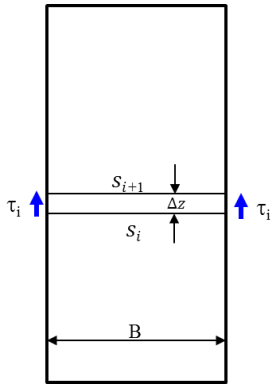

Figure 5.5 Schematic of the displacement calculation in the mobilized portion

In **Equation (5-5)**, the shear stress at the interface of the mobilized and stable portions at the element τ_i can be determined based on the rules as follows:

(1) when $s_i \geq s_f$ (i.e., the critical displacement), $\tau_i = \tau_f$ (i.e., the shear strength of the backfill material). The element *i* is in the fully-mobilized zone;

(2) when $s_i < s_f$, $\tau_i = \dfrac{s_i}{a + bs_i}$. The shear stress τ_i can be calculated using the hyperbolic model.

Clough and Duncan (1971) proposed to calculate the hyperbolic parameters as:

$$a = \frac{1}{k_i \gamma_w \left(\dfrac{\sigma_n}{p_a} \right)^n} \text{ and } b = \frac{0.9}{\tau_f}$$

where k_i = the dimensionless stiffness number which can be determined from the direct shear test or using the typical value suggested by Clough and Duncan (1971); γ_w = the unit weight of water; σ_n = the normal stress which can be determined using the overburden stress multiplying the later earth pressure coefficient at rest (i.e., K_o) ; p_a = the atmospheric pressure; n = the stiffness constant with values typically in a range of 0.5-0.8; τ_f = the shear strength of the backfill which can be calculated as $\tau_f = c + \sigma_n \tan\phi$, c is the cohesion of the backfill, ϕ is the friction angle of the backfill.

The critical displacement s_f can be calculated as:

$$s_f = \frac{a\tau_f}{1 - b\tau_f} \tag{5-6}$$

Procedures for solving of equations

To solve the equations for the partially-mobilized soil arching effect, **Equations (5-4) and (5-5)** are necessary to be combined together. Considering the difficulty to obtain the analytical solutions, the following procedures were adopted in this study:

(1) divide the mobilized portion as N layers (the value of N depends on the thickness of the backfill) and number them as 1, 2, 3, ……..N from bottom up. $\Delta z = \frac{H}{N}$, H is the thickness of the backfill;

(2) assume the settlement at the bottom of the mobilized portion is s_0, the displacement at element i can be calculated using **Equation (5-5)**. If $s_0 \le s_f$, $\Delta s_1 = \frac{\frac{2 s_0 \Delta h^2}{a + b s_0}}{BE}$; if $s_0 > s_f$, $\Delta s_1 = \frac{2 \tau_f \Delta h^2}{BE}$. $s_1 = s_0 - \Delta s_1$;

(3) repeat step (2). When $s_i = s_f$, the distance from the element i to the bottom of the mobilized portion H_f is the thickness of the fully-mobilized zone; when $s_i = 0$, the distance from the element i to the top of the fully-mobilized zone H_p is the thickness of the partially-mobilized zone. The top surface of the partially-mobilized zone has the same elevation with the equal settlement plane;

(4) assume the number of the top element in the partially-mobilized zone is M, the vertical stress at the top of the element M is $\sigma_M = \gamma(H - H_f - H_p) + \mathrm{p}$, p is the surcharge. The vertical stress at the top of the element M-1 is $\sigma_{M-1} = \sigma_M + \Delta\sigma_M = \left(\gamma - \frac{2\tau_M}{B}\right)\Delta z$; and

(5) repeat step (4), until the vertical stress at the bottom of the mobilized portion is obtained. A spreadsheet can be built to simplify the above procedures.

5.2.3 Verification of the Partially-Mobilized Soil Arching Equations

Two case histories were used in this study to verify the effectiveness of the partially-mobilized soil arching equations, namely, the trap door test presented by Terzaghi (1936) and model test investigation for the soil arching effect in a pile-supported highway embankment reported by Chen et al. (2008).

Verification using Trap Door Test

Terzaghi (1936) presented the famous trap door test to investigate the soil arching effect. The test setup is shown in **Figure 5.6**. The trap door had a width of 73 mm, the length of the box was 463 mm and the height of the sand filled in the box was 300 mm. The sand had a friction angle of 27^{o} and the unit weight of the sand was 16.7 kN/m^{3}. Other detail information can be found in Terzaghi (1936). The parameters used in the calculation are summarized in **Table 5.1**. **Figure 5.7** shows the comparison of the soil arching ratio (the ratio of the vertical stress to the overburden stress) at the top of the trap door versus the displacement ratio (the ratio of the trapdoor movement to the width of the trap door) of the trapdoor. The comparison of the calculated results using the partially-mobilized soil arching equations with the measured results demonstrates the effectiveness of the proposed method.

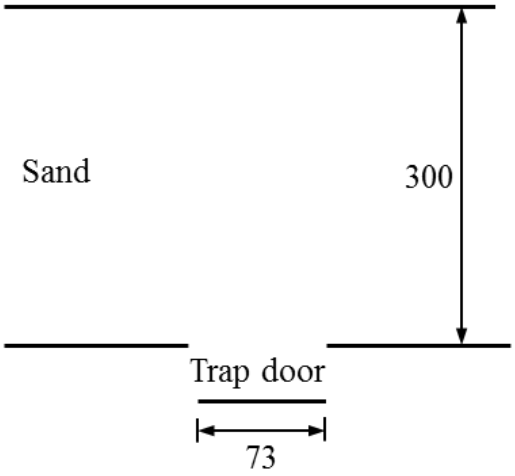

Figure 5.6 Schematic of the trap door test (unit: mm) (Terzaghi (1936))

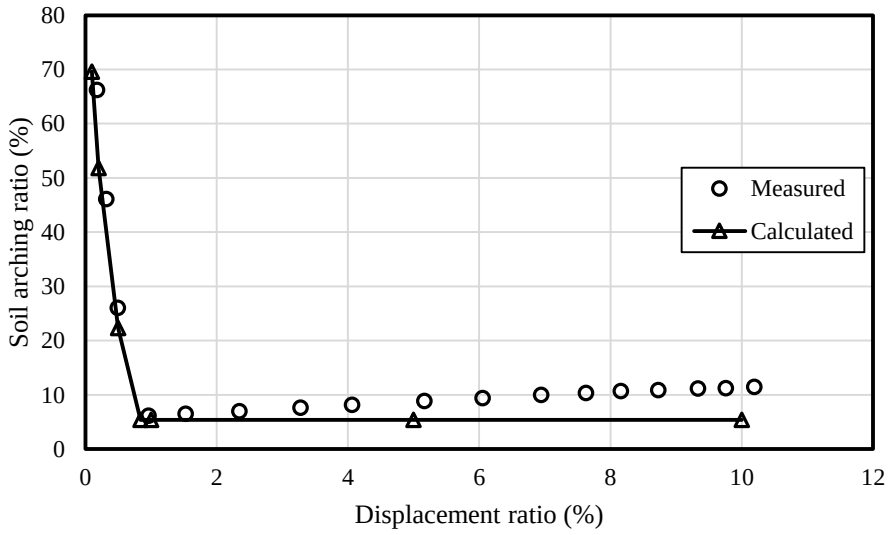

Figure 5.7 The comparison of the soil arching ratio versus the displacement ratio

Table 5.1 Summary of calculation parameters for the trap door test

Parameter	γ (kN/m^3)	ϕ (^{o})	B (m)	H (m)	k_i	E (kPa)	n
Value	16.74	27	0.073	0.31	2200	9541	0.5

Physical Model Test of A Pile-Supported Highway Embankment

Chen et al. (2008) conducted a physical model test of a pile-supported highway embankment to investigate the soil arching effect developing in the embankment. The model test setup is shown in **Figure 5.8**. Cap-beams and water bags were used to simulate the pile and the surrounding soil, respectively. Water releasing in the water bags was conducted to model the differential settlement between the pile and the surrounding soil. More detail information about this model test can be found in Chen et al. (2008). The unit weight of the sand used in the test was 15.3kN/m^3, and the friction angle was 44^o. The calculation parameters are summarized in **Table 5.2**. Since the embankment was relative high, the elastic modulus of the sand could not be assumed as a single value which was related to the depth (i.e., the confining pressure). AASHTO (2012) suggested typical values of constrained moduli for sand and gravel at different overburden stress level and different compaction which can be used to back-calculate the elastic modulus using **Equation (4-10)**. The relationship of the overburden stress, the compaction degree and the elastic modulus for sand can be plotted as shown in **Figure 5.9**. The relative density of the sand used in this test was 55% which corresponded to a compaction degree of 85%. Therefore, the elastic modulus of the sand can be calculated as:

$$E = 19\sigma_v + 9448.3 \tag{5-7}$$

where E = the elastic modulus of the sand (kPa), and σ_v = the overburden stress (kPa).

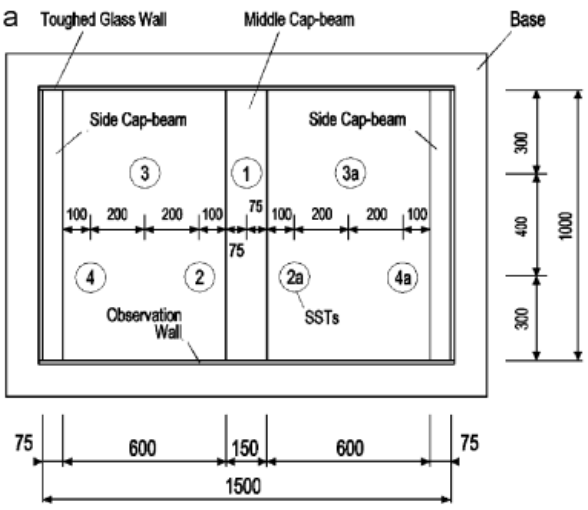

(a) plan view

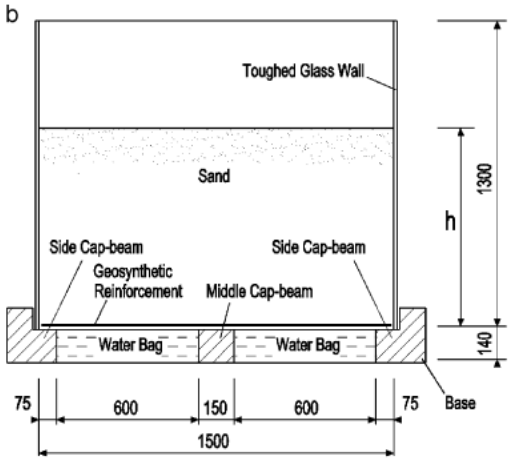

(b) side view

Figure 5.8 Schematic of the model test setup (unit: mm) (Chen et al. (2008))

Table 5.2 Summary of calculation parameters for the model test

Parameter	γ (kN/m^3)	ϕ (^{o})	B (m)	H (m)	k_i	n
Value	15.3	44	0.6	1.3	350	0.5

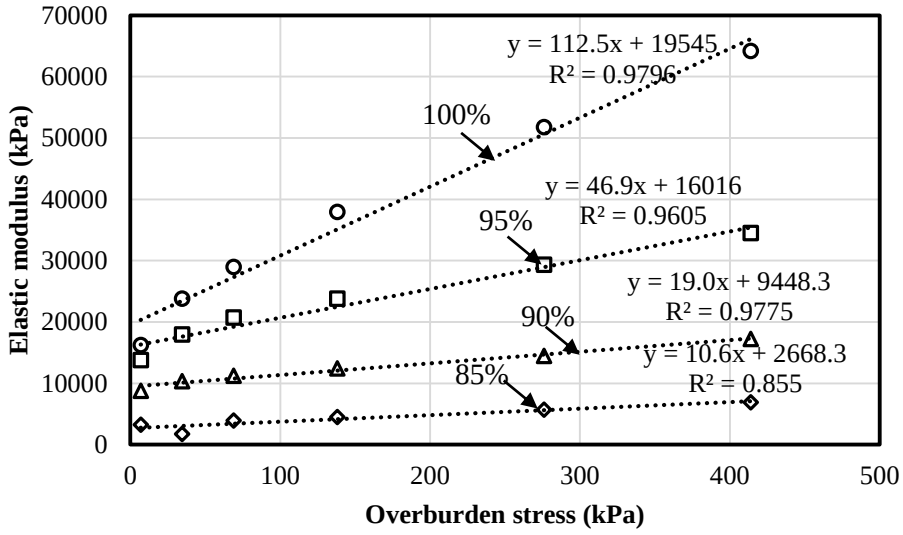

Figure 5.9 Elastic moduli versus the overburden stress of sand at different degree of compaction

Figure 5.10 shows the comparison of the earth pressure at point 3 (middle point of the water bag) shown in **Figure 5.8 (a)**. The comparison demonstrates that the proposed partially-mobilized soil arching equations are effective to calculate the earth pressure.

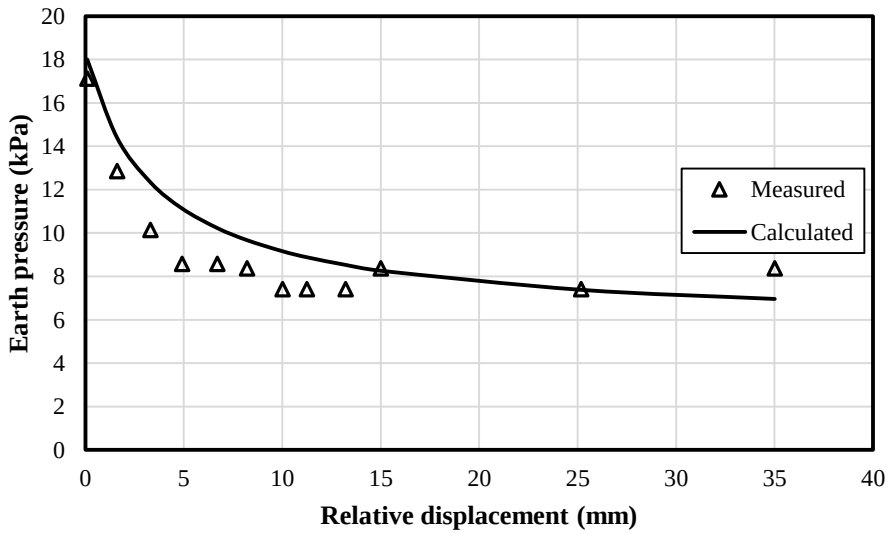

Figure 5.10 Comparison of the earth pressure at the top of the middle point of the water bag

5.2.4 Parameter Sensitivity Analysis of Partially-Mobilized Soil Arching Equations

To fully understand the partially-mobilized soil arching, parameter sensitivity analysis was conducted for six parameters involved in the partially-mobilized soil arching equations. These parameters include the unit weight of soil γ, the friction angle of soil ϕ, the width of the cavity B, the height of the embankment H, the surcharge at the embankment top p, and the degree of compaction (DOC). The degree of the compaction could influence both the elastic modulus and the friction angle. The elastic moduli at different degree of compaction were determined based on **Figure 5.9**. A baseline case was created first and the effects of the parameters on the soil arching effect were investigated by parametric study. The schematic of the baseline case is shown in **Figure 5.11**. The calculation cases are summarized in **Table 5.3**. For each case, the settlements above the cavity were 0.1, 0.5, 1, 5, and 10% of the cavity width (i.e., the displacement ratio).

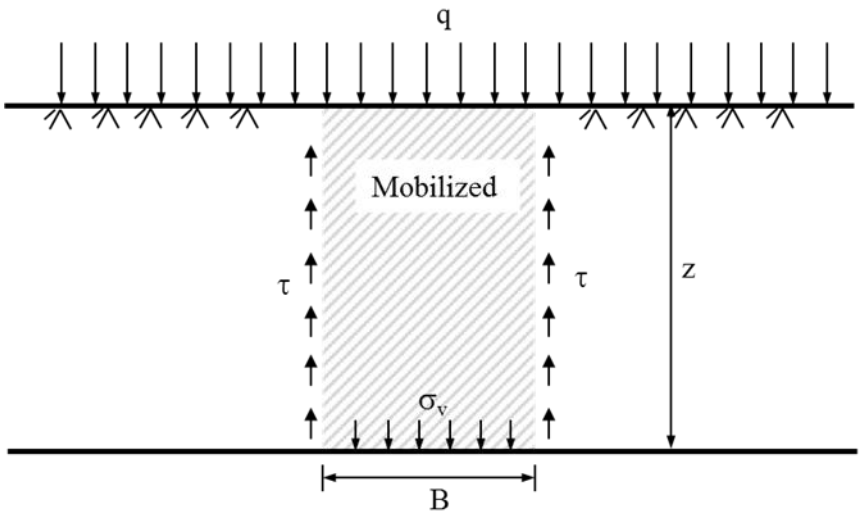

Figure 5.11 Schematic of the baseline case for the parameter sensitivity analysis

Table 5.3 Summary of the cases for the parameter sensitivity analysis

Case No.	γ (kN/m^3)	ϕ (^{o})	B (m)	H (m)	p (kPa)	DOC (%)
1*	16	30	2	4	0	90
2	18	30	2	4	0	90
3	20	30	2	4	0	90
4	16	40	2	4	0	90
5	16	50	2	4	0	90
6	16	30	1	4	0	90
7	16	30	4	4	0	90
8	16	30	2	2	0	90
9	16	30	2	8	0	90
10	16	30	2	4	10	90
11	16	30	2	4	20	90
12	16	30	2	4	0	85
13	16	30	2	4	0	95

Note: * represents Baseline case.

Baseline Case

Figure 5.12 shows the variation of the vertical stress with the depth at different displacement ratio. The vertical stress reduction from the overburden stress was significant when the displacement ratio was less than 0.5%, which demonstrated the partially-mobilized soil arching dominates. When the displacement ratio was greater than 5%, the vertical stress was almost constant along the depth, which indicated the fully-mobilized soil arching occurred. **Figure 5.13** presents the soil arching ratios (defined as the ratio of the vertical stress to the overburden stress) at the top of the cavity changing with the displacement ratio. The soil arching ratio became

constant when the displacement ratio was greater than 5%, which confirmed the fully-mobilized soil arching happened.

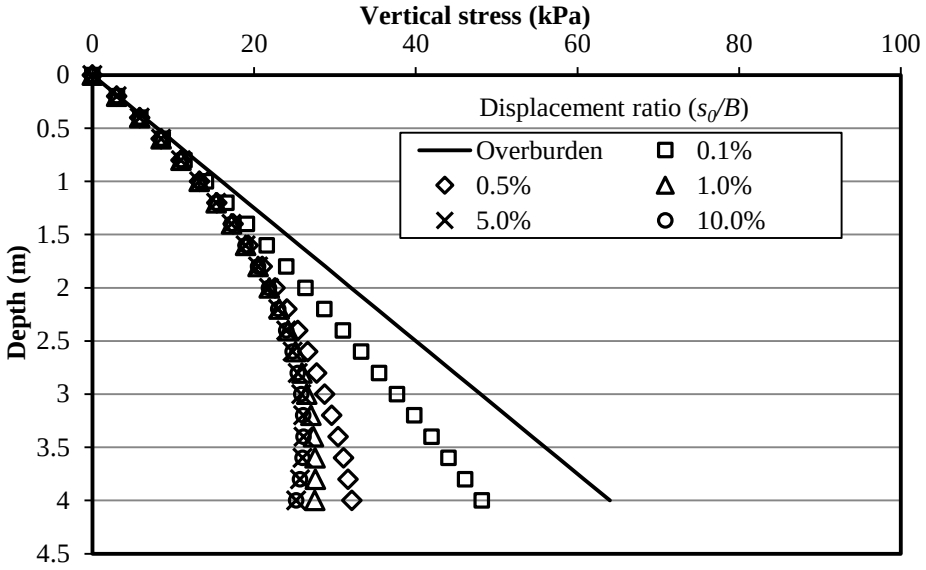

Figure 5.12 Variation of the vertical stress with the depth at different displacement ratio

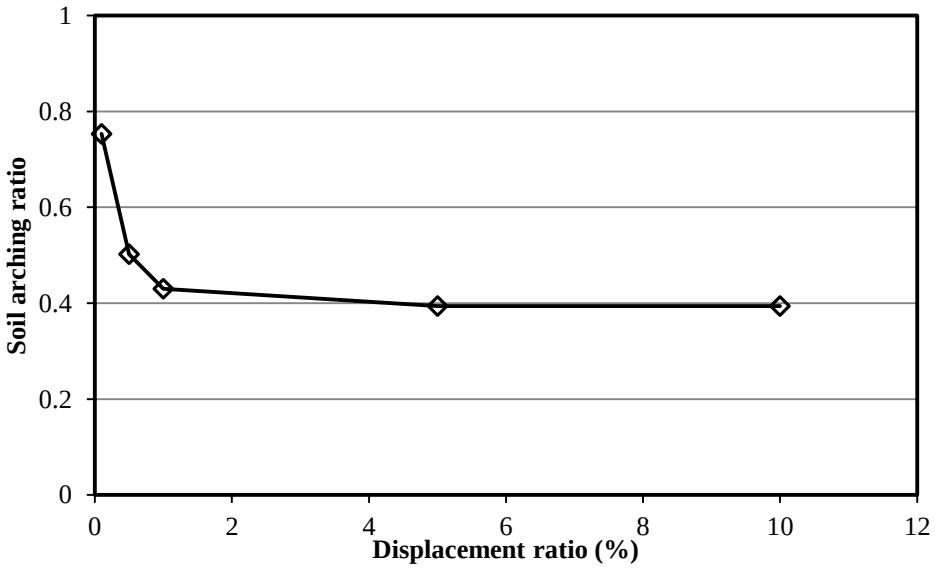

Figure 5.13 Soil arching ratio at the top of the cavity at different displacement ratio

Influence of the Unit Weight

Figure 5.14 presents the vertical stress along the depth at different displacement ratio in cases with different unit weight of soil. This figure shows the similar results as **Figure 5.12** for both cases with the soil unit weights of 18 and 20 kN/m^3: when the displacement ratio is less than 0.5%, partially-mobilized soil arching dominates the load transfer mechanism; while when the displacement ratio is greater than 5%, fully-mobilized soil arching controls the load transfer mechanism. **Figure 5.15** shows the effect of the soil unit weight on the soil arching ratio. It demonstrates that the soil unit weight effect is insignificant.

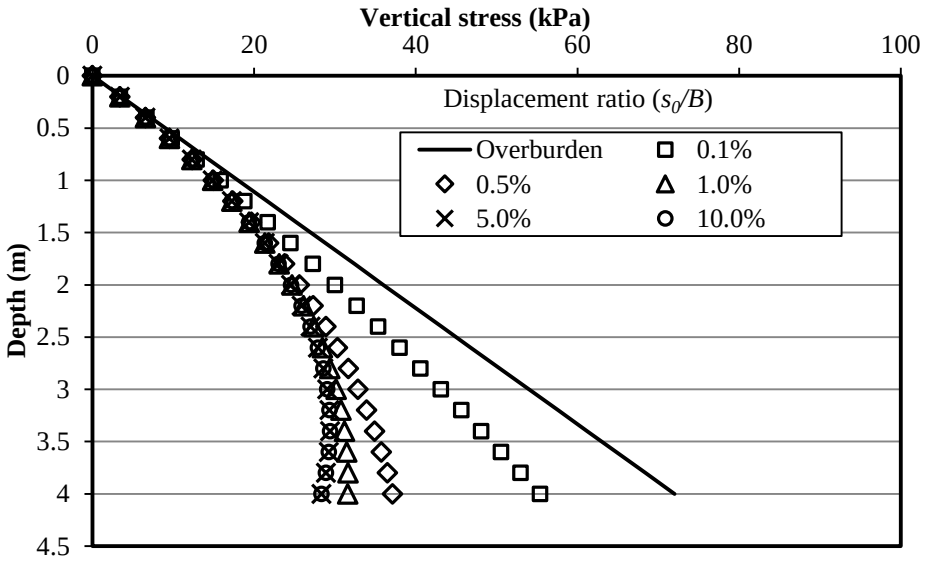

(a) 18 kN/m^3

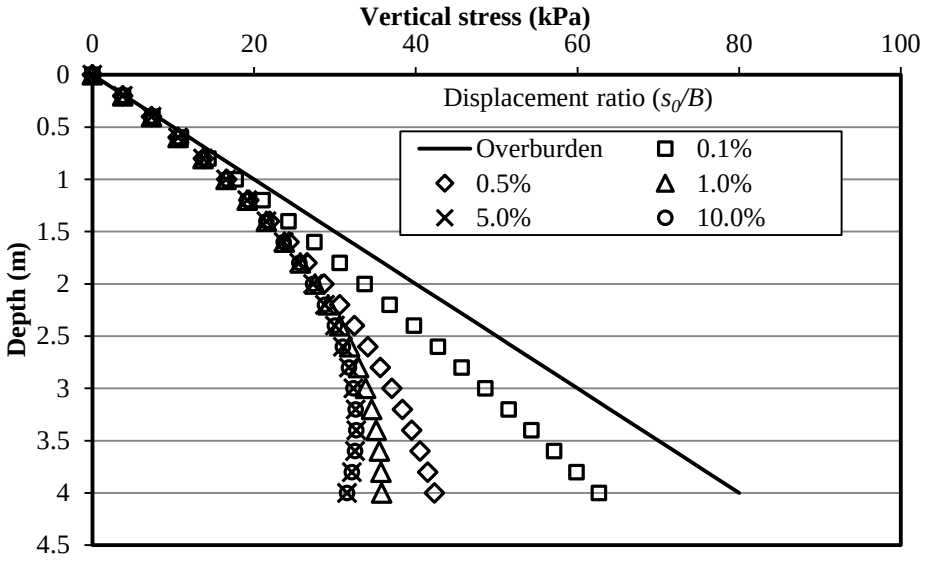

(b) 20 kN/m^3

Figure 5.14 Variation of the vertical stress with the depth at different displacement ratio in cases with different unit weight of the soil

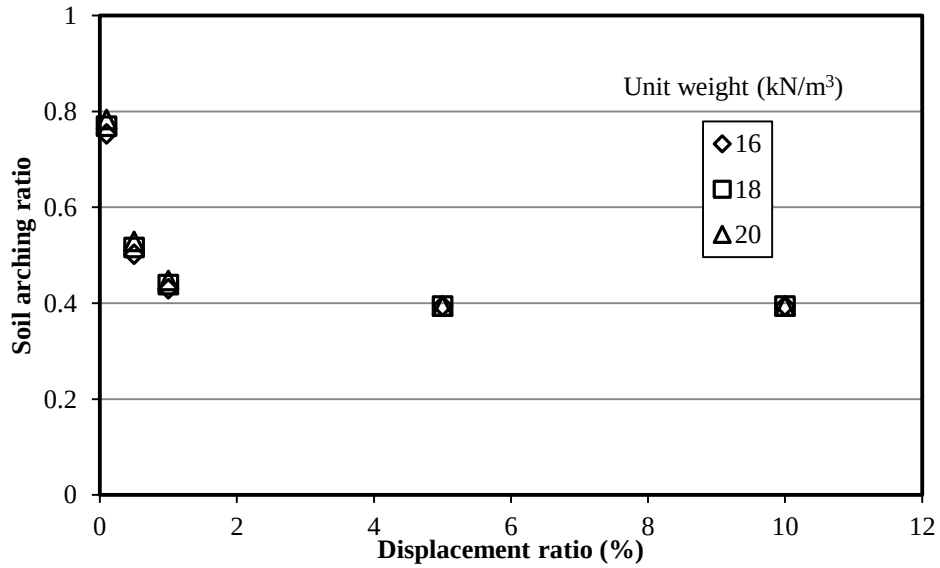

Figure 5.15 Effect of the unit weight of the soil on the soil arching ratio

Influence of the Friction Angle

Figure 5.16 presents the vertical stress along the depth at different displacement ratio in cases with different friction angle of soil. In cases with the soil friction angles of 40 and 50^o: partially-mobilized soil arching dominates the load transfer mechanism when the displacement ratio is less than 0.5%, while when the displacement ratio is greater than 5%, fully-mobilized soil arching controls the load transfer mechanism. **Figure 5.17** shows the effect of the soil unit weight on the soil arching ratio. It demonstrates that the soil unit weight effect is insignificant.

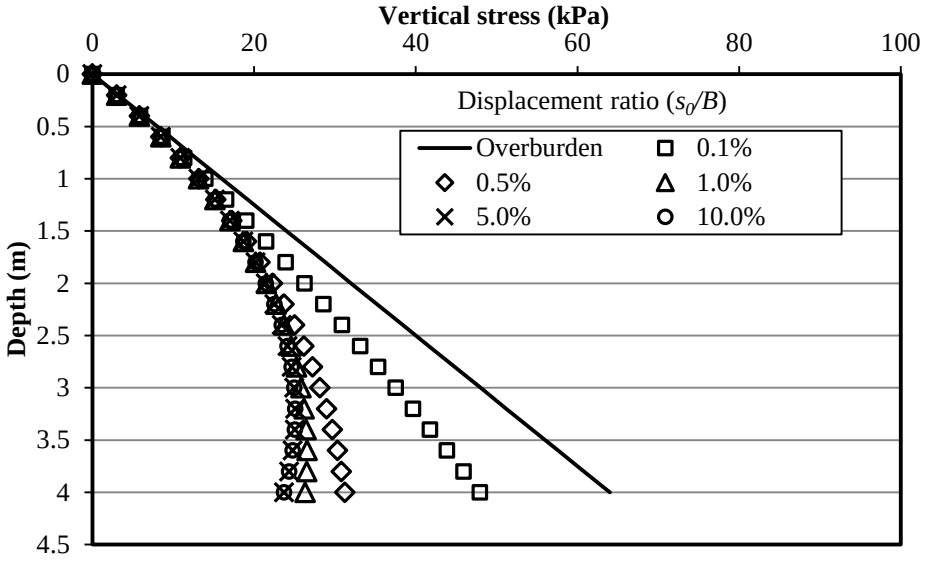

(a) 40^o

Figure 5.16 Variation of the vertical stress with the depth at different displacement ratio in cases with different friction angle of the soil

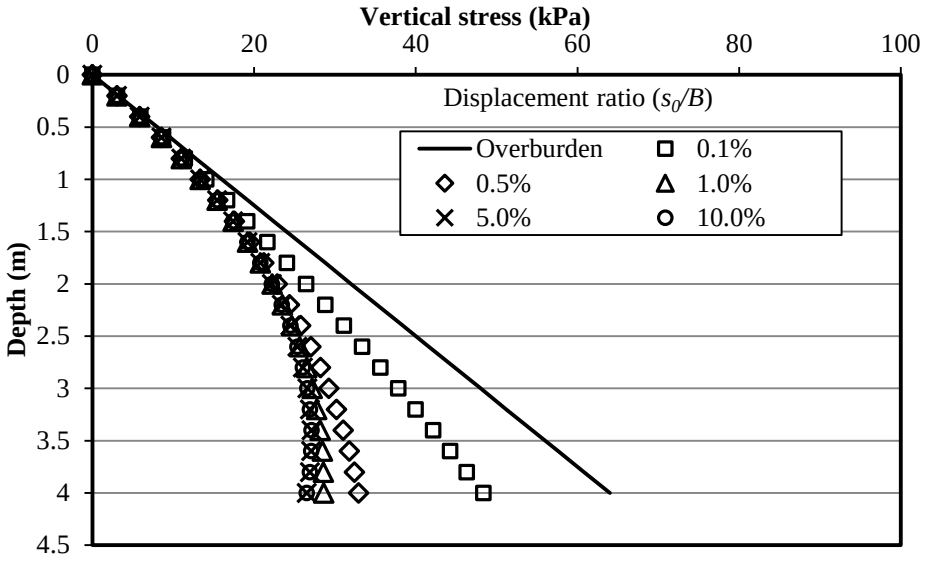

(b) 50^o

Figure 5.16 Variation of the vertical stress with the depth at different displacement ratio in cases with different friction angle of the soil (continued)

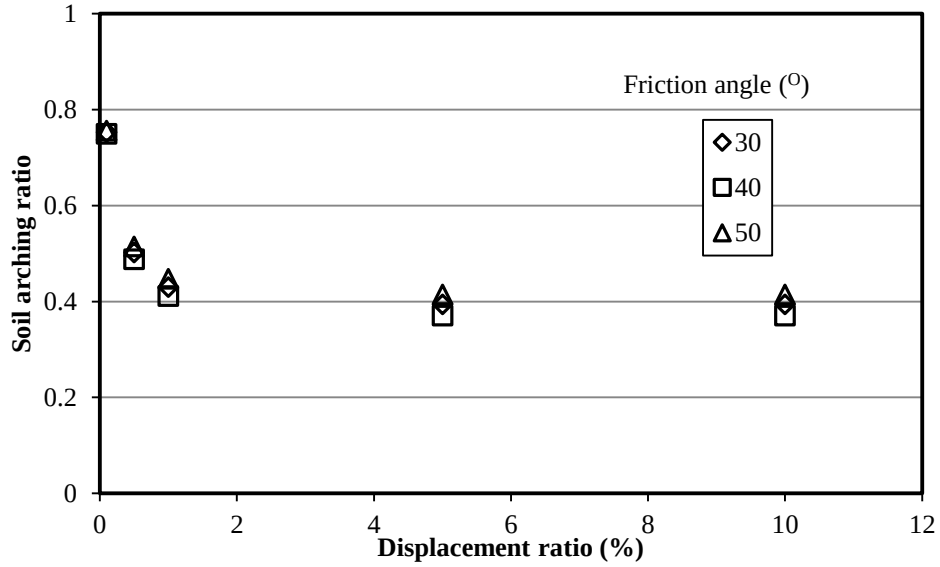

Figure 5.17 Effect of the friction angle of the soil on the soil arching ratio

Influence of the Width of the Cavity

Figure 5.18 is the variation of the vertical stress along the depth at different displacement ratio in the cases with different width of the cavity. **Figure 5.18 (a)** shows the case when the width of the cavity is 1 m (i.e., H/B = 4). The vertical stress decreased to zero when the displacement ratio increased to 1.0%. When the width of the cavity is getting smaller, the weight of the soil in the mobilized portion also becomes smaller; however, the friction at the interface would not have any reduction if the displacement is same. Therefore, the weight of soil in the mobilized portion could be significantly reduced and even becomes to zero. **Figure 5.19** is the effect of the cavity width on the soil arching ratio, which shows the effect of the cavity width on the soil arching ratio is significant. The soil arching ratio increased with a decrease of the value of H/B; after the falling down happened in the case with H/B = 4 (i.e., H = 4 m and B = 1 m), the soil arching ratio increased.

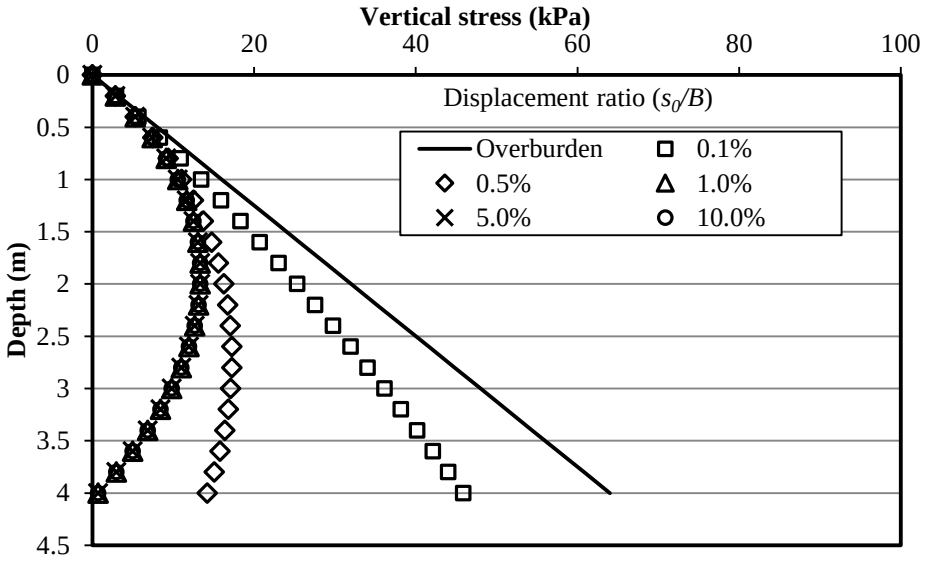

(a) B = 1 m

Figure 5.18 Variation of the vertical stress with the depth at different displacement ratio in cases with different width of the cavity

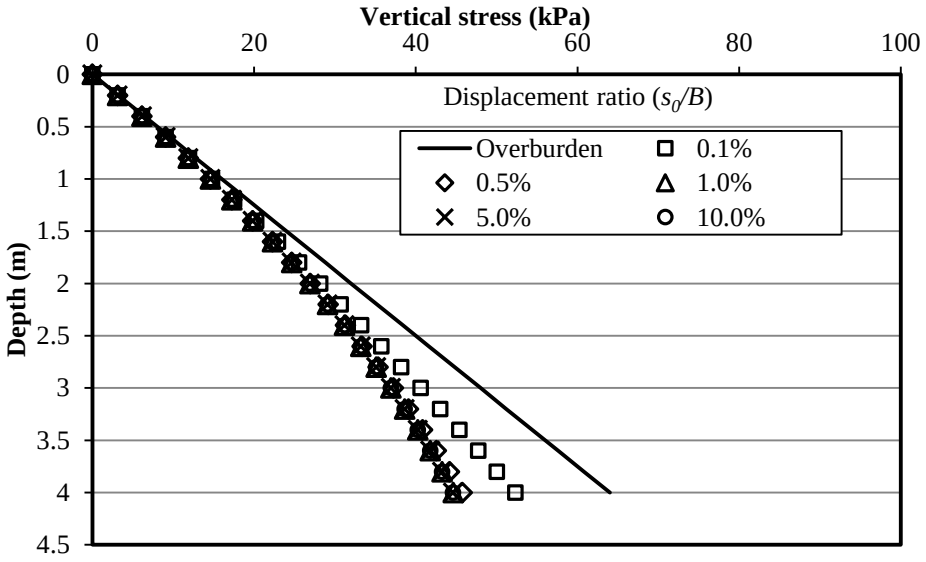

(a) B = 4 m

Figure 5.18 Variation of the vertical stress with the depth at different displacement ratio in cases with different width of the cavity (continued)

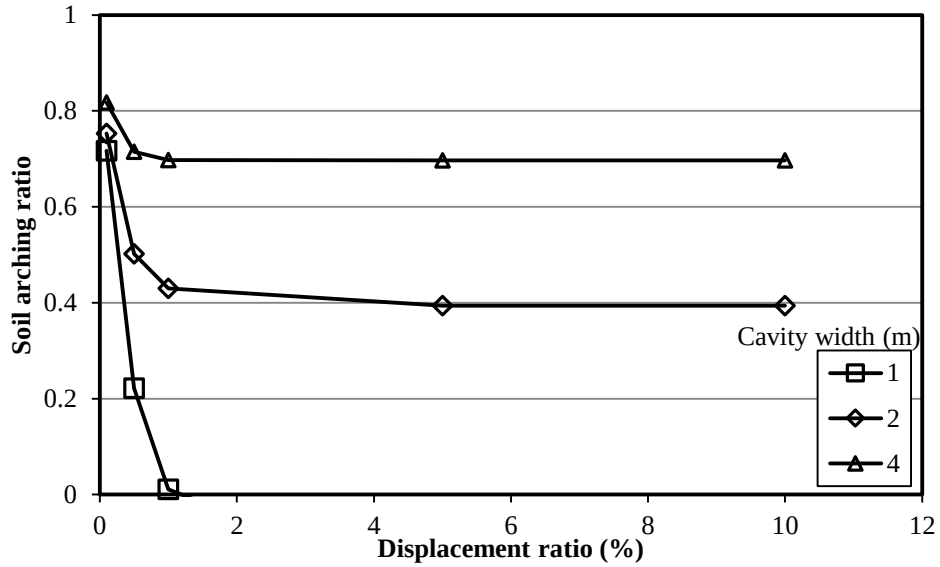

Figure 5.19 Effect of the width of the cavity on the soil arching ratio

Influence of the Height of the Embankment

Figure 5.20 presents the variation of the vertical stress with depth at different displacement ratio in cases with different height of embankment. **Figure 5.20(a)** is the case with 2 m high embankment (i.e., H/B = 1), which is similar with **Figure 5.18 (b)**. **Figure 5.20 (b)** shows the cases with 8 m high embankment (i.e., H/B = 4), which is similar with **Figures 5.18 (a)**. **Figure 5.23** is the effect of the embankment height on the soil arching ratio, which shows the effect of the embankment height on the soil arching ratio is significant. From the analysis of the cavity width and the embankment height, the soil arching soil is sensitive to the value of H/B.

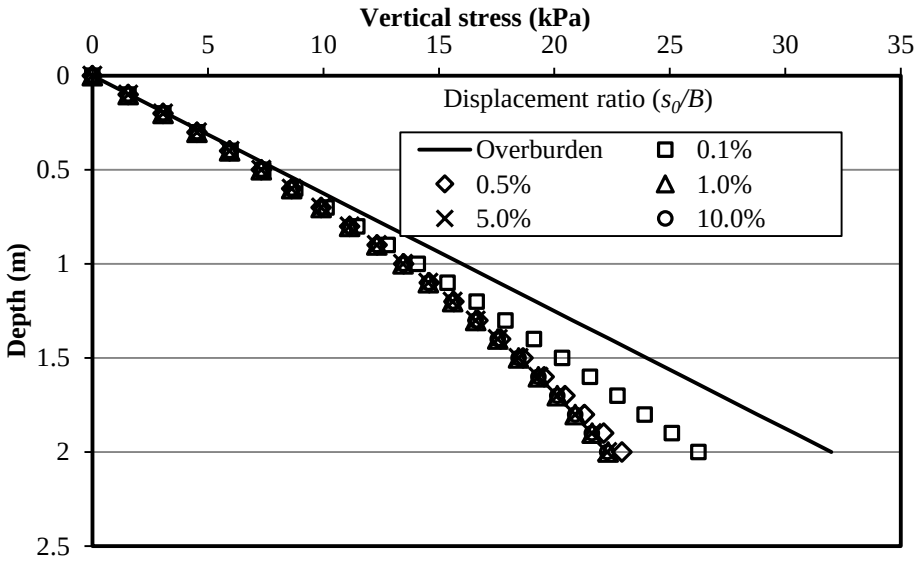

(a) H = 2 m

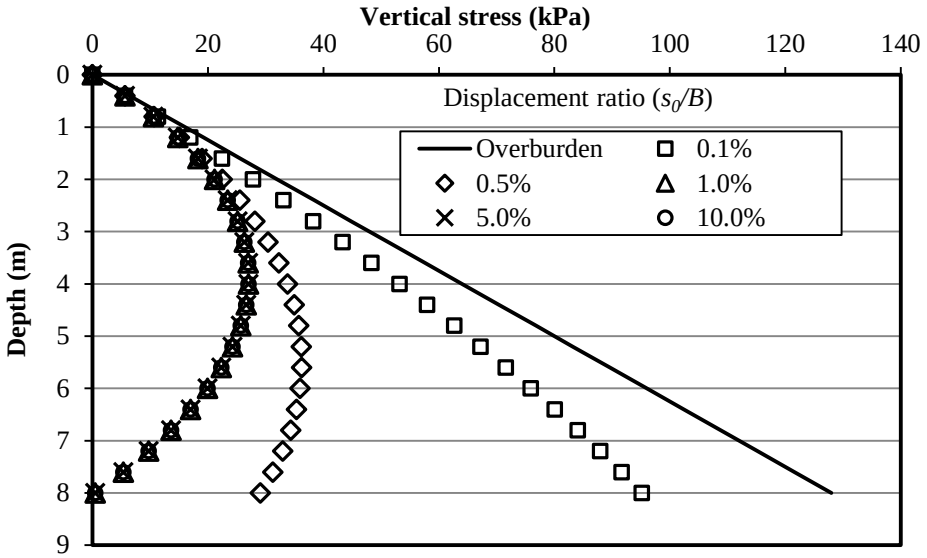

(b) H = 8 m

Figure 5.20 Variation of the vertical stress with the depth at different displacement ratio in cases with different height of the embankment

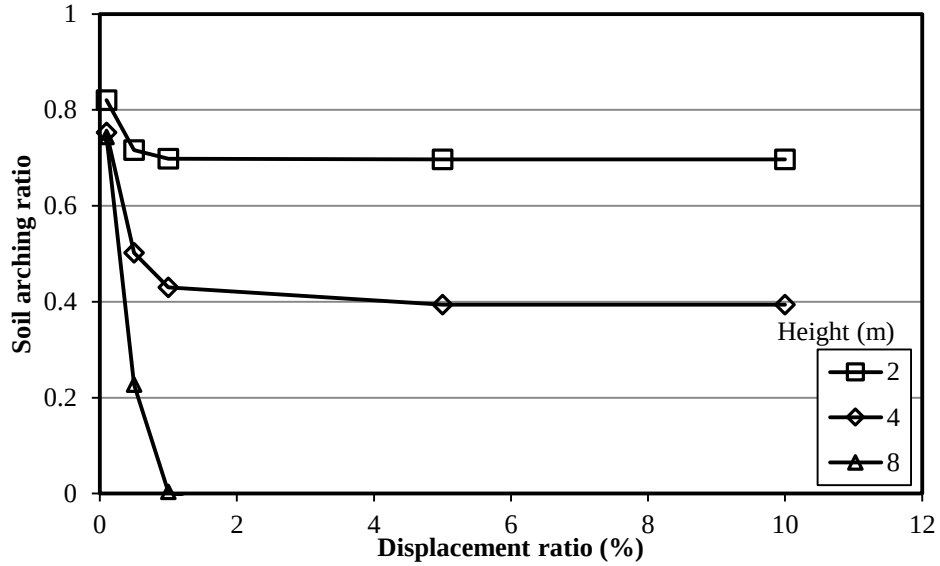

Figure 5.21 Effect of the height of the embankment on the soil arching ratio

Influence of the Surcharge at the Top of the Embankment

Figure 5.22 shows the variation of the vertical stress at different displacement ratio in the cases with different surcharge at the top of the embankment. This figure demonstrates that a bigger displacement ratio is needed to fully mobilize the soil arching with an increase of the magnitude of the surcharge. The possible reason is the higher surcharge pressure can increase the overburden stress in the embankment and the confining pressure of the backfill material which can in turn increase the shear strength and the critical displacement of the backfill material. **Figure 5.23** presents the effect of the surcharge on the soil arching ratio. Higher surcharge pressure induced higher shear strength and critical displacement of the backfill material which can reduce the soil arching ratio above the cavity.

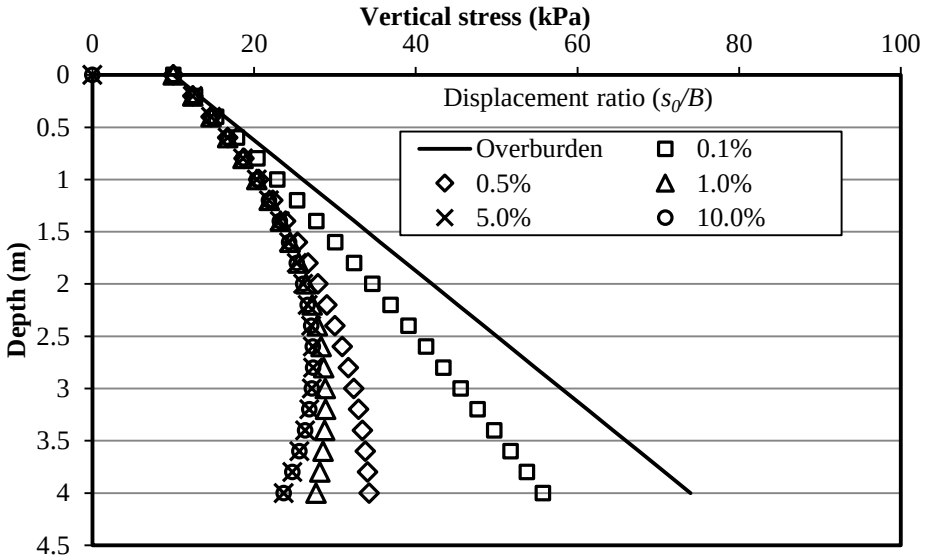

(a) 10 kPa

Figure 5.22 Variation of the vertical stress with the depth at different displacement ratio in cases with different surcharge at the top of the embankment

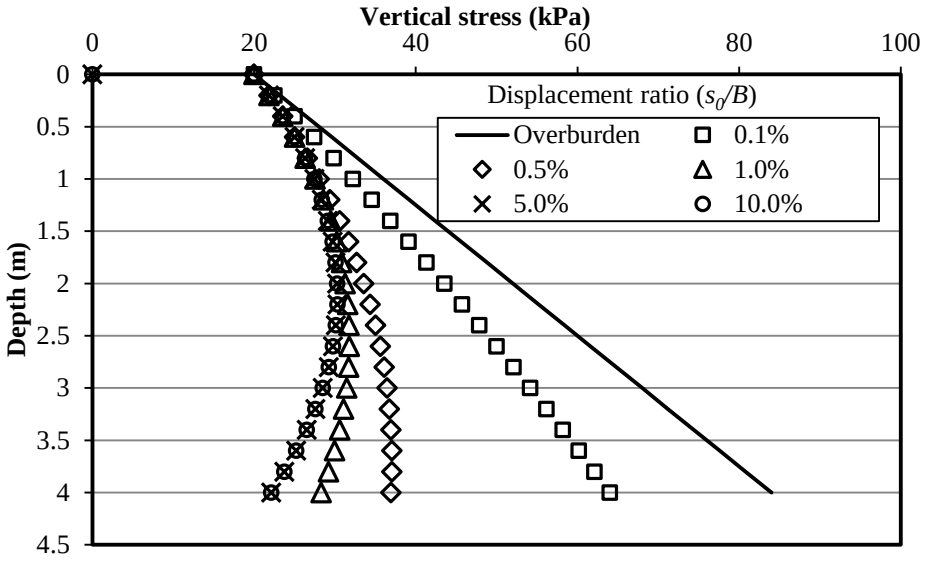

(b) 20 kPa

Figure 5.22 Variation of the vertical stress with the depth at different displacement ratio in cases with different surcharge at the top of the embankment (continued)

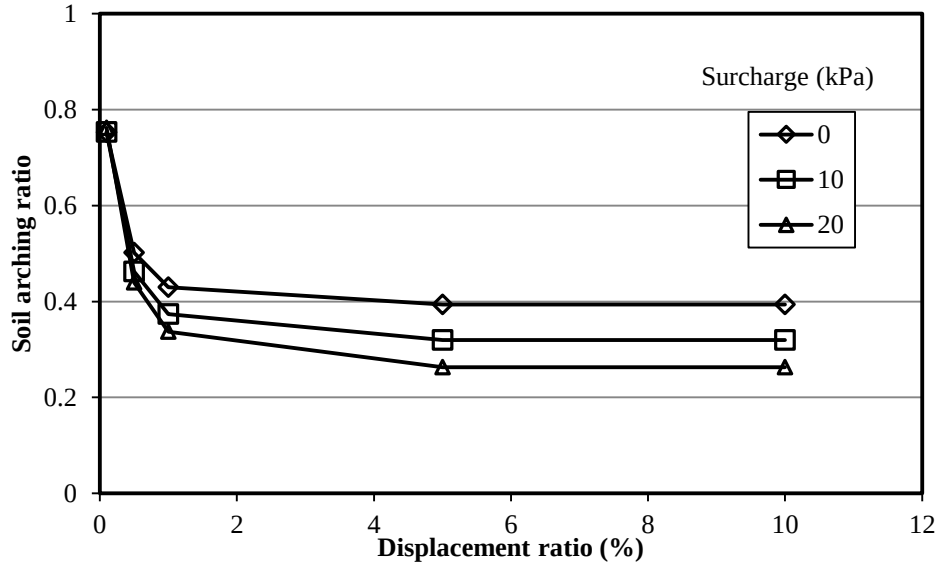

Figure 5.23 Effect of the surcharge at the top of the embankment on the soil arching ratio

Influence of the Degree of Compaction

Figure 5.24 is the variation of the vertical stress with the depth at different displacement ratio in the cases with different degree of compaction. Higher degree of compaction could result in higher elastic modulus which can decrease the critical displacement due to the dense state of the backfill material. It means that a lower displacement ratio is necessary to fully mobilize the soil arching in the embankment with a higher degree of compaction, vice versa. **Figure 5.25** shows the effect of the degree of the compaction on the soil arching ratio. Higher degree of compaction resulted in lower soil arching ratio when the soil arching in the embankment was partially mobilized, which demonstrated the importance of the sufficient compaction. However, the soil arching became approximately constant when the soil arching in the embankment was fully mobilized.

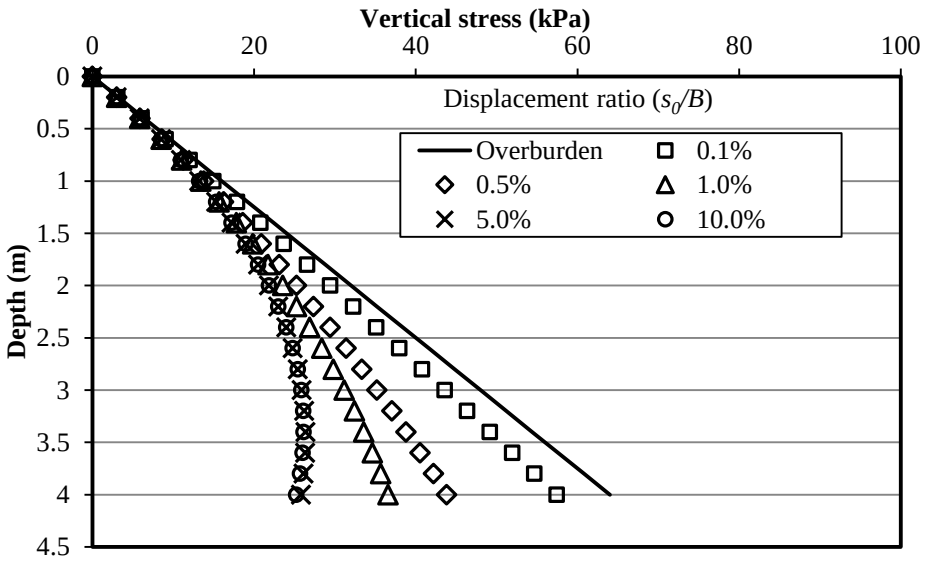

(a) 85%

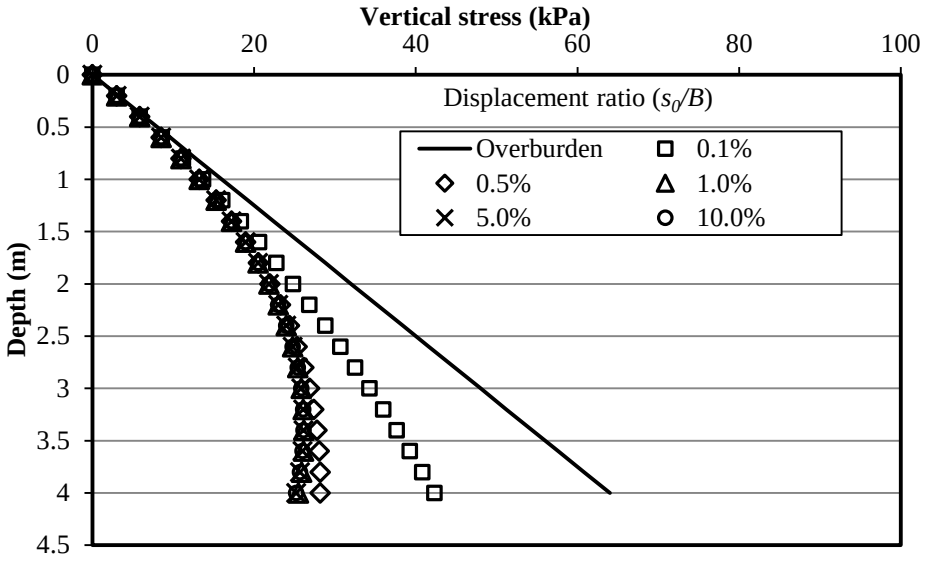

(b) 95%

Figure 5.24 Variation of the vertical stress with the depth at different displacement ratio in cases with different degree of compaction

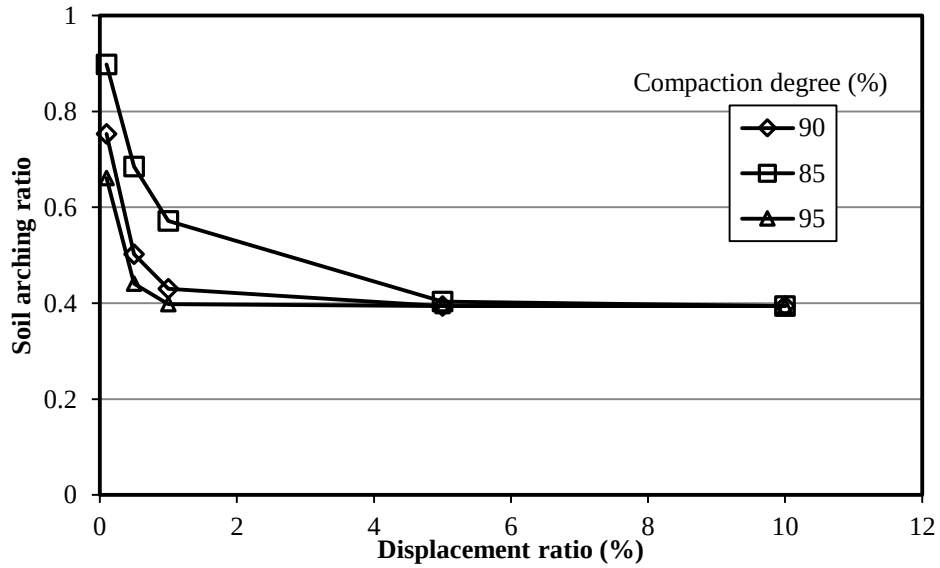

Figure 5.25 Effect of the degree of compaction on the soil arching ratio

5.3 Partially-Mobilized Soil Arching in the Soil Cover above the SRHDPE Pipe during Installation

5.3.1 Derivation Considerations

During the installation of the SRHDPE pipe, the soil arching would be caused in the soil cover due to the deflection of the pipe. Considering the relative small deflection of the SRHDPE pipe (i.e., 3 mm), the soil arching effect should be partially-mobilized soil arching. The soil arching developing process in the soil cover can be illustrated as follows: (1) when the soil is filled above the pipe, the soil load would induce pipe deflection; (2) the pipe deflection would induce the soil arching in the soil cover which can reduce the load on the top of the pipe; and (3) the deflection of the pipe would also decrease due to the decrease of the load, and in turn reduce the significance of the soil arching effect. Therefore, the soil arching developing in the soil cover should be an iteration process. An iteration should be used in the equations in Section 5.2 to calculate the load above the pipe.

5.3.2 Iteration Calculation of the Partially-Mobilized Soil Arching above the Pipe

Based on the derivation considerations, the iteration calculation can be expressed as following steps:

(1) after the first lift of the soil cover with a thickness of h_1 is placed, the pipe deflection can be calculated using **Equation (2-6)** (i.e., Iowa formula) assuming the load on the pipe is γh_1;

(2) use partially-mobilized soil arching equations to calculate the load at the pipe top. The calculated load to recalculate the pipe deflection;

(3) repeat steps (1) and (2) until the load on the pipe top and the pipe deflection become constant; and

(4) repeat steps (1), (2) and (3) with the increase of the soil cover thickness during installation until the construction is finished.

The whole procedures can be calculated by creating a spreadsheet program.

5.3.3 Calculation Example of the Iteration Process

The field test of the SRHDPE pipe in the AB3 aggregate section presented in Chapter 3 is used to illustrate the calculation of the partially-mobilized soil arching above the SRHDPE pipe. The soil cover thickness in the AB3 aggregate section was 0.64 m, which was constructed in two layers with thickness of 0.3 and 0.34 m, respectively. It has to be noted that the vertical earth pressure across the trench at the pipe top level is not uniform, and the pipe carries more soil load than the surrounding soil. **Figure 5.26** shows the vertical earth pressure distribution at the pipe top level from the numerical verification model of the AB3 aggregate section in Chapter 4. It illustrates that the vertical pressure in the pipe zone is higher than that in the sidefill. Based on the integration of the vertical pressure, the load carried by the pipe and the soil were 8.85 and 9.4 kN, respectively. The overburden load on the pipe top was 8.4 kN (i.e., 21.9 (unit weight of AB3 aggregate) x 0.6 (diameter of the pipe) x 0.64 (thickness of the soil cover) = 8.4 kN)). The VAF can be calculated as 1.06 (i.e., 8.85/ 8.4 = 1.06) which was close to that (i.e., 1.1) in both the field and the laboratory. The average vertical pressure in the trench is 12.2 kPa (i.e., (8.85 + 9.4) / 1.5 (the width of the trench) = 12.2 kPa), while the average vertical pressure at the pipe top is 14.8

kPa (i.e., 8.85 / 0.6 (the pipe diameter) = 14.8 kPa). Therefore, the vertical pressure at the pipe top is 1.21 times the average vertical pressure in the trench.

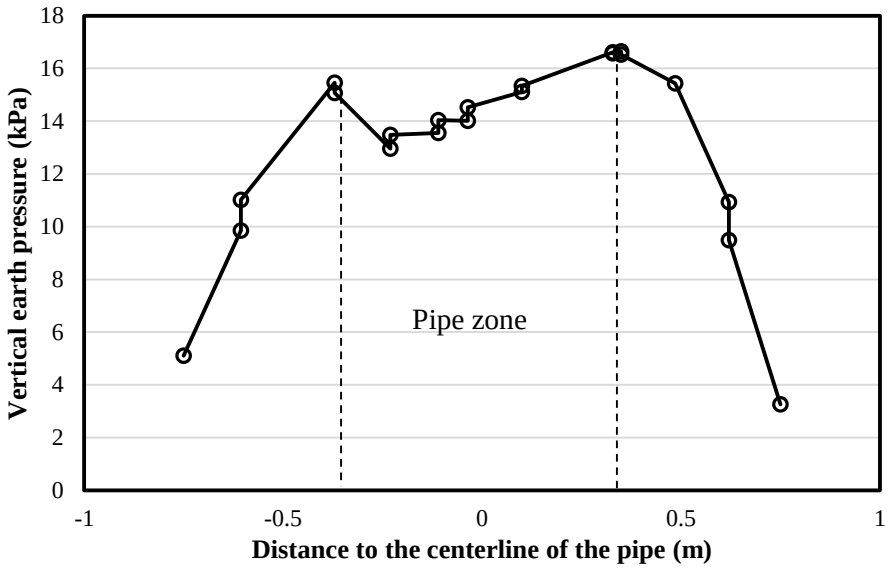

Figure 5.26 Vertical earth pressure distributions across the trench at the pipe top level

The calculated procedures can be expressed as follows:

(1) calculate the initial pipe deflection due to the weight of the first layer soil (i.e., 0.3 m thick soil on the pipe top) using the Iowa Formula as:

$$S_0 = \frac{D_L K W_c r^3}{EI + 0.061 e r^3} = \frac{1.0 \times 0.11 \times 0.3 \times 1.21 \times 21.9 \times 0.3^3}{0.149 \times 294 \times 0.3^3 + 0.061 \times 23556 \times 0.3^3} = 0.35\,\text{mm} \quad (5\text{-}8)$$

where $W_c = 1.21\gamma h_1 = 0.3 \times 21.9 \times 1.21 = 4.77 kN$;

(2) assume S_0 = 0.35 mm, calculating the vertical pressure at the pipe top using the partially-mobilized soil arching equations (i.e., **Equations (5-5) and (5-6)**). The parameters in the equations are summarized in **Table 5.4**. The elastic modulus was determined using **Figure 5.9** with the degree of compaction of 90%.

Table 5.4 Summary of calculation parameters for the AB3 aggregate section

Parameter	γ (kN/m^3)	ϕ(^{o})	B (m)	H (m)	k_i	n
Value	21.9	45	0.6	0.3	350	0.5

(3) use the vertical pressure calculated in step (2) times 1.21 as the vertical pressure at the pipe top to determine the pipe deflection with **Equation (5-8)**. The updated deflection was adopted to calculate the vertical stress using the partially-mobilized soil arching equations;

(4) repeat steps (3), until the error in the pipe deflection can be ignored;

(5) repeat steps (1-4) for the second layer of backfill material.

From the calculation, the pipe deflections after the first and second layers placed were 0.34 and 0.71 mm; while the vertical earth pressures at the pipe top after the first and second layers placed were 7.7 and 15.8 kPa. The measured results from the field test were 0.12 and 1.08 mm for the pipe deflections, and 5.4 and 17.6 kPa for the vertical earth pressures at the pipe top.

From the comparisons, the proposed method is effective to investigate the pipe performance during the installation.

5.4 Partially-Mobilized Soil Arching in the Soil Cover above the SRHDPE Pipe under Traffic Loading

SRHDPE pipes should be mainly used in highway and railway projects. The normal external load after the construction is the traffic loading. Considering the relative higher stiffness of the SRHDPE pipe, partially-mobilized soil arching under traffic loading should be adopted. However, no method is available for the soil arching calculation under traffic loading. Some

researchers did experimental and numerical studies to investigate the soil arching under traffic or dynamic loading. Chen et al. (1990) developed a small scale laboratory test equipment to investigate the soil arching under dynamic loading. The low velocity of impact load applied to simulate the dynamic loading; at the same time, the dynamic earth pressure caused by the impact load above the buried structure was measured. Helwany and Chowdhury (2011) developed a method to determine the lateral earth pressure on buried structures caused by a dynamic load. Han et al. (2014) used lab-scale model test and numerical method to investigate the soil arching effect in the pile-supported embankment under dynamic loading. They found out that the existing soil arch could be damaged by the dynamic load when the ratio of the embankment height to the pile clear spacing was less than three. Bhandari (2010) investigated the soil arching effect under the dynamic load in pile-supported embankments using DEM method. Partially-mobilized soil arching under traffic loading is necessary to reveal the load transfer mechanism in the soil cover above the SRHDPE pipe under traffic loading.

5.4.1 Derivation Considerations

To derive the partially-mobilized soil arching under traffic loading, the following problems have to be solved:

(1) how to consider the combined effect of the traffic loading and the "trap door" behavior (i.e., the settlement at the pipe top induced by the pipe deflection);

(2) the additional load on the pipe top induced by the traffic loading and the variation of the additional load with the number of passes of axle; and

(3) three-dimensional effect of the pipe under the traffic loading.

5.4.2 Derivation of the Partially-Developed Soil Arching Equations under Traffic Loading

Combined Effect of the Traffic Loading and "Trap Door" Behavior

Getzler et al. (1970) conducted a finite difference analysis of plane strain trap door problem under traffic loading. They simplified the numerical model as the superposition of two models, which included the surcharge model without the trap door and the trap door model without the surcharge. They verified the effectiveness of the simplified model. The same model was adopted in this research. The SRHDPE pipe model under the traffic loading was simplified as model A with traffic loading at the top and model B only with the pipe deflection at the pipe top as shown in **Figure 5.27.** The additional stress at the pipe top level was calculated from Model A, and then the pipe deflection can be determined from the additional load. Based on the pipe deflection, the soil arching developed in the backfill can be calculated from Model B.

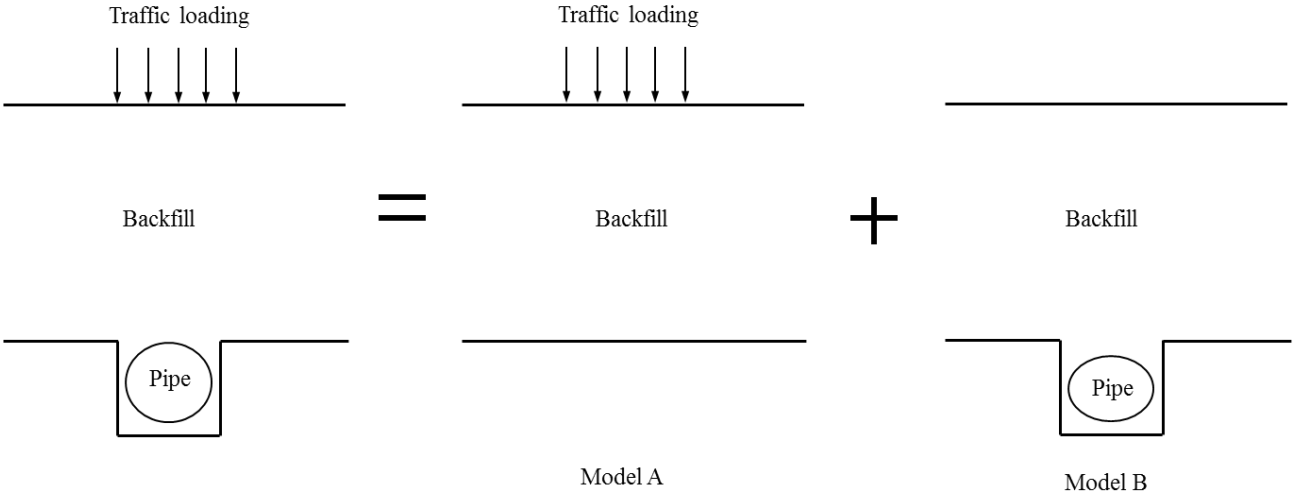

Figure 5.27 Schematic of the simplified model for the SRHDPE pipe under traffic loading

Calculation of Additional Load at the Pipe Top

Giroud and Han (2004) proposed a formula to calculate the stress distribution angle with the number of passes of axle as:

$$\frac{1}{\tan\alpha} = \frac{1.26 + 0.96\left(\frac{r}{H}\right)^{1.5} \log N}{1 + 0.204\left(R_E - 1\right)} \tag{5-9}$$

where α = the stress distribution angle in the soil cover; r = the radius of the equivalent tire contact area. AASHTO (2012) specified that the contact area for the H-25 truck is 0.13 m^2 (i.e., 0.51 m in length and 0.25 m in width) and the radius of the equivalent tire contact area is 0.20 m; H = the thickness of the soil cover; R_E = the modulus ratio of the soils, which can be assumed as 1.0 for the soil cover of the pipe; and N = the number of the passes of axle.

Based on **Equation (5-9)**, the stress distribution angle can be calculated with the thickness of the soil cover at different number of the passes of axle as shown in **Figure 5.28**. This figure illustrates that the stress distribution angle decreases with an increase of the number of the passes of axle, and the magnitude of reduction in the stress distribution angle with an increase of the number of the passes of axle is more significant when the soil cover is relative thin.

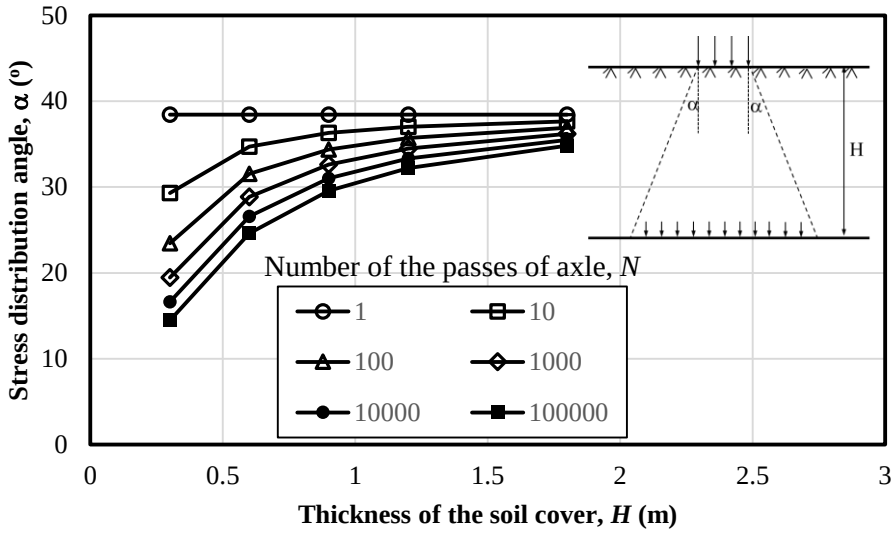

Figure 5.28 Stress distribution angle with the thickness of the soil cover at different number of the passes of axle

The additional pressure at the pipe top is expressed as follows:

$$p = \frac{P}{\pi\left(r + H\tan\alpha\right)^2} \tag{5-10}$$

where p = the additional pressure at the pipe top; P = the wheel load; H = the soil cover thickness; r = the radius of the equivalent tire contact area; and α = the stress distribution angle in the soil cover.

Three-Dimensional Effect of the SRHDPE Pipe under the Traffic Loading

The three-dimensional effect includes (1) the overlap of the additional load at the pipe top induced by traffic loads from two axles as shown in **Figure 5.29**; and (2) the pipe deflection difference in the longitudinal direction as shown in **Figure 5.30**. **Figure 5.29** shows that two wheels of the truck can cause stress overlap area on the top of the pipe, the overlap area depends on the stress distribution angle α and the spacing of the two wheels S_w. The worst case scenario

is some part of the pipe subjected to the overlap distributed pressure at the level of the pipe top which is two times of the distributed pressure. Therefore, the additional vertical pressure induced by the traffic loading in the calculation at the pipe top level should be two times of the additional pressure calculated by **Equation (5-10)**. **Figure 5.30** presents the schematic of the deformation in the longitudinal direction induced by the pipe deflection difference. From the field test results, the pipe strain in the longitudinal direction was more critical than strains in other directions. From **Figure 5.30**, the additional strain of the pipe in the longitudinal direction can be calculated as:

$$\varepsilon = \frac{\sqrt{L^2 + \Delta y^2} - L}{L} \tag{5-11}$$

where ε = the strain of the pipe in the longitudinal direction; L = half of the length of the distributed area of the additional stress; and Δy = the maximum pipe deflection under the traffic loading.

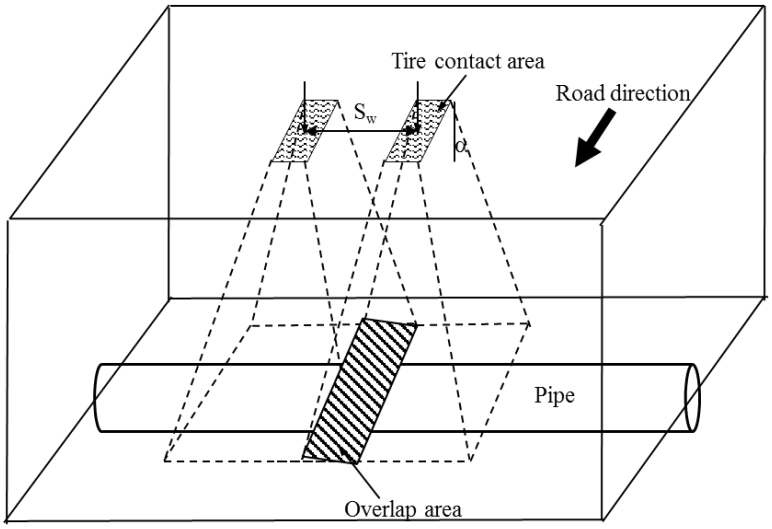

Figure 5.29 Schematic of the stress overlap above the pipe

The additional stress of the pipe in the longitudinal direction can be calculated using the strain determined by **Equation (5-11)** times the elastic modulus of the pipe in the longitudinal

direction. Since the SRHDPE pipe is a composite pipe including steel and HDPE, the elastic modulus of the pipe in the longitudinal direction has to be determined from the tests in the laboratory.

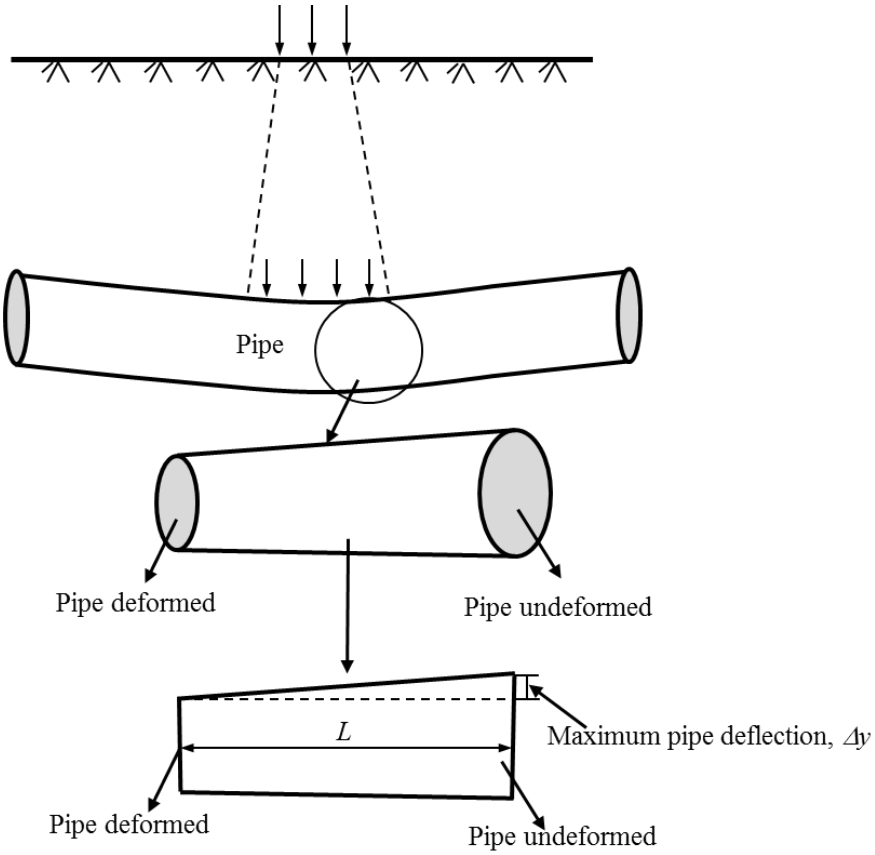

Figure 5.30 Schematic of the pipe deflection difference in the longitudinal direction

The SRHDPE pipe with a diameter of 0.6 m and a length of 1.0 m was compressed by a vertical load in a rate of 12.5 mm/min. **Figure 5.31** shows the photograph of the pipe during the compression test. **Figure 5.32** presents the pipe compression test results. In the longitudinal direction, the pipe behaves elastic first and yields due to the yield of the HDPE material when the deformation is greater than 2% of the pipe length. The elastic modulus of the SRHDPE pipe in the longitudinal direction is approximately 190 MPa from the test results.

Figure 5.31 Photograph of the pipe compression test

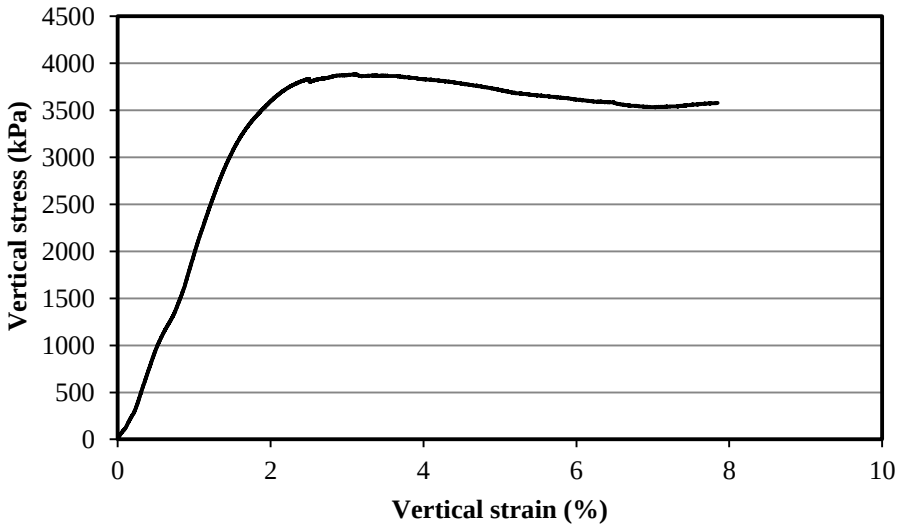

Figure 5.32 Test result of the pipe compression test

Calculation Procedures of the Partially-Developed Soil Arching in the Soil Cover under the Traffic Loading

Based on the description in this section, the partially-mobilized soil arching in the soil cover under the traffic loading was proposed as follows:

(1) determine the stress distribution angle based on the soil cover thickness and the number of the passes of axle by **Figure 5.28** and calculate the additional pressure on the top of the pipe using **Equation (5-10)**; if stress overlap exists; use the two times of the calculated pressure through **Equation (5-10)**;

(2) calculate the pipe deflection under the additional pressure calculated in step 1 by **Equation (2-6),**

(3) use partially-mobilized soil arching equations to calculate the load at the pipe top. The calculated load to recalculate the pipe deflection; and

(4) repeat steps (2) and (3) until the load on the pipe top and the pipe deflection become constant.

Calculation Example

Example problem: A SRHDPE pipe with a diameter of 0.6 m was installed in a 1.2 m wide trench which was filled with AB3 aggregate which has the unit weight of 21.9 kN/m^3 and the friction angle of 45^o. The elastic modulus of the pipe in the longitudinal direction is 190 MPa. The soil cover thickness was 0.6 m, while the degree of the compaction was 90%. The traffic load was induced by AASHTO H-25 truck. Determine (1) the vertical earth pressure at the

pipe top; (2) the pipe deflection; and (3) the additional stress and strain due to the traffic loading with the number of the passes of 1, 100, 10,000, and 100, 000.

Solution:

Since the truck is AASHTO h-25, the center to center spacing of the two wheels is 2.0 m. Based on the stress distribution calculation, there is no stress overlap at the pipe top level.

(1) the stress distribution angles and the additional earth pressure at the pipe top can be determined as tabulated in **Table 5.5**.

Table 5.5 Stress distribution angles and the additional earth pressure at the pipe top

N	1	100	10,000	100,000
α (°)	38.4	31.5	26.6	24.6
p (kPa)	62.1	87.9	113.1	129.6

(2) the pipe deflection under two time of the additional pressure calculated in step (1) can be determined as shown in **Table 5.6**.

Table 5.6 Pipe deflection in step (2)

N	1	100	10,000	100,000
Δy (mm)	3.3	4.7	6.1	7.0

(3) use the partially-developed soil arching equations to calculate the pipe deflection and vertical earth pressure at the pipe top through an iteration process, which is shown in **Figure 5.33**. This figure illustrates the pipe deflection and the vertical earth pressures are both linearly increase with the number of the passes in a semi-log plot. **Figure 5.34**

presents the vertical pressure along the depth at different number of the passes, which demonstrates the vertical pressure at a specific depth increases with an increase of the number of the passes.

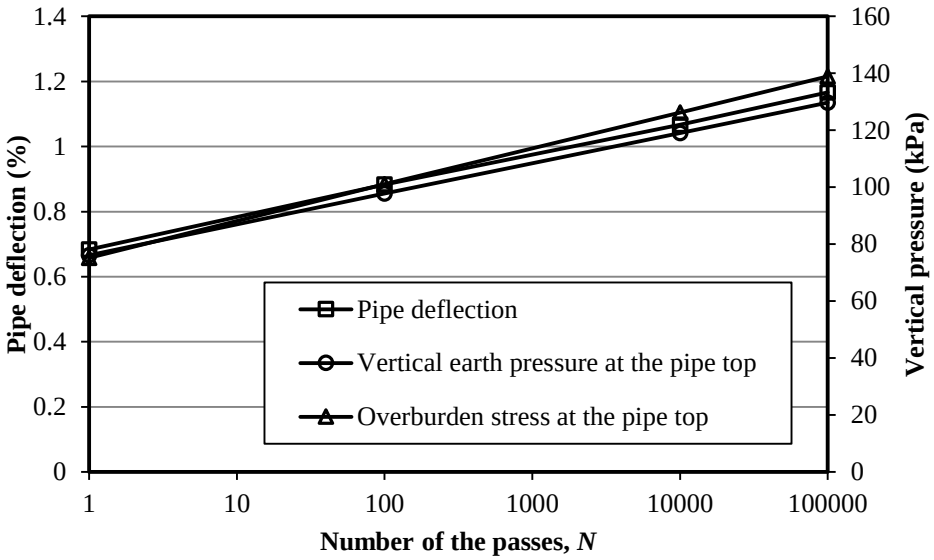

Figure 5.33 The pipe deflection and the vertical pressure at the pipe top with different number of the passes

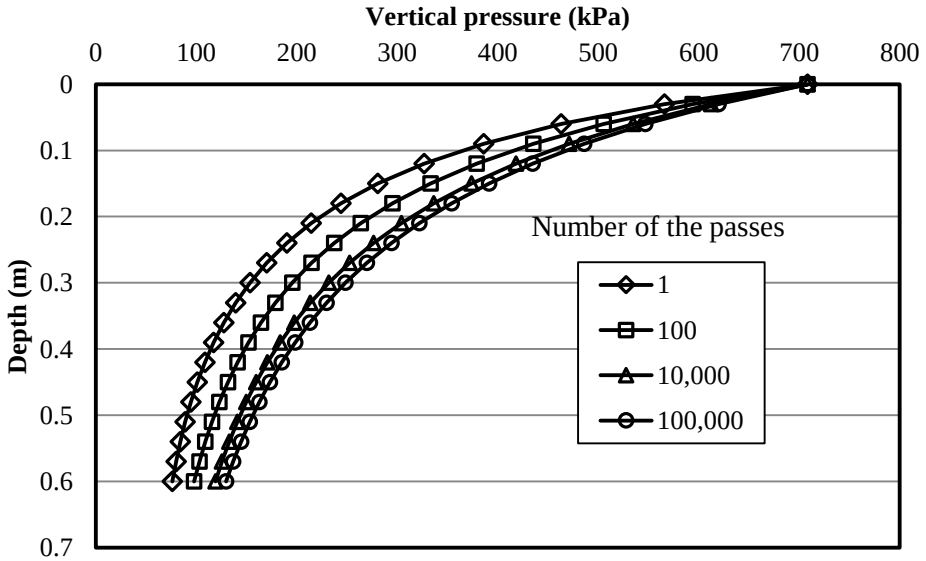

Figure 5.34 Vertical pressures along the depth at different number of the passes

(4) **Table 5.7** shows the calculation of the additional strain and stress of the pipe in the longitudinal direction induced by the traffic loading. This table demonstrates that the additional stress and strain both increase with an increase of the number of the passes.

Table 5.7 Calculation of the additional strain and stress of the pipe in the longitudinal direction induced by the traffic loading

N	α	$\tan\alpha$	L (m)	Δy (mm)	ε (%)	σ_a (kPa)
1	38.4	0.79	0.60	4.1	0.0023	4.40
100	31.5	0.61	0.49	5.3	0.0057	10.90
10,000	26.6	0.50	0.43	6.4	0.0112	21.29
100,000	24.6	0.46	0.40	7.5	0.0174	33.11

5.5 Summary

Considering the relative high stiffness of the SRHDPE pipe, the partially-mobilized soil arching equations under the uniformly-distributed static loading and traffic loading were developed. The following conclusions can be drawn from the research of this chapter:

(1) Partially-mobilized soil arching equations were derived with the consideration of the coupled effect of the relative displacement and the shear stress at the interface of the mobilized and stable portions. Two case histories from the literature were used to verify the effectiveness of the proposed equations;

(2) Sensitivity of the parameters in the partially-mobilized soil arching equations was conducted. The results indicated that the effects of the unit weight and the friction angle of the backfill were insignificant; while the effects of the cavity width, the embankment height, the surcharge and the degree of compaction were significant;

(3) The partially-mobilized soil arching equations were used to calculate the soil arching effect in the soil cover above the SRHDPE pipe during installation. A calculation example was provided to illustrate the procedures; and

(4) The partially-mobilized soil arching equations were also used to develop the soil arching equations in the soil cover above the SRHDPE pipe under traffic loading. An example was given to show the calculation details.

CHAPTER 6 EVALUATION OF THE LONG-TERM PERFORMANCE OF THE SRHDPE PIPE

6.1 Introduction

As discussed in Chapter two, the long-term behavior of the HDPE pipe is different from that in the short-term due to the creep and degradation of the pipe material (i.e., HDPE) with time. The reduction of the stiffness of the pipe material in a long-term condition has been included in the calculation of the pipe deflection (AASHTO, 2012). Even though most of the load above the SRHDPE pipe is carried by the steel ribs, the plastic valley of the pipe shares some load, which may control the design. Therefore, the creep and degradation of the HDPE material may influence the long-term performance of the SRHDPE pipe. It is necessary to investigate the SRHDPE pipe performance in a long-term condition. The SRHDPE pipes installed in a field test in Lawrence, KS reported in Han et al. (2015) were monitored continuously for 22 months. The observation data include the earth pressures around the pipe, the pipe deflections, and the strains of the steel ribs, the plastic cover, and the plastic valley. This chapter evaluates the changes of the pipe stiffness, the load above the pipe, and the strains of the pipe developed with time.

6.2 Brief Description of the Field Test

The field test was located on E 1000 Road in Lawrence, KS. The test sections had a rectangular trench of 2 m wide and 1.72 m. deep. The total length of the trench was 24 m long. Half length of the trench was backfilled with AB3 aggregate and the other half was backfilled with crushed stone. The trench consisted of 0.15 m thick bedding material, 1m thick backfill, and 1 m thick soil cover. Three pipes with the length of 8 m were installed in the trench. The dimeter of

the pipes was 0.9 m. For the Section A (i.e., the AB3 aggregate section), the pipe was instrumented as Sections 1 and 2, whereas for the Section B (i.e., the crushed stone section), the pipe was instrumented as Sections 3 and 4. Section 2 in the Section A and Section 3 in the Section B were instrumented under the traffic wheel paths close to the centerline of the roadway. Sections 2 and 3 were instrumented extensively to capture deflections using displacement transducers, strains on pipes using strain gages, and earth pressures around the pipe using vibrating wire type pressure cells. In addition, Sections 1 and 4, which were close to the shoulder, had only one vibrating wire pressure cell installed at the crown of the pipe under each path. **Figure 6.1** shows the strain gauges distribution in the field test. **Figure 6.2** presents the earth pressure cells installation in the test sections. Four displacement transducers were installed in Sections 2 and 3 in horizontal and vertical directions respectively (i.e., two displacement transducers in each section) to measure the pipe deflection. Detail information can be found in Han et al. (2015).

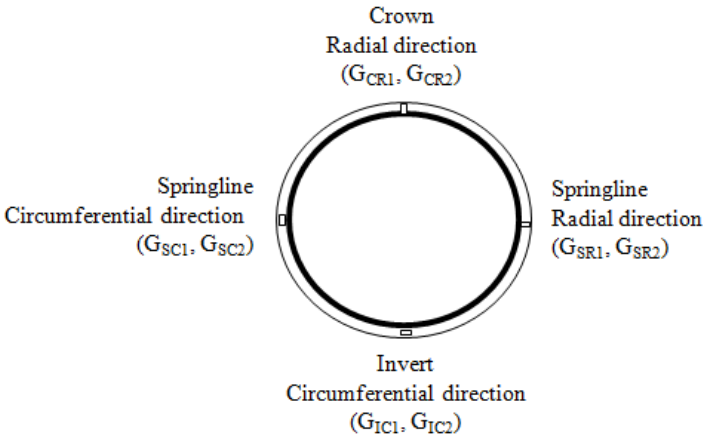

(a) On the steel at ribs

Figure 6.1 Symbols, locations, and orientations of the strain gages on the pipe

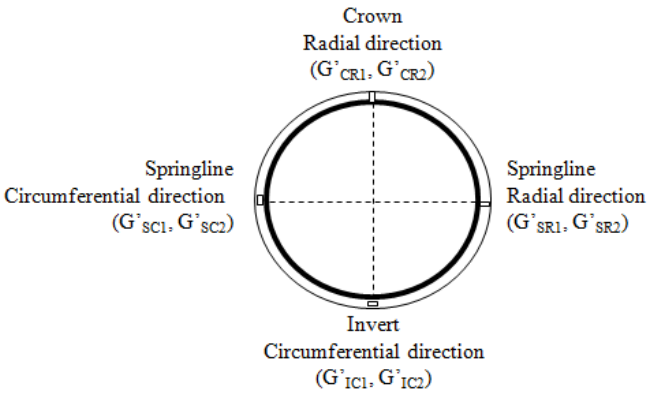

(b) On the plastic at ribs

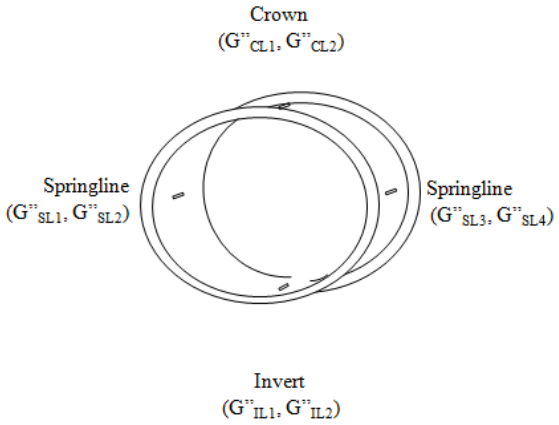

(c) In the longitudinal direction on the plastic at valley

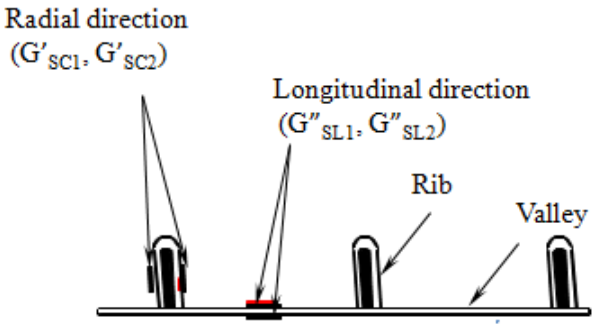

(d) Strain gages on the plastic surface

Figure 6.1 Symbols, locations, and orientations of the strain gages on the pipe (continued)

(Han et al. (2015))

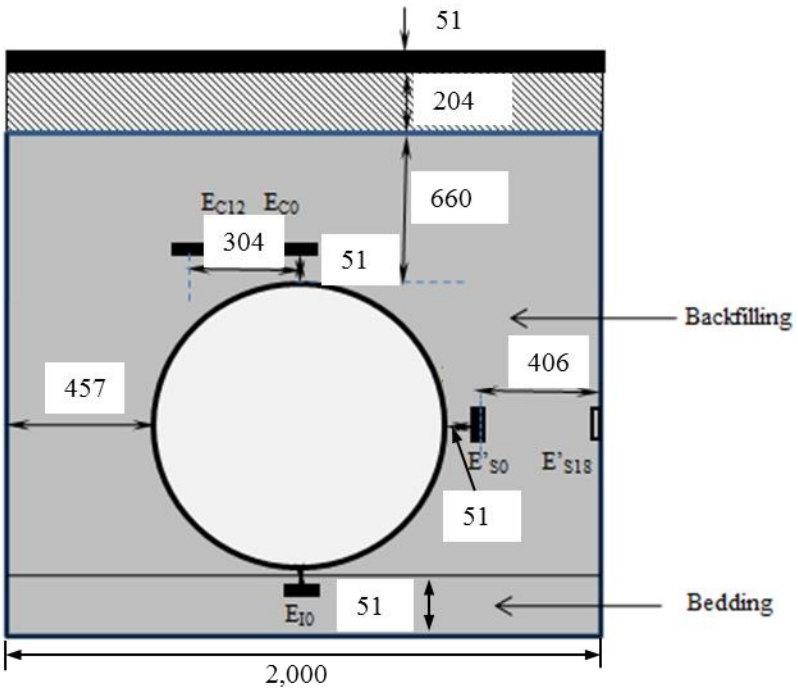

Figure 6.2 Earth pressure installation in the test sections (unit: mm Not to Scale)

6.3 Data Analysis

6.3.1 Earth Pressure

Temperature Correction Procedures of the Measured Earth Pressure

Figure 6.3 shows the vertical earth pressures at the pipe crown in the crushed stone section at a distance of 2.8 m from the roadway centerline. This figure shows that the earth pressure varied with the temperature. To eliminate temperature effect on the variations of earth pressures with time, the earth pressures should be presented at the same temperature. Therefore, all the measured earth pressure must be corrected.

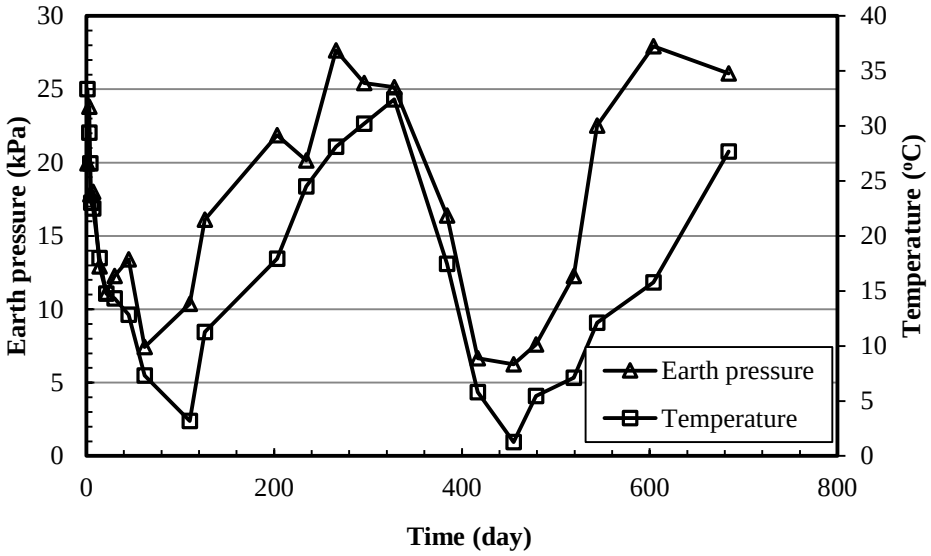

Figure 6.3 Measured vertical earth pressure and temperature at the pipe crown in the crushed stone section at a distance of 2.8 m

Geokon total pressure cells 4810-350KPA were used in the field test to measure the earth pressures around the pipes. The manufacturer provided the temperature correction method as follows (Geokon, 2011):

$$\sigma_C = \sigma_M + C(T - T_0) \tag{6-1}$$

where σ_C = the corrected earth pressure; σ_M = the measured earth pressure; C = the temperature correction factor, which can be determined by **Equation (6-2)**; T = the temperature; and T_0 = the initial temperature.

$$C = \frac{3EKD}{R} \tag{6-2}$$

where E = the elastic modulus of the surrounding medium (23.5 MPa for the AB3 aggregate and 20.1 MPa for the crushed stone); K = the thermal expansion coefficient of the oil film in the

pressure cell (0.000792/C^{o}); D = the thickness of the oil film in the pressure cell (1.52 mm for the Geokon total pressure cell); and R = the radius of the pressure cell (114 mm for the Geokon total pressure cell). Based on **Equation (6-2)**, the temperature correction factor C for the AB3 aggregate is 0.63 and that for the crushed stone is 0.58.

Test Section A

Figure 6.4 shows the measured and the corrected vertical earth pressure with time at the pipe crown in Section A. The vertical earth pressure at the pipe crown in Section A slightly increased with the time. The vertical earth pressure after 680 days of the construction was approximately 34.5 kPa. The vertical soil arching factor (VAF) was approximately 1.57 (overburden stress = 21.9 × 1 = 21.9 kPa).

Figure 6.5 shows the measured and corrected lateral earth pressures at the pipe springline in Section A. The lateral earth pressure at the pipe springline increased to 20 kPa within 680 days after the construction. Since there is no measured vertical earth pressure at the pipe springline, the lateral earth pressure coefficient was calculated as 0.72 using the theoretical overburden stress at the springline (K = 20 / (21.9 x 1.27) = 0.72). The lateral earth pressure coefficient at the pipe springline in Section A was much higher than K_0 (i.e., 0.209).

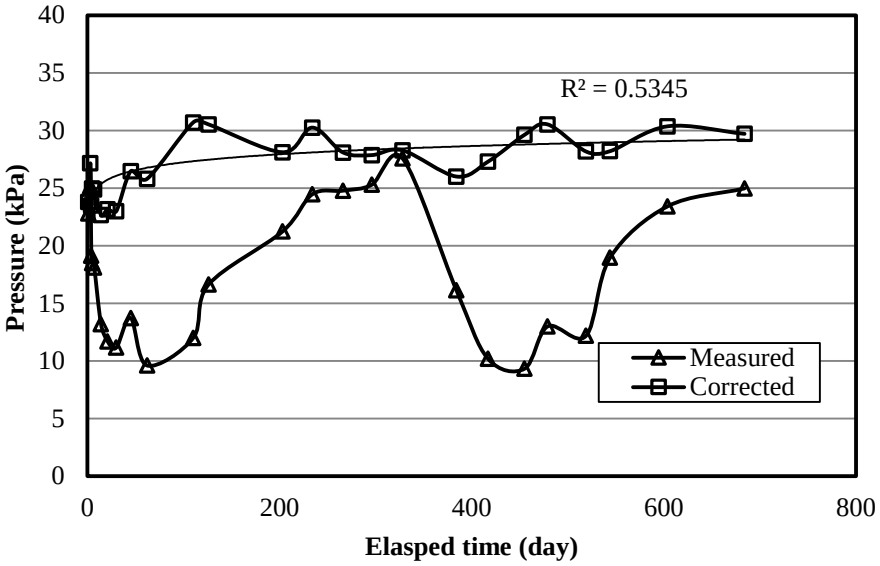

(a) 0.96 m from the roadway centerline

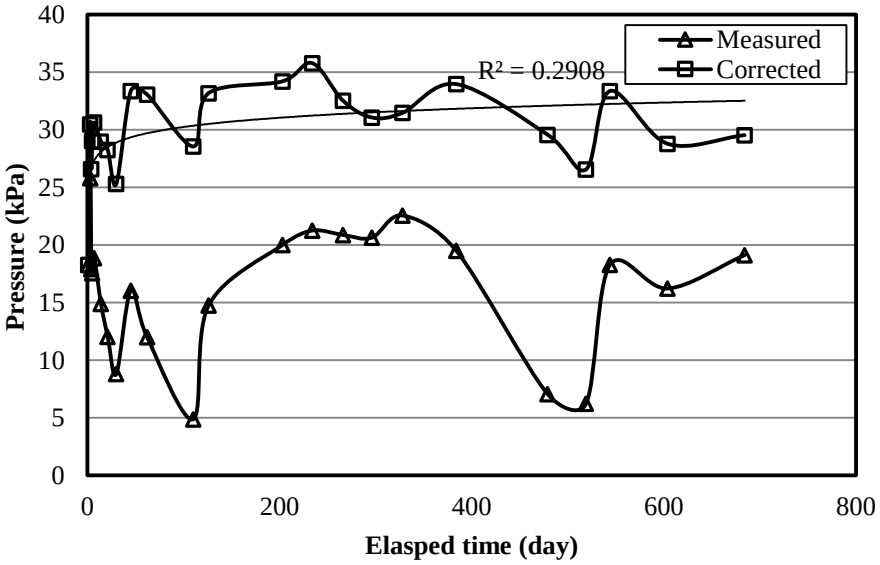

(b) 3.6 m from the roadway centerline

Figure 6.4 Corrected vertical earth pressure at the pipe crown in Section A

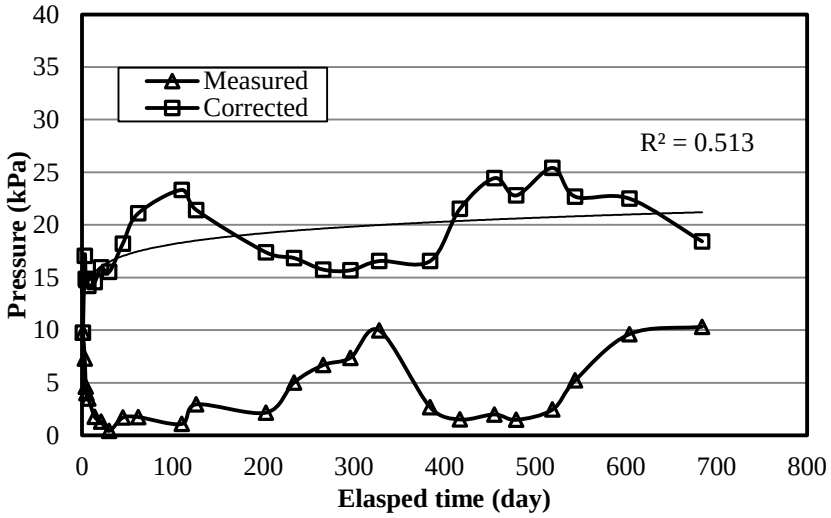

Figure 6.5 Corrected lateral earth pressure at the pipe springline in Section A

Figure 6.6 shows the measured and corrected vertical earth pressures at the shoulder in Section A. This figure also shows the corrected vertical earth pressure at the shoulder increased with the time and was approximately 31.8 kPa at within 680 days, i.e., the VAF at the shoulder was equal to 1.84.

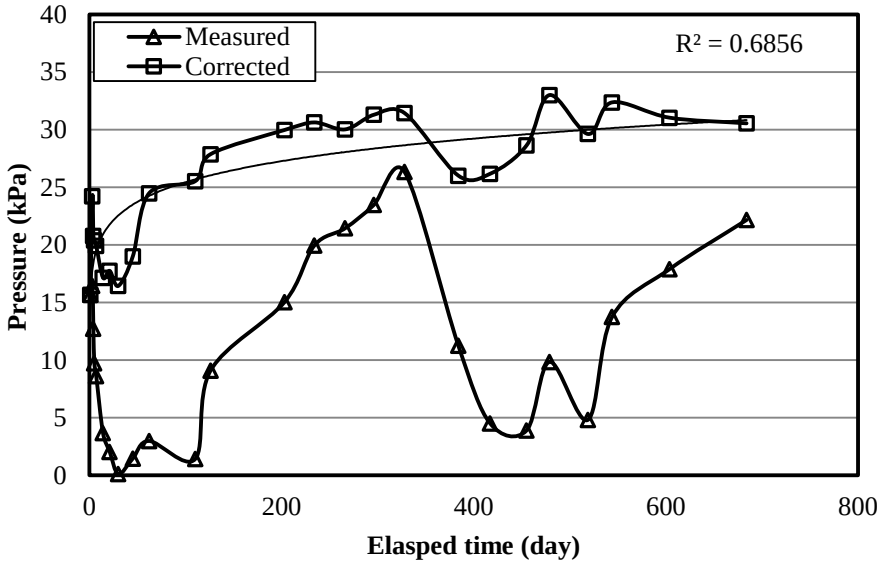

Figure 6.6 Corrected vertical earth pressure at the shoulder in Section A

Figure 6.7 shows the measured and corrected lateral earth pressures at the trench wall. The corrected lateral earth pressure at the trench wall was almost constant as 20 kPa, indicating the long-term effect on the trench wall was insignificant.

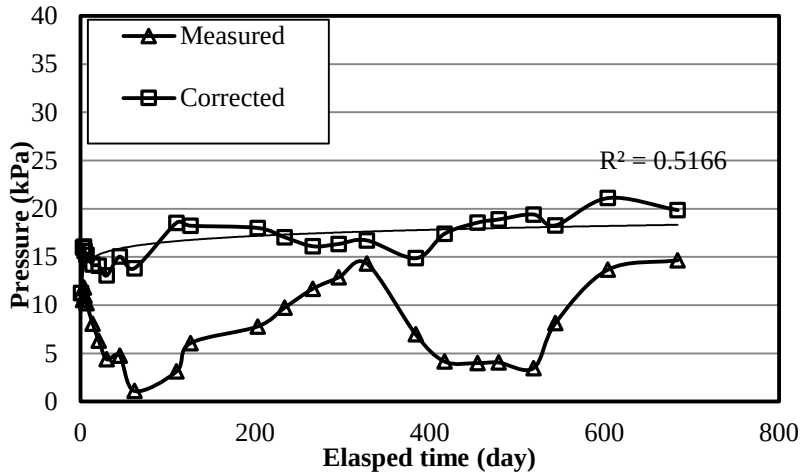

Figure 6.7 Corrected lateral earth pressure at the trench wall at the pipe springline level in Section A

Figure 6.8 shows the vertical earth pressures at the pipe invert. The corrected vertical earth pressure was approximately 32.4 kPa at the end of the monitoring.

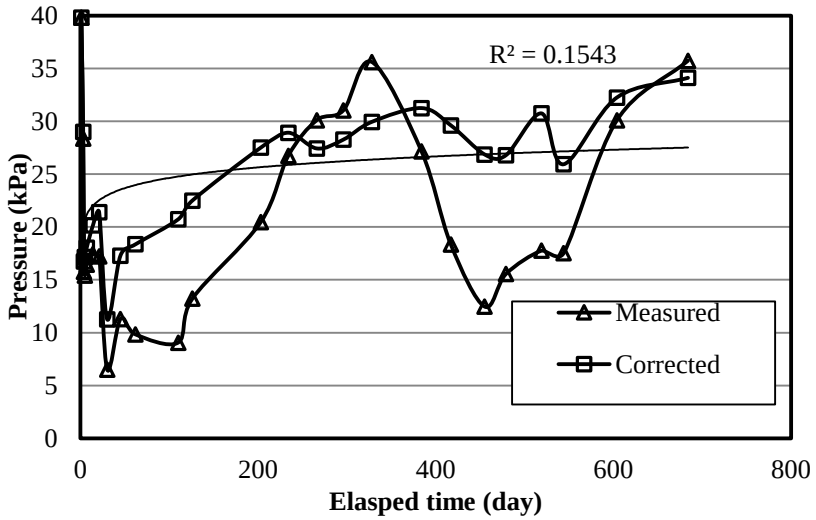

Figure 6.8 Corrected vertical earth pressure at the pipe invert in the Section A

Test Section B

Figure 6.9 shows the measured and the corrected earth pressures with the time at the pipe crown in Section B. The earth pressure at the pipe crown increased with the time. The earth pressure after 680 days of the construction was approximately 31 kPa. The vertical soil arching factor (VAF) was approximately 1.98 (overburden stress = 15.6 × 1.0 = 15.6 kPa). The VAF in the Section A was lower than that in Section B. The load carried by the pipe in Section A (the AB3 aggregate section) was higher than that in Section B (the crushed stone section) due to the higher unit weight of the AB3 aggregate than the crushed stone. **Figure 6.10** shows the measured and corrected lateral earth pressures at the pipe springline in Section B. The corrected lateral earth pressure at the pipe springline increased to approximately 27.6 kPa at 680 days after the construction. Since there was no measured vertical earth pressure at the pipe springline, the lateral earth pressure coefficient was calculated as 1.39 based on the theoretical overburden stress at the springline (K = 27.6 / (15.6 x 1.27) = 1.39).

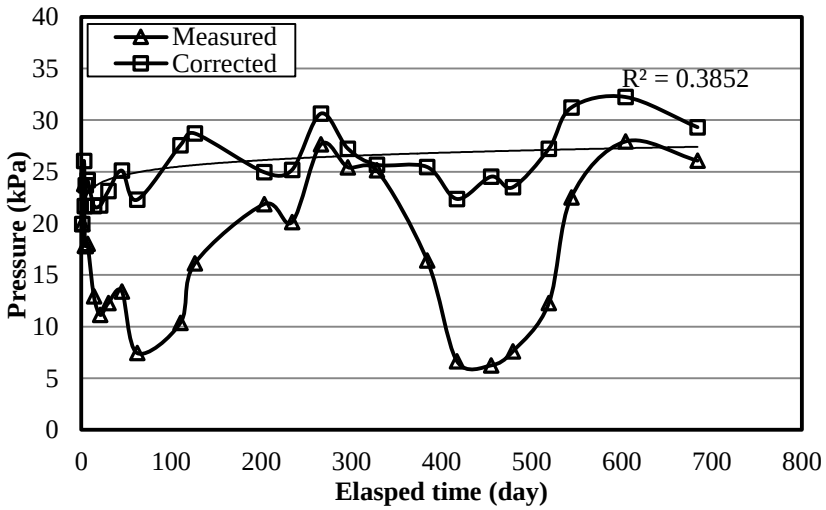

(a) 0.96 m from the roadway centerline

Figure 6.9 Corrected vertical earth pressure at the pipe crown in Section

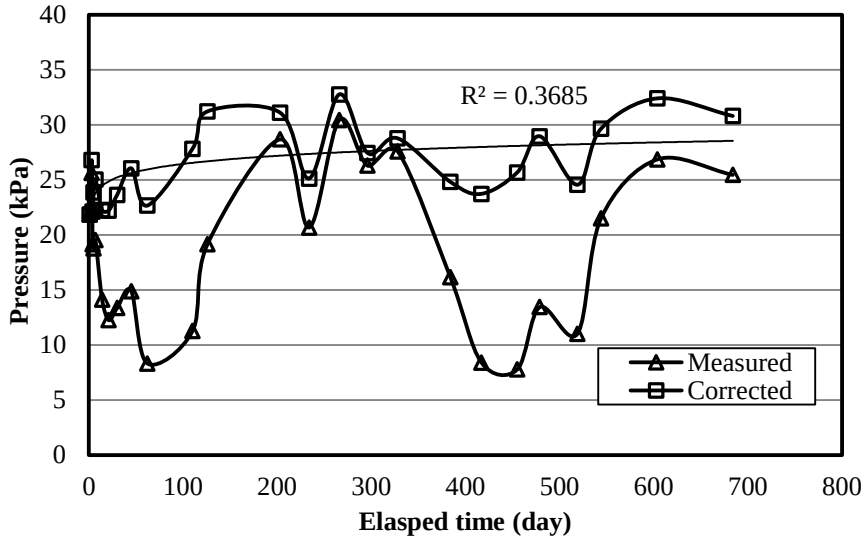

(b) 3.6 m from the roadway centerline

Figure 6.9 Corrected vertical earth pressure at the pipe crown in Section B (continued)

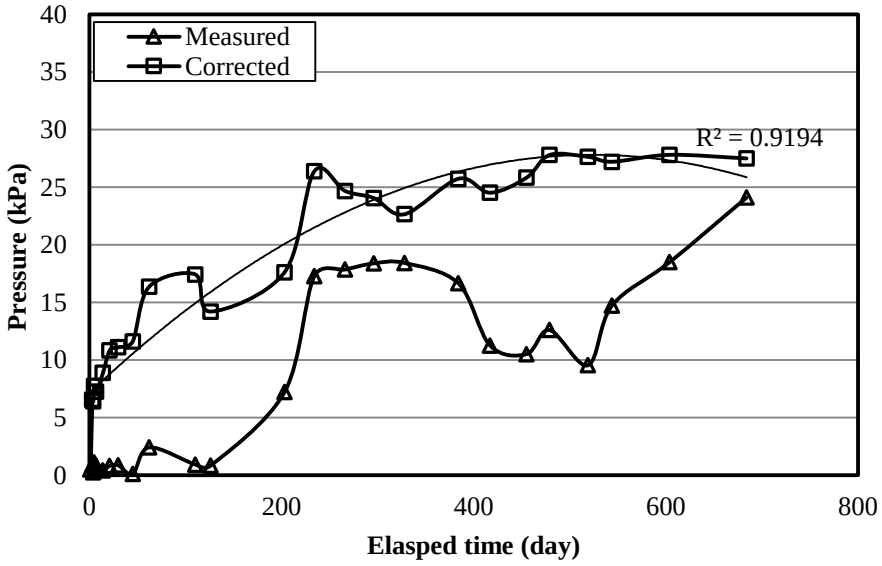

Figure 6.10 Corrected lateral earth pressure at the pipe springline in Section B

Figure 6.11 shows the measured and corrected vertical earth pressures at the shoulder in Section B. This figure also shows the corrected earth pressure at the shoulder generally increased with time and was around 35 kPa at 680 days. The VAF at the shoulder was 2.43.

Figure 6.12 shows the measured and corrected lateral earth pressures with time at the trench wall. The earth pressure at the trench wall generally increased with time and was approximately 20 kPa, which is lower than that next to the pipe at the same level. The earth pressure cell next to the pipe was subjected to additional lateral pressure from the pipe.

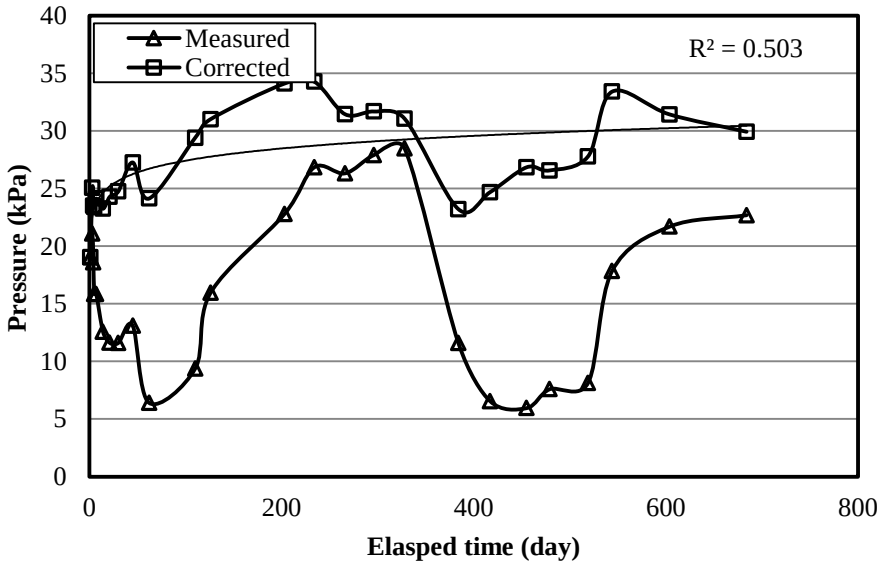

Figure 6.11 Corrected vertical earth pressure at the shoulder in Section B

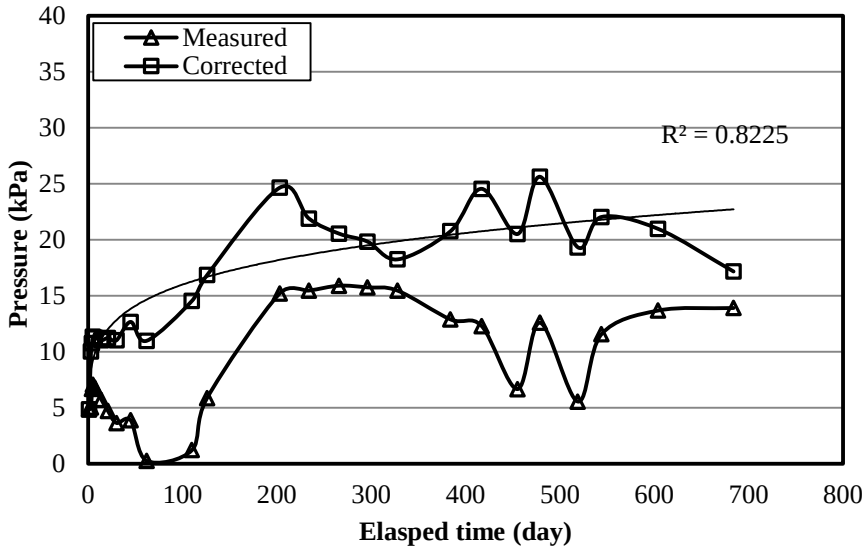

Figure 6.12 Corrected earth pressure at the trench wall at the pipe springline level in Section B

Figure 6.13 shows the measured and corrected vertical earth pressures at the pipe invert. The readings after the construction to 300 days were not reliable due to the wire connection problem; therefore, they are not provided. After the problem was fixed, the earth pressure was almost constant at 22.1 kPa.

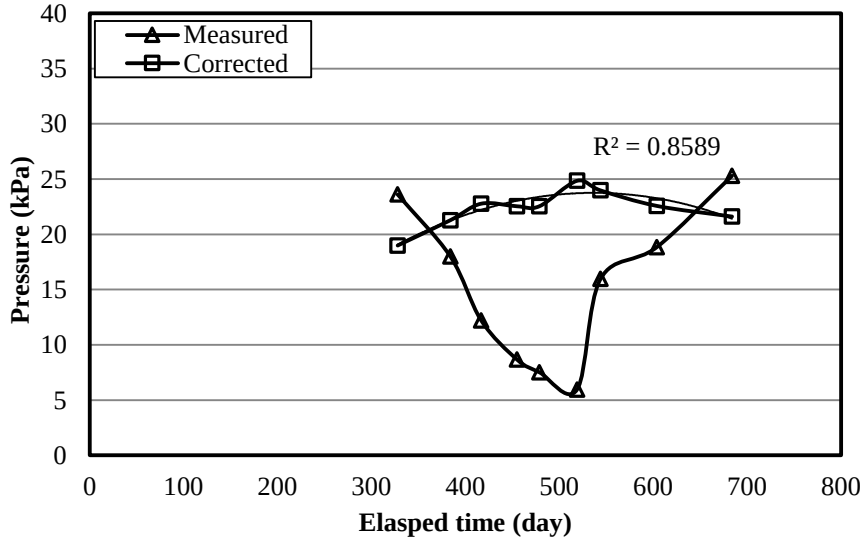

Figure 6.13 Corrected vertical earth pressure at the pipe invert in Section B

6.3.2 Deflections

Figure 6.14 shows the pipe deflection with the time in Section A. The pipe deflection in the horizontal direction increased up to approximately 0.6% while that in the vertical direction was 0.4% at 680 days. The diameter change at an angle of 45^{o} from the pipe crown decreased slightly with the time. These changes indicate that the pipe returned to a round shape after the installation due to the traffic loading and the creep of the pipe material.

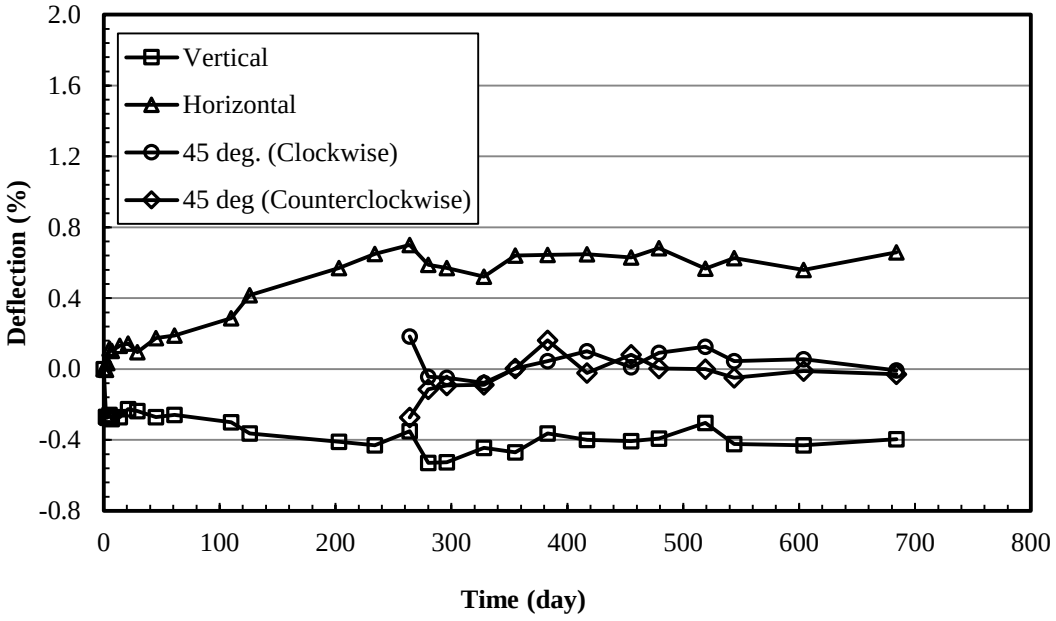

Figure 6.14 Pipe deflections with time in Section A

Figure 6.15 shows the pipe deflection with the time in Section B. The pipe deflections in the vertical and horizontal directions increased with the time and reached approximately 0.8% the pipe diameter in 680 days. This deflection increase can be attributed to the increase of the vertical earth pressure on the crown and the pipe creep deformation, which will be discussed in the next section. The diameter change at an angle of 45^{o} from the pipe crown decreased slightly with time.

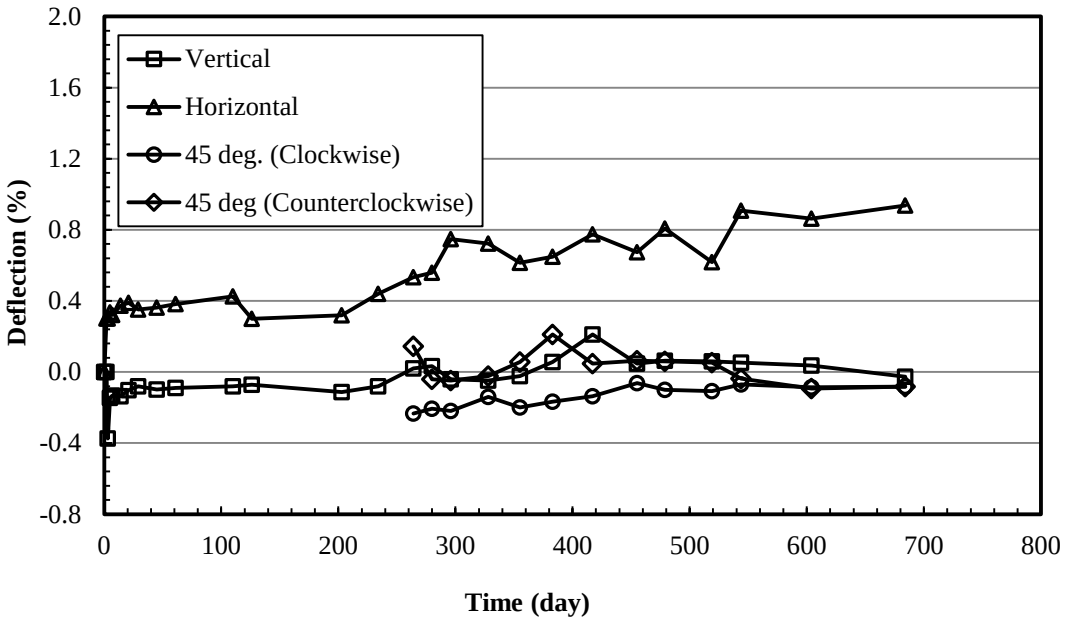

Figure 6.15 Pipe deflections with time in Section B

The deflections in the vertical and horizontal directions in Section A were smaller than those in Section B. The reason for this difference is that the AB3 aggregate in Section A had a higher modulus than the crushed stone in Section B and provided more lateral support for the pipe.

6.3.3 Strains

Test Section A

Four pairs of strain gages (outside and inside of the pipe) were attached on the plastic valley at the pipe crown in the longitudinal direction. Their distances to the roadway centerline were 838, 533, 228, and 76 mm, respectively. They are labeled as "L1, L2, L3, and L4" from the farthest point to the closest point to the centerline. Strains at the plastic valley and the plastic cover in this section were also adjusted using a factor of 1.29 according to Brachman et al. (2008). **Figure 6.16**

shows the longitudinal strains on the plastic valley at the pipe crown in Section A. Compared with the temperature curve, the longitudinal strains of the plastic valley at the pipe crown were not apparently affected by the temperature. As compared with the temperature curve, the longitudinal strains of the plastic valley at the pipe crown were not apparently affected by the temperature. For a clear presentation, the variation of the temperature is not included in later figures except for the case with an apparent temperature effect. The general trend is that the strains increased slightly with the time. The magnitude of the strains decreased with an increase of the distance to the centerline. The maximum longitudinal strain on the plastic valley at the pipe crown was approximately 0.3% at 75 mm from the roadway centerline.

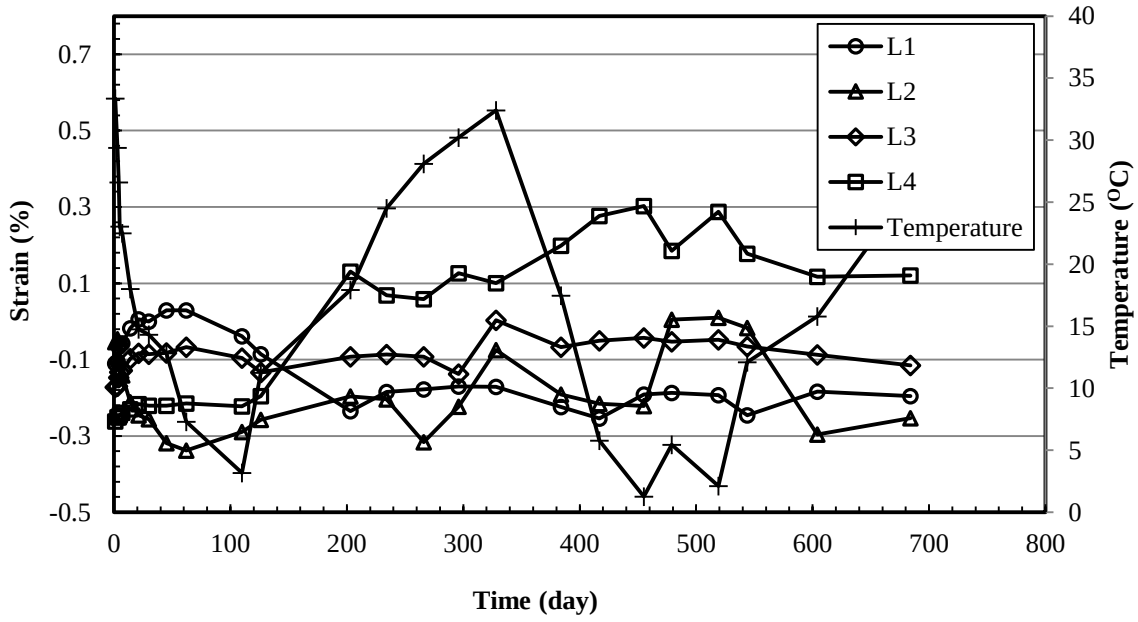

Figure 6.16 Longitudinal strains on the plastic valley at the pipe crown in Section A

Figure 6.17 shows the longitudinal strains on the plastic valley at the pipe springline and the invert in Section A. The longitudinal strains at the springline and the invert were not influenced by the temperature. The strains at the pipe invert and the springline varied with the maximum

value of -0.14 to -0.33%. The negative strains indicate that the plastic valley of the pipe in the longitudinal direction at the pipe springline and the pipe invert was under compression.

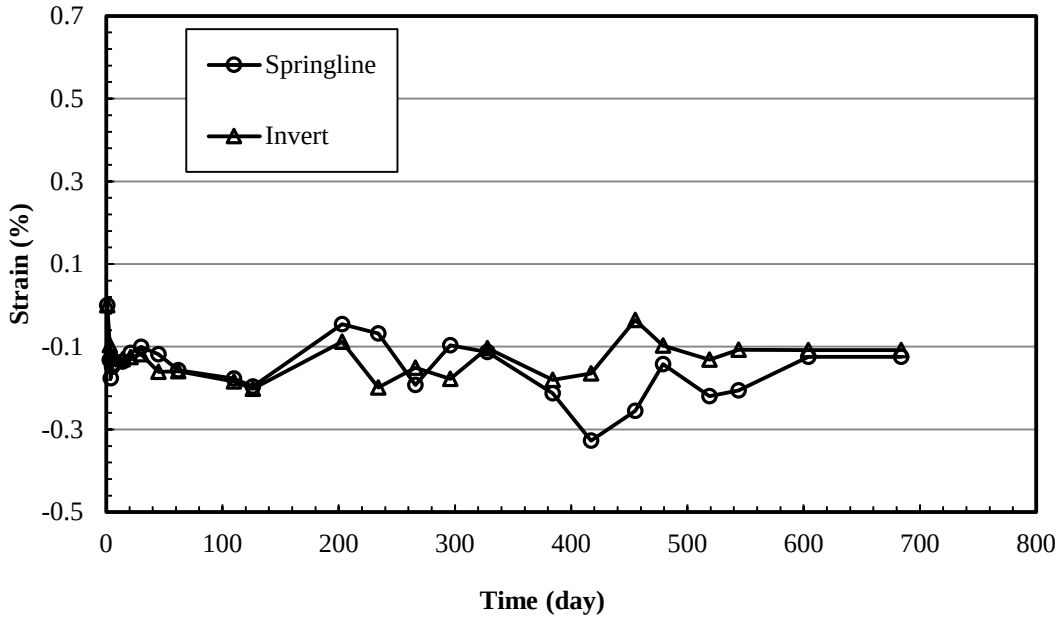

Figure 6.17 Longitudinal strains on the plastic valley at the pipe springline and invert in Section A

Figure 6.18 presents the circumferential strains of the plastic covers at the pipe crown, invert, and springline. The strains of the plastic cover varied with the temperature at all three locations. The maximum strain variation was 0.79% with a temperature change 27.^{o}C (i.e., from 5 to 32 ^{o}C). The strains at the pipe crown changed more significantly than other two locations. The strains at the pipe invert were the lowest ones. The strains at the springline and the crown increased from negative to positive values. The strains at the pipe invert were always negative.

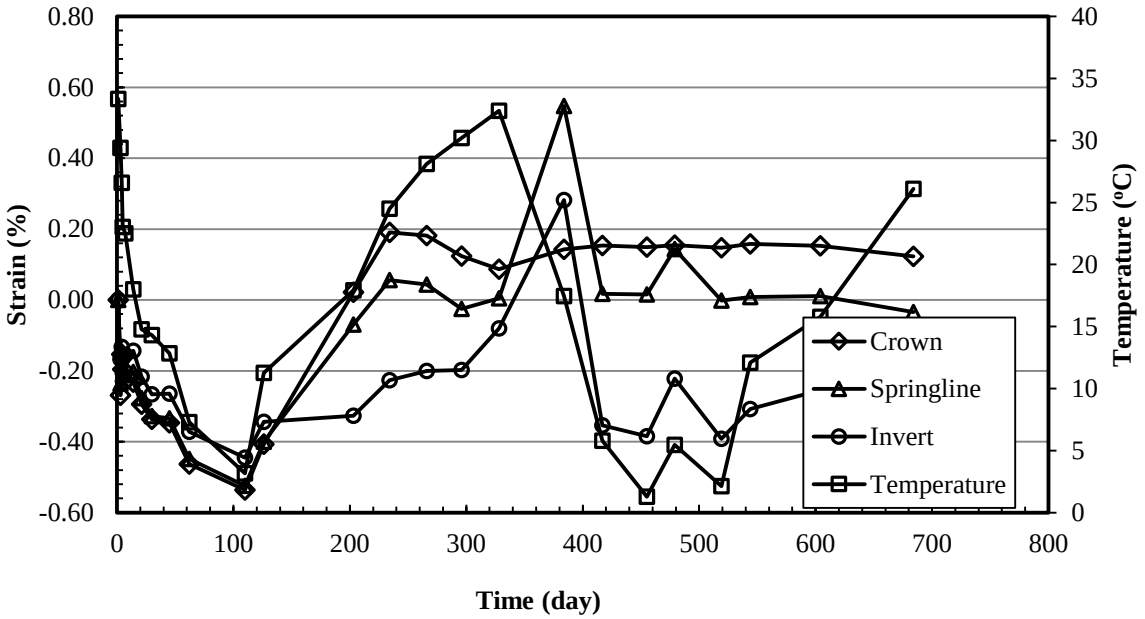

Figure 6.18 Circumferential strains of the plastic cover in Section A

Figure 6.19 presents the circumferential strains of the steel ribs at the pipe crown and the springline in Section A. The measured strains were not affected by the temperature. The strains at both the pipe crown and the springline were negative, indicating that the steel ribs were under compression. The strains at the pipe springline generally increased with time to 400 days after construction and then decreased. The strains at the pipe crown increased with the time. The maximum strain of the steel ribs in Section A was 0.17% at the pipe crown, which is less than the steel yield strain of 0.5%.

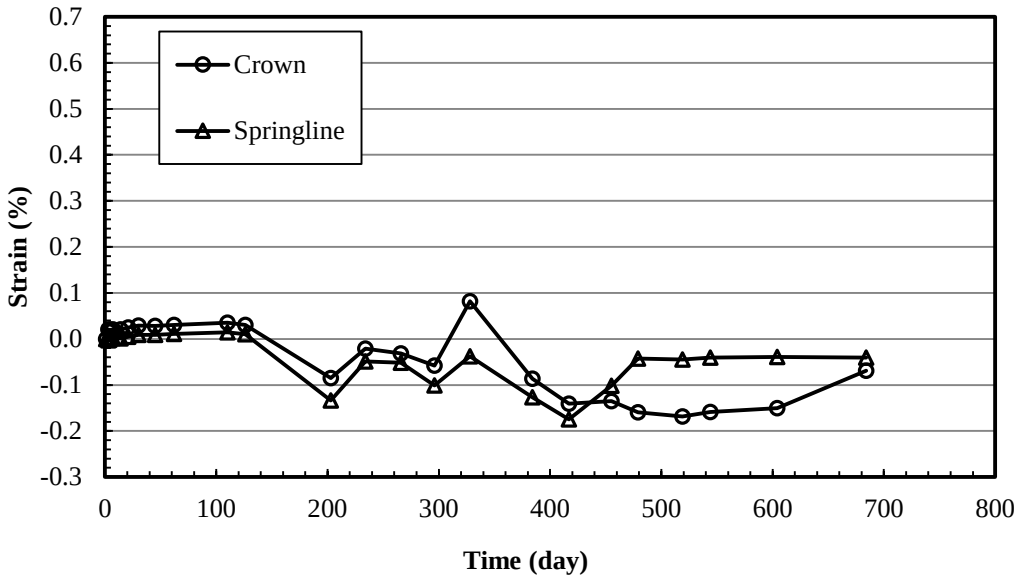

Figure 6.19 Circumferential strains of steel ribs in Section A

Test Section B

Figure 6.20 shows the longitudinal strains at the pipe valley at the pipe crown in Section B. There are some variations of the measured strains but generally the strains on the plastic valley in the longitudinal direction were almost constant through the observation time. Strains at the plastic valley and the plastic cover in this section were also adjusted using a factor of 1.29 according to Brachman et al. (2008). The magnitudes of the strains decreased with an increase of the distance to the centerline, which was consistent with that in Section A. The maximum strain on the plastic valley in the longitudinal direction was approximately 0.35% at 228.6 mm from the roadway centerline, which is 1.3 times that in Section A.

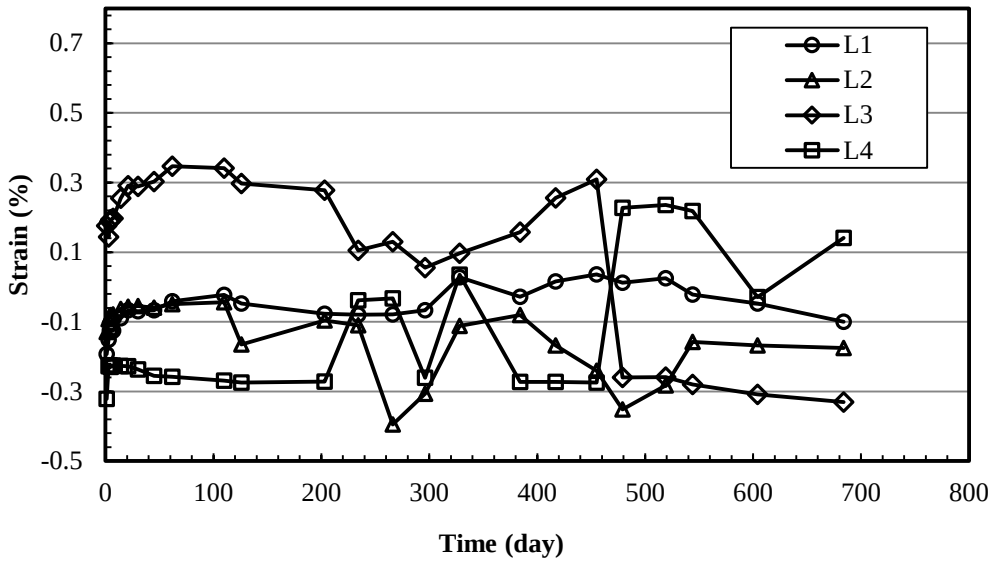

Figure 6.20 Longitudinal strains on the pipe valley at the pipe crown in Section B

Figure 6.21 shows the longitudinal strains of the plastic valley at the pipe springline and invert in Section B. The longitudinal strains of the plastic valley at the springline and the pipe invert mostly varied within 0.2%.

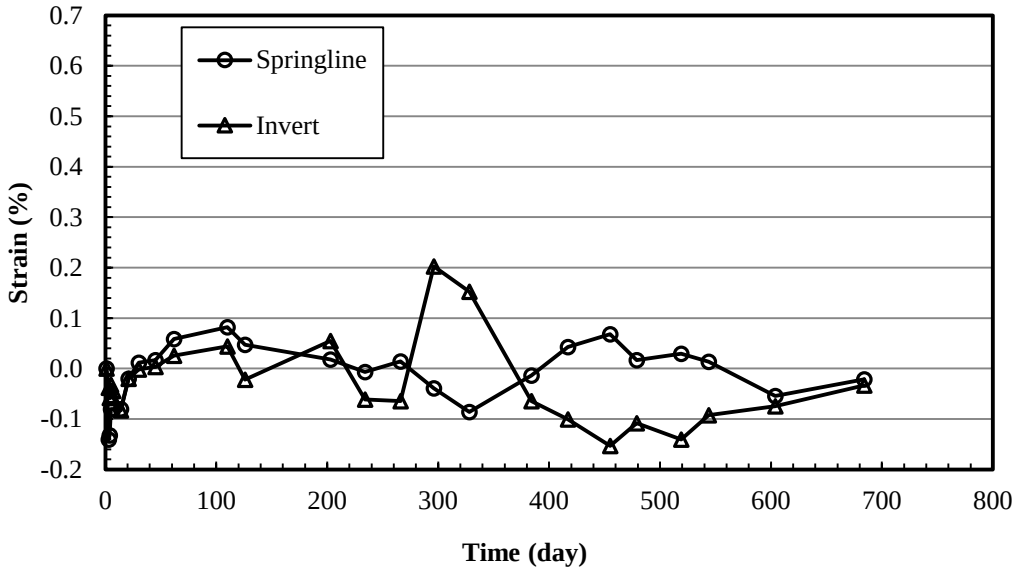

Figure 6.21 Longitudinal strains on the pipe valley at the pipe springline and the invert in Section B

Figure 6.22 presents the circumferential strains of the plastic covers at the pipe crown, invert, and springline. The strains of the plastic covers varied with the temperature at all three locations. The maximum strain variation was 0.57% with a temperature change of 27.^{o}C (i.e., from 5 to 32 ^{o}C). The strains at three locations were similar, and the strains at the pipe crown were slightly larger than strains at other locations. Their difference was approximately 0.1%. Most measured strains of the plastic covers were negative, indicating that the pipes in the circumferential direction in Section B were under compression.

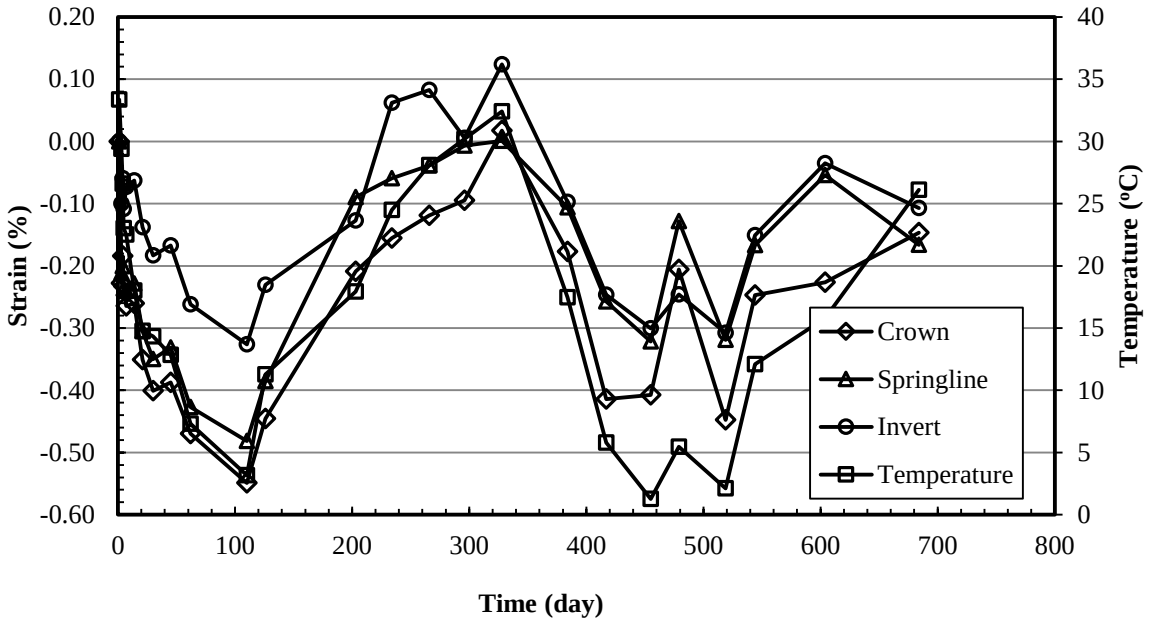

Figure 6.22 Circumferential strains of the plastic covers in Section B

Figure 6.23 presents the circumferential strains of the steel ribs at the pipe crown and the springline. They were not affected by the temperature. The positive strains at the springline illustrated the steel rib at the pipe springline was under tension. The negative strains at the pipe crown demonstrated that the steel rib at the pipe crown was under compression. The strains of the

steel ribs increased with the time. The maximum strain of the steel rib in Section B was 0.18%, which is lower than the steel yield strain of 0.5%.

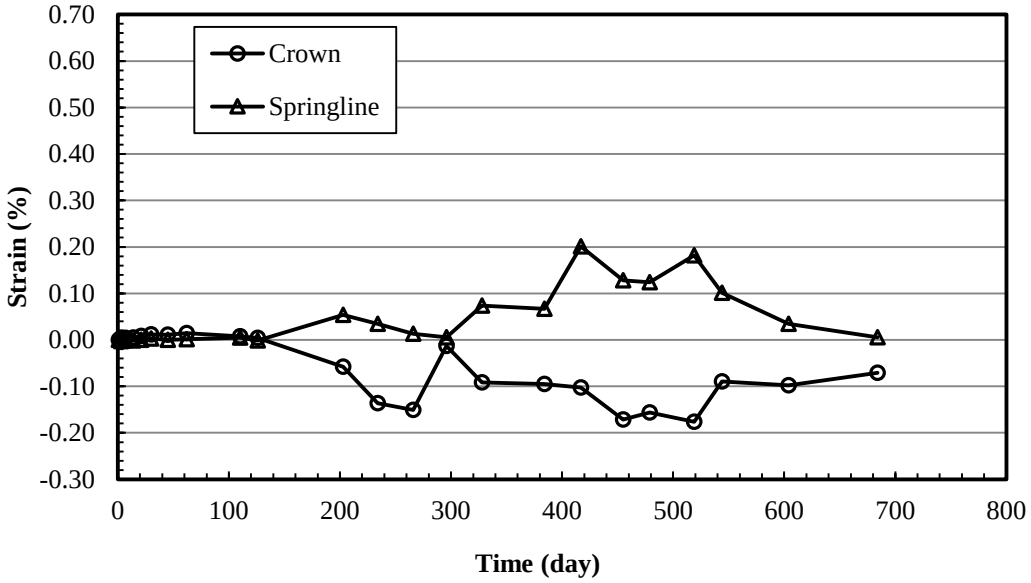

Figure 6.23 Circumferential strains of steel ribs in Section B

6.4 Long-Term Empirical Correlations

The design service life of a pipeline system is typically 100 years. So far, no field test data is available to evaluate the SRHDPE pipe performance in its design service life. A typical way to evaluate long-term performance of pipes is to establish an empirical correlation with the time based on field data in a relative long time. This method was also adopted in the current study. Based on the literature review, two parameters are important for the evaluation of long-term performance of HDPE pipes: VAF and pipe stiffness. VAF is essential to calculate the load above the pipe in the design, which can be used to calculate pipe deflections and strains. Internal forces, deflections, and strains of pipes depend on pipe stiffness or relative stiffness between pipe and backfill material.

The long-term stiffness of HDPE pipes has been investigated by several researchers (e.g., Hsuan and Zhang, 2005; and Hsuan and McGrath, 2005). Creep and degradation of the HDPE material with time influence long-term stiffness of the HDPE pipes. However, the stiffness of the SRHDPE pipe is expected to be different from the HDPE pipe since the SRHDPE pipe includes steel reinforcements. Therefore, it is necessary to evaluate the SRHDPE pipe stiffness under a long-term condition.

6.4.1 Vertical Soil Arching Factor

Figure 6.24 shows the variation of the VAFs with the time in Sections A and B, which can be approximately expressed by a linear relationship as follows:

$$VAF = 0.11\log(t) + 1.20 \text{ (AB3 aggregate)} \quad \text{(6-3a)}$$

$$VAF = 0.15\log(t) + 1.53 \text{ (crushed stone)} \quad \text{(6-3b)}$$

where VAF = the vertical soil arching factor at the pipe top and t = the time after the pipe installation (days).

Based on Equations (6-3a) and (6-3b), the VAFs for 50 and 100 years in Section A (the AB3 aggregate section) are 1.67 and 1.70, respectively, while they are 2.17 and 2.21 in Section B (the crushed stone section).

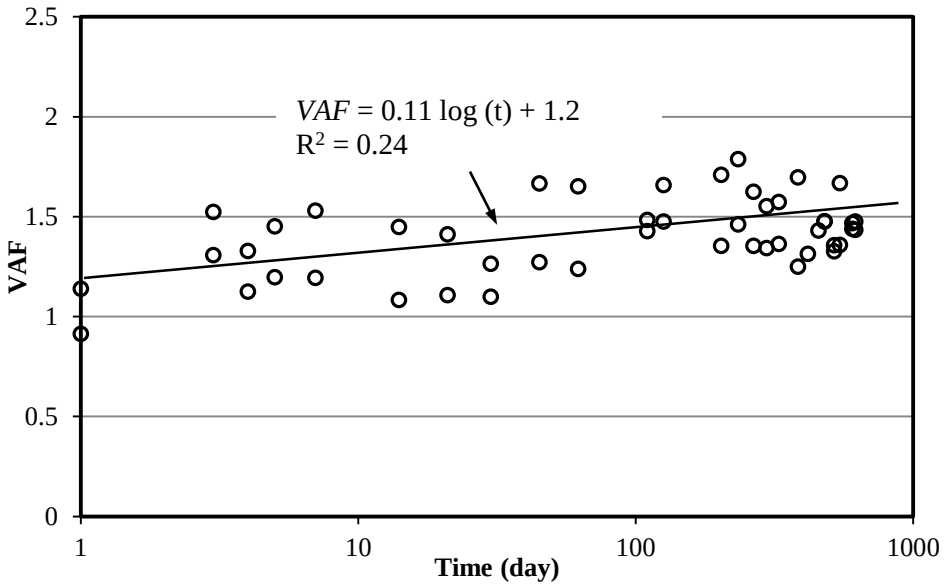

(a) Section A

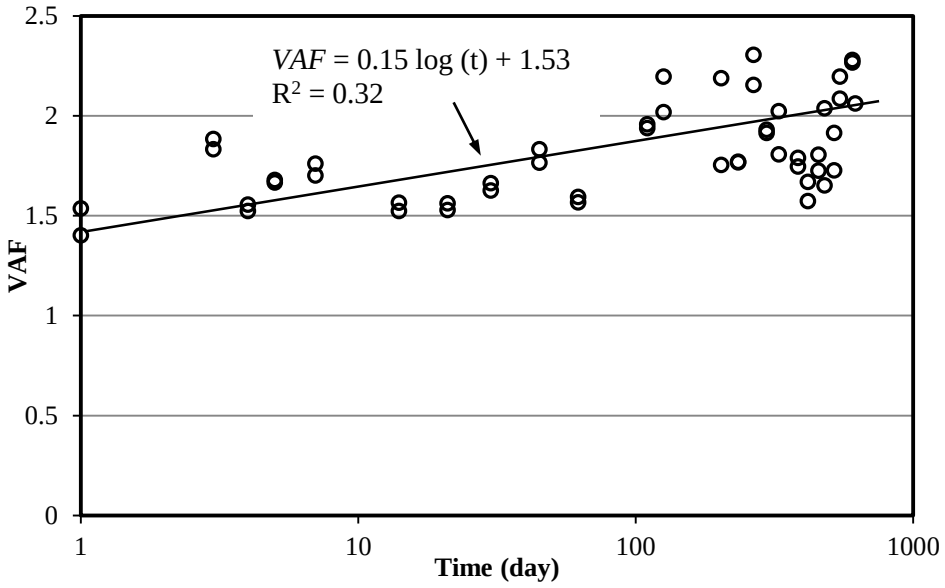

(b) Section B

Figure 6.24 Variation of the VAFs with the time

6.4.1 Pipe Stiffness

Pipe creep tests can be used to determine the pipe stiffness under a long-term condition. Khatri (2012) conducted a creep test on the SRHDPE pipe in air using a loading frame in the laboratory for 700 hours. Khatri (2012) found the stiffness (*EI*) factor of the pipe decreased by 25% in 700 hours, which can significantly influence the pipe performance. He pointed out that the stiffness reduction with time should be less if the pipe is buried in soil. Khatri (2012) used **Equation (6-4)** to back-calculate *EI*:

$$EI = 0.149R^3PS = 0.149R^3\frac{F}{\Delta y} \tag{6-4}$$

where R = the pipe radius, PS = the pipe stiffness, F = the load on the pipe, and Δy = the pipe deflection.

It should be noted that **Equation (6-4)** is only valid for pipes in air. The pipe stiffness of the pipe buried in the ground should be calculated using the Iowa Formula as follows:

$$\Delta Y = \frac{D_L K W_c r^3}{EI + 0.061E'r^3} \tag{6-5}$$

where D_L = the deflection lag factor; K = a bedding constant; W_c = Marston's load; r = the mean radius of a pipe; E = the modulus of elasticity of pipe material; I = the moment of inertia of pipe wall; E' = the modulus of passive resistance of side fill; ΔY = the vertical deflection or change in pipe diameter.

Figure 6.25 shows the variation of the pipe stiffness factor based on the field data calculated using **Equation (6-5)**, which can be approximately expressed as follows:

$$EI = -5.2\log(t) + 27.1 \text{ (AB3 aggregate)} \quad (6\text{-}6a)$$

$$EI = -3.73\log(t) + 19.9 \text{ (crushed stone)} \quad (6\text{-}6b)$$

where EI = pipe stiffness factor (kN·m^2/m) and t = the time after the pipe installation (days).

Based on Equations (6-6a) and (6-6b), the pipe stiffness factors at 1 day, 50 years, and 100 years in the AB3 aggregate section are 27.1, 4.9 and 3.4kN·m^2/m, respectively, while they are 19.9, 4.0, and 2.9 kN·m^2/m in the crushed stone section at the same time periods. The pipe stiffness factor in the AB3 aggregate section was higher than that in the crushed stone section due to the higher soil reaction modulus of the AB3 aggregate as compared with the crushed stone. The pipe stiffness factors at 100 years decreased by 87.5 and 85.2% from the initial values at 1 day in the AB3 aggregate section and the crushed stone section, respectively.

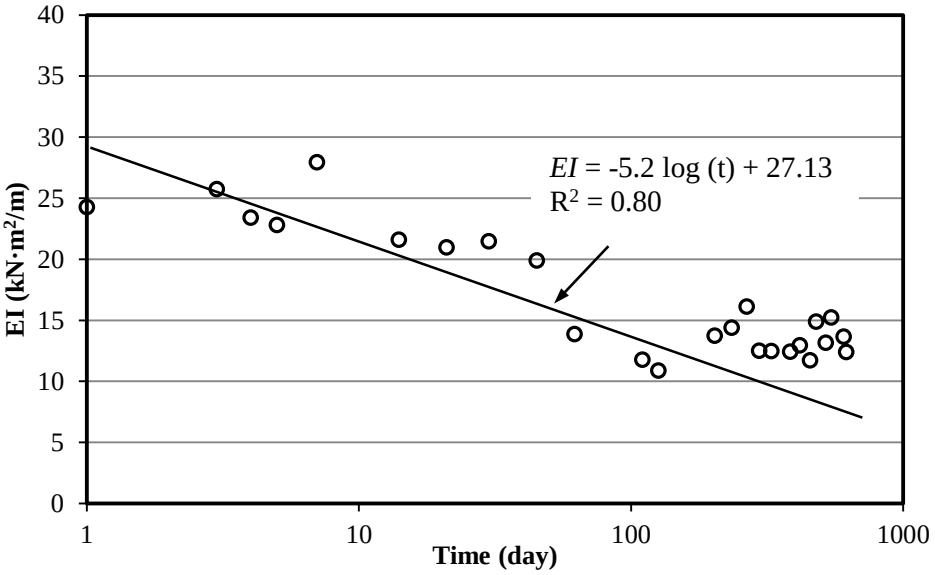

(a) Section A

Figure 6.25 Variation of the pipe stiffness factor with time for Sections A and B

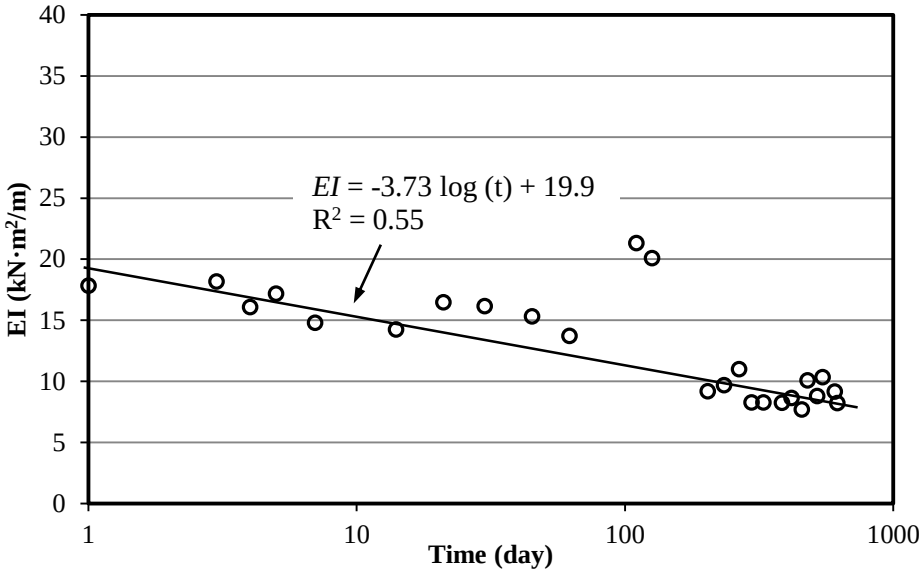

(b) Section B

Figure 6.25 Variation of the pipe stiffness factor with time for Sections A and B (continued)

6.5 Summary

The pipes in the Lawrence field test were monitored for 680 days after the construction. The variations of the earth pressures around the pipes, the deflections of the pipes, and the strains of the pipes with time were analyzed in this chapter. Long-term empirical correlations were developed for the vertical soil arching factor (VAF) and the pipe stiffness factor (*EI*) based on the field data. The following conclusions can be made from the analysis:

(1) The earth pressures generally increased at all locations in both sections. The VAFs were 1.57 and 1.98 after 680 days of construction in the AB3 aggregate section and the crushed stone section,

respectively. The lateral earth pressure coefficients next to the pipes were 0.72 and 1.39 in the AB3 aggregate section and the crushed stone section, respectively.

(2) The deflections of the pipe generally increased with time in the vertical and horizontal directions. The pipe diameter change was insignificant at 45^{o} from the pipe crown in both sections. The maximum deflections were 0.6 and 0.8% the pipe diameter in the AB3 aggregate section and the crushed stone section, respectively.

(3) The strains of the pipes mostly increased with time at all locations in both sections. The maximum strains occurred on the plastic valley in the longitudinal direction at the pipe crown, which were 0.30 and 0.35% in the AB3 aggregate section and the crushed stone section, respectively.

(4) Long-term empirical correlations were proposed based on the field data for vertical soil arching factor (VAF) and the pipe stiffness factor (*EI*). The VAFs would increase to 1.7 and 2.21 in the AB3 aggregate section and the crushed stone section in 100 years, respectively. The pipe stiffness factors in 100 years would decrease by 87.5% and 85.2% from the initial value at 1 day in the AB3 aggregate section and the crushed stone section, respectively.

CHAPTER 7 CONCLUSIONS AND RECOMMENDATIONS

7.1 Conclusions

SRHDPE pipe was developed and introduced to the market to overcome the disadvantages of HDPE pipes and steel pipes. However, no widely accepted design method is available for the SRHDPE pipe. To recommend design parameters, the performance of the SRHDPE pipe during installation and under traffic loading was investigated in this research using field test, numerical modeling and theoretical derivation. The following conclusions can be made from the results of this study:

1. The vertical arching factor (VAF) in the field tests during the installation was approximately 1.1, which indicated the SRHDPE pipe behaving like a metal pipe. The lateral earth pressure coefficient of the SRHDPE in the AB3 aggregate or the crushed stone was approximately 0.65. Peaking deflections were observed during pipe installation in both tests in a range of 0.25 to 1.80% pipe diameter. The maximum strain of the pipe occurred on the plastic valley in the longitudinal direction at the pipe crown, but it was much smaller than the strain limit of 5% suggested by AASHTO (2012);
2. The vertical pressure on the SRHDPE pipe induced by static loading on unpaved roads (i.e., during construction) can be calculated by the Giroud and Han (2004) method and the AASHTO (2012) method. The deflection of the SRHDPE pipe during the installation and the loading can both be calculated based on the Iowa formula;
3. The SRHDPE pipe behaved like a metal pipe in the cross section direction but like an HDPE pipe in the longitudinal direction;
4. No obvious damage was observed after the installation of SRHDPE pipes in the field;

5. Hardening soil model and EMM were effective to simulate the performance of the SRHDPE pipes under compaction in the numerical modeling;
6. Parametric study was conducted to evaluate the effects of the soil cover thickness, the trench width, the compaction pressure and the friction angle of the backfill material on the performance of the SRHDPE pipe under installation. Both of the vertical and horizontal deflections at end of the construction linearly increased with an increase of the soil cover thickness. The peaking deflections increased with an increase of the trench width and the magnitude of the compaction pressure. The effect of the friction angle on the pipe deflection is insignificant;
7. Based on the numerical results, the VAFs at the pipe top was 1.1 and the lateral earth pressure coefficient at the pipe springline was 0.65, which were both recommend for the design;
8. Partially-developed soil arching equations were derived to investigate the load transfer mechanism in the soil cover above the SRHDPE pipe during installation and under traffic loading. Two examples were provided to illustrate the calculation procedures of the proposed methods;
9. Sensitivity analysis was conducted for parameters in the partially-developed soil arching equations. The results indicated that the effects of the unit weight and the friction angle of the backfill were insignificant; while the effects of the cavity width, the embankment height, the surcharge and the degree of compaction were significant;
10. The VAFs were 1.57 and 1.98 in the AB3 aggregate and the crushed stone, respectively after 680 days of construction;

11. The vertical and horizontal deflections of the pipes generally increased with time and the maximum deflections were 0.6 and 0.8% pipe diameter in the AB3 aggregate and the crushed stone, respectively;
12. The measured strains generally increased with time at most locations in the field sections. The maximum strains occurred on the plastic valley in the longitudinal direction at the pipe crown were 0.3 and 0.35% in the AB3 aggregate and the crushed stone, respectively up to 680 days after pipe installation; and
13. Long-term empirical correlations were developed for the VAF and the pipe stiffness factor (*EI*) with time based on the field data.

7.2 Recommendations

Based on the results in this study, the load on the pipe, the pipe deflection, the strain and stress of the longitudinal direction can be calculated during installation and under traffic loading. The author would like to make the following recommendations:

1. Hardening soil model and EMM can be used to simulate the performance of the SRHDPE pipe under compaction;
2. Partially-developed soil arching equations should be adopted to investigate the coupled effect of the displacement and load transfer in the soil cover above the SRHDPE pipe during installation and under traffic loading;
3. Earth pressure, pipe deflection and strains of the pipe all increased with time. The empirical correlations proposed in this study can be used to investigate the long-term behavior of the SRHDPE pipe;
4. The VAF at the pipe top can be assumed as 1.1 during installation in the design;

5. This research was based on SRHDPE pipes with diameters of 0.6 and 0.9 m. Pipe size may affect the behavior and performance of SRHDPE pipes. Further research is needed to verify the results and conclusions from this research for other pipe sizes;
6. All pipes investigated in this research were installed above the groundwater table. Possible effects of groundwater on the behavior and performance of SRHDPE pipes were not investigated in this research and deserve further research;
7. The time effect on the behavior and performance of SRHDPE pipes was investigated in the field up to 680 days. Long-term behavior of the pipes should be verified with a longer time period; and
8. SRHDPE pipes are made of a composite material (steel ribs and plastic covers), which has anisotropic behavior. A design method considering anisotropic pipe materials should be developed to better design SRHDPE pipes.

REFERENCES

American Association of State Highway and Transportation Officials (AASHTO). (2012): *AASHTO LRFD Bridge Design Specifications* (Third Edition), Washington, D. C.

American Association of State Highway and Transportation Officials (AASHTO) M145. (2003). "Classification of soil and soil-aggregate mixtures for highway construction purposes." Washington, D. C.

American Concrete Pipe Association (ACPA) (2009). *Steel-Reinforced High-Density Polyethylene Pipe*. A education document for users and specifiers.

Arockiasamy, M., Chaallal, O., and Limpeteeprakarn, T. (2006). "Full-scale field tests on flexible pipes under live load application." *Journal of performance of constructed facilities*, 20(1), 21-27.

Antaki, G. A. (1997). *A Review of Methods for the Analysis of Buried Pressure Piping*. *Welding Research Council Bulletin* 425, New York.

ASTM A798-13 (2013). "Standard practice for installing factory-made corrugated steel pipe for sewers and other applications." *Annual Book of ASTM Standards, ASTM International*, West Conshohocken, PA.

ASTM C1479-13 (2013). "Standard practice for installation of precast concrete sewer, storm drain, and culvert pipe using standard installations." *Annual Book of ASTM Standards, ASTM International*, West Conshohocken, PA.

ASTM D1557-12 (2012). "Standard test methods for laboratory compaction characteristics of soil using modified effort." *Annual Book of ASTM Standards*, ASTM International, West Conshohocken, PA.

ASTM D2321-14 (2014). “Standard practice for underground installation of thermoplastic pipe for sewers and other gravity-flow applications.” *Annual Book of ASTM Standards, ASTM International*, West Conshohocken, PA.

ASTM D2412-11(2011). “Standard test method for determination of external loading characteristics of plastic pipe by parallel-plate loading.” *Annual Book of ASTM Standards, ASTM International*, West Conshohocken, PA.

ASTM D2487-11 (2011). “Standard practice for classification of soils for engineering purpose.” *Annual Book of ASTM Standards*, ASTM International, West Conshohocken, PA.

ASTM D4253-14 (2014). “Standard test methods for maximum index density and unit weight of soils using a vibratory table.” *Annual Book of ASTM Standards*, ASTM International, West Conshohocken, PA.

ASTM F2562-08 (2008). “Specification for steel reinforced thermoplastic ribbed pipe and fittings for non-pressure drainage and sewerage.” *Annual Book of ASTM Standards, ASTM International*, West Conshohocken, PA.

Bhandari, A. (2010). *Micromechanical Analysis of Geosynthetic-Soil Interaction under Cyclic Loading*. Ph.D. Dissertation, the University of Kansas, Lawrence, KS.

Blake, A. (1959). “Deflection of a thick ring in diametral compression by test and by strength of material theory.” *Journal of Applied Mechanics*, 26(2), 294-295.

Brachman, R.W.I., Moore, I.D., and Munro, S.M (2008). “Compaction effects on strains in thermoplastic culverts.” *Geosynthetic International*, 15(2), 72-85.

Cameron, D.A. (2006). *Analysis of Buried Pipes in Granular Backfill Subjected to Construction Traffic*. Ph.D. Dissertation, the University of Sydney, Sydney, Australia.

Centers for Diseases Control and Prevention (2015). *Fluoridation of Drinking Water and Corrosion of Pipes in Distribution Systems Fact Sheet*. http://www.cdc.gov/fluoridation/factsheets/engineeering/corrosion.htm

Chaallal, O., Arockiasamy, M. and Godat, A. (2013). "Laboratory tests to evaluate mechanical properties and performance of various flexible pipes." *Journal of Performance of Constructed Facilities*, 04014130, 1-15.

Chen, H.L., Shah, S.P., and Keer, L.M. (1990). "Dynamic response of shallow-buried cylindrical structures." *ASCE Journal of Engineering Mechanics*, 116 (1), 152-171.

Chen, Y.M., Cao, W.P., and Chen, R.P. (2008). "An experimental investigation of soil arching within basal reinforced piled embankments." *Geotextiles and Geomembranes*, 26, 164-174.

Chen, T.J. and Fang, Y.S. (2008). "Earth pressure due to vibratory compaction." *ASCE Journal of Geotechnical and Geoenviromental Engineering*, 134(4), 437-444.

China Association for Engineering Construction Standardization (CECS). (2004). "Technical specification for buried PE pipeline of sewer engineering." *China Architecture and Building Specifications*, Beijing, China.

Clough, W., and Duncan, J.M. (1971). "Finite element analysis of retaining wall behavior." *Journal of the Soil Mechanics and Foundation Division*, 97(SM12), 1657-1673.

Corey, R., Han, J., Khatri, D. K., and Parsons, R. L. (2014). “Laboratory study on geosynthetic protection of buried steel-reinforced HDPE pipes from static loading.” ASCE *Journal of Geotechnical and Geoenvironmental Engineering*, 140(6), 1-10.

Duncan, J.M. and Seed, R.B. (1986). “Compaction-induced earth pressures under K0 conditions.” *Journal of Geotechnical Engineering*, 112(1), 1-12.

Duncan, J.M., Williams, G.W., Sehn, A.L. and Seed, R.B. (1991). “Estimation earth pressure due to compaction.” *Journal of Geotechnical Engineering*, 117(12), 1833-1847.

Elshimi, T.M., and Moore, I.D. (2013). “Modeling the effects of backfilling and soil compaction beside shallow buried pipes.” *Journal of Pipeline System Engineering and the Practice*, 04013004, 1-7.

Evans, C.H. (1983). *An Examination of Arching in Granular Soils*, M.S. Thesis, MIT.

Filz, G.M. and Duncan, J.M. (1996). “Earth pressures due to compaction: comparison of theory with laboratory and field behavior.” *Transportation Research Record*, 1526, 28-37.

Flener, E.B. (2010). “Soil-steel interaction of long-span box culvert-performance during backfilling.” *Journal of Geotechnical and Geoenviromental Engineering*, 136(6), 823-832.

Folkman, S.L. (2011). *Monitoring of DuroMaxx Pipes Installed on Manhead Road in Rich County Utah (First Three Inspections). Final Report* Submitted to Utah Department of Transportation Research Division by Utah State University.

Geokon (2011) “Instruction manual for VW earth pressure cells.” *Geokon, Inc*.

Getzler, Z., Gellert, M., and Eitan, R. (1970). “Analyis of arching pressures in ideal elastic soil.” *Journal of the Soil Mechanics and Foundations Division*, 96(SM4), 1357-1372.

Giroud, J.P. and Han, J. (2004). "Design method for geogrid-reinforced unpaved roads, part I theoretical development." *ASCE Journal of Geotechnical and Geoenvironmental Engineering*, 130 (8), 776-786.

Hall, W. J., and N. M. Newmark. (1977). "Seismic design criteria for pipelines facilities." In *Proceedings of the Conference on the Current State of Knowledge of Lifeline Earthquake Engineering*. American Society of Civil Engineers. New York.

Han, G.X., Gong, Q.M., and Zhou, S.H. (2011). "Mechanical analysis of soil arching under dynamic Loads." *Proceedings of Pan-AM CGS Geotechnical Conference*.

Han, J. (2015). *Principles and Practice of Ground improvement*, John Wiley and Sons, Hoboken, New Jersey.

Han, J., Wang, F., Khatri, D.K., and Parsons, R.L. (2015). *Establishing a Design Procedure for Buried Steel-Reinforced High Density Polyethylene (SRHDPE) Pipes (Phase II)*, Final Report, KDOT, K- TRAN: KU-14-4.

Hardert, M.T., (2011). *Shape Measurement of Existing 120" Diameter*. Report Submitted to Contech Construction Products, Inc.

Harris, G.W. (1974). "A sandbox model used to examine the stress distribution around a simulated longwall coal-face." *International Journal of Rock Mechanics, Mining Sciences and Geomechanical Abstracts*, 11, 325-355.

Hartley, J.P. and Duncan, J.M. (1987). "*E*' and its variation with depth." ASCE *Journal of Transportation Engineering*, 113 (5), 538-553.

Helwany, S. B., and A. H. Chowdhury (2004). "Laboratory impulse tests for soil-underground structure interaction." *Journal of Testing and Evaluation*, 32 (4), 262-273.

Hewlett, W.J., and Randolph, M.F. (1998). "Analysis of piled embankments." *Ground Engineering*, 21(3), 12-18.

Hsuan, Y.G. and McGrath, T.J. (2005) *Protocol for Predicting Long-term Service of Corrugated High Density Polyethylene Pipes*, Final report prepared for Florida DOT.

Hsuan, Y.G., and Zhang, J.Y. (2005). "Stress crack resistance of corrugated high-density polyethylene pipes in different test environments and temperatures." *Transportation Research Record*, 1928, 221-225.

Howard, A. (1996). *Pipeline Installation*, Relativity Publishing, Lakewood, Colo.

Iglesia, G., Einstein, H.H., and Whitman, R.V. (1990). *Stochastic and Centrifuge Modeling of Jointed Rock Vol II – Centrifuge Modeling of Jointed Rock*. US Air Force Office of Scientific Research.

Kansas Department of Transportation (2007). *Standard Specification for Pipe and Culvert*, Kansas Department of Transportation (KDOT), Topeka, KS.

Katona, M.G. (1978). "On the analysis of long-span culverts by the finite element method." *Transportation Research Record*, 678, 59-66.

Katona, M.G. (1988). *Minimum Cover Heights for HDPE Corrugated Plastic Pipe under Vehicular Loading*, Report to Corrugated Plastic Tubing Association.

Katona, M.G. (2015a). "Modifying duncan-selig soil model for plastic-like behavior." Presented at *the 94th Annual Meeting of the Transportation Research Board*, Washington, D.C., 2015.

Katona, M.G. (2015b). “Influence of soil models on performance of buried culverts.” Presented at *the 94th Annual Meeting of the Transportation Research Board*, Washington, D.C., 2015.

Khatri, D.K. (2012). *Experimental Evaluation of the Behavior of Steel-Reinforced High Density Polyethylene (SRHDPE) Pipes*, MS Thesis, the University of Kansas, Lawrence, KS, USA.

Khatri, D. K., Han, J., Parsons, R. L., Young, B., Brennan, J. J., and Corey, R. (2013). “Laboratory evaluation of deformations of steel-reinforced high-density polyethylene pipes under static loads.” *Journal of Materials in Civil Engineering*, 25(12), 1964-1969.

Khatri, D. (2014). *Laboratory and Field Performance of Buried Steel-Reinforced High Density Polyethylene (SRHDPE) Pipes in a Ditch Condition under a Shallow Cover*. Ph.D. Dissertation, the University of Kansas, Lawrence, KS.

Khatri, D.K., Han, J., Corey, R., Parsons, R.L., and Brennan, J.J. (2015). “Laboratory evaluation of installation of a steel-reinforced high-density polyethylene pipe in soil.” *Tunnelling and Underground Space Technology*, 49, 199-207.

Konder, R.L. and Zelasko, J.S. (1963). “A hyperbolic stress strain formulation for sands.” *Proceedings of 2nd Pan-Am Conference on Soil Mechanics and Foundation Engineering*, Rio de Janeiro, Brazil, 1, 289-324.

Krizek, R.J., Parmelee, R.A., Kay, N.J., and Elnaggar, H.A. (1971). “Structural analysis and design of buried culverts.” *National Cooperative Highway Research Program Report 116*. Washington: National Research Council.

Li, Y.G. (2009). *Study on Unified Calculation Theory of Earth Pressure on Top of Trench-Buried Culverts and Positive-Buried Culverts*. PhD thesis. Taiyuan University of Technology, Taiyuan, China.

Lischer, V.C. (1969). "AWWA pipe standards in pipeline engineering." *Journal of American Water Works Association*, 455-459.

Mai, V. T., Hoult, N. A., and Moore, I. D. (2014). "Effect of deterioration on the performance of corrugated steel culverts." *Journal of Geotechnical and Geoenvironmental Engineering*, *140*(2).

Mamlouk, M. S., and Zaniewski, J. P. (2011). *Materials for Civil and Construction Engineers*, Third Edition, Pearson Prentice Hall, Upper Saddle River, NJ, USA.

Matyas, E.L., and Davis, J.B. (1983). "Prediction of vertical earth loads on rigid pipes." *Journal of Geotechnical Engineering*, 109(2), 190-201.

Marston, A., and Anderson, A. O. (1913). *The Theory of Loads on Pipes in Ditches and Tests of Cement and Clay Drain Tile and Sewer Pipe*. Iowa State College of Agriculture and Mechanic Arts.

Marston, A. (1930). "The theory of external loads on closed conduits in the light of the latest experiments." *Highway Research Board Proceedings*, 9.

Masada, T., and Sargand, S. M. (2007). "Peaking deflections of flexible pipe during initial backfilling process." *Journal of Transportation Engineering*, *133*(2), 105-111.

McAffee, R.P., and Valsangkar, A.J. (2008). "Field performance, centrifuge testing, and numerical modelling of an induced trench installation." *Canadian Geotechnical Journal*, 45(1), 85-101.

McGrath, T.J. (1998). "Replacing E' with the constrained modulus in flexible pipe design." In *Proceedings of the Pipeline Division Conference*, San Diego, ASCE.

McGrath, T. J., Selig, E. T., Webb, M. C., and Zoladz, G. V. (1999). *Pipe Interaction with the Backfill Envelope.* No. *FHWA-RD-98-191,* Final Report, the National Science Foundation and the Federal Highway Administration, University of Massachusetts, Amherst, Mass.

Meyerhof, G. G., and Adams, J. I. (1968). "The ultimate uplift capacity of foundations." *Canadian Geotechnical Journal*, 5(4), 225-244.

Meyerhof, G. G., and L. D. Baike. (1963). "*Strength of steel culverts sheets bearing against compacted sand backfill*." *Highway Research Board Proceedings* 30.

Mlynarski, M., Katona, M.G., and McGrath, T.J. (2007). Modernize and Upgrade CANDE for Analysis and Design of Buried Structures. *NCHRP Final Report 15-28*, 46p.

Molin, J. (1981). "Flexible pipe buried in clay." *Proceedings of International Conference on Underground Plastic Pipes*, ASCE, J. Schrock (ed.), New Orleans, 322-337.

Moore, I.D. (2009). *DuroMaxx Pipe Assessment.* Final Report Submitted to Contech Construction Products Inc.

Moser, A. P., and Folkman, S. (2008). *Buried Pipe Design (Third Edition)*. New York: McGraw-Hill Professional.

Rogers, C.D.F., Fleming, P.R., Loeppky, M.W.J., and Faragher, E. (1995). "The structural performance of profile-wall drainage pipe-stiffness requirements contrasted with the results of laboratory and field tests." *Transportation Research Record 1514*, Transportation Research Board, Washington, D.C., 83–92.

Sakaguchi, H. and Ozaki, E. (1992). "Analysis of the formation of arches plugging the flow of granular materials." *Proceedings of the Second International Conference On Discrete Element Method*, MIT, Cambridge, Massachusetts, 153-163.

Sargand, S., Masada, T.J., and Hurd, J.O. (1998). "Effect of rib spacing on deformation of profile wall plastic pipes buried in coarse granular backfill." *ASTM Geotechnical Testing Journal*, 19(2), 217-222.

Sargand, S.M., Masada, T., and Schehl, D.J. (2001). "Soil pressure measured at various fill heights above deeply buried thermoplastic pipe." *Transportation Research Record* 1770, 227-235.

Sargand, S., Masada, T., Tarawneh, B., and Gruver, D. (2008). "Deeply buried thermoplastic pipe field performance over five years." *Journal of Geotechnical and Geoenvironmental Engineering*, 134(8), 1181-1191.

Schofield, A.N. (1980). "Cambridge geotechnical centrifuge operations." *Geotechnique*, 30(3): 227-268.

Seed, R.B. and Duncan, J.M. (1986). "FE analysis: compaction-induced stresses and deformations." *Journal of Geotechnical Engineering*, 112(1), 23-43.

Spangler, MG. (1941). *The Structural Design of Flexible Pipe Culverts*, Iowa State College Engineering Experimental Station, Iowa State College, Ames, Iowa.

Spangler, M.G. (1962). *Culverts and Conduits*. New York: McGraw-Hill. 965-999.

Taleb, B., and Moore, I.D. (1999). "Metal culvert response to earth loading performance of two-dimensional analysis." *Transportation Research Record*, 1556, 25-36.

Terzaghi, K. (1936). "Stress distribution in dry sand and in saturated sand above a yielding trap door." *Proceedings of Frist International Conference on Soil Mechanics and Foundation Engineering*, Cambridge, Massachusetts, 307-311.

Terzaghi, K. (1943). *Theoretical Soil Mechanics*. John Wiley and Sons, New York, 66-76.

Wang, F., Han, J., Khatri, D. K., Parsons, R. L., Brennan, J.J. and Guo, J. (2015). "Field installation effect on buried steel-reinforced high density polyethylene pipes." *Journal of Pipeline System Engineering and the Practice*, published online.

Watkins, R. K., & Spangler, M. G. (1958). "Some characteristics of the modulus of passive resistance of soil: a study in similitude." *Highway Research Board Proceedings*, Vol. 37.

Webb, M.C., McGrath, T.J., and Selig, E.T. (1996). "Field tests of buried pipe installation procedures." *Transportation Research Record* 1541, 97-106.

Yang, X., Han, J., Leshchinsky, D. and Parsons, R.L. (2012). "A three-dimensional mechanistic-empirical model for geocell-reinforced unpaved roads." *Acta Geotechnica*, 8(2), 201-213.